



**HAL**  
open science

# Shaping the spectrum of carbon nanotube quantum dots with superconductivity and ferromagnetism for mesoscopic quantum electrodynamics

Tino Cubaynes

► **To cite this version:**

Tino Cubaynes. Shaping the spectrum of carbon nanotube quantum dots with superconductivity and ferromagnetism for mesoscopic quantum electrodynamics. Quantum Physics [quant-ph]. Sorbonne Université, 2018. English. NNT : 2018SORUS195 . tel-02448439

**HAL Id: tel-02448439**

**<https://theses.hal.science/tel-02448439>**

Submitted on 22 Jan 2020

**HAL** is a multi-disciplinary open access archive for the deposit and dissemination of scientific research documents, whether they are published or not. The documents may come from teaching and research institutions in France or abroad, or from public or private research centers.

L'archive ouverte pluridisciplinaire **HAL**, est destinée au dépôt et à la diffusion de documents scientifiques de niveau recherche, publiés ou non, émanant des établissements d'enseignement et de recherche français ou étrangers, des laboratoires publics ou privés.

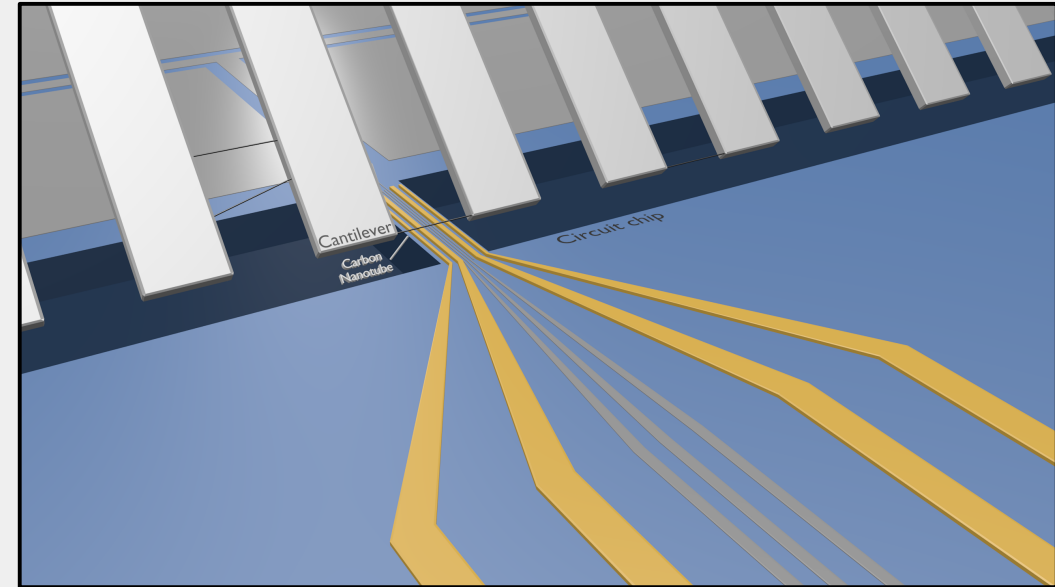
In this thesis, we study carbon nanotubes based quantum dot circuits embedded in a microwave cavity. This general architecture allows one to simultaneously probe the circuit via quantum transport measurements and using circuit quantum electrodynamics techniques. The two experiments realized in this thesis use metallic contacts of the circuit as a resource to engineer a spin sensitive spectrum in the quantum dots. The first one is a Cooper pair splitter which was originally proposed as a source of non-local entangled electrons. By using cavity photons as a probe of the circuit internal dynamics, we observed a charge transition dressed by coherent Cooper pair splitting. Strong charge-photon coupling in a quantum dot circuit was demonstrated for the first time in such a circuit. A new fabrication technique has also been developed to integrate pristine carbon nanotubes inside quantum dot circuits. The purity and tunability of this new generation of devices has made possible the realization of the second experiment. In the latter, we use two non-collinear spin-valves to create a coherent interface between an electronic spin in a double quantum dot and a photon in a cavity. Highly coherent spin transitions have been observed. We provide a model for the decoherence based on charge noise and nuclear spin fluctuations.

Tino Cubaynes

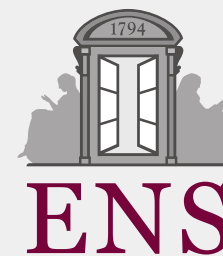
Shaping the spectrum of carbon nanotube quantum dots with superconductivity and ferromagnetism for mesoscopic quantum electrodynamics

2018

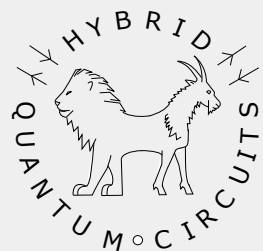
## Shaping the spectrum of carbon nanotube quantum dots with superconductivity and ferromagnetism for mesoscopic quantum electrodynamics



**Tino Cubaynes**  
LPENS- PARIS



Département  
de Physique  
—  
École Normale  
Supérieure



# SORBONNE UNIVERSITÉ

THÈSE de DOCTORAT préparée à L'ÉCOLE NORMALE SUPÉRIEURE

Spécialité : Physique

présentée par

**Tino Cubaynes**

Pour obtenir le titre de  
DOCTEUR de SORBONNE UNIVERSITÉ

Sujet de la thèse :

**SHAPING THE SPECTRUM OF CARBON NANOTUBE  
QUANTUM DOTS WITH SUPERCONDUCTIVITY AND  
FERROMAGNETISM FOR MESOSCOPIC QUANTUM  
ELECTRODYNAMICS**

Soutenue le 7 décembre 2018 devant le jury composé de :

M.	Kasper GROVE-RASMUSSEN	Rapporteur
M.	Christopher BÄUERLE	Rapporteur
Mme.	Hélène BOUCHIAT	Examinatrice
M.	Denis FEINBERG	Examineur
M.	Michel BRUNE	Examineur
M.	Takis KONTOS	Directeur de thèse
Mme.	Audrey COTTET	Membre invité

## Abstract

In this thesis, we study carbon nanotubes based quantum dot circuits embedded in a microwave cavity. This general architecture allows one to simultaneously probe the circuit via quantum transport measurements and using circuit quantum electrodynamics techniques. The two experiments realized in this thesis use metallic contacts of the circuit as a resource to engineer a spin sensitive spectrum in the quantum dots. The first one is a Cooper pair splitter which was originally proposed as a source of non-local entangled electrons. By using cavity photons as a probe of the circuit internal dynamics, we observed a charge transition dressed by coherent Cooper pair splitting. Strong charge-photon coupling in a quantum dot circuit was demonstrated for the first time in such a circuit. A new fabrication technique has also been developed to integrate pristine carbon nanotubes inside quantum dot circuits. The purity and tunability of this new generation of devices has made possible the realization of the second experiment. In the latter, we use two non-collinear spin-valves to create a coherent interface between an electronic spin in a double quantum dot and a photon in a cavity. Highly coherent spin transitions have been observed. We provide a model for the decoherence based on charge noise and nuclear spin fluctuations.

**Key words:** Carbon nanotube quantum dots; Cavity quantum electrodynamics; Cooper pair splitter; strong coupling; spin-qubit.

## Résumé

Dans cette thèse, nous étudions des circuits de boîtes quantiques à base de nanotubes de carbone intégrés dans une cavité micro-onde. Cette architecture générale permet de sonder le circuit en utilisant simultanément des mesures de transport et des techniques propre au domaine de l'Electrodynamique quantique sur circuit. Les deux expériences réalisées durant cette thèse exploitent la capacité des métaux de contact à induire des corrélations de spins dans les boîtes quantiques. La première expérience est l'étude d'une lame séparatrice à paires de Cooper, initialement imaginée comme une source d'électrons intriqués. Le couplage du circuit aux photons dans la cavité permet de sonder la dynamique interne du circuit, et a permis d'observer des transitions de charge habillées par le processus de séparation des paires de Cooper. Le couplage fort entre une transition de charge dans un circuit de boîtes quantiques et des photons en cavité, a été observé pour la première fois dans ce circuit. Une nouvelle technique de fabrication a aussi été développé pour intégrer un nanotube de carbone cristallin au sein du circuit de boîtes quantiques. La pureté et l'accordabilité de cette nouvelle génération de circuit a rendu possible la seconde expérience. Cette dernière utilise deux vannes de spins non colinéaire afin de produire une interface cohérente entre le spin d'un électron dans une double boîte quantique, et un photon dans une cavité. Des transitions de spins très cohérentes ont été observé, et nous donnons un modèle sur l'origine de la décohérence du spin comprenant le bruit en charge et les fluctuations des spins nucléaires.

**Mots clés :** Boîtes quantiques en nanotubes de carbone; Electrodynamique quantique en cavité; Lame séparatrice à paires de Cooper; couplage fort; qubit de spin.

# *Acknowledgements*

First I would like to thank Christopher Bauërle, Kasper Grove-Rasmussen, Denis Feinberg, H el ene Bouchiat, and Michel Brune, for agreeing to be members of my defense committee, and for their remarks that improved the quality of the present manuscript.

J'ai beaucoup appr eci e ces quatre ann ees pass ees   Paris et je le dois en grande partie   toutes les personnes que j'ai pu rencontrer. Je commence naturellement par Takis Kontos, que je remercie d'avoir  t e un directeur de th ese aussi pr esent. Parce qu'il arrive parfois que la nanofab   base de nanotubes soit un petit peu frustrante, son optimisme sans faille a  t e d'un grand support moral. Sa *funkitude* participe pour beaucoup   la bonne ambiance qui r egne dans le groupe. A c ot e de cela, il se trouve que Takis est aussi un excellent conteur d'histoire, ce qui peut donner lieu   des moments assez m emorables.

Je voudrais aussi bien-s ur dire un grand merci   tous les membres de l' equipe HQC. Merci   Laure qui a  t e ma mentor pendant le d ebut de cette th ese et dont j'ai repris le projet sur la lame s eparatrice   paire de Cooper. Merci pour m'avoir form e   la nanofabrication et aux techniques de mesures, je te souhaite moult succ es dans ton investissement pour la cause climatique. J'aimerais aussi remercier Audrey Cottet pour son support th eorique, qui a grandement particip e   ma compr ehension de la physique des exp eriences dans le groupe. M eme s'il n'est arriv e que pendant ma troisi eme ann ee, j'ai aussi beaucoup appris de Matthieu Delbecq, en plus des bon moments pass es   manipuler ou   courir au Luco.

Je voudrais aussi remercier les autres membres du groupe avec qui j'ai eu beaucoup de plaisir   travailler: Lauriane, Matthieu Dartiailh, Matthieu Desjardins, Federico, Rapha el, Franois, Zaki. Merci pour faire que le labo soit un environnement aussi agr eable et stimulant.

Il y a aussi la nouvelle g en eration de th esards, Vincent, Romaine, Marius   qui je souhaite bonne chance pour la suite ! Je remercie  galement R eouven Assouly pour son enthousiasme et son efficacit e. Mes pens ees vont aussi   tous les th esards et post-docs du d epartement de physique avec qui j'ai pass e de bon moments au d etour d'un Friday bar ou autre.

Bien-s ur, aucune des exp eriences pr esent ees dans cette th eses n'aurait pu  tre r ealis ee sans les services techniques du labo. Merci aux  lectroniciens David Darson, Philippe

Pace, Anne Denis, pour le design des PCBs, et les coups de mains dans les soudures difficiles. Merci au service administratif Anne Matignon, Olga Hodge pour toutes ces commandes passées. Merci à l'équipe du service logistique, Didier Courtiade, Catherine Gripe, Célia Ruschinzik, et Théo Charpentier pour leur efficacité redoutable, et le magnifique nouveau labo qu'ils nous ont fait. Merci à l'atelier mécanique et au bureau d'étude, pour leur patience même quand les pièces se ressemblent étrangement beaucoup. Merci à Florent et Olivier du service cryo, j'ai beaucoup apprécié discuter de course à pied et écouter religieusement les conseils de ce dernier.

Et bien-sûr, un grand merci à ceux qui font que la salle blanche du département – dans laquelle j'ai quand même passé beaucoup de temps – fonctionne : Michaël Rosticher, José Palomo, et Aurélie Pierret. Toujours plein d'idées pour les soucis de salle blanche, merci pour votre aide et les rires partagés.

Enfin, je tiens à remercier mes parents pour m'avoir témoigné leur fierté et leur soutien et mes soeurs Léa et Hannah, pour leur curiosité tous au long de ces années. Aurélie, pour tout le soutien que tu m'apportes, dans toutes ces étapes franchies ensemble, et sans qui pour sûr j'en serais jamais arrivé là.



# Contents

	Page
<b>Abstract</b>	<b>ii</b>
<b>Acknowledgements</b>	<b>iv</b>
<b>Acronyms and notations</b>	<b>1</b>
<b>Introduction</b>	<b>3</b>
<b>1 Hybrid double quantum dots in carbon nanotube</b>	<b>9</b>
1.1 Carbon nanotube based quantum dot circuits . . . . .	10
1.1.1 Properties of carbon nanotubes . . . . .	10
1.1.2 Quantum dots in carbon nanotubes . . . . .	13
1.2 Basics of double quantum dots . . . . .	14
1.2.1 Characteristic energy scales . . . . .	14
1.2.2 Stability diagram . . . . .	17
1.2.3 Charge qubit in a double quantum dot . . . . .	20
1.3 The superconducting double quantum dot . . . . .	22
1.3.1 Mesoscopic superconductivity . . . . .	22
1.3.2 Cooper pair splitting . . . . .	29
1.4 Spin qubits in quantum dots . . . . .	32
1.4.1 The big family of spin qubits . . . . .	33
1.4.2 The ferromagnetic spin qubit . . . . .	38
<b>2 Mesoscopic - QED</b>	<b>43</b>
2.1 Quantum dot circuit - Cavity coupling description . . . . .	44
2.1.1 Microscopic description of electron-photon coupling . . . . .	44
2.1.2 Input-Output formalism . . . . .	47
2.1.3 Jaynes-Cummings hamiltonian . . . . .	50
2.2 Master equation of the coupled system . . . . .	52
2.2.1 Semi classical description . . . . .	52
2.2.2 Lindbladian formalism . . . . .	54
2.3 Cavity read-out engineering . . . . .	55
2.3.1 Phase and Transmission read-out . . . . .	55
2.3.2 Improving the cooperativity . . . . .	56
<b>3 Experimental techniques</b>	<b>61</b>

3.1	Toward more tunable carbon nanotube quantum-dot circuits . . . . .	62
3.1.1	Various Nanofabrication approaches . . . . .	62
3.1.2	Stapling in a meso-QED device . . . . .	63
3.2	Device nanofabrication . . . . .	65
3.2.1	Sample overview . . . . .	65
3.2.2	Nanofabrication steps . . . . .	68
3.2.3	Niobium cavity fabrication . . . . .	70
3.2.4	Quantum dot circuit contacts and gates . . . . .	71
3.2.5	Etching side trenches . . . . .	71
3.2.6	Growth of carbon nanotube . . . . .	72
3.2.7	Embedding of the carbon nanotube . . . . .	76
3.3	Measurement techniques . . . . .	84
3.3.1	Isolating the device from environment . . . . .	84
3.3.2	Transport measurements . . . . .	85
3.3.3	Cavity transmission measurement . . . . .	88
<b>4</b>	<b>The superconducting double quantum dot</b>	<b>95</b>
4.1	Introduction . . . . .	96
4.2	Sample and Measurement setup . . . . .	99
4.3	Low energy spectrum of the hybrid superconductor DQD in the absence of the cavity . . . . .	101
4.4	Electron-photon coupling of the hybrid DQD . . . . .	105
4.5	Resonant interaction between the hybrid DQD and the cavity . . . . .	106
4.6	Strong coupling . . . . .	111
4.7	Conclusion . . . . .	115
<b>5</b>	<b>Carbon nanotube platform for spin qubit</b>	<b>117</b>
5.1	Highly coherent spin transition . . . . .	118
5.1.1	Introduction . . . . .	118
5.1.2	Working principle . . . . .	119
5.1.3	Nano-fabrication . . . . .	120
5.1.4	Stability diagram . . . . .	122
5.1.5	Two-tone spectroscopy . . . . .	123
5.1.6	Time-domain measurement . . . . .	125
5.1.7	Cavity-Bloch equations . . . . .	126
5.1.8	Decoherence model . . . . .	128
5.2	Design and characterization of the spin-qubit device . . . . .	130
5.2.1	Design of Ferromagnetic contacts . . . . .	130
5.2.2	Further characterization of the circuit . . . . .	132
	<b>Conclusion and perspectives</b>	<b>137</b>
<b>A</b>	<b>Detailed fabrication recipes</b>	<b>139</b>
A.1	Spin-qubit circuit recipe . . . . .	139
A.2	Carbon nanotube growth . . . . .	146

---

<b>B</b>	<b>Supplementary material on chapter 4</b>	<b>150</b>
B.1	Theory of the low energy spectrum of a Cooper pair splitter . . . . .	150
B.2	Experimental details . . . . .	153
B.3	Vacuum Rabi splitting power dependence modelling . . . . .	155
<b>C</b>	<b>Stapling carbon nanotubes</b>	<b>157</b>
C.1	Growth and localization of the carbon nanotubes . . . . .	157
C.2	Preparation of the stapling . . . . .	161
C.3	Stapling . . . . .	163
C.4	Tranfering the circuit to the cryostat . . . . .	167
<b>D</b>	<b>SNR improvement with a I/Q-mixer</b>	<b>169</b>
	<b>Bibliography</b>	<b>172</b>



---

# Acronyms

AC	Alternative current
ABS	Andreev Bound States
AFM	Atomic force microscope
B/AB	Bonding/Anti-bonding
CNT	Carbon nanotube
CPS	Cooper pair splitter
CPW	Coplanar waveguide
cQED	Circuit quantum electrodynamics
CQED	Cavity quantum electrodynamics
CVD	Chemical vapour deposition
DC	Direct current
DOS	Density of states
DQD	Double quantum dot
FWHM	Full width at half maximum
IF	Intermediate frequency
IPA	Isopropanol
LO	Local oscillator
MIBK	Methyl-iso-butyl ketone
NMR	Nuclear magnetic resonance
PCB	Printed circuit board
PMMA	Poly methyl methacrylate
QD	Quantum dot
QED	Quantum electrodynamics
RF	Radio frequency
RIE	Reactive ion etching
RMS	Root mean square
RWA	Rotating wave approximation
SEM	Scanning electron microscope
SMA	SubMiniature version A (microwave connector norm)
SWNT	Single wall carbon nanotube
UHV	Ultra high vacuum
2DEG	Two-dimensional electron gas



# Introduction

## Mesoscopic physics

Mesoscopic physics is the branch of condensed matter physics that focuses on systems of scale lying in between the microscopic and the macroscopic world. Such systems typically contains millions of atoms, and are micrometers long. Building electronic circuits at this scale is particularly appealing since the quantum nature of electrons starts to emerge. Electrons in these circuits can be described as waves with a well defined phase relation over the whole circuit. In the ballistic regime, this was firstly demonstrated in nano-constriction called quantum point contact in 1988 [1, 2], where the quantization of the conductance was measured for the first time.

Nevertheless, the coherence of these electronic waves can easily be lost due to collisions with other electrons or vibrations of the lattice. Besides the need to go to very small dimensions, one also need a clean material to limit these scattering events. This explains why the evolution of mesoscopic physics is closely connected to the progress in materials discovery and synthesis. Nowadays, the variety of these high purity materials is impressive: 2D electron gas (GaAs/AlGaAs, Si/SiGe,...), semiconducting nanowire (InAs, InSb, SiGe,...), Graphene, Carbon nanotubes, Transition metal dichalcogenide monolayers (MoS<sub>2</sub>, WSe<sub>2</sub>, ...). Transport experiments usually require low temperature partly to limit inelastic scattering. Today, temperatures down to  $20mK$  are routinely achieved in the lab using standard cryogenic refrigerators based on liquid <sup>3</sup>He and <sup>4</sup>He.

In condensed matter systems, one is often dealing with physical process involving a large number of particle. Interestingly, it is possible to identify elementary collective excitations, with defined quantum numbers. Such elementary excitations are sometimes called quasiparticles, and this approach of collective phenomena has been very prolific in the past century. In practice there is a large zoology of such quasiparticles, and among the most known, one can think of the Landau quasiparticles in Fermi liquid, the holes which are absence of electron in a Fermi sea, the vibrations in a crystal lattice called phonons, and many others. The family of quasiparticles also include non-collective excitations such as electron-hole bound state: the excitons, or the bogoliubons in superconductors, which are two of the many examples. Mesoscopic circuits open the possibility to isolate a single quasiparticle and make it interact with other kinds of quasiparticles. In that sense, mesoscopic physics appears as an extraordinary workbench for testing quantum theory.

## Quantum dots circuits

In this thesis, we are interested in a special type of mesoscopic circuits: quantum dot circuits. When electrons are confined in a small region of a ballistic conductor they behave as standing waves, and display discrete energy levels, recalling the ones of an atom. A single quantum dot circuit has the same architecture of a transistor including a source and a drain electrode carrying a current and a gate electrode to change the state of the transistor. This is the reason why many of the nanofabrication techniques developed in the microelectronic industry can be transposed to quantum dot circuit fabrication.

Carbon nanotubes are excellent candidates for hosting such electron boxes [3]. Because of their small transverse dimension (diameter  $\simeq 1nm$ ), one only needs to confine electrons in a short section of the nanotube to realize 3D confinement. This is generally done by applying an electrostatic potential on a nearby gate electrode. Circuits studied in this thesis are double quantum dots, but one can envision more complex ones such as the one illustrated in figure 1.

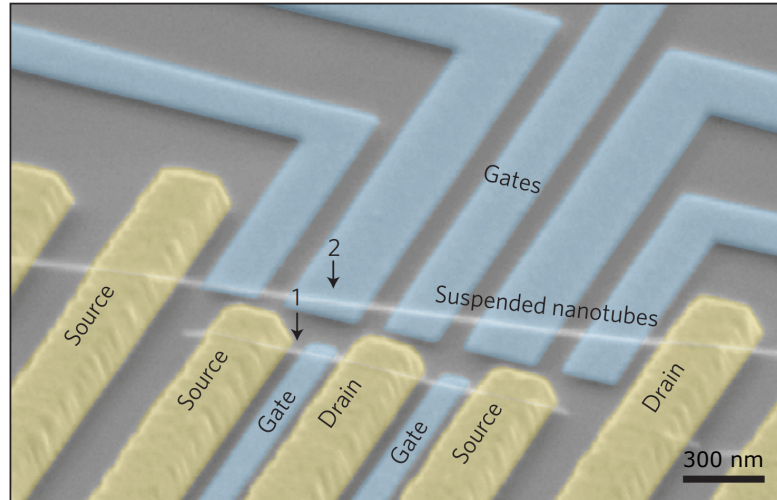


FIGURE 1: **multiple carbon nanotube quantum dot circuit:** False-color scanning electron micrograph showing two carbon nanotubes (in white) suspended over gate arrays (in blue), and contacted by separated sources and drain contacts (in yellow). Using multiple gate electrodes allows to shape in a controlled way the confinement potential of electrons in the carbon nanotube. Source [4]

### Cavity and circuit quantum electrodynamics (C-QED)

In parallel to the progress made in mesoscopic physics, a strong effort in the AMO community (Atom, Molecule, Optics) was given to the study of light-matter interaction at its most fundamental level, by manipulating a single atom and a single mode of the electromagnetic field. Cavity QED is now a resource for entangling photons and atoms, quantum non-demolition read-out of states or the generation and stabilization of non-classical states of light [5]. This exquisite control over the atom-photon system is possible thanks to a strong decoupling to the outside world. Indeed, the very weak interaction with the environment allows the atom to have a fully quantum dynamics over long periods of time (the decoherence time of Rydberg atom is typically  $T_{atom} \sim 10ms$  [6]).

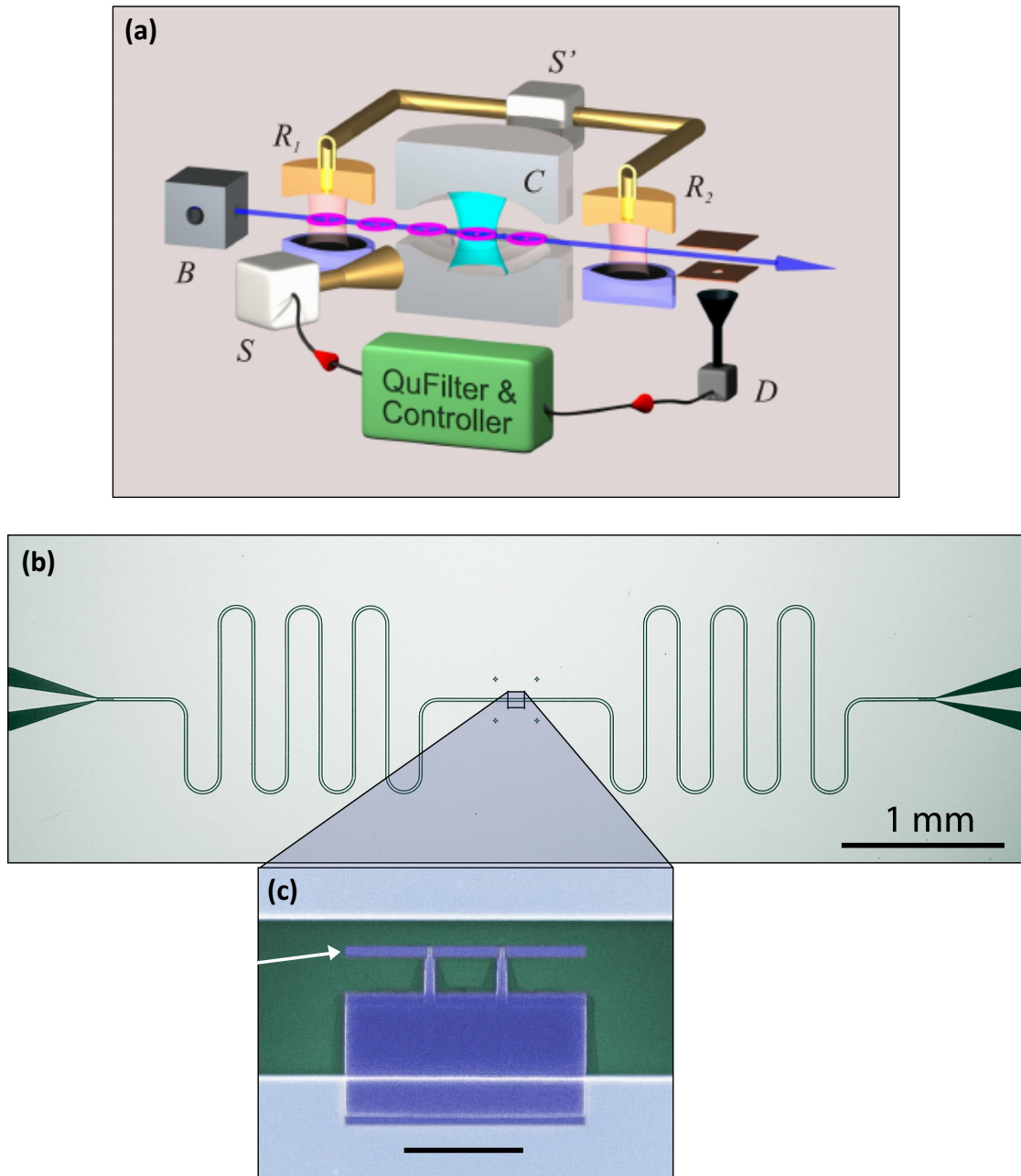


FIGURE 2: **Cavity and circuit QED:** **a.** Schematic of a cavity-QED experiment such as the one performed in the group of Serge Haroche. Rubidium Rydberg atoms are produced in an oven labeled  $B$  and are then flying through a high finesse microwave cavity  $C$ . Two adjacent low finesse cavities,  $R_1$  and  $R_2$  are used to manipulate the state of the flying Rydberg atoms. Source: [7]. **b.** False-color scanning electron micrograph of a typical circuit-QED chip. The long conductor forming meanders is a coplanar waveguide microwave cavity. **c.** At one of the antinodes of the cavity electric field a Cooper pair box is embedded playing the role of the atom. Source: [8]

While the realization of such closed systems in a condensed matter environment may seem unrealistic, the use of a non-dissipative circuit element, the Josephson junction, has made the transposition of such experiment in mesoscopic circuits possible. The Josephson junction inherits the quantum macroscopic coherence of superconductivity,

and led to numerous architectures of superconducting circuits [9]. The possibility to realize two-level systems, analogous to a single spin  $1/2$ , with such circuits has been particularly investigated. Although, this artificial atom has significantly shorter coherence time than atoms ( $T_2$  of several  $100 \mu\text{s}$  have been reached with transmon qubit in a 3D-cavity [10]), they have large electric dipoles compensating the reduction of coherence times with respect to atoms. This places them very well in the race for quantum computing architectures.

## Mesoscopic quantum electrodynamics

The idea of using a cavity has then been transposed to quantum dot circuits [11]. One can reproduce experiments achieved in Cavity and circuit-QED with new degrees of freedom. The most natural two-level system (TLS) one can think of is probably the spin  $\frac{1}{2}$  of an electron and an implementation of such a spin qubit is presented in chapter 5. The charge distribution in a double quantum dot can also encode a TLS. These two types of qubit have recently reached the strong coupling regime with a photon in a cavity in different platform (see figure 3 for the charge qubit) and the chapter 4 presents one of them. In this regime, the TLS and the cavity coherently exchange energy faster than any decoherence rate in the coupled system.

One of the resources in quantum dot circuit is the possibility to use specific contact reservoirs such as ferromagnet or superconductor to induce electronic correlation in the quantum dots. This idea is at the heart of the two experiments presented in chapter 4 and 5 and can be understood as the shaping of the electronic spectrum in quantum dots.

This thesis is organized as follows: the first chapter introduces double quantum dot circuits in carbon nanotubes, and emphasizes on two realizations that are the Cooper pair splitter and the ferromagnetic spin-qubit. In the second chapter a theoretical description of the cavity-circuit coupling is given. In particular, this chapter details the coupling of microwave cavity photons to double quantum dot circuits and how to improve the cavity-quantum dot circuit interface. Chapter three describes the nanofabrication of the mesoscopic-QED devices, and the measurement techniques used in this thesis work. Finally Chapters four and five present the two experiments realized in this thesis, namely the indirect observation of coherent Cooper pair splitting and the strong charge-photon

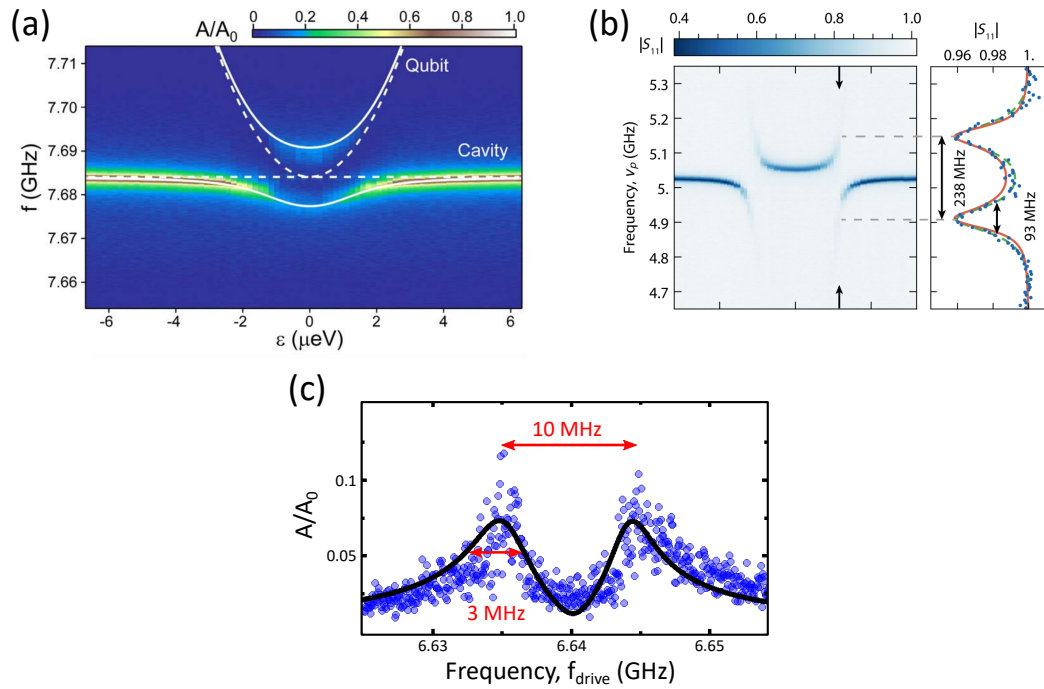


FIGURE 3: **strong charge-photon coupling in mesoscopic-QED:** **a.** Cavity transmission measurement showing the avoiding crossing between a silicon charge qubit energy and the cavity resonance frequency [12]. **b.** Similar measurement with a GaAs charge qubit coupled to a high impedance resonator [13]. A vertical cut of the left panel measurement display a splitting of the cavity resonance, called vacuum Rabi splitting. **c.** Vacuum Rabi splitting observed with a carbon nanotube charge-like qubit [14].

coupling in a superconducting double quantum dot for the chapter four, and the observation of highly coherent spin transition in a carbon nanotube based spin qubit.

## Chapter 1

# Hybrid double quantum dots in carbon nanotube

When an electron is confined to a small region of space, its spectrum will reveal discrete energy levels. Such systems are often called *quantum dots* or *artificial atoms* because of the analogy with an electron confined in the potential generated by a nucleus. In the same philosophy, one can also realize artificial molecules by bringing closely enough two quantum dots. Among the solid state platforms to implement such double quantum dots, one finds two-dimensional electron gases in semiconducting hetero-structures (GaAs/GaAlAs [15], Si/SiGe [16]), nanowires (InAs [17], InSb [18],... ), graphene [19], and carbon nanotubes [20].

The double quantum dot (DQD) have more complex internal dynamics, and transition between the two dots can occur. Thanks to nanofabrication techniques, the tunneling rate between the two dots can easily be tuned in the microwave range, which make double quantum dot particularly attractive for quantum computing applications.

In this chapter, I will present several properties of carbon nanotubes (section 1.1), and introduce basic concepts about double quantum dots (see section 1.2). Then I will describe two specific implementations of hybrid double quantum dots (see sections 1.3 and 1.4) which experimental realization are detailed in chapters 4 and 5.

## 1.1 Carbon nanotube based quantum dot circuits

Carbon nanotubes possess several properties that make them very attractive for quantum dot circuit applications. In this section I review few of them.

### 1.1.1 Properties of carbon nanotubes

The atomic structure of carbon nanotubes is identical to the one of graphene, hence they share similar transport features. Their hexagonal atomic arrangement is built on covalent bonds between  $sp_2$  orbitals with the three neighboring atoms. The forth valence electron occupy the  $p_z$  orbital and is responsible for transport in carbon nanotubes. Because  $p_z$  orbitals are pointing out of plan, it is easy to realize good electrical contacts with almost every metal. Ferromagnetic and superconducting metals have thus been widely used to contact hexagonal carbon materials, with the idea of inducing specific

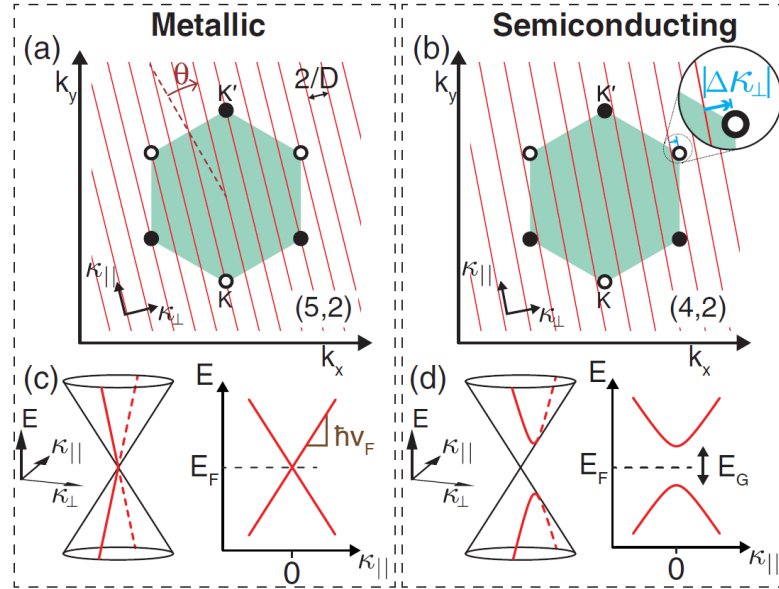


FIGURE 1.1: **The zone folding approximation:** The rolling-up of a graphene sheet impose new boundary conditions to the transverse part of the wave vector. The Brillouin zone of a carbon nanotube is form of parallel lines. Whether or not one of the line is passing right through the middle of a Dirac cone will determine if the carbon nanotube is semiconducting or metallic. Source: [3].

electronic spin correlations in it [21], [22], [23], [24], [25], [26]. This represents a big advantage compared to 2DEGs for which the choice of contacting metal is limited. In return, this makes transport in graphene and carbon nanotubes very sensitive to their environment. This motivated the use of suspended carbon nanotubes to avoid interactions with the substrate [27]. In the case of graphene, the encapsulation between two boron-nitride sheets has been found to be very efficient [28].

Many features of the band structure of carbon nanotube inherit from the graphene one. Indeed, carbon nanotubes can be seen as a rolled-up graphene sheet. A good approximation is to consider that curvature does not modify the bands dispersion, but only adds new boundary conditions to the transverse component of the wave vector  $k_{\perp}$ . This is the zone-folding approximation, and holds as long as the overlap between neighboring  $p_z$  orbital remains negligible. The quantization of  $k_{\perp}$  limits the first Brillouin zone of carbon nanotube (CNT) to a set of parallel lines in the Brillouin zone of graphene with an angle determined by the rolling condition (see figure 1.1). Depending on whether or not one of the lines is passing by the center of one of the Dirac cones, the carbon nanotube can be semiconducting (a typical value of the semiconducting gap is  $E_G = 4\hbar v_F/3D \approx 700$  meV for  $D = 1$  nm) or metallic. Nevertheless, when one starts to consider the overlap between  $p_z$  orbital, the Dirac cones can be slightly shifted in the

reciprocal space. Consequently, CNT initially predicted to be metallic (according to the zone folding approximation) can turn out to be semiconducting. Those CNTs are often referred to as "narrow gap" carbon nanotubes and have a semiconducting gap  $E_G$  ranging between 10 meV and 100 meV. Strain in carbon nanotubes can produce similar effects [29], but in the end, metallic CNTs are fairly rare.

Two distinct low energy regions in the momentum space of electrons in CNT play a central role in transport experiments. They originate from K and K' Dirac cones of graphene, and are commonly referred to as K and K' valleys. This valley orbital degree of freedom can be pictured as whether the electron is rotating clockwise or counter-clockwise around the nanotube. Because the transverse confinement in carbon nanotube is very strong, the first band above these K and K' valley is few hundreds of mV above, hence one can safely restrict himself to the K and K' bands to describe transport experiment. Since K and K' valleys are far apart from each other in momentum space, the valley is a robust quantum number to describe the state of an electron. K and K' states are degenerate in absence of magnetic field, hence each energy level defined by longitudinal confinement is four-fold degenerate ( $2 \times 2$ , for the electronic spin and the valley degree of freedom). However the presence of disorder can induce scattering with large momentum transfer, and mix K and K' states. This leads to the lifting of the valley degeneracy, which is defined by an energy coupling constant  $\Delta_{K,K'}$ . Spin-orbit coupling in carbon nanotube has also been reported, with values ranging from  $\Delta_{SO} = 150 \mu\text{eV}$  [30] ( $\Delta_{SO} = 300 \mu\text{eV}$  in [27]), to  $\Delta_{SO} = 3.4 \text{ meV}$  [31].

The Fermi velocity in carbon nanotube is  $v_F \approx 1.10^6 \text{ m.s}^{-1}$ , and sets the minimal size of the dot  $L$  required to ensure well separated energy levels, since  $\Delta E_{conf} = \frac{\hbar v_F}{2L}$  (see the review paper [3]). Another interesting property of carbon nanotubes is the low density of nuclear spins, which make them particularly attractive for spin qubit experiments (see chapter 5). Indeed they are composed of 98.9% of  $^{12}\text{C}$  which has no nuclear spin, and 1.1% of  $^{13}\text{C}$  in normal synthesis conditions. With a diameter about 1 – 2 nm, carbon nanotubes can be considered as 1D conductor which is highly beneficial for Cooper pair splitting for instance (see chapter 4).

### 1.1.2 Quantum dots in carbon nanotubes

The small transverse dimension of carbon nanotubes already provides a 1D confinement. The longitudinal confinement in semiconducting CNT is commonly created by Schottky barriers, originating from a mismatch between the work functions of the contact metal and the CNT. Such Schottky barriers can be detrimental to obtain very transparent contact and reach the ballistic transport limit. Palladium have been found to produce low Schottky barriers [32], since its work function ( $\phi_{Pd} = 5.1$  eV) is very close to the one of carbon nanotubes. This is advantageous for reaching the Kondo or the Fabry-Perot regimes which demand very opened quantum dot. Low Schottky barriers are also beneficial for the closed quantum dot regime, since the height barrier can be subsequently tuned using a capacitively coupled gate electrode, in a controllable way.

When measuring the current through a quantum dot as a function of the gate voltage defining the dot, one sees peaks of current whenever an energy level in the dot is aligned with the chemical potential in the reservoirs (in the limit of small bias voltage,  $V_{SD} = \frac{1}{e}(\mu_S - \mu_D) \simeq 0$  with  $\mu_S$  (resp.  $\mu_D$ ) the chemical potential in the source (resp. drain) reservoir). The observed spectroscopic level spacing  $E_{add}(N)$  is the difference between the chemical potentials of the dot for two successive numbers of electron in the dot ( $E_{add}(N) = \mu_N - \mu_{N-1}$ ), where the chemical potential of the dot is defined by:  $\mu_N = E(N) - E(N-1)$ , with  $E(N)$  the total energy of the  $N$  electrons in the dot. In the constant interaction model,  $E(N)$  reads:

$$E(N) = \sum_{i=1}^N \epsilon_i + U(N) \quad (1.1)$$

The first term is the sum of the different orbital energies filled by electrons. The distribution of orbital levels  $\epsilon_i$  is determined by the longitudinal confinement potential in the carbon nanotube ( $\Delta E_{conf} = \frac{\hbar v_F}{2L}$ ), and the eventual spin-orbit coupling  $\Delta_{SO}$ , and valley splitting  $\Delta_{K,K'}$ . The second term is the electrostatic energy due to electron-electron interactions in the dot and capacitive energy between the dot and all neighboring conductors, and it reads:

$$U(N) = \frac{e^2 N^2}{2C_\Sigma} + eN \sum_{j=1}^M \frac{C_j}{C_\Sigma} V_j \quad (1.2)$$

Where  $C_\Sigma$  is the total capacitance of the dot,  $C_j$  is the capacitance between the dot and the conductor  $j$ , and  $V_j$  is the voltage of the conductor  $j$ . The spectroscopic level

spacing  $E_{add}(N)$  can then be rewritten as:

$$E_{add}(N) = e \frac{C_G}{C_\Sigma} \Delta V_G = \frac{e^2}{C_\Sigma} + \epsilon_{N+1} - \epsilon_N \quad (1.3)$$

$\frac{C_G}{C_\Sigma}$  is the conversion factor from gate voltage to energy shift of levels in the dot, and is called the *lever arm* of the gate  $G$  on the dot.  $\Delta V_G = V_G(N+1) - V_G(N)$  (with  $V_G(N)$  the gate voltage at which the number of charge in the dot oscillate between  $N$  and  $N-1$ ) is the distance between two current peaks in the gate voltage space.  $\frac{e^2}{C_\Sigma}$  is the charging energy of the dot. A standard transport measurement in a single quantum dot is to measure the current (and/or the conductance) through the dot as a function of the gate voltage  $V_G$  and the bias voltage  $V_{SD}$ . In transport experiment, charging energies and lever arms are the two quantities that electrostatically describe the circuit. In the following, I will focus on the case of a double quantum dot, which is the circuit that has been used in the two presented experiments (chapter 4, and 5).

## 1.2 Basics of double quantum dots

When two quantum dots are close enough for electrons to jump from one dot to the other, the system behave as an artificial molecule. Such circuits have a more complex internal dynamics and are at the heart of charge qubits [33], and several spin qubit architectures [34], [35], [26].

### 1.2.1 Characteristic energy scales

A few characteristic energy scales are sufficient to define the operating regime of a double quantum dot.

**Charging energy** The on-site charging energy originates from coulomb interaction between all the electrons in the quantum dot, and is expressed in terms of an effective capacitance  $C_\Sigma$  :  $E_C = \frac{e^2}{C_\Sigma}$  (see the review [36] for the full formula). In the quantum dot geometry considered in this thesis, the on-site charging energy is ranging from 1 meV to 10 meV, and is the dominant contribution to the spectroscopic level spacing

$E_{add}(N)$ . There is also a mutual charging energy  $U_m$  arising from the finite capacitance  $C_m$  between the two dots, and typical mutual charging energy value is few 10 meV.

**Orbital energy** Like in an atom, a set of discrete orbital energy level originates from confinement in the CNT. the spacing between these levels depends on the shape of the confinement potential and on the energy dispersion of electron close to the Fermi energy [3]. For carbon nanotubes (linear dispersion:  $E(k_{\parallel}) \approx \hbar v_F k_{\parallel}$ ) in the approximation of strong confinement (valid for large number of confined electrons), the spacing between orbital levels is  $\Delta E_{conf} \approx \frac{\hbar v_f}{2L}$ . For a 500 nm long quantum dot,  $\Delta E_{conf} = 4$  meV. As explained in the section 1.1.1, each orbital energy level is four-fold degenerated, nevertheless spin-orbit coupling and K-K' valley mixing ( $\Delta_{SO}$  and  $\Delta_{K-K'}$  respectively) can lift this degeneracy, giving rise to a more complex energy level ladder.

**Dot-lead tunnel rate** The coupling to each dot to its adjacent lead is described by the tunneling rates  $\Gamma_L$  and  $\Gamma_R$ . For a double quantum dot well coupled to the leads ( $\Gamma \gg k_B T$ ), dot energy levels will be broadened by the  $\Gamma$ 's. In a C-QED perspective, the regime with low tunneling rates ( $k_B T \gg \Gamma$ , often called "closed quantum regime") is favored since internal degrees of freedom such as the electron spin will not suffer from virtual exchange processes with electrons in the reservoirs [37].

**Interdot tunnel rate** An other type of tunneling rate, is the one in between the two dots, labeled  $t$ . This tunneling rate plays a dominant role in the internal dynamic of the double quantum. Its value is typically between 1 GHz and 10 GHz, which make double quantum dot easy to probe with standard excitation and read-out techniques using basic RF equipment. When  $t \gg k_B T$ , coherent tunneling between dot orbitals occur, thus forming molecular orbitals. These regime is called *coherent regime* of a double quantum dot [36].

**Bias voltage** In all transport experiments, a voltage bias  $V_{SD}$  is applied between the two electron reservoirs. This voltage drop along the circuit define what we call a "bias window":  $\mu_S - \mu_D = eV_{SD}$  (see figure 1.2.b). All electronic states in the double quantum dot laying in this energetic window will contribute to the transport, hence measuring the current flowing through the circuit or its conductance provide a spectroscopy of the

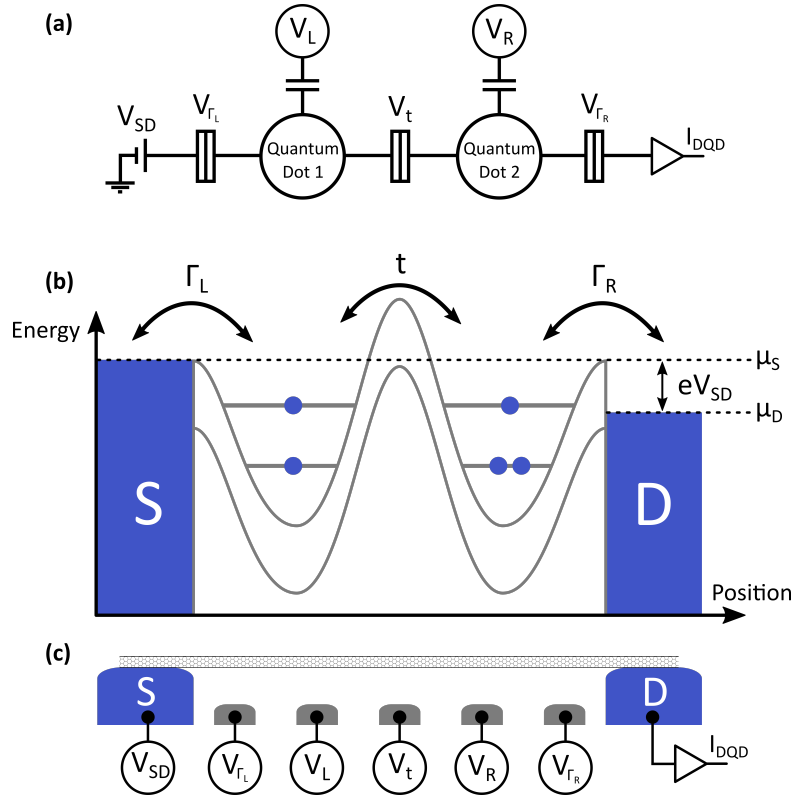


FIGURE 1.2: **Double quantum dot circuit:**

**a.** Circuit representation of a double quantum dot, in which the three tunnel barriers can be tuned with the gate voltages:  $V_{\Gamma_L}$ ,  $V_t$ , and  $V_{\Gamma_R}$ . The two quantum dots are capacitively coupled to gate electrodes with voltages  $V_L$  and  $V_R$ , allowing to tune independently the chemical potential in each dot. **b.** Landscape of the confinement potential in the carbon nanotube felt by conduction electrons. The two curvy lines delimit the semiconducting gap inside the carbon nanotube. The two fermionic reservoirs associated to the source and drain electrodes are shown in blue. **c.** Side view of a suspended carbon nanotube quantum dot circuit.

levels in the double quantum dot. A lot of attention has been given to such spectroscopy in the high bias regime where multiple levels participate to the transport [38], [39], [40].

**Electronic temperature** All those energies have to be compared with the thermal energy of the electrons in the circuit,  $k_B T_{elec}$ , which sets the smaller resolvable energy in transport measurement. This temperature can be quite different from the base temperature of the cryostat. All experiment in this thesis work have been carried at  $T_{elec} \leq 50$  mK  $\approx 4$   $\mu$ eV (with  $T_{cryostat} \simeq 20$  mK).

At the single dot level, three main transport regimes can be identified, each with a specific energy ladder: the Coulomb blockade regime ( $\Gamma_L, \Gamma_R, k_B T_{elec} \ll E_C$ ), the Kondo regime ( $k_B T \ll \Gamma_L, \Gamma_R \ll E_C$ ), and the Fabry-Perot regime ( $k_B T, E_C \ll \Gamma_L, \Gamma_R$ ). Using a five gates architecture allows us to tune independently  $\Gamma_L$ ,  $\Gamma_R$ ,  $t$ ,  $\mu_L$ ,  $\mu_R$  (see figure 1.2) and

in principle, one can access any of these three regimes. It also provides a full tunability of the stability diagram of the double quantum dot (see the section 1.2.2).

### 1.2.2 Stability diagram

To fully characterize the transport in a double quantum one has to measure the current as a function of the five gate voltages and the bias voltage  $V_{SD}$ . This would produce a six-dimensional array, which is not very handy. A first approach is to look at the current as a function of  $V_L$  and  $V_R$  tuning energy levels in the left and the right dot respectively, while keeping  $V_{\Gamma_L}$ ,  $V_{\Gamma_R}$ ,  $V_t$  constant, and  $V_{SD} \ll \Delta E_{conf,L}, \Delta E_{conf,R}$ . An example of such 2D plot is shown in figure 1.3. This plot is the *charge stability diagram* of a double quantum dot measured on the device nicknamed *SPN15R*. Inside each hexagon of this *honeycomb pattern* the number of electrons in each dot is fixed.

When one begins to increase the bias voltage  $V_{SD}$  across the double quantum dot, the condition for current is now satisfied over two triangles at the triple point positions in the gate-gate plane. Electron can tunnel through multiple levels, and this allows to probe directly the energy spacing between the  $\epsilon_i$  which contains information about spin-orbit coupling and valleys mixing [31], [41], without paying the price of the charging energy price, since only single electron processes occur. Since the bias voltage provides an absolute energy scale, this regime is useful for calibrating the lever arms of the gates with respect to the two dots <sup>1</sup>, and the complete procedure is detailed in the review paper ref.[36]. In figure 1.3, a change of behavior appears in the bottom-left region, the triple points are close to each other (small  $U_m$ , see figure 1.3.b) and there is transport only at the triple point locations (small  $t$ ) indicating that the two quantum dots are weakly coupled. In the top-right corner,  $U_m$ , and  $t$  are larger showing that the two quantum dots are more coupled to each other.

In semiconducting carbon nanotube transport can occurs either through electron states or hole states in the dots. From that statement, four different regimes can be identified according to through which state transport is taking place in each of the two dots. For narrow-gap carbon nanotubes it is possible to access those four different regimes, and an example of such measurement is shown in figure 1.4.

<sup>1</sup>A full capacitance calibration also requires to measure a full hexagon of the stability diagram.

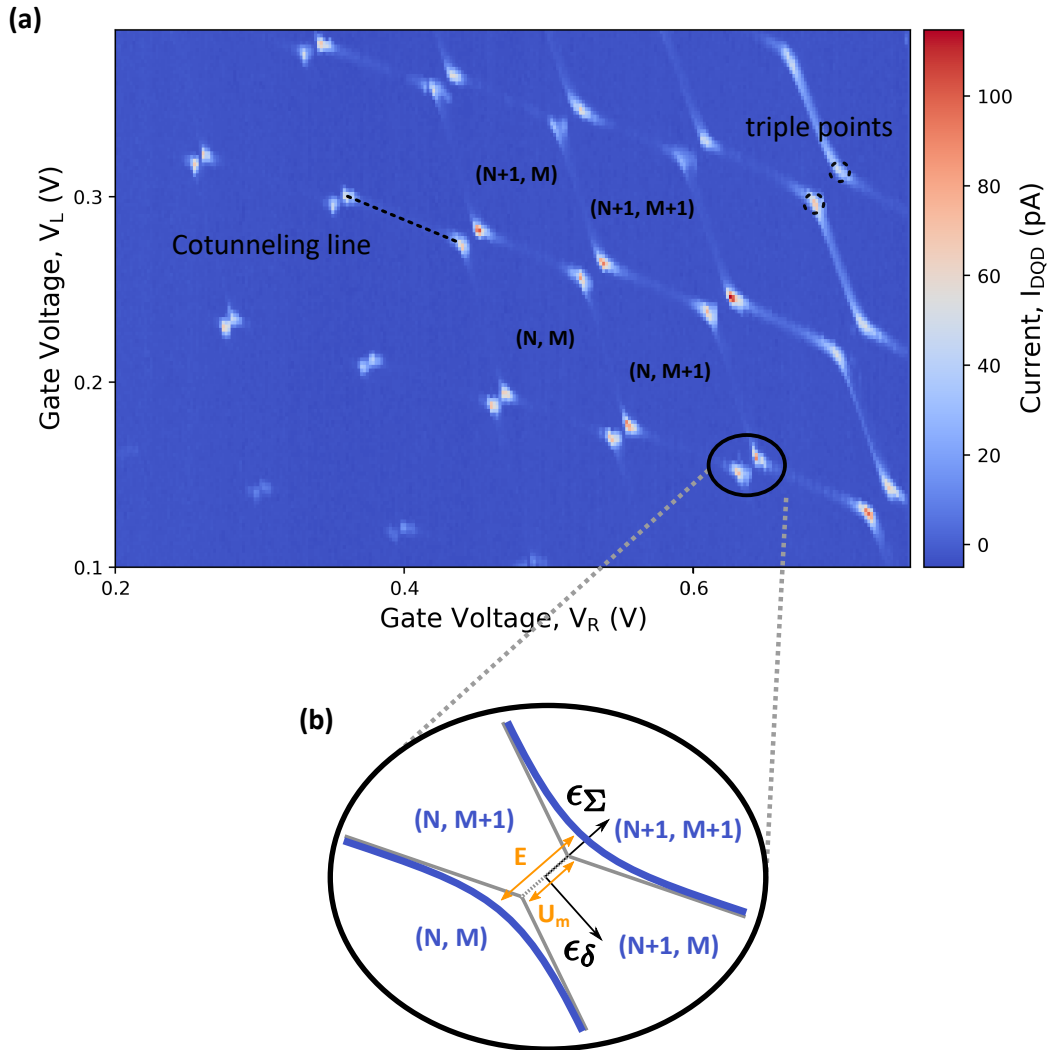


FIGURE 1.3: **Charge Stability diagram of a double quantum dot:**

**a.** Current through a double quantum dot as a function of the gates voltage  $V_L$   $V_R$  showing the characteristic honeycomb pattern of double quantum dots (measurement taken on device SPN15R). The points with high current are called "triple points" and correspond to the situation where levels in each of the dots are in the bias window. The white lines describing the hexagons are cotunneling lines. In such second order process, one of the dot is detuned from the bias window, and electrons tunnel through this dots via a state only virtually accessible. **b.** Schematic of the region in between two triple points. The grey lines represent delimitation between lower-energy electronic configuration considering only capacitances between dots and conductors. The avoiding crossing in the current line (in blue) is due to the interdot tunneling. This region is of paramount importance since it is where (0,1) and (1,0) charge configurations are degenerate, thus an electron is allowed to jump between the two dots. the new eigenstates are the molecular bonding and anti-bonding state in which a charge qubit can be encoded (see section 1.2.3).

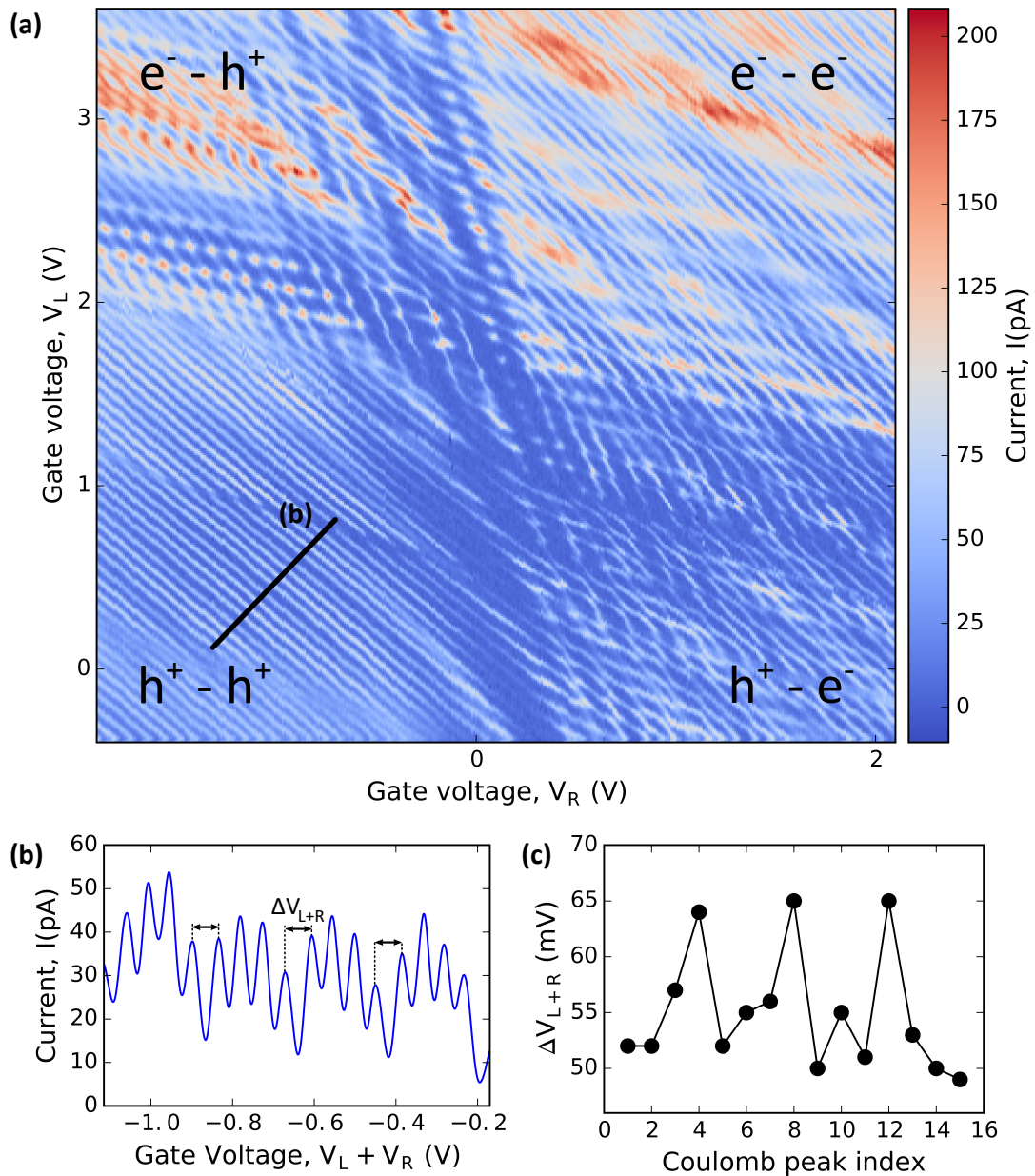


FIGURE 1.4: **Stability diagram in a narrow-gap carbon nanotube:** **a.** The four regimes (electron,electron), (electron, hole), (hole, hole), and (hole, electron) are visible on this measurement. When the circuit is deeply in the (e, e) or the (h, h) regime, it does not behave as a double quantum dot anymore, but as a large single quantum dot. In the bottom left region, one can observe a four-fold degeneracy. **b.** Coulomb peaks extracted from **a.** along the black line. Every four peaks the spacing is larger, which is reminiscent of the four-fold degeneracy in carbon nanotubes due to spin and valley degeneracy. **c.** Coulomb peak spacing  $\Delta V_{L+R}$  (as defined in section 1.1.2) as a function of the peak index. This representation highlights the four fold degeneracy. Measurement taken on device SPN8R

### 1.2.3 Charge qubit in a double quantum dot

One of the reasons for the large interest in double quantum dots is the possibility to use it as a qubit (basic logic unit of a quantum computer). The simplest way to realize a qubit in a double quantum dot is to encode the two states '0' and '1' in two orbital levels, namely the bonding  $|B\rangle = 1/\sqrt{2}(|0,1\rangle + |1,0\rangle)$  and anti-bonding  $|AB\rangle = 1/\sqrt{2}(|0,1\rangle - |1,0\rangle)$  states, with  $|0,1\rangle$  (resp.  $|1,0\rangle$ ) the state with 0 (resp. 1) in the left dot, and 1 (resp. 0) in the right quantum dot. Since the information is stored in the charge configuration of the DQD, such a qubit is called a *charge qubit*. The working point in the stability diagram is close to the degeneracy line between the states (1, 0) and (0, 1) (see figure 1.3.b). In this area, no charge is exchanged with the reservoirs, hence the double quantum dot forms a closed system. The qubit frequency is  $\hbar\Omega = E_{AB} - E_A = \sqrt{\epsilon_\delta^2 + 4t^2}$ , with  $E_{AB}$  and  $E_B$  the energies of the anti-bonding and bonding states respectively, and the detuning  $\epsilon_\delta = \epsilon_L - \epsilon_R$ , where  $\epsilon_i$  is orbital energy in the dot  $i$ . The qubit frequency can easily be tuned by acting on the detuning  $\epsilon_\delta$ . In the perspective of quantum information processing [42], one can perform detuning DC gate for the initialization [43], and modulating  $\epsilon_\delta$  at the qubit frequency allows to perform a rotation of the qubit state around an axis (determined by the phase of the modulating signal) lying on the equator of the Bloch sphere (see figure 1.5-b). The read-out of the qubit state can be done through charge sensing [33], direct DC current measurement, or using c-QED like read-out scheme [44], [45]. Until very recently, the various implementation of charge qubit had never shown good coherence properties. The reason for such short coherence times is the charge noise inherent to the environment. It originates from uncontrolled charge jumps resulting in random fluctuation of the electric field in the vicinity of the qubit. one strategy to circumvent this issue consists in placing the qubit in a regime (often called *sweet spot*) where its energy is insensitive to charge noise at first order. Nevertheless, even by taking care to this last point, it is difficult for the coherence times  $T_2$  to exceeded the few ns [46], [47], [48], [49], [50] (more recently a coherence times  $T_2 = 50ns$  has been measured in GaAs [51]). Such coherence times correspond to a  $1/f$  noise density of a few  $10^{-4} e/\sqrt{Hz}$  at 1 Hz. To reach longer coherence time, one can also try to hybridize the orbital degree of freedom to the electron spin (see section 1.4 for more details), to benefit from its excellent coherence property ( $T_2 \simeq 0.6s$  in a NV center using dynamical decoupling pulses[52]).

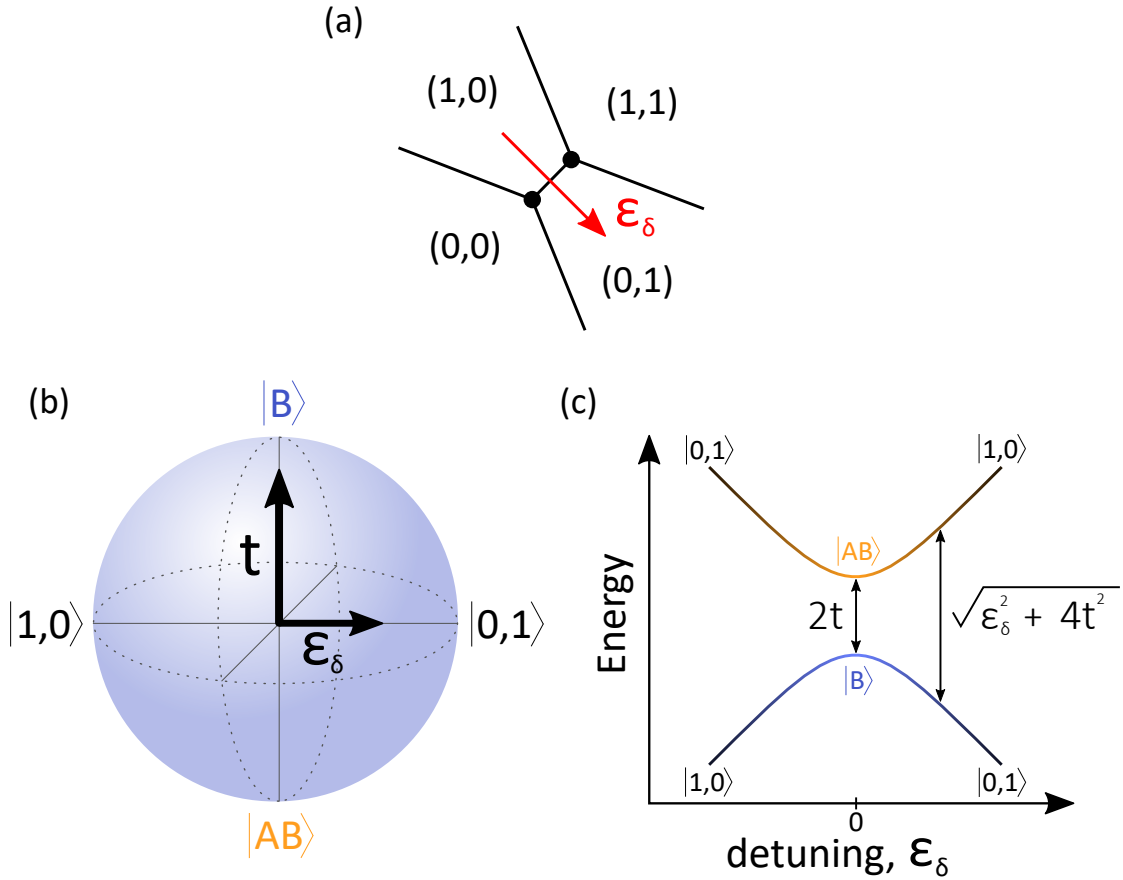


FIGURE 1.5: **Charge qubit in a double quantum dot:** **a.** Zoom on the stability diagram in the region between two triple points. The red arrow define the detuning axis which control the energy difference between the states  $|0,1\rangle$  and  $|1,0\rangle$ . In this area  $|B\rangle$  and  $|AB\rangle$  are the eigenstates states of the double quantum hamiltonian. **b.** The subspace of the charge qubit can be represented on a Bloch sphere. The two poles are the two logical states and can be reach only for  $\epsilon_\delta = 0$ . Close to  $\epsilon_\delta = 0$  the energy transition is mainly set by the tunnel coupling  $t$ . Like in NMR experiment [43], small amplitude modulations of  $\epsilon_\delta$  at the frequency of the transition between  $|B\rangle$  and  $|AB\rangle$  (originating from a cavity electric field for instance) will make the state vector rotate about the  $\epsilon_\delta$  axis. Such a coupling scenario is called *transverse coupling* since the rotation axis is perpendicular to the quantization axis. **c.** Energy dispersion of the double quantum dot states. For  $\epsilon_\delta = 0$ , the first derivative of  $\hbar\Omega(\epsilon_\delta, t)$  is zero, which means that the energy transition is insensitive at first order to  $\epsilon_\delta$ -noise. This region is called a *sweet spot*. Placing the qubit in such region allows to limit the decoherence of the qubit due to charge noise.

in a c-QED experiment, an important step toward quantum computing is to reach the strong coupling, where the coupling strength between cavity photons and the two-level system overcomes the decoherence rates of both parts (see chapter 2). This regime reveals the coherent exchange of excitations between the two systems. Surprisingly, the strong coupling regime had first been reached with charge qubit in double quantum dot [14], [13], [12], then followed closely by spin qubits [53], [54], [55].

### 1.3 The superconducting double quantum dot

Whereas superconductivity has been discovered more than a century ago, it is still an active domain of research. One direction is the research of exotic superconductivity, such as high- $T_C$  superconductor [56]. Another line of research consists in studying superconductivity at the  $\mu m$ -scale and is often referred to as *mesoscopic superconductivity*. In this section, I first briefly introduce few results of the BCS (Bardeen Cooper Schrieffer) theory of conventional superconductor as well as concepts in mesoscopic superconductivity, which are necessary for the understanding of the experiment presented in chapter 4.

#### 1.3.1 Mesoscopic superconductivity

##### 1.3.1.1 Homogeneous superconductor

In 1950, H. Fröhlich [57] (and subsequently J. Bardeen and D. Pines with a more complete approach [58]) showed that phonons in solids can mediate an attractive interaction between electrons. Nevertheless, the resulting force can be very weak. The next step was carried out in 1956 by L.N. Cooper [59]. He noticed that such attractive interaction can create bound pairs of two electrons above the Fermi sea no matter how weak the interaction is. Cooper's argument explains qualitatively the formation of a condensate of such Cooper pairs around the Fermi sea. In 1957 J. Bardeen, L.N. Cooper, and J.R. Schrieffer found out the resulting ground state of such a scenario [60], and showed that it naturally provides an explanation for all the observed phenomenon about superconductivity at that time. The conventional superconductor are the one described by the BCS theory, where phonons are responsible for the formation of bound electron pairs. While

the electron-phonon interaction is in principle present for all pairs of electron ( $\mathbf{k}, \mathbf{k}'$ ), the most efficient mechanism occurs for pairs ( $\mathbf{k}\uparrow, -\mathbf{k}\downarrow$ ), since a broader range of  $q_{\text{phonons}}$  can be involved<sup>2</sup>. By treating these pairing correlations  $\langle c_{-k\downarrow} c_{k\uparrow} \rangle$  with a mean-field approximation, one can write the following hamiltonian:

$$H_{BCS} = \sum_{k,\sigma} \xi_{k\sigma} c_{k\sigma}^\dagger c_{k\sigma} + \sum_k \Delta_k c_{k\uparrow}^\dagger c_{-k\downarrow}^\dagger + \Delta_k^* c_{-k\downarrow} c_{k\uparrow} \quad (1.4)$$

Where  $c_{k\sigma}$ , and  $c_{k\sigma}^\dagger$  are respectively the annihilation and creation operator of an electron in the plane wave state ( $\mathbf{k}, \sigma$ ) with kinetic energy  $\xi_{k\sigma}$  (where  $\mathbf{k}$  denotes the vector momentum, and  $\sigma \in \{\uparrow, \downarrow\}$ ). We also introduced  $\Delta_k = -\sum_{k'} V_{kk'} \langle c_{-k'\downarrow} c_{k'\uparrow} \rangle$  with  $V_{kk'}$  the pairing potential. This hamiltonian can be diagonalize using the Bogoliubov transformation [61]:

$$\gamma_{k,\uparrow} = u_k c_{k\uparrow} - v_k c_{-k\downarrow}^\dagger \quad \text{and} \quad \gamma_{-k,\downarrow}^\dagger = u_k^* c_{-k\downarrow}^\dagger + v_k^* c_{k\uparrow} \quad (1.5)$$

with:

$$u_k = \frac{1}{\sqrt{2}} \sqrt{1 + \frac{\xi_k}{\sqrt{\xi_k^2 + \Delta^2}}} \quad \text{and} \quad v_k = \frac{e^{i\theta}}{\sqrt{2}} \sqrt{1 - \frac{\xi_k}{\sqrt{\xi_k^2 + \Delta^2}}} \quad (1.6)$$

Here we have considered  $\Delta$  to be independent of  $k$ . the diagonalized hamiltonian takes the form:

$$H_{SC} = \sum_{k,\sigma} E_k \gamma_{k\sigma}^\dagger \gamma_{k\sigma} \quad (1.7)$$

The operators  $\gamma_{k,\uparrow}$  and  $\gamma_{-k,\downarrow}$  correspond to elementary excitations of the Cooper pair condensate. From the Bogoliubov transformation, they appear as superposition of electron and hole excitations. They are often called *Bogoliubons* quasiparticles and their energy dispersion is  $E_k = \sqrt{\xi_k^2 + |\Delta|^2}$ . One can derive the corresponding density of state of the quasiparticles:  $\rho_{BCS}(E) = \frac{E}{\sqrt{E^2 - \Delta^2}} \rho_N(\xi_F)$  characterized by the energy gap  $|\Delta|$ .

The form of the ground state describing the Cooper pair condensate has been postulated prior to the diagonalization of the pairing hamiltonian, and it can be checked after that it coincides with the vacuum of excitations:  $\gamma_{k,\uparrow} |GS\rangle = \gamma_{-k,\downarrow} |GS\rangle = 0$ . The ground

<sup>2</sup>The general situation where a phonon mediates a transfers of momentum between two electrons can be depicted as:  $(k, k') \rightarrow (k-q, k'+q)$ . Knowing that the  $k-q$  and  $k'+q$  have to remain out of the Fermi sea and assuming a spherical Fermi sea, one find that a possible solution is  $q = k - k'$ . Nevertheless, for  $k' = -k$ , there is no condition on  $q$ , hence the interaction is expected to be much larger.

state reads:

$$|GS\rangle = \prod_k (u_k + v_k c_{k,\sigma}^\dagger c_{-k,-\sigma}^\dagger) |0\rangle \quad (1.8)$$

Where  $|0\rangle$  is the Fermi sea. One can identify  $(|u_k| + e^{i\phi} |v_k| c_{k,\sigma}^\dagger c_{-k,-\sigma}^\dagger) |0\rangle$  as an elementary block of Cooper pair condensate. We will see in the next section that such a elementary block can be partially isolated in a quantum dot. Importantly, all the terms of this product are linked to the same phase factor  $e^{i\phi}$ . Hence it plays a macroscopic role in the wavefunction of the condensate. Besides, because each elementary block is a coherent superposition of zero electron and two electrons in the pairs, the number of electron is undefined in the condensate. This is reminiscent of the uncertainty principle between phase and number  $\Delta N \Delta \phi \geq 1$ , where the BCS ground state is a well-defined phase state, hence realizing an example of macroscopic quantum coherence [62]. This result could be anticipated since the mean-field hamiltonian does not conserve the number, but only the parity.

**Cooper pairs** In conventional superconductors, the Cooper pair wavefunction is an S-orbital and the spins are in the singlet state. However, triplet states are also possible (as long as the total wavefunction remain antisymmetric) and attracted a lot of attention in the perspective to create Majorana modes [63]. Besides, Cooper pairs do not verify bosons statistic ( $[S_p, S_q^\dagger] = \delta_{pq}(1 - n_{p\downarrow} - n_{p\uparrow})$  with  $S_q = c_{-q\downarrow} c_{q\uparrow}$ ), hence they do not forms a Bose-Einstein condensate. An important length scale is  $\xi_0 = \frac{\hbar v_F}{\pi \Delta}$  which correspond to the minimal length over which superconductivity can be established (for instance, it sets the diameter of superconducting vortices, or the depth of induced superconductivity in a normal metal). It can be interpreted as the spatial extension of a Cooper pair, and is an important parameter to determine the Cooper pair splitting efficiency (see chapter 4).

### 1.3.1.2 Excitation and semiconducting pictures

In the previous description of superconductivity, we are only dealing with positive excitation energies. Hence the most straightforward way to represent the state of the system is to fix the energy of the condensate at zero and then represent the density of excitation states as previously introduced above the condensate energy. This is called the *excitation picture* and is illustrated in figure 1.6-a.

Nevertheless, when one want to describe tunneling experiments, one is interested in transfers of charges and not of quasi-particles, which are two distinct things in superconductivity. For instance, when a normal metal and a superconducting metal are separated from each other by a tunnel barrier, the excitation picture is not the most handy. To illustrate this statement, lets consider the situation in which the normal metal is negatively biased with respect the superconductor such that  $eV_{normal} < -\Delta$ . In this situation one can inject a hole in the superconductor which decompose on the Bogoliubon states as:

$$c_{k\uparrow}|GS\rangle = (u_k^* \gamma_{k\uparrow} + v_k \gamma_{-k\downarrow}^\dagger)|GS\rangle = -v_k \gamma_{-k\downarrow}^\dagger|GS\rangle \quad (1.9)$$

with  $k > k_F$ . This can seem a priori surprising and is due to the fact that a *bogoliubon* quasiparticles are a superposition of an electron and a hole. To clarify this point, one can introduce two hole-like and two electron-like quasi-particles excitations, connected by the fact that creating a hole-like excitation is equivalent to annihilate a pair and create an electron-like excitation. The new set of four excitation operators is:

$$\begin{aligned} \gamma_{e,k\uparrow}^\dagger &= u_k^* c_{k\uparrow}^\dagger - v_k^* S^\dagger c_{-k\downarrow} \\ \gamma_{h,k\uparrow}^\dagger &= u_k^* S c_{k\uparrow}^\dagger - v_k^* c_{-k\downarrow} \\ \gamma_{e,-k\downarrow}^\dagger &= u_k^* c_{-k\downarrow}^\dagger + v_k^* S^\dagger c_{k\uparrow} \\ \gamma_{h,-k\downarrow}^\dagger &= u_k^* S c_{-k\downarrow}^\dagger + v_k^* c_{k\uparrow} \end{aligned} \quad (1.10)$$

which are related by  $\gamma_{h,k\sigma} = S \gamma_{e,k\sigma}$  with  $S = c_{k\uparrow} c_{-k\downarrow}$ . One can notice that the two hole-like excitations  $\gamma_{h,k\uparrow}^\dagger$  and  $\gamma_{h,-k\downarrow}^\dagger$  lower the number of electron by one. Hence the same process can be rewritten as:

$$c_{k\uparrow}|GS\rangle = u_k^* \gamma_{e,k\uparrow}^\dagger + v_k \gamma_{-k,\downarrow}^\dagger|GS\rangle = v_k \gamma_{-k,\downarrow}^\dagger|GS\rangle \quad (1.11)$$

Now the annihilation of an electron in the superconductor corresponds to the creation of a hole-like excitation in the superconductor. The use of these four operators correspond to the *semiconducting* picture, and the previous situation is depicted in figure 1.6-b. It is worth noticing that such a picture does not take into account the superconducting

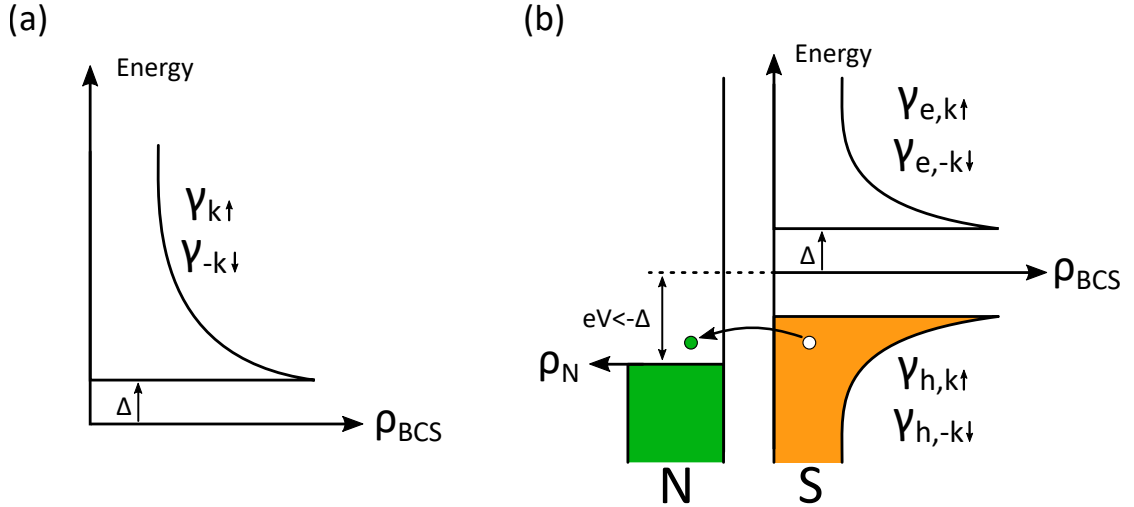


FIGURE 1.6: **The excitation and semiconductor pictures:** **a.** Representation of the BCS ground state in the excitation picture. The ground state is by definition the vacuum of Bogoliubon excitations. **b.** Schematic of a tunneling event where an electron is tunneling from a superconductor into a normal metal. The decomposition of Bogoliubon operators into electron-like and hole-like parts allows to conveniently represent tunneling event. The lower band correspond to the hole-like part of Bogoliubons. This representation is widely used to describe transport experiments. Notice that as it is represented the BCS density of state is twice smaller than in the excitation picture.

phase, hence it is not adapted to describe coherent phase effects such as the Josephson effect, or to predict the appearance of Andreev bound states (see next section).

### 1.3.1.3 Andreev reflections

At the interface between a superconductor and a normal metal, an incident electron from the normal metal with an energy  $E \ll \Delta$  has no directly accessible states in the superconductor. It can be either reflected back into the normal metal (specular reflection), or as a hole of equal energy and opposite spin. This last process is called *Andreev reflection*. It is the basic mechanism responsible for superconducting proximity effect, namely the fact that normal metal contacted by a superconductor becomes superconducting over a length characterized by  $\xi_0$ . During Andreev reflection, particle number conservation implies the creation of two electrons inside the superconductor which then decay into the Cooper pair condensate.

**Crossed Andreev reflection** When two spatially separated normal metal conductors are connected to the same superconductor, the reflected hole can propagate in a different conductor from which the incident electron is coming, provided that the two

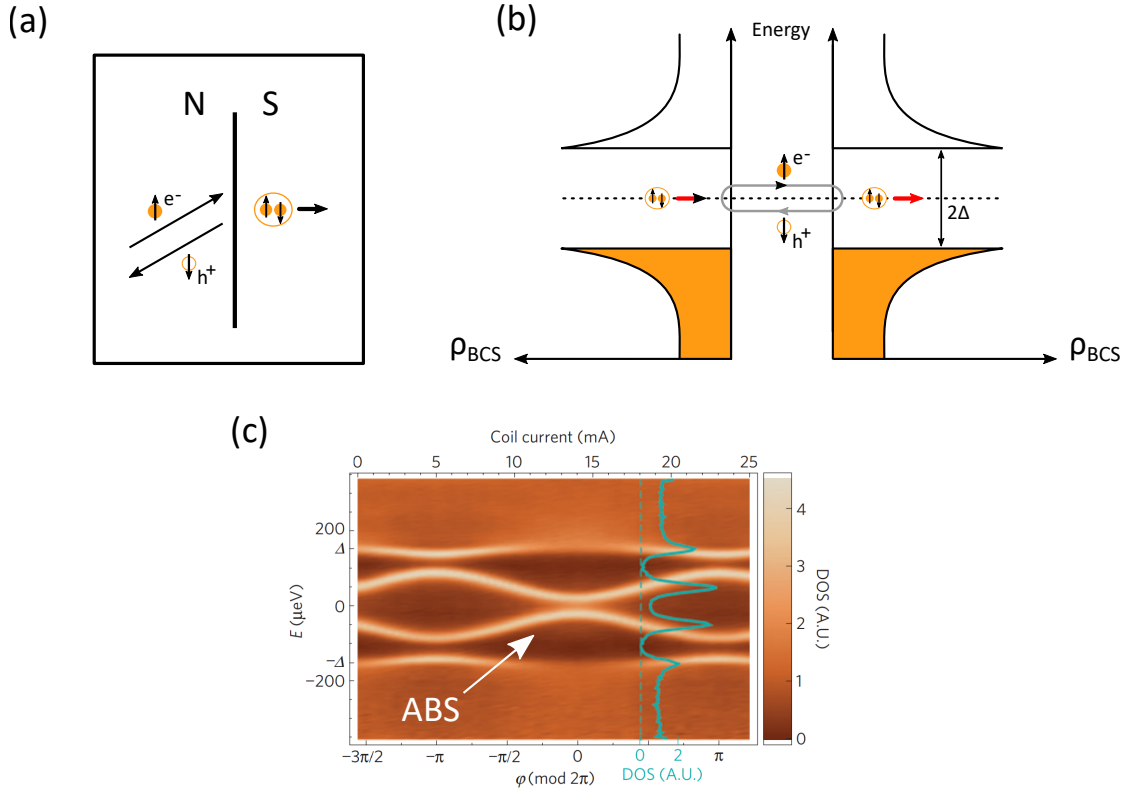


FIGURE 1.7: **Andreev reflection and Andreev Bound States:**

**a.** Schematic of the Andreev reflection process. An electron incoming from a normal metal with a wave-vector  $k$  has a finite probability to be reflected on a normal-superconductor interface as a hole of opposite wave-vector and spin. **b.** Mechanism responsible for the emergence of Andreev bound states in a superconductor - coherent conductor - superconductor junction. **c.** First observation of individually resolved Andreev bound states in a tunnelling spectroscopy experiment. In this experiment, a carbon nanotube plays the role of the coherent conductor. source: [64]

interfaces are distant than less that the superconducting coherence length  $\xi_0$ . This is the mechanism one want to exploit to split Cooper pair [65] (see chapter 4).

#### 1.3.1.4 Proximity effect in quantum dots

When the superconductor is well coupled to a coherent conductor ( $\Gamma \gg \Delta$ ), reflecting the fact that the time spent in the dot ( $\hbar/\Gamma$ ) is small compare to the correlation time of a Cooper pair ( $\hbar/\Delta$ ), multiple Andreev reflection occurs before the electron and the hole loose their relative phase. It gives rise to standing wave, forming *Andreev bound states*. Because the reflected hole takes a phase factor:  $-\phi - \arccos(\frac{E}{\Delta})$  with  $\phi$  being the macroscopic phase of the superconductor, the energy spectrum of such Andreev bound states is  $E_A = \Delta \sqrt{1 - \tau \sin^2(\frac{\phi}{2})}$ . These states carry supercurrent, as they depend on

the superconducting phase (see schematic in figure 1.7-b,c), hence they can be detected via transport spectroscopy experiment [64].

When  $\Gamma, \epsilon_d \ll \Delta$ , one can treat Andreev reflection in a perturbative manner, and derive a low energy effective hamiltonian. Consider only one superconductor connected to a quantum dot with one orbital level  $\epsilon_d$ . The hamiltonian of such system reads:

$$H_{QD-SC} = \sum_{\sigma} \epsilon_d d_{\sigma}^{\dagger} d_{\sigma} + t \sum_{k,\sigma} (d_{\sigma}^{\dagger} c_{k\sigma} + h.c.) + \sum_{k,\sigma} E_{k,\sigma} \gamma_{k,\sigma}^{\dagger} \gamma_{k,\sigma} \quad (1.12)$$

Where  $d_{\sigma}$ , and  $d_{\sigma}^{\dagger}$  are respectively the annihilation and creation operator of an electron in the dot with a spin  $\sigma$ . At low enough temperature ( $T \ll T_C$ ), there are no quasiparticles in the superconductor, nevertheless the existence of these empty states can have a renormalization effect on the spectrum of the dot via second-order virtual processes involving them. A Schrieffer-Wolff transformation accounts for such second-order processes, by eliminating first order terms in  $\gamma_{k\sigma}$ , and then subsequently preserving only second-order terms in  $\gamma_{k\sigma}$ . This procedure is similar to the *adiabatic elimination* in atomic physics [66]. The Schrieffer-Wolff transformation reads:  $H_{SW} = e^{iS} H_{QD-SC} e^{-iS}$  with  $S = i \sum_{k\sigma} X_{k\sigma} \gamma_{k\sigma} - h.c.$ . Noting  $H_{QD-SC} = H_0 + H_t$  with  $H_t$  being the linear part in  $t$ , and using the Baker-Hausdorff-Campbell formula<sup>3</sup>, one has to find the  $X_{k\sigma}$  such that  $H_t + i[S, H_0] = 0$ . The  $X_{k\sigma}$  that verify such a condition are:

$$\begin{aligned} X_{k\uparrow} &= \frac{tu_k^*}{E_k - \epsilon_d} d_{\uparrow}^{\dagger} + \frac{t^* v_k^*}{E_k + \epsilon_d} d_{\downarrow} \\ X_{k\downarrow} &= \frac{tu_k^*}{E_k - \epsilon_d} d_{\downarrow}^{\dagger} - \frac{t^* v_k^*}{E_k + \epsilon_d} d_{\uparrow} \end{aligned} \quad (1.13)$$

After keeping only up to the 2<sup>nd</sup> order terms of  $H_{SW}$  in  $\gamma_{k\sigma}$ , one obtains:

$$H_{eff} = H_0 + \frac{i}{2} [S, H_t] = \tilde{\epsilon}_d \hat{n}_d + (\Gamma_C d_{\uparrow}^{\dagger} d_{\downarrow}^{\dagger} + h.c.) \quad (1.14)$$

with:

$$\tilde{\epsilon}_d = \epsilon_d - \pi |t|^2 \rho_N(E_F) \frac{\epsilon_d}{\Delta} F\left(\frac{\epsilon_d}{\Delta}\right) \quad \text{and} \quad \Gamma_C = e^{i\phi} \pi |t|^2 \rho_N(E_F) F\left(\frac{\epsilon_d}{\Delta}\right) \quad (1.15)$$

noting  $F(x) = 1/\sqrt{1-x^2}$ . Since the term  $\Gamma_C d_{\uparrow}^{\dagger} d_{\downarrow}^{\dagger} + h.c.$  only couples states with the same parity, we can fully capture its effect by restricting ourselves to the subspace spanned

<sup>3</sup>Baker-Hausdorff-Campbell formula:  $H_{SW} = H_0 + H_t + i[S, H_0] + i[S, H_t] - \frac{1}{2}[S, [S, H_0]] + O(t^3)$

by  $|0\rangle$ , and  $|\uparrow\downarrow\rangle$ . The two eigenstates reads:

$$|\Psi_{\pm}\rangle = \left( \frac{\Gamma_C^*}{\sqrt{|\Gamma_C|^2 + E_{\pm}}} + \frac{E_{\pm}}{\sqrt{|\Gamma_C|^2 + E_{\pm}}} d_{\uparrow}^{\dagger} d_{\downarrow}^{\dagger} \right) |0\rangle \quad (1.16)$$

with eigenenergies:

$$E_{\pm} = \tilde{\epsilon}_d \pm \sqrt{\tilde{\epsilon}_d^2 + |\Gamma_C|^2} \quad (1.17)$$

interestingly, the form of the eigenstates strongly recall the expression of the elementary block of the BCS ground state. In this calculation we have considered the on-site Coulomb repulsion energy  $U = 0$ .

### 1.3.2 Cooper pair splitting

Originally proposed as a source of electronic Einstein-Podolski-Rosen pairs [65], the Cooper pairs splitter uses superconductivity as a natural source of electronic spin entanglement. As illustrated in figure 1.8, one superconductor tunnel coupled to two well-separated quantum dots can generate non-local spin-entangled pairs of electrons reminiscent of the Cooper pairs in the superconductor. To favor crossed Andreev reflection, the two dots are placed in the Coulomb blockade regime where two electrons on the same dot is highly unlikely. To realize such an experiment, one want to be able to state whether or not this splitting process occurs in a coherent fashion. In other words: Is the Cooper pairs still forming a entangled state once the two electrons are spatially separated from each other ? Most of the experimental realizations so far have only demonstrated splitting of Cooper pairs by measuring cross correlated transport quantities (differential conductivity [23] [67], current noise[68], [24]) and in multiple host materials (carbon nanotube [24] [69], graphene [70], InAs nanowires [23] [68]. Few of these experiment shown high splitting efficiency [68], [69], [70]. However, they do not conclude on the coherence of the splitting. One experiment have demonstrated coherent splitting of Cooper pairs by measuring a supercurrent in a superconductor - parallel DQD - superconductor junction [71]. They measure the supercurrent in their circuit while turning independently the two dots ON and OFF. Nevertheless, in such experiment, it is tricky to discriminates the respective contribution of each processes, local and non-local. In addition, this experiment requires to recombine the Cooper pairs, thus it doest not constitute a splitter.

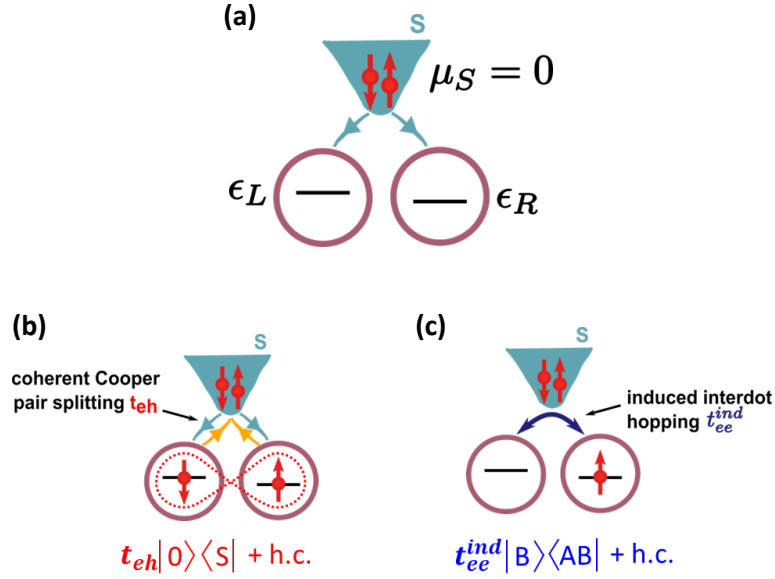


FIGURE 1.8: **Double quantum dot dressed by Cooper pairs:** **a.** Schematic of a *closed* Cooper pair. The two normal contacts are not represented since not considered in the hamiltonian. **b.** The coherent Cooper pair splitting of amplitude  $t_{eh}$  give rise to hybridization of  $|0\rangle = (0, 0)$  and  $|S\rangle = 1/\sqrt{2}(|\uparrow, \downarrow\rangle - |\downarrow, \uparrow\rangle)$ . **c.** The superconductor can also induce a second order process where an electron from one of the dot can virtually excite a Bogoliubon in the superconductor and then tunnel in the next dot.

Detecting entanglement in a splitter geometry using only transport spectroscopy is indeed very challenging, since one ask to the system to be closed (weak coupling to the leads) to preserve coherence of quantum states, and at the same time, the DQD has to be sufficiently coupled to the leads to ensure measurable current. Besides, light-matter interaction has proven to be a powerful probe for closed system [6], and has been widely applied to probe internal dynamics of quantum dot circuits [44], while weakly affecting its coherence [72],[73].

Consider a simplified geometry of a Cooper pair splitter, where a superconductor is connected to two quantum dots as depicted in figure 1.8-a. Similarly to the previous section one can derive a low energy hamiltonian (more details about this derivation are given in chapter 4):

$$H_{eff} = \sum_{i \in L, R} \epsilon_i n_i + \left( t_{eh} (d_{L\uparrow}^\dagger d_{R\downarrow}^\dagger - d_{L\downarrow}^\dagger d_{R\uparrow}^\dagger) + t_{ee}^{ind} \sum_{\sigma} d_{L\sigma}^\dagger d_{R\sigma} + h.c. \right) \quad (1.18)$$

with:

$$t_{eh} = \pi t_L t_R e^{i\phi} \rho_{BCS}(E_F) f(\delta x) \sum_{i \in L, R} \frac{1}{2} F\left(\frac{\epsilon_i}{\Delta}\right) \quad (1.19)$$

$$t_{ee}^{ind} = -\pi t_L t_R^* \rho_{BCS}(E_F) f(\delta x) \frac{\epsilon_L + \epsilon_R}{\Delta} \sum_{i \in L, R} \frac{1}{2} F\left(\frac{\epsilon_i}{\Delta}\right) \quad (1.20)$$

$$f_{1D}(\delta x) = \cos(k_F \delta x) \frac{\sum_i F\left(\frac{\epsilon_i}{\Delta}\right) e^{-|\delta x|/F\left(\frac{\epsilon_i}{\Delta}\right)\xi_0}}{\sum_i F\left(\frac{\epsilon_i}{\Delta}\right)} \quad (1.21)$$

One can distinguish two main effects of the superconductor on the double quantum dot spectrum (see figure 1.8). The Cooper pair injection term, which hybridize the two states  $|0\rangle$  (double dot empty) and  $|S\rangle$  (one electron in each dot in a singlet state) and leads to eigenstates in the even sector  $|V_1\rangle$  and  $|V_2\rangle$ :

$$|V_{1(2)}\rangle = \frac{\sqrt{2}t_{eh}^*}{\sqrt{2|t_{eh}|^2 + E_{1(2)}}}|0\rangle + \frac{E_{1(2)}}{\sqrt{2|t_{eh}|^2 + E_{1(2)}}}|S\rangle \quad (1.22)$$

with eigenenergies (shown in figure 1.8):

$$E_{V_{1(2)}} = \frac{1}{2} \left( \epsilon_\Sigma \pm \sqrt{\epsilon_\Sigma^2 + 8|t_{eh}|^2} \right) \quad (1.23)$$

The last term in  $H_{eff}$  is the interdot tunneling assisted by Cooper pairs which is distinct from the direct tunneling term in between the two dots. Importantly,  $t_{ee}^{ind}$  depends on the energy sum  $\epsilon_\Sigma = \epsilon_L + \epsilon_R$  which can be used to engineer a specific coupling scheme between a double quantum dot and a microwave cavity (see chapter 4).

**Geometrical factor** The width of the superconducting contact plays a crucial role in the splitting efficiency since, if the two QD-superconductor interfaces are too far apart from each other no splitting is expected. Thus, it is necessary to write the hamiltonian in real space and not in reciprocal space. When one is evaluating the Cooper pair splitting rate, terms such like:  $\sum_{k < k_F} e^{\mathbf{k} \cdot (\mathbf{r}_L - \mathbf{r}_R)} \propto \sin(k_F(r_L - r_R))/k_F(r_L - r_R)$  (in 3D) appears, with  $\mathbf{r}_L$  and  $\mathbf{r}_R$  being the position of the QD-superconductor interfaces. Similarly to Friedel oscillations, such terms are damped oscillations in real space whose damping depends on the dimension of the system (the sharp Fermi-Dirac distribution in reciprocal space give rise to damped oscillations in real space).

The geometrical factor presented here correspond to a one-dimensional geometry (meaning a point contact), which is relevant for carbon nanotube with a diameter about 1 nm. This factor sets a constraint on the distance  $\delta x = x_L - x_R$ . One notices that using a

superconducting material with a large  $\xi_0$  loosen this constraint (for instance  $\xi_0 \simeq 100$  nm for Aluminum in the dirty limit [23]). Going to a two-dimensional system (meaning a 1D contact, which is the case of nanowire with diameters above 50 nm) leads to a geometrical factor:  $f_{2D}(\delta\mathbf{r}) \propto \frac{\cos(k_F\delta r)}{\sqrt{k_F\delta r}} e^{-\delta r/\pi\xi}$  for  $k_F\delta r \gg 1$  [74], which is more restrictive than in the 1D scenario. Hence, carbon nanotubes appears as good candidate to host such a circuit.

## 1.4 Spin qubits in quantum dots

The founding paper of Divincenzo and Loss [42] sets the different requirements of a qubit for quantum computing, comprising, initialization, coherent manipulation, and read-out. The most natural candidate for a qubit and the one envision in this early proposal is the spin of an electron. Various platforms other than quantum dot have been study to realize such a spin qubit, and few of the more promising are [75] (Silicon carbide), [76] (P donor in Si), [77] (NV centers), [78] (CMOS technology). In this section, we only focus on the different realizations of spin qubit in quantum dots circuits.

The electron spin is a very promising platform for quantum computing because of its extremely long coherence time ( $T_1 \approx 1s$  [79] and  $T_2 = 0.87ms$  using appropriate dynamical decoupling sequences [80]). Such coherence properties reflect the fact that the electron spin is well decoupled from its environment. The drawback is that this decoupling from the environment makes it hard to manipulate the state of spin. Indeed, the magnetic coupling strength between an electronic spin and a photon confined in a coplanar waveguide resonator with a standard geometry is very weak ( $g_{spin} \approx 10\text{Hz}$  [81]).

Strategies to circumvent this issue, are either to manipulate two-electron spin states by acting on the exchange energy (the case of triple quantum dot spin qubit) or to implement a coherent spin-charge interface allowing to control spin with electrical means which can be realized by using spin-orbit coupling [82], inhomogeneous Overhauser field [34], or a micromagnet [35], [83], [26]. At the end of this section another spin-qubit geometry is introduced [83].

### 1.4.1 The big family of spin qubits

#### 1.4.1.1 Singlet-triplet qubit

The singlet-triplet qubit is one of the first implementations of a spin qubit in quantum dot circuit [34]. It is based on a double quantum dot architecture and the information is encoded in the two-electron spin states  $T_{0,(1,1)}$  and a superposition of  $S_{(0,2)}$  and  $S_{(1,1)}$ . Here the label  $(i, j)$  describe the charge occupation of the dots ( $i, j \in \{0, 1, 2\}$ ) and  $|S\rangle = 1/\sqrt{2}(|\uparrow, \downarrow\rangle - |\downarrow, \uparrow\rangle)$ ,  $|T_+\rangle = |\uparrow\uparrow\rangle$ ,  $|T_-\rangle = |\downarrow\downarrow\rangle$ ,  $|T_0\rangle = 1/\sqrt{2}(|\uparrow, \downarrow\rangle + |\downarrow, \uparrow\rangle)$  are respectively the singlet and the three triplet states, describing the spin part of the state. For triplet states, the orbital part of the wavefunction has to be antisymmetric to satisfy the Pauli principle, thus one of the two electron of the states  $T_{0,(0,2)}$ ,  $T_{+,(0,2)}$ ,  $T_{-,(0,2)}$  has to sit on an higher energy orbital. This is the reason why these three states have a much higher energy and can be ignore in the rest of the discussion.

This qubit is operated close the degeneracy line between the charge filling states  $(1, 1)$  and  $(0, 2)$ , then one can safely ignore other charge distribution in the double quantum dot. For  $\epsilon_\delta > 0$  (see figure 1.9), the ground state is the singlet state  $S_{(0,2)}$ . For  $\epsilon_\delta < 0$ , in absence of electron tunneling and magnetic field, the three triplets and the singlet are degenerate. Applying a magnetic field allows to push the triplets  $T_{+,(1,1)}$  and  $T_{-,(1,1)}$  away from  $S$  ( $= \alpha S_{(1,1)} + \beta_{(0,2)}$ , with  $|\alpha|^2 + |\beta|^2 = 1$ ) and  $T_{0,(1,1)}$  which form the logical subspace of the qubit. Interestingly, both  $S_{(1,1)}$  and  $T_{0,(1,1)}$  have  $S_Z = 0$ , which make them insensitive to noise in  $B_Z$ , hence the  $S$ - $T_{0,(1,1)}$  qubit is a simple example of a *decoherence free subspace*. Since electron tunneling between the two dots conserves spin, close to  $\epsilon_\delta = 0$ ,  $S_{(1,1)}$  and  $S_{(0,2)}$  hybridize resulting in a avoiding crossing. The tunneling  $t$  and the detuning  $\epsilon_\delta$  set the energy difference  $\Delta E = E_{T_{0,(1,1)}} - E_S$ , often referred to as the exchange energy. This exchange interaction originate from the sign inversion under exchange of fermionic particles and can be electrically controlled via electrostatic gate voltages. The exchange interaction can be recast from the hamiltonian of a double quantum dot:

$$H_{hub} = \sum_{i=L,R} U_i \hat{n}_i (\hat{n}_i - 1) + U_m \hat{n}_L \hat{n}_R + \epsilon_L \hat{n}_L + \epsilon_R \hat{n}_R + \sum_{\sigma=\uparrow,\downarrow} (t \hat{c}_{L,\sigma}^\dagger \hat{c}_{R,\sigma} + h.c.) \quad (1.24)$$

Where  $U_i$  is the charging energy on the  $i$  dot,  $U_m$  is the mutual charging energy between the two dots,  $\epsilon_i$  is the orbital dot energy occupied by the electron in the dot  $i$ , and  $t$  is the

tunnel coupling between the two dots. Here we focus on the (1,1) charge configuration, where tunneling  $t$  is small compare to the other energy scales (Zeeman splitting and charging energies) and by considering only virtual tunneling to the doubly occupied singlet  $S_{(0,2)}$  one can perform a Schrieffer-Wolff transformation and obtain a low-energy hamiltonian of the double dots [84]:

$$H_{heis} = J(\epsilon_\delta) \hat{S}_L \hat{S}_R \quad (1.25)$$

In this Heisenberg hamiltonian, the exchange interaction reads [84]:

$$J(\epsilon_\delta, t) \approx 4t^2 U / (U^2 - \epsilon_\delta^2) \quad (1.26)$$

With  $U = U_L = U_R$ . By acting on the detuning  $\epsilon_\delta$  it is then possible to modulate  $J(\epsilon_\delta)$ . If one look at the Bloch sphere of the  $S$ - $T_0$  subspace (figure 1.9), such modulation represent a rotation of the state vector around the z-axis. The full control of the qubit state requires a second rotation axis which can be provided by an inhomogeneous magnetic field:  $H_{S-T} = J(\epsilon_\delta) \hat{\sigma}_z + \Delta B_{inh} \hat{\sigma}_x$ , where  $\Delta B_{inh}$  is the magnetic field difference between the right and the left quantum dot. Experimentally, this inhomogeneous magnetic field  $\Delta B_{inh}$  is created either by random nuclear magnetic field (as in GaAs [34]) or by embedding a micromagnet close to the double quantum dot in case of material with a low density of nuclear spins (as in Si [85]). The latter allows a better control over the field gradient and going to materials with a low number of nuclear spins, such as silicon or carbon nanotube, improves the coherence of the spin qubit.

To initialize a singlet-triplet qubit in  $S_{(1,1)}$ , first, one has to go to positive detuning to set the qubit in the  $S_{(0,2)}$  state, and then go to large negative detuning in an adiabatic way with respect to the tunnel splitting. The read-out is commonly done using Pauli spin blockade. It consists in a spin-charge conversion mechanism exploiting the fact that state  $S_{(1,1)}$  can tunnel toward  $S_{(0,2)}$  whereas  $T_{0,(1,1)}$  cannot tunnel in the (0,2) region, due to Pauli principle. The spin part of the wavefunction (singlet or triplet) is then mapped-out on the charge states (1,1) or (0,2), which can be easily distinguished by measuring the conductance in a nearby quantum point contact. Such a measurement technique is projective (no-QND measurement) and does not allow to coherently couple qubits to each other. Coherence time  $T_2^* \approx 240ns$  [85] have been measured and its limitation is attributed to charge noise (local charge fluctuator that feed through to

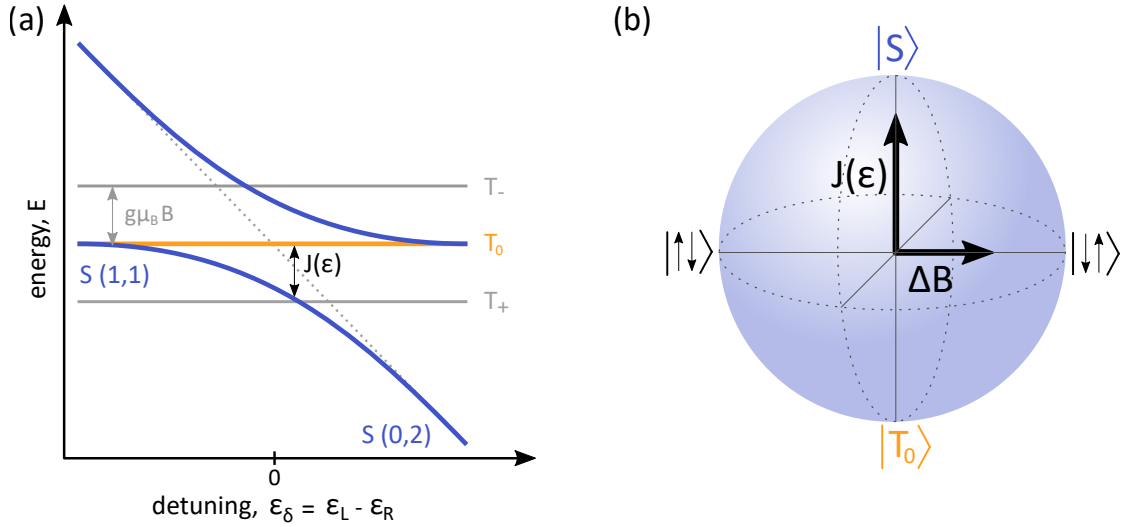


FIGURE 1.9: **Singlet-triplet qubit in a double quantum dot:**

**a.** Energy dispersion of the two-electron states in a double quantum dot. An external magnetic field  $B$  lifts the degeneracy between the three triplet states by  $g\mu_B B$ . **b.** Bloch sphere illustrating the subspace of the singlet-triplet qubit. The exchange interaction  $J$  sets the transition energy. When  $J$  is small compared to  $\Delta B$ , the quantization axis of the qubit aligns with the  $|\uparrow\downarrow\rangle - |\downarrow\uparrow\rangle$  axis of the Bloch sphere. In this situation, coherent oscillations between  $|\uparrow\downarrow\rangle$  and  $|\downarrow\uparrow\rangle$  can be driven via an RF modulation of  $J(\epsilon)$  [34].

noise in gate voltages) and fluctuations in magnetic field, since relative phase evolution of the two electron spins results in mixing of singlet and triplet.

#### 1.4.1.2 Three-electron spin qubits

The original motivation to use triple quantum dots to encode a spin qubit is the possibility to fully control the state of the qubit using exchange interaction only. Furthermore, such geometry allows one to reduce sensitivity to charge noise by operating the qubit at highly symmetric point in the stability diagram.

**Exchange-only qubit** The spectrum of a triple quantum dots is much more complex than the one of a double quantum dots. To simplify the description we restrict ourselves to 3 electrons and to one orbital per dot. With these constraints, the Hilbert space still contains 20 states. Applying a magnetic field allows to separate in energy the different subspaces ( $S = 3/2$  and the two subspaces with  $S = 1/2$  and  $S_Z = \pm 1/2$ ). In the following we focus on the subspace  $S = 1/2$  and  $S_Z = +1/2$  which contains eight states [84]. Two of these eight states lie in the (1,1,1) charge stability region (see figure 1.10)

and are the logical states of the exchange-only qubit[84] :

$$|0\rangle = \frac{1}{\sqrt{6}}(|\uparrow\uparrow\downarrow\rangle + |\downarrow\uparrow\uparrow\rangle - 2|\uparrow\downarrow\uparrow\rangle) = |\uparrow\rangle_1|S\rangle_{23} + |S\rangle_{12}|\uparrow\rangle_3 \quad (1.27)$$

$$|1\rangle = \frac{1}{\sqrt{2}}(|\uparrow\uparrow\downarrow\rangle - |\downarrow\uparrow\uparrow\rangle) = |S\rangle_{13}|\uparrow\rangle_2 \quad (1.28)$$

The dispersion of the two states is shown in figure 1.10. Similarly to the singlet-triplet qubit an effective low energy hamiltonian can be obtained:

$$H_{eff} = J_L(\epsilon_\delta)\hat{\sigma}_L + J_R(\epsilon_\delta)\hat{\sigma}_R \quad (1.29)$$

Where  $\hat{\sigma}_L = (1/4)(\sqrt{3}\hat{\sigma}_X - \hat{\sigma}_Z)$ , and  $\hat{\sigma}_R = (1/4)(-\sqrt{3}\hat{\sigma}_X - \hat{\sigma}_Z)$ . As illustrated in figure 1.10,  $J_L(\epsilon_\delta)$  and  $J_R(\epsilon_\delta)$  drive rotations about two axis that are  $120^\circ$  apart from each other. When moving in the detuning space  $\epsilon$ ,  $\epsilon_M$  (where  $\epsilon = (\epsilon_1 - \epsilon_3)/2$  and  $\epsilon_M = \epsilon_2 - (\epsilon_1 + \epsilon_3)/2$ ), one change the strength of one exchange coupling relatively to the other (see formula 1.26) hence changing the global effective rotation axis via  $\epsilon$ -pulses. An other strategy is to control the  $J$ 's through their dependence of the tunnel couplings  $t$ 's (see formula 1.26). It allows to stay at fixed position in the detuning space, and maintaining the qubit at a charge double sweet spot (where first derivatives of  $(E_1 - E_0)(\epsilon, \epsilon_M)$  with respect to  $\epsilon$  and  $\epsilon_M$  are zero), hence reducing decoherence due to charge noise during manipulation steps. Such a procedure is often called: *symmetric operation point* [86–88]. Similarly to the singlet-triplet qubit the read-out can be performed via spin-to-charge conversion [89] or c-QED technique [26]. it worth noticing that  $|0\rangle$  and  $|1\rangle$  both belong to the subspace  $S = 1/2$  and  $S_Z = +1/2$ , hence like for the singlet-triplet qubit, the logical subspace is a decoherence free subspace for noise in  $B_Z$ .

**Resonant exchange qubit (RX)** The resonant exchange qubit is very similar to the exchange only qubit, and it mainly differs in the way it is operated. Instead of applying only DC-pulses via  $\epsilon$  or  $t$ , manipulation of the RX qubit state is performed via resonant modulation of the exchange interaction via  $\epsilon$ . In addition, the triple quantum dot is tuned in the charge stability diagram such that the exchange interactions  $J_L$  and  $J_R$  are always ON. This provides a large modulation of the coupling strength [84]  $\eta = \frac{1}{2\omega_{RX}}(J\frac{\partial J}{\partial \epsilon} + 3j\frac{\partial j}{\partial \epsilon})$  with  $\hbar\omega_{RX} = \sqrt{J^2 + 3j^2}$  and  $J = (J_L + J_R)/2$  and  $j = J_L - J_R$ . Such an operation principle has led to  $\pi$ -pulse time as low as  $5ns$  [90]. Moreover, since

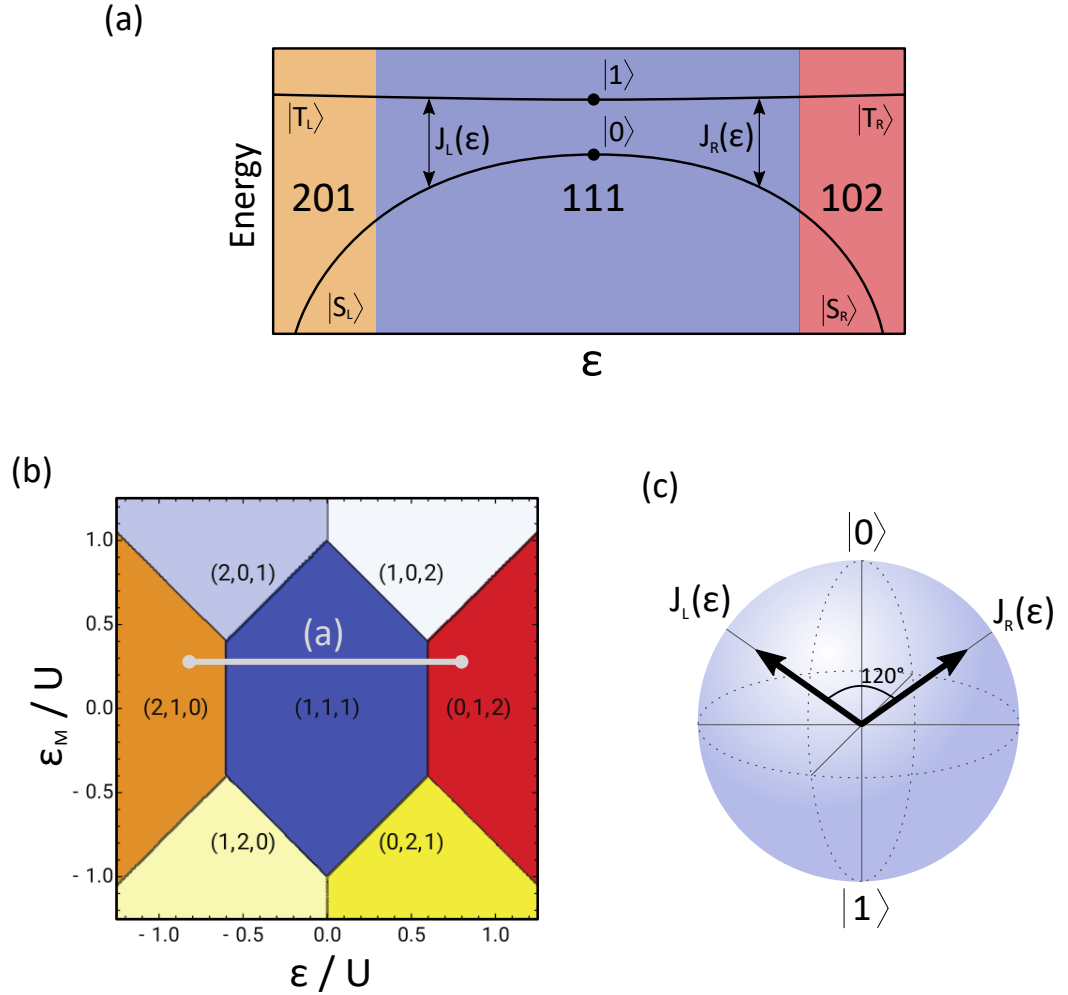


FIGURE 1.10: **Principle of a three electron spin qubit:**

**a.** Energy dispersion of the two relevant states of the spin qubit according to the detuning  $\epsilon = (\epsilon_1 - \epsilon_3)/2$ . The detuning is spanning three different charge stability regions (2,0,1), (1,1,1), (1,0,2). **b.** Charge stability diagram in the  $\epsilon$ - $\epsilon_M$  plan. The position of the 1D cut shown in **a.** is approximately indicated. **c.** Bloch sphere showing the two axis  $\sigma_L$  and  $\sigma_R$ .

no DC pulses are required, one can use only filtered gate line to limit low-frequency charge noise in the vicinity of the qubit. Recently, the realization of a RX qubit in a circuit QED architecture in GaAs have demonstrated strong coupling regime [54].

#### 1.4.1.3 Spin-orbit qubit

An alternative method to the control of the spin via exchange interaction, is to slightly hybridize the spin degree of freedom to the orbital degree of freedom of an electronic system, in order to open a fast manipulation channel of the qubit transition. Qubits based on this idea are called *spin-orbit qubit*, and it gathers a large variety of physical

implementations. The first realization was in a InAs nanowire [82] where the intrinsic spin-orbit coupling is large enough to realize this spin-charge hybridization. An alternative wording to describe the spin-orbit qubits, is to say that its operation principle rely on the implementation of an AC Zeeman splitting ( $g\mu_B B$ ). Such AC Zeeman splitting can be engineered either through an oscillating motion of the electron in an inhomogeneous magnetic field [35] [91], or via a modulation of the Landé factor  $g$  [92].

To further improve coherence properties of spin qubits, the general trend is to use nuclear-spin free host material (Si/SiGe, isotopically purified Si, carbon nanotube) to limit decoherence due to hyperfine interaction with nuclear spin which is the main limitation on coherence time in GaAs based spin-qubit. Nevertheless a possible strategy that has not been implemented yet to circumvent this issue is to use hole spin instead of electron spin. Because valence band is made out of p orbitals which has zero amplitude at the nuclei location, The Fermi contact hyperfine interaction between holes spin and nuclear spin is expected to be zero [93].

## 1.4.2 The ferromagnetic spin qubit

The goal of this section is to give a brief description of a peculiar type of spin-orbit qubit: the ferromagnetic qubit. The idea stemming from the proposal [83], is to use non collinear ferromagnetic contacts in a double quantum dot geometry to induce spin-charge hybridization. This implementation displays the same energy spectrum than spin qubit realizations using a micromagnet [35], [91]. Experimental results on such a spin qubit are presented in chapter 5.

### 1.4.2.1 Principle of the ferromagnetic qubit

The ferromagnetic qubit has a double quantum dot architecture where the two source and drain contacts are ferromagnet with non-collinear magnetizations (see figure 1.11). the different directions of the magnetization induce different quantization axis on the two dots. Hence when an electron tunnels from one dot to the other, it experiences a modification of the orientation the magnetic field. Such a mechanism can be viewed as an artificial spin-orbit like interaction limited to two sites. This qubit has been design to be coupled to photons in a microwave coplanar waveguide resonator, via the charge

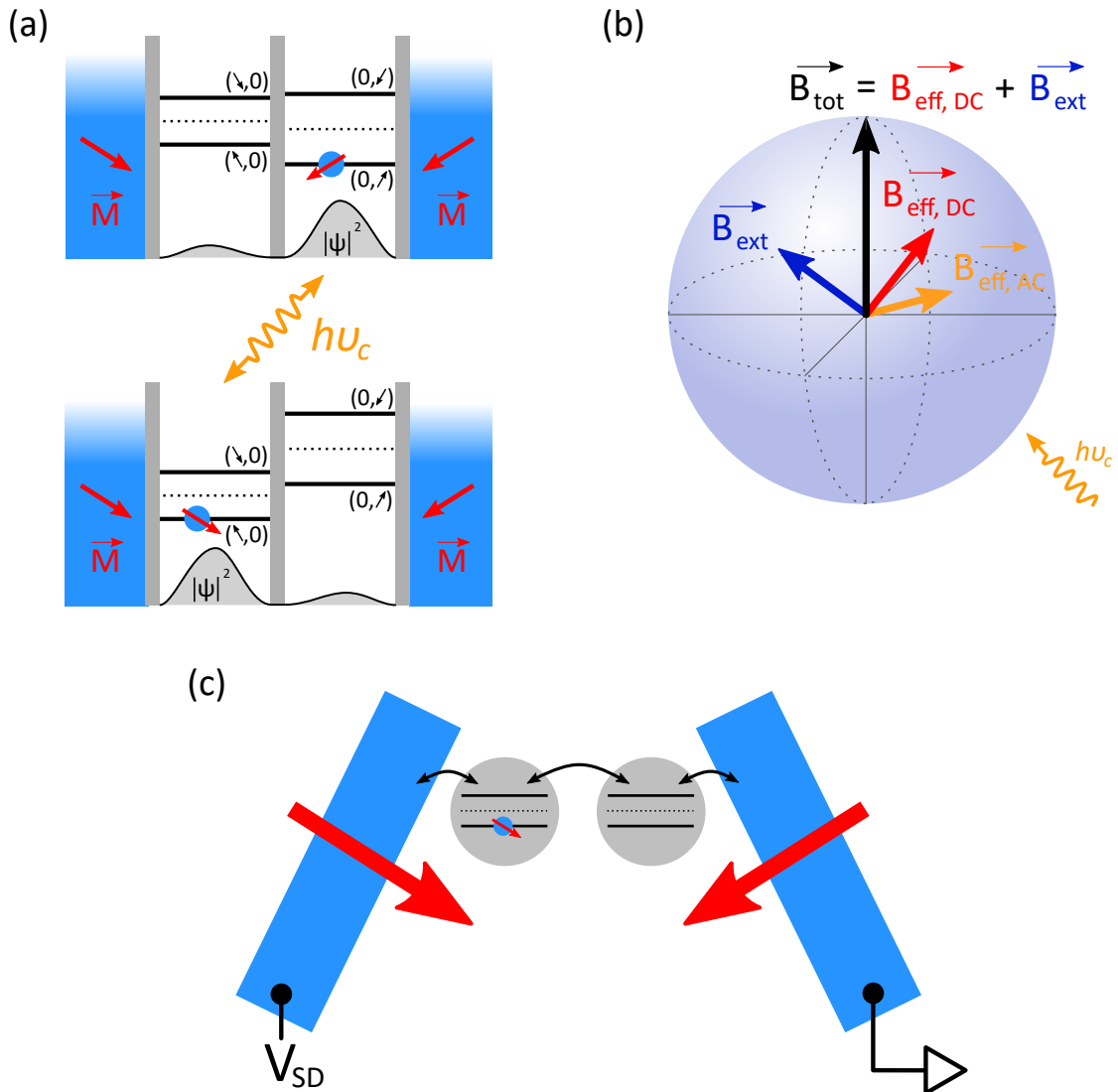


FIGURE 1.11: Working principle of the ferromagnetic spin qubit:

**a.** Each ferromagnetic contact has a different magnetization represented by the large red arrows, which induced different quantization axis in each dot. Thus by driving tunneling between the two dots with the microwave electric field, the electron spin experiences a modification of its quantization axis, which is equivalent to an orthogonal AC magnetic field  $B_{eff,\perp}^{AC}$ . **b.** Bloch sphere summarizing the qubit-photon coupling mechanism. The overall quantization axis is set by an externally applied magnetic field  $B_{ext}$  and the DC part of the induce magnetic field  $B_{eff}^{DC}$ . **c.** Schematic representation of the ferromagnetic spin qubit with the two non-collinear ferromagnetic contacts.

dipole in the double quantum dot, to enhance the coupling strength up to a few MHz [83]. However, hybridizing spin with charge will also affect the coherence, since the qubit will start to be sensitive to charge noise. A more detailed discussion about the most favourable degree of hybridization is given in chapter 5.

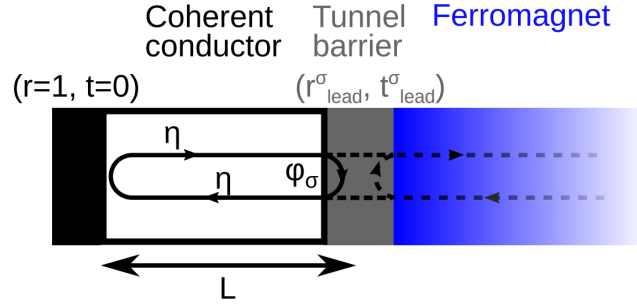


FIGURE 1.12: **Principle of the reflection-induced Zeeman splitting:**

The energy of an electron confined in a coherent conductor is set by the constructive interference condition. If the coherent conductor is connected to a ferromagnet via a tunnel barrier, when the electron reflect on this interface, it will acquire a spin-dependent phase  $\phi_\sigma$  that adds to the phase acquired during the propagation into the conductor  $\eta$ . This results in a Zeeman splitting of the spectrum in the conductor.

#### 1.4.2.2 Ferromagnetic interface-induced exchange fields

Consider a coherent conductor in contact with a ferromagnet via a tunnel barrier, as depicted in the figure 1.12. The ferromagnet can polarize electron spins in the coherent conductor via three different mechanism. The most obvious one is the straight magnetic field generated by the ferromagnet. This mechanism is not expected to be the dominant one.

A spin dependent phase shift acquired by the electron when reflecting on the barrier can also induce a polarization of the spectrum. This phase shift does not depends on the quality of the electrical contact since it also happens for ferromagnetic insulator [83]. This mechanism requires a coherent conductor with a finite length (typically a quantum dot) for constructive interferences to occur. In the single electron picture, this phase shift yields to an effective Zeeman splitting (sometimes called *confinement-induced exchange field*) in the spectrum of the coherent conductor [94]:

$$2\delta = \frac{hv_F}{2L} \frac{\phi_\uparrow - \phi_\downarrow}{2\pi} \quad (1.30)$$

where  $v_F$  is the Fermi velocity,  $L$  is the size of the coherent conductor (size of one of the two dots, for the ferromagnetic spin qubit), and  $\phi_{\uparrow(\downarrow)}$  is phase shift for a spin-up(down) electron.

The last polarization mechanism is a kind of proximity effect, where the electronic wavefunction spreads over the ferromagnet and hybridize with first atomic layers, hence

resulting in a spin polarization of the total quantum state. Its strength depends on the amplitude of the transmission ( $t_{lead}$ ) and vanishes for opaque barrier ( $t_{lead} = 0$ ).

With the idea of implementing a long-lived spin qubit, the last mechanism is not very interesting since a finite  $\Gamma_{lead} \propto |t_{lead}|^2$  means that the qubit subspace is coupled to other states in the leads through which it can lose its coherence. Therefore, the ability to tune in-situ the coupling  $\Gamma_{lead}$  is highly desirable for a ferromagnetic spin qubit.



## Chapter 2

# Mesoscopic - QED

The idea of coupling photons in a cavity to atomic system originates from cavity quantum electrodynamics (C-QED) where a lot of effort has been given to study light-matter interaction at the most fundamental level. The first experiments have been done with Rydbergs atoms [6] and trapped ions [95]. Such architectures provide a controlled environment for the atoms, but allows also to manipulate their state. The idea had then been transposed on chips forming the circuit-QED community [96], [97], where superconducting circuit are coupled to microwave resonator. Such systems exploit the rigidity of the superconducting phase to engineer macroscopic coherent few levels systems. In these experiment, the properties of the artificial atoms can be easily tuned, whereas in cavity-QED they are set by natural constant. The cavity has then been used as a quantum bus to couple several artificial atoms to each other [98], [99], [100]. Once again, this idea can be extended to quantum-dot circuits. While atoms and superconducting circuits are intrinsically closed systems, quantum dot circuits are able to be well coupled to their condensed matter surrounding. In this regime, the cavity endorses a new role since it is used as a powerful probe for condensed matter [101]. The aim of this chapter is to introduce a theoretical description of the coupling between the microwave cavity and the quantum dot circuit, as well as the relevant experimental parameters for designing the circuit-cavity interface. The section 2.1 focus on theoretical description of the coupling. The section 2.2 introduces formalisms on the dynamics of the full coupled system. The last section 2.3 describes few strategies to improve the quality of the cavity-quantum dot interface.

## 2.1 Quantum dot circuit - Cavity coupling description

### 2.1.1 Microscopic description of electron-photon coupling

In Cavity-QED, the cavity electric field is approximated to be constant in the vicinity of the atom (dipolar approximation). It enables to write the light-matter interaction as  $H_{int} = \vec{E} \cdot \vec{d}$  where  $\vec{E}$  is a the uniform cavity electric field felt by the atom, and  $\vec{d}$  is the atomic electrical dipole. Such a description is not necessarily true for circuit-QED experiments. Indeed, superconducting circuits strongly influence the distribution of the electric field. Moreover the degrees of freedom of interest are macroscopic, hence the

dipolar approximation is not valid. Circuit description of the full system with capacitive couplings between the different conductors is more appropriate. Although the microscopic description of Cavity-QED and circuit-QED can be different, the physics of both systems is described by the same Jaynes-Cummings hamiltonian (see section 2.1.3).

Mesoscopic-QED can be thought of as an intermediate between Cavity and circuit-QED [102]. The discrete levels in quantum dot are reminiscent of cavity-QED atomic degrees of freedom. Besides, because of the high density of state in the fermionic reservoir, field screening occurs, resulting in a strong inhomogeneity of the electric field, similarly to circuit-QED (see figure 2.1-a). These screening effects are due to plasmons living in cavity conductors but also in the fermionic reservoirs of the nano-circuit. Tunneling events also happen inside the nano-conductor, and between fermionic contact and the nano-conductor. These tunneling events are the focus of most mesoscopic experiments. Noticing that the dynamics of plasmons is much faster than the tunneling events, one can consider plasmons only via their average contribution, and introduce a photonic pseudo-potential  $V_{\perp}(\vec{r})$  containing the strong inhomogeneities [102].

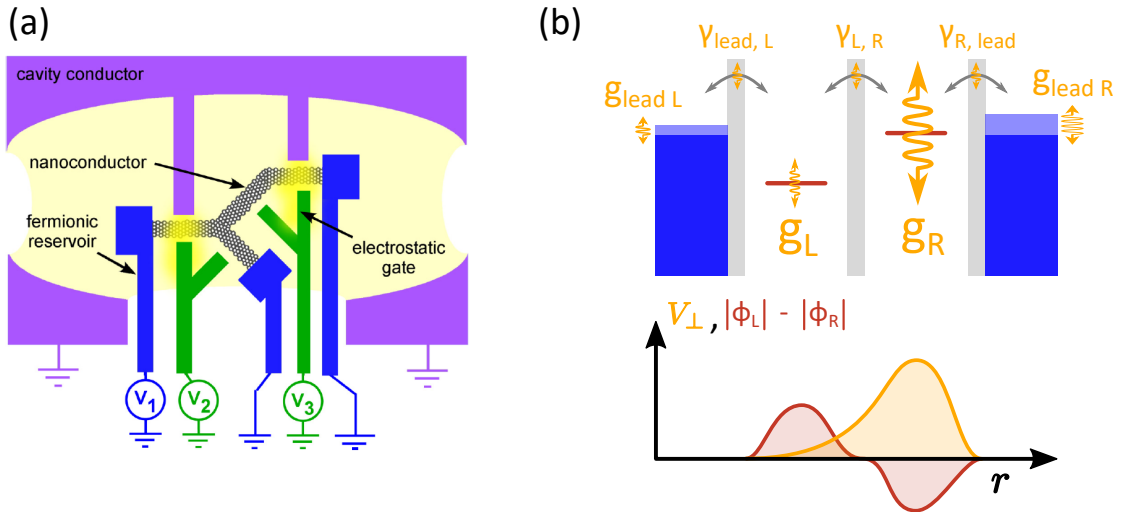


FIGURE 2.1: **Light-matter coupling in mesoscopic-QED:** **a.** Schematic of a mesoscopic-QED device. The cavity electric field in yellow is strongly modified due to the presence of cavity conductor protrusion, fermionic reservoirs, and also electrostatic gates. **b.** By designing protrusion in the cavity conductor (as shown in **a.**), one can make the amplitude of the AC electric field vary over the size of the circuit, thus the amplitude of the modulation of the orbital levels, the tunnel rates, and the chemical potentials can be very different (represented by the varying size of the zigzag arrows). One can choose which dipole in the circuit to address with light by designing the shape of these protrusion.

In this picture, the interaction between cavity photons and discrete electronic orbitals in the nano-conductor is described by the following hamiltonian:

$$H_{e-ph} = -e \int d^3r \hat{\Psi}^\dagger(\vec{r}) \hat{\Psi}(\vec{r}) V_\perp(\vec{r}) (\hat{a}^\dagger + \hat{a}) \quad (2.1)$$

Where  $\hat{\Psi}(\vec{r})$  is the field operator of conduction electrons in the nano-conductor. Interestingly, the photonic pseudo-potential can account both for cavity and circuit-QED experiments. Indeed,  $V_\perp(\vec{r}) = \vec{E} \cdot \vec{r}$  corresponds to cavity-QED boundary conditions, whereas in circuit-QED,  $V_\perp(\vec{r})$  is a constant different in each conductors. To identify the different coupling mechanism, the interaction hamiltonian can be expressed <sup>1</sup> as  $H_{e-ph} = \hat{h}_{int}(\hat{a}^\dagger + \hat{a})$ , with:

$$\hat{h}_{int} = \sum_n g_n \hat{c}_n^\dagger \hat{c}_n + \sum_{n \neq n'} (\gamma_{n,n'} \hat{c}_{n'}^\dagger \hat{c}_n + h.c.) \quad (2.2)$$

and:

$$g_n = -e \int d^3r |\phi_n(\vec{r})|^2 V_\perp(\vec{r}) \quad (2.3)$$

$$\gamma_{n',n} = -e \int d^3r \phi_n(\vec{r}) \phi_{n'}(\vec{r}) V_\perp(\vec{r}) \quad (2.4)$$

The first term in the expression of  $\hat{h}_{int}$  corresponds to the modulation of quantum dot orbitals by the AC-field of the microwave cavity, where  $g_n$  is the spatial overlap between the orbital wavefunction and the photonic pseudo-potential. The second term describes the modulation of the hopping amplitude  $t_{n,n'}$ , and is proportional to the overlap of the two involved orbital wavefunctions and the photonic pseudo-potential. Although this last mechanism explains light-matter coupling in Cavity-QED, it is generally very small in mesoscopic-QED because of the larger spatial separation of the relevant orbitals. In the following only the coupling mechanism due to  $g_n$  term will be considered. According to the physics one want explore, a specific electrical dipole in the circuit can be addressed (for instance the dot-dot dipole or the dot-lead dipole) via the shaping of  $V_\perp(\vec{r})$ .

---

<sup>1</sup>This reformulation is valid only if tunneling events are perturbative, so that the discrete orbitals still form an orthogonal basis on which one can expand the field operator.

### 2.1.1.1 Coupling to a double quantum dot

Consider a double quantum dot, with only one orbital on each dot as illustrated in figure 2.1-b. The interaction hamiltonian of the double quantum dot reads:

$$H_{e-ph,DQD} = (g_L \hat{n}_L + g_R \hat{n}_R)(\hat{a} + \hat{a}^\dagger) \quad (2.5)$$

Where  $\hat{n}_i = \hat{c}_i^\dagger \hat{c}_i$  with  $i \in (L, R)$ . Close to zero detuning ( $\epsilon_\delta = \epsilon_L - \epsilon_R = 0$ ), the two eigenstates of the double quantum dot hamiltonian (see formula 4.1) are the bonding state  $|-\rangle = -v|L\rangle + u|R\rangle$  and the anti-bonding state  $|+\rangle = u|L\rangle + v|R\rangle$  (expressions of  $u$  and  $v$  are given in section 4.3). The electron-photon coupling to the bonding/anti-bonding transition then reads:

$$\begin{aligned} g_{DQD}(\hat{a} + \hat{a}^\dagger) &= \langle + | H_{e-ph,DQD} | - \rangle \\ &= \langle + | (g_L \hat{n}_L + g_R \hat{n}_R)(\hat{a} + \hat{a}^\dagger) | - \rangle \\ g_{DQD} &= \frac{t}{\sqrt{\epsilon_\delta^2 + 4t^2}} \left( -e \int d\vec{r}^3 (|\phi_L(\vec{r})|^2 - |\phi_R(\vec{r})|^2) V_\perp(\vec{r}) \right) \end{aligned} \quad (2.6)$$

Where  $\phi_L(\vec{r})$  and  $\phi_R(\vec{r})$  are the wavefunctions of one electron on the left and on the right dot respectively. It appears that a constant photonic potential  $V_\perp(\vec{r})$  results in no coupling, and one have to engineer a gradients of potential to realize a DQD-cavity coupling (see section 2.3.2 for more details).

### 2.1.2 Input-Output formalism

In this section we describe the dynamic of a bare microwave cavity with an high quality factor  $Q$ . The so-called *input-output* formalism is well adapted to the description of a resonator coupled to its electromagnetic environment. It establishes a relation between the drive tone, the cavity features, and the outgoing signals, which are experimentally accessible quantities. In this section we follow the presentation given in appendix E of [103], and only provide a brief review of the main results by trying to emphasize the physics behind the equations. The microwave cavities used in this thesis work are connected to two transmission lines, which carry the input and output signals. Consider a single mode of such a two-sided cavity. The Hamiltonian of the cavity mode coupled

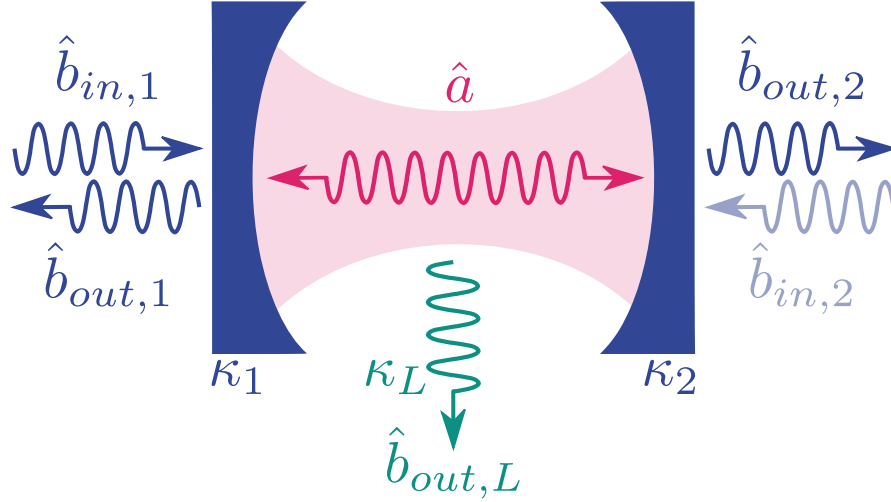


FIGURE 2.2: **Input-Output representation of the relevant modes:** The microwave cavities used in this thesis work are probed via transmission measurement. In a simple representation only two outside modes are considered  $\hat{b}_{in,1}$  and  $\hat{b}_{out,2}$ . A third mode is commonly used to describe internal losses of the cavity:  $\hat{b}_{out,L}$ .

to its environment reads:

$$H = H_{cav} + H_{bath} + H_{int} \quad (2.7)$$

with:

$$\begin{aligned} H_{cav} &= \hbar\omega_c \hat{a}^\dagger \hat{a} \\ H_{baths} &= \hbar\omega_q \sum_{i=1,2} \sum_q \hat{b}_{q,i}^\dagger \hat{b}_{q,i} \\ H_{int} &= -i\hbar \sum_{i=1,2} \sum_q (f_q \hat{b}_{q,i} \hat{a}^\dagger - f_q^* \hat{b}_{q,i}^\dagger \hat{a}) \end{aligned}$$

$\hat{b}_{q,1}$  and  $\hat{b}_{q,2}$  are the annihilation operator of modes on both sides of the cavity (see figure 2.2).  $H_{cav}$  and  $H_{baths}$  are the hamiltonians for the isolated cavity and the external electromagnetic baths respectively.  $H_{int}$  describes the exchange of photons between the cavity mode and the outside modes. It is expressed within the rotating wave approximation (RWA), which is valid only for high quality factor cavity ( $|f_q|/\omega_c \ll 1$ ). Then one can write the three Heisenberg equations of motion for the operators  $\hat{a}$ ,  $\hat{b}_{q,1}$ , and  $\hat{b}_{q,2}$ . The evolution of  $\hat{a}$  is given by:

$$\frac{d\hat{a}}{dt} = \frac{i}{\hbar} [\hat{H}, \hat{a}] = -i\omega_c \hat{a} - \frac{\kappa}{2} \hat{a} - \sqrt{\kappa_1} \hat{b}_{in,1}(t) \quad (2.8)$$

The first term of equation (2.8) describes the free evolution of the cavity mode. The second term regroups all dissipation processes, with  $\kappa = \kappa_1 + \kappa_2$ . The last term represents

the incoming field from the driving port 1. Since no drive tone is applied on the port 2, one consider  $\hat{b}_{in,2} = 0$ . Besides, It has been assumed that the bath modes are Markovian which justify  $\kappa_i(\omega) = \kappa_i = 2\pi|f|^2\rho_i$ , where  $\rho_i$  is the constant density of state in the surrounding electromagnetic field. The newly introduced operator  $\hat{b}_{in,1}$  reads:

$$\hat{b}_{in,1}(t) = \frac{1}{\sqrt{2\pi\rho_1}} \sum_q e^{-i\omega_q(t-t_0)} \hat{b}_{q,1}(t_0) \quad (2.9)$$

Thus,  $\hat{b}_{in,1}$  is constructed as the sum of all incoming modes from a reference time  $t_0 < t$  normalized by the density of modes  $\rho_1$ . Such a normalization give the dimension of  $\sqrt{\omega}$  to  $\hat{b}_{in,1}$  which can be misleading since  $a$  and  $b_q$  have no dimension. Similarly, one can define an outgoing field  $\hat{b}_{out,2}$  (which is the one of interest in transmission measurement). With these new operators the system of three linear equations is simplified to the two following expression (and the expression of  $\hat{b}_{in}$ ):

$$\hat{b}_{out,2}(t) = \sqrt{\kappa_2} \hat{a}(t) \quad (2.10)$$

$$\hat{b}_{out,1}(t) = \sqrt{\kappa_1} \hat{a}(t) + \hat{b}_{in,1}(t) \quad (2.11)$$

From an experimental perspective, the two quantities of interest are the transmission of the cavity and the average photon number in it. By definition the cavity transmission  $T$  reads:

$$T \equiv \frac{\langle \hat{b}_{out,2} \rangle}{\langle \hat{b}_{in,1} \rangle} = \frac{-\sqrt{\kappa_1 \kappa_2}}{-i(\omega - \omega_c) + \frac{\kappa}{2}} \quad (2.12)$$

In practice, the cavity is not perfect and possess internal dissipation channels. These internal losses are artificially introduced by adding a third port without source term ( $\hat{b}_{in,L} = 0$ ) and then only influence the total decay rate  $\kappa = \kappa_1 + \kappa_2 + \kappa_L$ . The mean photon number in the cavity  $n_0 \equiv \langle \hat{a}^\dagger \hat{a} \rangle_{\omega=\omega_c}$  can be obtain using the two relations 2.11 and 2.10, and by introducing the two powers  $P_{in}(t) = \hbar\omega \langle \hat{b}_{in,1}^\dagger(t) \hat{b}_{in,1}(t) \rangle$ , and  $P_{out}(t) = \hbar\omega \langle \hat{b}_{out,t}^\dagger(t) \hat{b}_{out,2}(t) \rangle$ :

$$n_0 = \frac{2\sqrt{AP_{in}P_{out}}}{\hbar\omega_c \Delta f_{-3dB}} \quad (2.13)$$

$A$  is the asymmetric ratio  $A = \frac{\kappa_1}{\kappa_2}$  (equal to the ratio of coupling capacitances).

### 2.1.3 Jaynes-Cummings hamiltonian

When cavity photons are coupled to an internal dipole of the quantum dot circuit (ie: no transition toward the leads), a realistic first approximation is to ignore dissipation in the system, and describe the full system with the Rabi hamiltonian:

$$H_{Rabi} = \hbar\omega_c \hat{a}^\dagger \hat{a} + \frac{\hbar\omega_q}{2} \hat{\sigma}_z + \hbar g (\hat{a} + \hat{a}^\dagger) \hat{\sigma}_x \quad (2.14)$$

where  $\omega_c/2\pi$  is the cavity resonance frequency,  $\omega_q/2\pi$  is the qubit frequency (having in mind that any transition in the quantum dots can form a qubit), and  $g$  is the coupling strength whose exact expression greatly depends on the physical nature of the quantum dot transition (for a DQD:  $g = 2(g_L - g_R)t/\sqrt{\epsilon_\delta^2 + 4t^2}$ ). This kind of photon-qubit interaction is often referred as *transverse coupling* since it involve a coupling axis (here  $\hat{\sigma}_x$ ) transverse to the quantization axis  $\hat{\sigma}_z$ .

By assuming  $\omega_c \simeq \omega_q$  and  $g \lesssim \omega_c$ , one can further simplify the interaction term, and neglect the effect of counter rotating terms <sup>2</sup> (Rotating Wave Approximation). This results in the Jaynes-Cummings hamiltonian:

$$H_{JC} = \hbar\omega_c \hat{a}^\dagger \hat{a} + \frac{\hbar\omega_q}{2} \hat{\sigma}_z + \hbar g (\hat{a} \hat{\sigma}_+ + \hat{a}^\dagger \hat{\sigma}_-) \quad (2.15)$$

Although dissipation is not negligible in most mesoscopic-QED devices ( $\Gamma_2$  is ranging from a few *MHz* [14], [12] to hundreds of *MHz* [104],[50], [105]), the Jaynes-Cummings hamiltonian still provides qualitative understanding of the energy spectrum.

**Dispersive regime** When the qubit frequency is far detuned from the cavity resonance frequency ( $|\Delta_{qc}| = |\omega_q - \omega_c| \gg g$ ), the two sub-systems cannot exchange energy. Nevertheless, virtual exchange of photon via second order processes can still occur, and change the cavity frequency as well as the qubit frequency. These effects can be captured by going into the dispersive picture associated with the unitary transformation:

$$U = e^{\frac{g}{\Delta_{qc}} (\hat{\sigma}_+ \hat{a} - \hat{\sigma}_- \hat{a}^\dagger)} \quad (2.16)$$

<sup>2</sup>When reaching the ultra-strong regime coupling ( $g \gtrsim \omega_c$ ) the counter rotating terms  $\hat{\sigma}_+ \hat{a}^\dagger$ , and  $\hat{\sigma}_- \hat{a}$  are not negligible anymore.

and the effective hamiltonian up to the second order in  $g/\Delta_{qc}$  reads:

$$H_{disp} = UH_{JC}U^\dagger = \hbar(\omega_c + \chi_{disp}\hat{\sigma}_z)\hat{a}^\dagger\hat{a} + \frac{\hbar}{2}(\omega_q + \chi_{disp})\hat{\sigma}_z \quad (2.17)$$

where  $\chi_{disp} = \frac{g^2}{\Delta}$  is the dispersive charge susceptibility (it is a susceptibility in the sense of the linear response theory). Interestingly the term  $\hbar\chi_{disp}\hat{\sigma}_z\hat{a}^\dagger\hat{a}$  can either be interpreted as a shift of the cavity frequency  $\Delta f_c = \chi_{disp}\langle\sigma_z\rangle$  or as a change of the qubit frequency  $\chi_{disp}\hat{a}^\dagger\hat{a}$  (AC-stark shift [96]). The Lamb shift  $\chi_{disp}/2$  is also present in  $H_{disp}$ .

The dispersive regime is widely used in cavity and circuit-QED [106] for the read-out of the qubit state since the measurement of  $f_c$  directly inform about the state of the qubit  $\sigma_z$ . Such a read-out technique is almost QND (Quantum Non Demolition) because  $[H_{disp}, \hat{\sigma}_z\hat{a}^\dagger\hat{a}] = 0$ . Nevertheless, it is not purely QND since  $H_{disp}$  is only an effective hamiltonian, and one would need to go towards real longitudinal coupling to ensure a QND-measurement of the qubit [107].

**Resonant regime** When the qubit frequency is close to the cavity resonance frequency ( $|\Delta_{qc}| = |\omega_q - \omega_c| \ll g$ ), the spectrum of the full system is drastically modified. Photons and electronic excitations cannot be distinguished anymore, and the new eigenstates are light-matter hybrid states. For instance in the subspace with  $n$  excitation ( $|e, n-1\rangle, |g, n\rangle$ ), the two eigenstates are:

$$|n, -\rangle = -\sin(\theta_n)|e, n\rangle + \cos(\theta_n)|g, n+1\rangle \quad (2.18)$$

$$|n, +\rangle = \cos(\theta_n)|e, n\rangle + \sin(\theta_n)|g, n+1\rangle \quad (2.19)$$

$\theta_n$  is the mixing angle and verify:  $\tan(2\theta_n) = (2g\sqrt{n+1})/\Delta_{qc}$  [96]. These two states are called the  $n$ -th order dressed states. An illustration of this so-called Jaynes-Cummings ladder is given in figure 2.3-c. Nevertheless, the Jaynes-Cummings hamiltonian is a non-dissipative description and observing this dressed states in experiments is a challenging task. The broadening of the spectroscopic peaks due to dissipation ( $\kappa/2$  and  $\Gamma_2$ ) has to be small enough to resolve the 1-st order doublet of the Jaynes-Cummings ladder. When such condition is meet, one reach the *strong coupling regime* ( $g > \kappa/2, \Gamma_2$ ). In the literature, one refer to this splitting of the cavity resonance as the *vacuum Rabi splitting* [108], [97](the hallmark of the strong coupling regime). Resolving higher order doublet

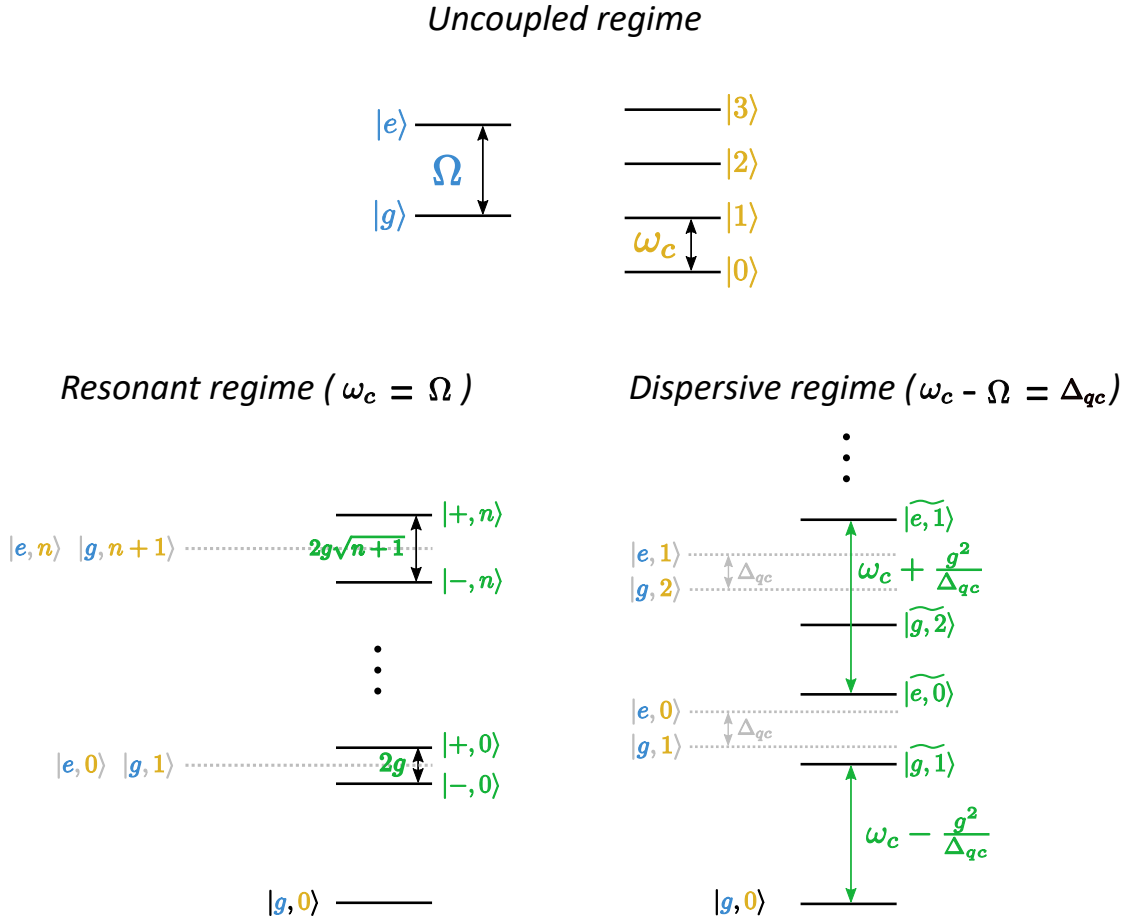


FIGURE 2.3: Energy spectrum of the qubit-cavity system

is more challenging, since the coupling strength has to verify:  $g/\sqrt{n} > \kappa/2, \Gamma_2$ . It has been observed in circuit-QED architecture [109], as well as in cavity-QED [108].

## 2.2 Master equation of the coupled system

### 2.2.1 Semi classical description

The master equation approach is very efficient to describe the dynamics of a mesoscopic-QED system. Here, we will focus on a single transition in the circuit between two states  $|0\rangle$  and  $|1\rangle$ , called the qubit in the following. The full hamiltonian reads:

$$H = \underbrace{\frac{\hbar\omega_q}{2}\hat{\sigma}_z + \hbar g(\hat{a}^\dagger\hat{\sigma}_- + \hat{a}\hat{\sigma}_+) + \hbar\omega_c\hat{a}^\dagger\hat{a}}_{\text{Jaynes-Cummings Hamiltonian}} + \underbrace{i\hat{a}^\dagger\epsilon_{in}e^{-i\omega_{RF}t} - i\hat{a}\epsilon_{in}^*e^{i\omega_{RF}t}}_{\text{Driving tone}} + H_{diss} \quad (2.20)$$

With  $\hat{\sigma}_- = |g\rangle\langle e|$  and  $\hat{\sigma}_+ = |e\rangle\langle g|$ .  $\epsilon_{in}$  is the amplitude and  $\omega_{RF}$  the frequency of the drive applied on one of the two ports of the cavity. Dissipation in the cavity is taken into account by considering its coupling to an external bosonic bath  $\hat{b}_\epsilon$ :  $H_{diss} = \int d\epsilon \eta (\omega_\epsilon \hat{b}_\epsilon^\dagger \hat{b}_\epsilon + \beta \hat{b}_\epsilon^\dagger \hat{a} + \beta^* \hat{b}_\epsilon \hat{a}^\dagger)$ . When going into the rotating frame of the drive tone, the Heisenberg equation of  $\hat{a}$  and  $\hat{\sigma}_-$  read:

$$\frac{d}{dt} \hat{a} = \frac{1}{i\hbar} [\hat{a}, H] = -(i\Delta_{cd} + \kappa/2) \hat{a} - ig\hat{\sigma}_- + \epsilon_{in} e^{-i\omega_{RF}t} \quad (2.21)$$

$$\frac{d}{dt} \hat{\sigma}_- = \frac{1}{i\hbar} [\hat{\sigma}_-, H] = -(i\Delta_{qd} + \Gamma_2) \hat{\sigma}_- + ig\hat{\sigma}_z \hat{a} \quad (2.22)$$

With  $\kappa = 2\pi\eta|\beta|^2$  is twice the decay rate and correspond to the spectroscopic linewidth of the bare cavity. The term  $\Gamma_2 \hat{\sigma}_-$  has been added manually to describe decoherence of the qubit. We also define two frequency detunings:  $\Delta_{cd} = \omega_c - \omega_{RF}$  and  $\Delta_{qd} = \omega_q - \omega_{RF}$ . When the photon number in the cavity is high enough ( $\langle \hat{a}^\dagger \hat{a} \rangle \gtrsim 10$ ), the semiclassical approximation is valid, meaning one can treat  $\hat{a}$  as a classical quantity  $\hat{a} \simeq \langle \hat{a} \rangle$ , and in the resonant case ( $\omega_c \simeq \omega_{RF}$ ) one can use:  $\hat{a} \simeq \bar{a} e^{-i\omega_{RF}t}$ . In the stationary regime,  $\bar{a}$  reads:

$$\bar{a} = \frac{\epsilon_{in}}{\Delta_{cd} + i\kappa/2 - \chi(\omega_{RF}) \langle \hat{\sigma}_z \rangle} \quad (2.23)$$

With the charge susceptibility of the transition  $\chi$ :

$$\chi(\omega_{RF}) = \frac{g^2}{\Delta_{qd} + i\Gamma_2} \quad (2.24)$$

The quantity  $\chi(\omega_{RF})$  characterizes the change of the qubit population due to a small amplitude modulation at the frequency  $\omega_{RF}/2\pi$  of the potential, hence it is the charge susceptibility in the linear response theory. Note that for  $\Gamma_2 = 0$  we recover  $\chi(\omega_{RF}) = \chi_{disp}$ , obtained in the dispersive regime ( $|\omega_q - \omega_c| \gg g$ ) without dissipation. To quantify the coherence of a qubit-cavity interface, a key parameter is the ratio:  $C = \frac{g^2}{(\kappa/2)\gamma}$  called cooperativity. For  $C > 1$ , a coherent regime can be defined. In the resonant regime ( $|\Delta_{qc}| \ll g$ ), it manifest itself as the strong coupling regime, and the presence of the vacuum Rabi splitting.

In the dispersive regime, the relevant quantity that have to be compared to decoherence rates is the dispersive shift  $\chi n_{ph}$ . This shift being dependent on the photon number

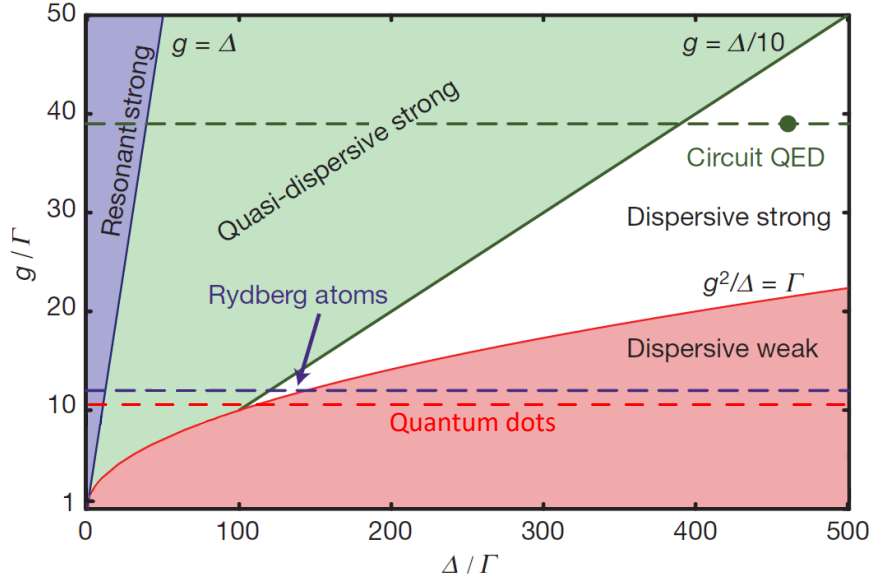


FIGURE 2.4: **Parameter space diagram for cavity, circuit and meso-QED:** The  $\Gamma$  normalizing the two axis contains all sources of decoherence, arising both from the cavity and the qubit. Adapted from: [110]

in the cavity, one can in principle resolve two successive photon numbers as long as  $\chi > (\kappa/2), \Gamma_2$  [110]. Such a condition defines the strong dispersive regime (see figure 2.4). This regime provides an absolute calibration of the photon number in the microwave cavity [111], and allows to distinguish between a coherent state, a thermal state, or a quantum state such as a Fock state.

## 2.2.2 Lindbladian formalism

When the number of photon in the cavity is close to one, the semiclassical approximation is not valid anymore. A more general method to account for dissipation in quantum systems is to describe the evolution in terms of a Lindblad master equation. This fully quantum description has been used to model experimental results presented chapter 4 using the Qutip python package. The Lindblad master equation reads (a detailed derivation can be found in [112]):

$$\frac{d}{dt}\rho_S(t) = \frac{1}{i\hbar}[H, \rho_S(0)] + \sum \alpha_{\hat{x}} D_{\hat{x}}(\rho_S(t)) \quad (2.25)$$

with:

$$D_{\hat{x}}(\rho_S(t)) = \hat{x}\rho(t)\hat{x}^\dagger - \frac{1}{2}\rho(t)\hat{x}^\dagger\hat{x} - \frac{1}{2}\hat{x}^\dagger\hat{x}\rho(t) \quad (2.26)$$

the operators  $\hat{x}$  are called collapse operator and each of them describe a different decoherence process. Hence, together with their corresponding rates  $\alpha_{\hat{x}}$ , they have a direct physical interpretation. This is one of the reason why Lindbladian formalism is very handy for describing experimental results. In our case the different process taken into account are the cavity relaxation ( $\hat{x} = \hat{a}$  and  $\alpha_{\hat{a}} = \frac{\kappa}{2}$ ), the qubit relaxation ( $\hat{x} = \hat{\sigma}_-$  and  $\alpha_{\hat{\sigma}_-} = \gamma$ ), and the pure phase decoherence of the qubit ( $\hat{x} = \hat{\sigma}_+\hat{\sigma}_-$  and  $\alpha_{\hat{\sigma}_+\hat{\sigma}_-} = \Gamma_\phi$ ). When the temperature is non negligible compared to cavity photon energy one has to include thermal population of the cavity ( $\hat{x} = \hat{a}^\dagger$  and  $\alpha_{\hat{a}^\dagger} = \sqrt{n_{th}}\kappa/2$ ), likewise for electronic temperature and the electronic transition energy ( $\hat{x} = \hat{\sigma}_+$  and  $\alpha_{\hat{\sigma}_+} = \sqrt{n_{th}}\gamma$ ). Because the numerical resolution time increases with the size of the Hilbert space, this approach requires to limit oneself to a finite photon number. Therefore, this technique is complementary to the semiclassical approach described earlier.

## 2.3 Cavity read-out engineering

### 2.3.1 Phase and Transmission read-out

In presence of a quantum dot circuit the expression of the transmission  $T$  reads:

$$T(\omega_{RF}) \equiv \frac{\langle \hat{b}_{out,2} \rangle}{\langle \hat{b}_{in,1} \rangle} = \frac{-\sqrt{\kappa_1\kappa_2}}{-i(\omega_{RF} - \omega_c) + \frac{\kappa}{2} + i\chi(\omega_{RF})\langle \hat{\sigma}_z \rangle} \quad (2.27)$$

In the presented experiments (chapter 4, and 5), the two measured quantities are the phase shift  $\Delta\phi$  and the amplitude shift  $\Delta A$  of the transmitted signal, and they are defined by:

$$T = (A_0 + \Delta A)e^{i(\phi_0 + \Delta\phi)} \quad (2.28)$$

With ( $A_0$  the reference amplitude and  $\phi_0$  the reference phase in absence of coupling to the circuit. Knowing that the cavity response is measured at  $\omega_{RF} = \omega_c$ , the phase shift  $\Delta\phi$  and the amplitude shift  $\Delta A$  read:

$$\Delta\phi = \frac{\Delta\omega_c}{\kappa/2} = \frac{Re(\chi(\omega_c))}{\kappa/2} \langle \hat{\sigma}_z \rangle \quad (2.29)$$

$$\Delta A = \frac{\Delta(\kappa/2)A_0}{\kappa/2} = Im(\chi(\omega_c)) \frac{A_0}{\kappa/2} \langle \hat{\sigma}_z \rangle \quad (2.30)$$

$\Delta\omega_c$  is the cavity resonance frequency shift and  $\Delta(\kappa/2)$  is the broadening of the cavity resonance. Those two expressions are valid in the limit of  $\Delta\omega_c \ll \omega_c$  and  $\Delta(\kappa/2) \ll \kappa/2$ . Notice that one can recover the frequency shift  $\Delta\omega_c$  by measuring only the phase shift  $\Delta\phi$  at  $\omega_{RF} = \omega_c$ . Hence,  $\Delta\phi$  informs us about the dispersive effect of the circuit on the cavity. Similarly, the broadening of the resonance is proportional to  $\Delta A$  and is related to the circuit induced dissipation. This free ourself from measuring the full cavity resonance, and allows a much faster characterization of the circuit state. This informs us also on the central role of the susceptibility  $\chi(\omega_{RF})$  which encompass these two phenomenon through its real and imaginary part. Typical phase and amplitude signals are shown in figure 2.5.

### 2.3.2 Improving the cooperativity

There are two strategies to improve the cooperativity of the system  $2g^2/\kappa\Gamma$ ; either increase the coupling strength  $g$  or reduce the decoherence rates of the coupled system.

**Increasing of  $g$ :** We focus here on the coupling strength between cavity photons and the dipole associated to one electron in a double quantum dot. From the expression of  $g_{DQD}$  (equation 2.6) one can identify the different strategy to improve the DQD-cavity coupling. For a given photonic potential gradient, one can fabricate the two dots far apart from each other while preserving tunneling between the dots, thus increasing the potential difference felt by the electron whether it is in the left or in the right dot. Other than increasing the double quantum dot dipole, the coupling strength can be enhanced by engineering strong spatial variation of the potential. The shaping of the photonic potential is done by acting mainly on its screening and one can use high frequency electromagnetic simulation (such as the HFSS software) to finely tune the geometry of the circuit.

One can also enhance the overall value of potential  $V_{\perp}(\vec{r})$ . Recalling that for an LC-resonator, the operator for the potential inside the capacitance reads:

$$\hat{V} = \frac{\hat{q}}{C} = V_{ZPF}(\hat{a} + \hat{a}^{\dagger}) \quad (2.31)$$

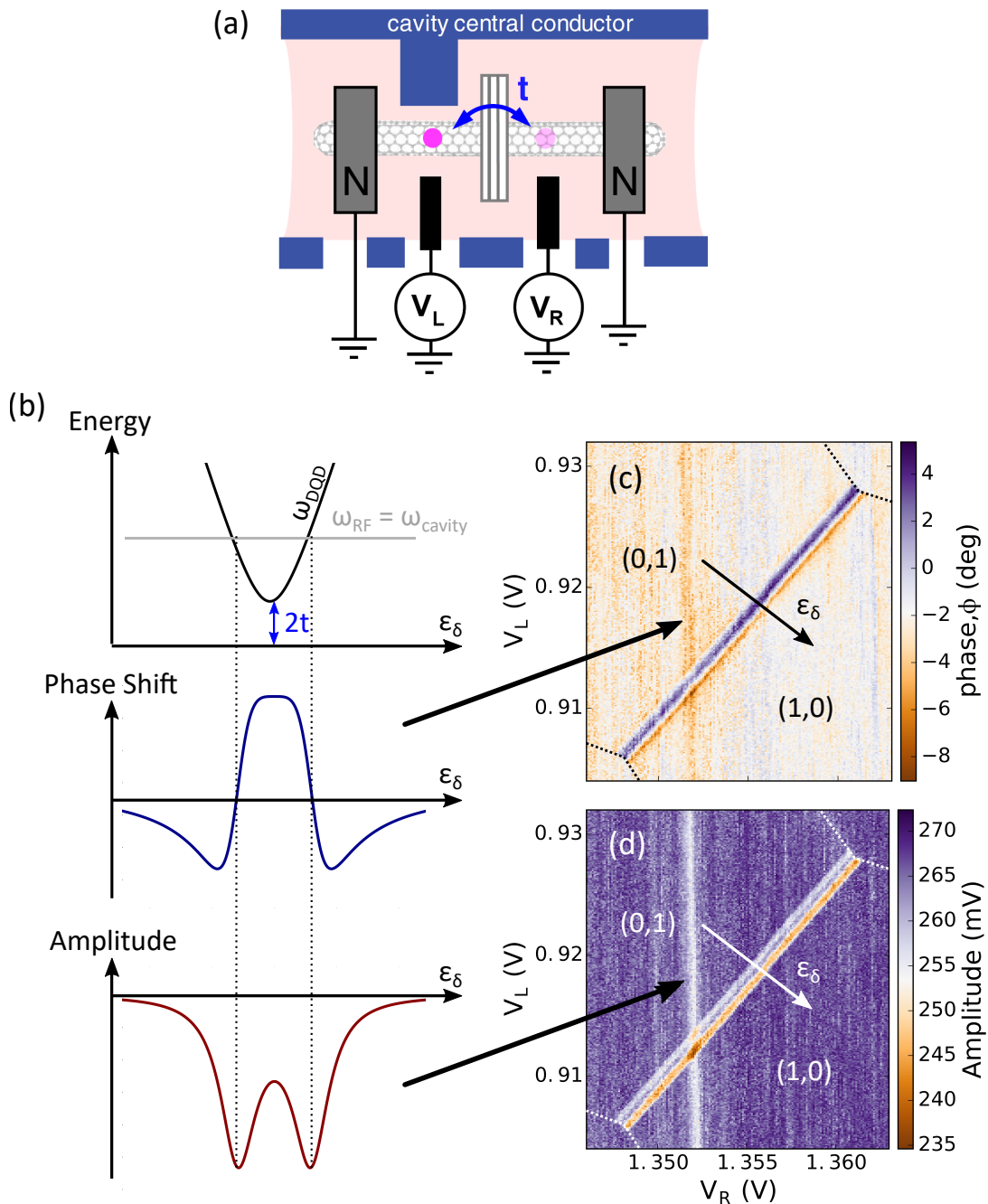


FIGURE 2.5: **Cavity signal for Double quantum dot:** **a.** Schematic of the coupling scenario to a double a quantum dot. In order to couple photons to left-right electronic transition, a protrusion of the cavity central conductor is created close to one of the quantum dot, to maximize the gradient of  $V_\perp(r)$  (schematic taken from ref. [113]). **b.** (top panel) Energy dispersion of the left/right hopping transition inside a double quantum dot as a function of the detuning  $\epsilon_\delta = \epsilon_L - \epsilon_R$ . The minimum of the transition energy is set by the tunnel rate  $t$ . (middle and bottom panels) Phase and amplitude signals in a resonant situation ( $\omega_{DQD} = \omega_{cavity}$ ), along the detuning axis  $\epsilon_\delta$ . **c.**, **d.** Measured phase and amplitude in the region of the stability diagram where  $(0,1)$  and  $(1,0)$  are the stable electronic configuration in the double quantum dot. The visible diagonal is the degeneracy line between the two configuration  $(0,1)$  and  $(1,0)$ . Measurement take on device *SPN15R*

With:

$$V_{ZPF} = \sqrt{\frac{\hbar\omega_c^2 Z_c}{\pi}} \quad (2.32)$$

$V_{ZPF}$  is the RMS zero-point uncertainty of  $\hat{V}$  when the LC-resonator is in its ground state, and  $Z_c = \frac{\pi}{2}\sqrt{\frac{L}{C}}$  is the impedance of the resonator. Notice that the larger the impedance  $Z_c$  the larger the potential, hence going to highly inductive resonator enhance the coupling strength. The few implementation of this approach has been done using, josephson junction SQUID array ( $Z_c = 1.8k\Omega$  in [13]), compact resonator ( $Z_c = \text{few } 100\Omega$  in [114]), modified CPW geometry ( $Z_c = 200\Omega$  in [55]), or high kinetic inductance material such as NbTi ( $Z_c = 1k\Omega$  in [115],[53]).

In general, the increase of the electrical dipole of the double quantum makes the qubit also more sensitive to surrounding charge noise. In the same way, going to higher impedance resonator is accompanied by an increase of the photon loss rate  $\kappa$ . It is then important to simultaneously work on improving the cleanliness of the environment in order to limit  $\Gamma_2$  and  $\kappa$  to low values.

**Reduction of  $\Gamma_2$  and  $\kappa$ :** The two main sources of qubit loss of coherence are electrical noise caused by charge fluctuators mostly located at the interfaces in the device and in oxide layers [116], and magnetic noise due to random fluctuations of the surrounding nuclear spins [117]. Improvement of the fabrication process (removing oxide layers [118]), and of the material purity (using spin nuclear low density material, as isotopically purified Si), have shown to be very efficient for limiting the decoherence of the qubit as well as photon loss rate of the cavity. To limit the impact of these electromagnetic noises, another approach is to operate the qubit at an optimal working point, called *sweet-spot*, where the qubit is insensitive to noise at first order. This means to find an extrema of the qubit frequency as a function of gate voltages (on which charge noise is acting). In the same spirit, flattening the dispersion of the qubit frequency with respect to gate voltages limits the second order noise dependence. This idea originates from the superconducting qubit community and has lead to the transmon design [119].

As previously seen in the section 2.1.2, the photon loss rate has an internal contribution  $\kappa_{int}$  and an external contribution  $\kappa_{ext}$  due to the coupling to input and output transmission lines. While lowering  $\kappa_{int}$  is beneficial for any experiment, a low  $\kappa_{ext}$  is not always wanted in C-QED experiments. Indeed, the time for manipulating and reading

---

the state of a qubit using a dispersively coupled cavity is set by  $1/\kappa_{ext}$ . As a result, the target value is  $\kappa_{ext} = \kappa_{int}$ , allowing a manipulation and read-out time of few  $100ns$  as a typical value; without degrading too much the total photon loss rate  $\kappa$ .



## Chapter 3

# Experimental techniques

This chapter begins by giving a motivation for a new fabrication technique of carbon nanotubes circuits (section 3.1). Then, most of the technical aspects involved in this thesis are introduced. It goes from the nanofabrication of the devices carried out in the clean room facility of ENS (section 3.2), to low temperature measurements (section 3.3). A particular emphasis is given to the integration of the carbon nanotube into the quantum dot circuit, whose development represent a large part of this thesis work.

## 3.1 Toward more tunable carbon nanotube quantum-dot circuits

### 3.1.1 Various Nanofabrication approaches

Carbon nanotubes appear as excellent candidates for hosting quantum dot circuits (cf section 1.1). Nevertheless, it remains a challenge to experimentally access these properties, and obtain a defect free 1D conductor over several  $\mu\text{m}$ . The method to integrate the nanotube in the quantum dot circuit is to a large extent responsible for his damaging.

One of the earliest and easiest way to fabricate carbon nanotube devices is by post-growth processing [120]. In this technique, carbon nanotube are grown all over the substrate, then they are imaged by atomic force microscopy or scanning electron microscopy. The circuit is subsequently patterned over the choosen carbon nanotube. But post-growth nanofabrication of the circuit electrodes contaminates the carbon nanotube with organic residues. Indeed, carbon nanotube easily absorbs polymer contained in cleanroom resist, and knowing that transport in CNT occurs through  $p_z$ -orbitals which are pointing outwards, it will drastically affect the transport spectrum. In addition, carbon nanotube growth produces amorphous carbon on the substrate which is an highly dissipative medium for microwave, hence making this technique incompatible with c-QED application.

A way to circumvent this last issue is to grow the carbon nanotubes on a separate chip with a predefined mesa structured, and stamp it in a dedicated area of the microwave resonator. This local transfer technique has been developped by J. Viennot [121], and allows to combine high quality factor microwave cavity and carbon nanotube quantum

dot circuits on the same chip. But such sample still suffer from post growth contamination, since all the electrode of the circuit are fabricated after the integration of the CNT.

In case of transport-only devices, one strategy to obtain ultraclean carbon nanotube consist in growing carbon nanotube on a fully-patterned device requiring no further nanofabrication. This technique enabled to produce suspended CNT and provided one of the cleanest transport spectrum in a CNT [27]. Its main drawback is the very low yield of electrically connected nanotubes, which begin to be a problem for devices with increasing complexity. Moreover the high temperature and the chemically aggressive gas mixture needed for the growth of CNT (900°C in the used recipe) can make metallic thin film to melt and strongly deform. In particular, the superconducting metal realizing the microwave cavity can display a strong decrease of its critical temperature. Recent efforts have been made to realize microwave cavity based on MoRe superconductor which exhibit high quality factor even after exposure to CNT growth [122].

The most recent technique [123], [41], [124], [125], [126] is similar to the previous local transfer technique, only differing in the fact that the circuit is patterned before the transfer step (see figure 3.1). This last point requires a deterministic transfer which is the main difference with previous transfert technique where few carbon nanotubes were transferred to the circuit chip and a post selection is needed. This technique allows to combine pristine carbon nanotube based quantum dot circuits with high quality factor microwave cavity but has remained unused in this perspective. In the following this new technique will be called *stapling*.

### 3.1.2 Stapling in a meso-QED device

As discussed in the previous section, one of the advantages of this technique is the possibility to produce suspended carbon nanotubes, which make it attractive for realizing mechanical oscillator with carbon nanotube [127]. The suspended nature is also expected to reduce charge noise in carbon nanotubes (see figure 3.2). Indeed, substrate is believed to host numerous charge oscillators, hence putting some distance between the CNT and the substrate is expected to result in a less electrically noisy environment for the CNT. This is particularly interesting when one is willing to embedded an electrically-addressable qubit in a CNT. Up to now, the confinement in most of the quantum dot

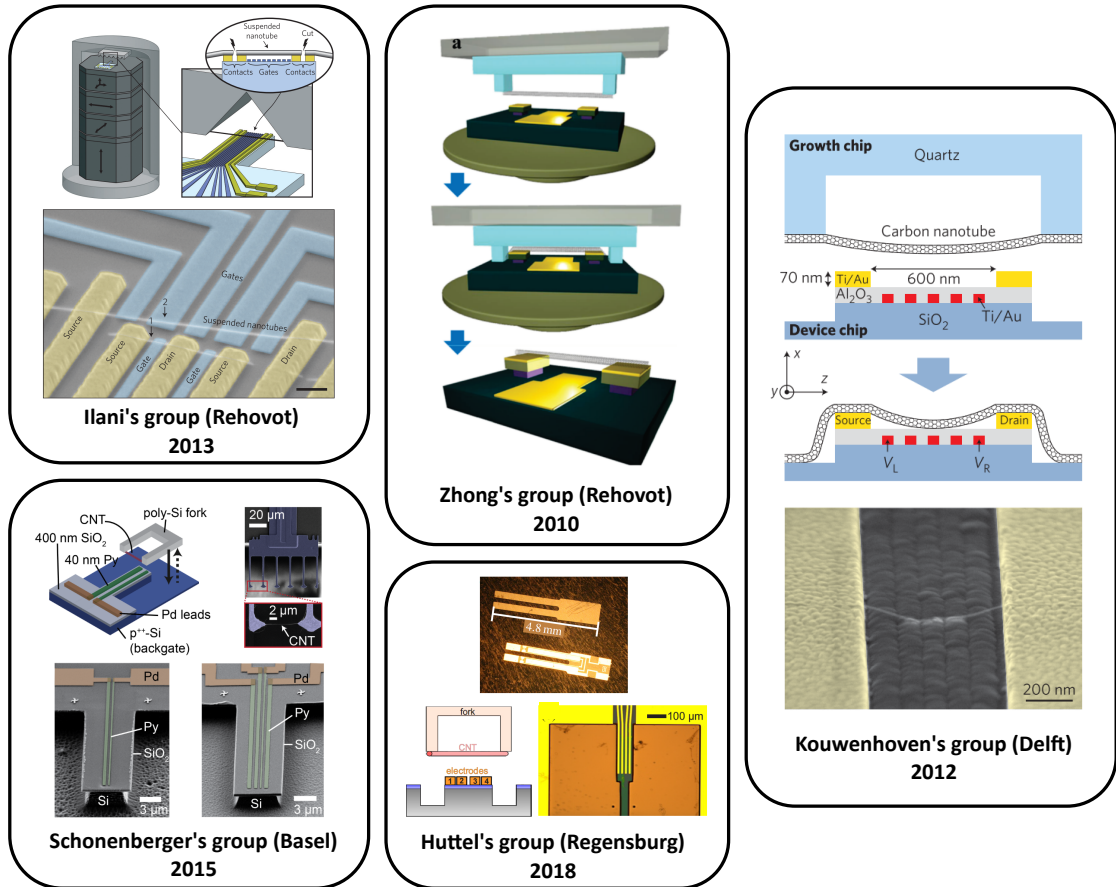


FIGURE 3.1: The development of this *stapling* technique started in the group of Z. Zhong [123], and inspired a few other groups. Each of them have different technical approach but the principle remains the same. Such a method allows to envision arbitrarily complex carbon nanotube circuit. Up to now the most successful one has been developed in the group of S. Ilani [124], where circuits with up to 16 gates, and multiple carbon nanotubes have been realized as shown in the top left box. Sources: [123], [41], [124], [125], [126]

circuit made in the group was believed to be dominated by disorder originating from interaction with the substrate and nano-fabrication residues. Such a disorder yields a low tunability of the circuit. The stapling technique reduces the contamination of the CNT to a minimum. Thus, one can fully controlled the confinement potential in the CNT by means of electrostatic gates. One can start to envision more complex circuit and to modified independently the different properties of CNT based circuit. For instance, control over the lead-dot coupling rate can be instrumental for switching between a closed system regime to an open one ( chapter 4), or to modulate the induced Zeeman splitting in the Ferromagnetic spin qubit (chapter 5).

To summarize, the increasing complexity of quantum dot circuits, the low yield of nanofabrication, and the weak tunability are the reasons why going towards a new

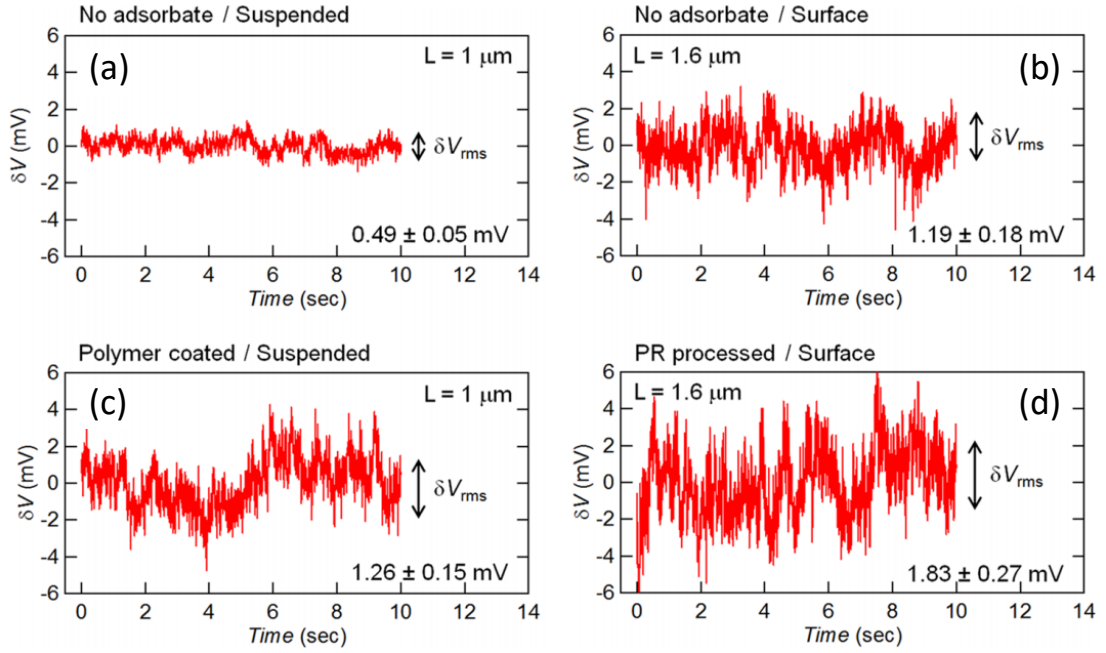


FIGURE 3.2: The impact of environment on charge noise of single CNT device: **a.** pristine suspended CNT, **b.** pristine CNT laying on Si substrate, **c.** Polymer coated suspended CNT, **d.** photoresist processed CNT laying on Si substrate. Source: [128]

generation of sample is essential.

## 3.2 Device nanofabrication

### 3.2.1 Sample overview

The chips fabricated in this thesis consist in a carbon nanotube-based quantum dot circuit coupled to a microwave cavity (see figure 3.3). This microwave cavity is a centimeter-long superconducting coplanar waveguide resonator (CPW) with a fundamental mode around  $6.5\text{GHz}$ . The quantum dot circuit is embedded at an anti-node of the cavity electric field and its characteristic length is of the order of the micrometer. All the clean-room process is performed on a  $10\text{mm} \times 10\text{mm}$  chip containing two devices. By doing so, it is easier to handle the chip, and it allows to be faster on all nanofabrication steps. The substrate used in all experiments shown in this thesis, is a standard high resistivity ( $10\text{k}\Omega\cdot\text{cm}$ ) silicon wafer covered with  $500\text{nm}$ -thick layer of silicon oxide. The high resistivity silicon allows for low microwave dissipation, and the  $500\text{nm}$  of thermal oxide prevents DC gates from leaking between each other.

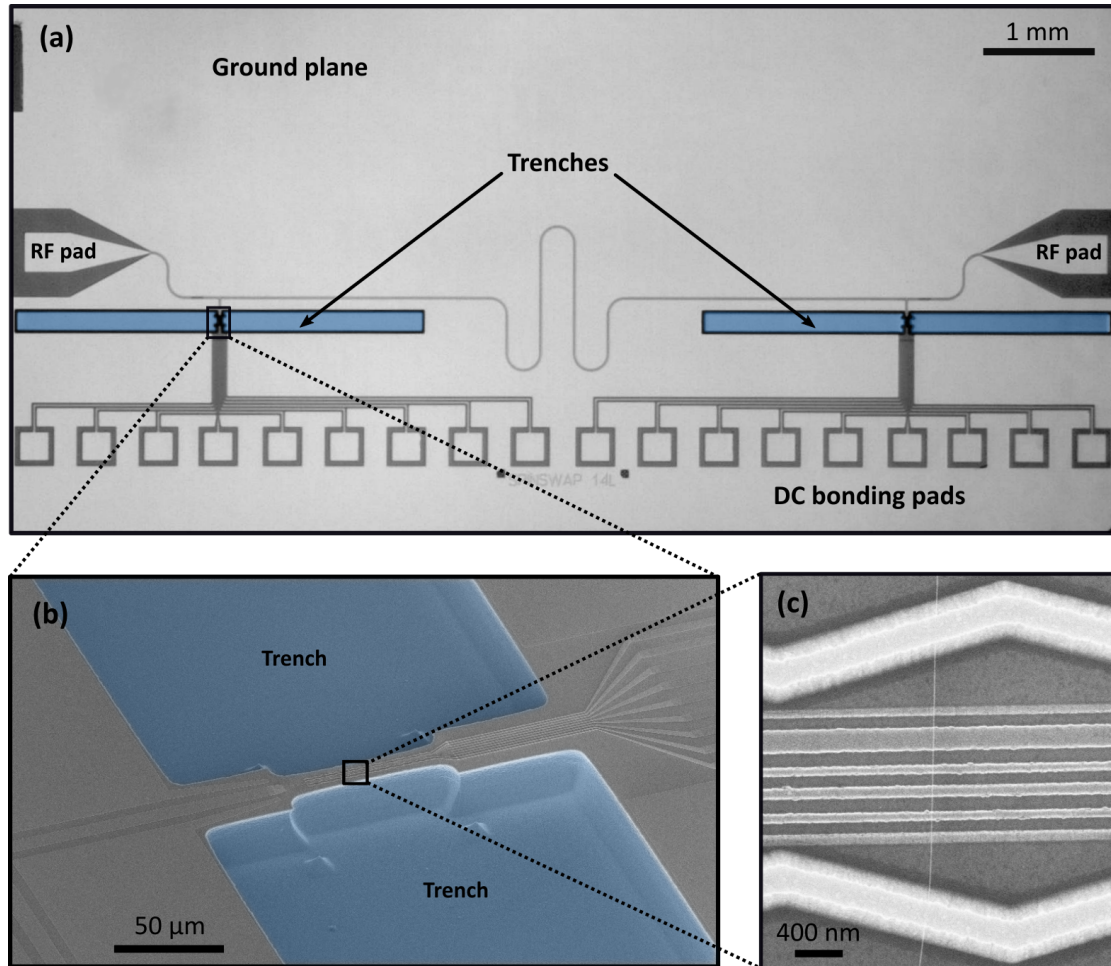


FIGURE 3.3: **Quantum dot circuit coupled to a microwave resonator**

**a.** Optical image of the whole device. RF pads used for wire-bonding to the PCB board are visible on both sides of the microwave cavity. Two trenches for each QD-circuit region ensure the smooth running of the integration of the carbon nanotube (colored in blue). DC bonding pads are also visible in the lower part of the picture. **b.** SEM micrograph of the QD-circuit. In the left part of the image we can see the central conductor of the resonator to which the QD circuit is capacitively coupled, and on the right part the different electrodes are visible. **c.** Zoom-in on the QD-circuit where the carbon nanotube is positioned. The gate array below the carbon nanotube is dedicated to the shaping of the confinement potential for electron inside the CNT.

A widely used instrument in the fabrication of these chips is the Scanning Electron Microscope (SEM). It can be used as a microscope with a resolution down to  $10\text{nm}$ , but the SEM is mainly used to draw pattern in electrosensitive resist with a similar resolution. The basic idea is to use the electrosensitive resist as a stencil on which the desired metal is evaporated and the resist layer can subsequently be removed during the lift-off step (see figure 3.4 for more details).

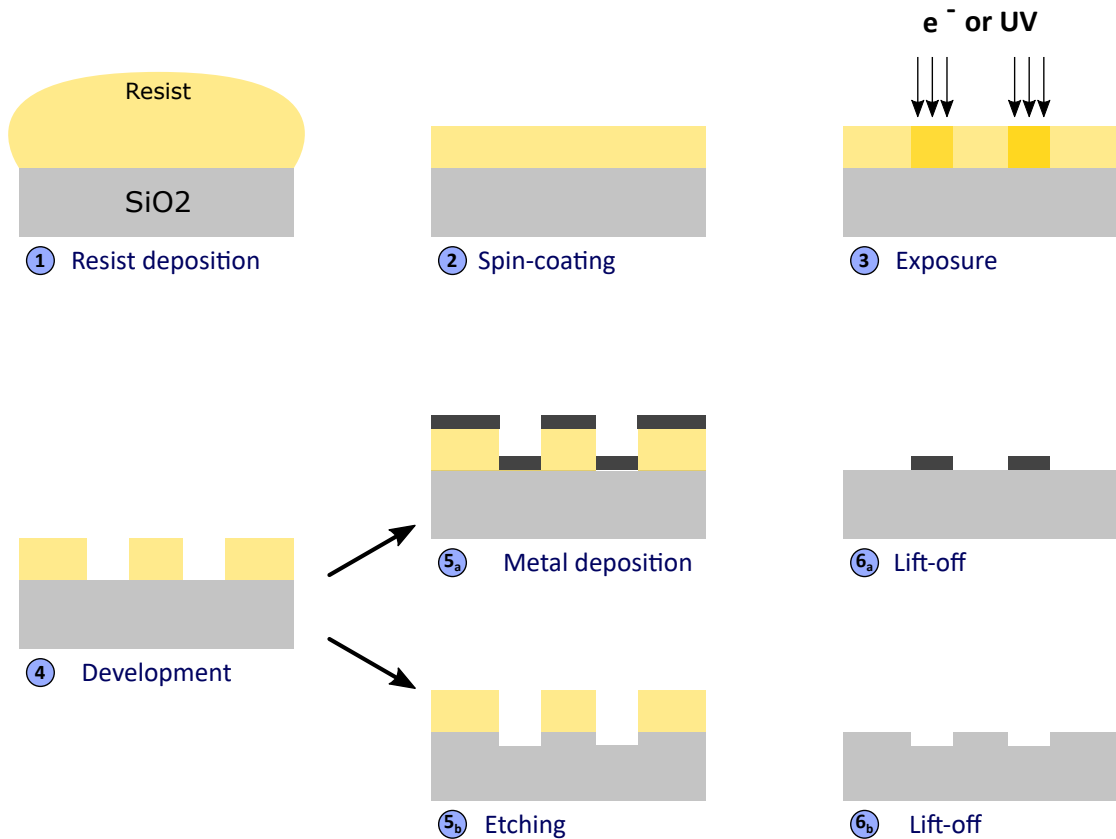


FIGURE 3.4: **Lithography steps:**

The lithography technique is used whenever one wants to pattern a structure on the device. It can be applied for metal deposition as well as for etching a defined area. The fabrication of our samples typically contains around five different lithography steps.

1. A few drops of resist are deposited on the substrate.
2. Spin-coating of the resist in order to obtain a homogeneous layer of resist.
3. The resist layer is exposed to an electron or photon beam depending on the sensitivity of the resist. The nature of the beam is chosen according to the smaller dimension of the pattern one wants to draw.
4. In case of a positive resist (as illustrated) the exposed areas are removed using the appropriate chemical. For negative resist only the exposed areas remain on the chip.
5. The remaining resist then acts as a mask either for metal deposition or etching of an underlying layer.
6. Finally the resist mask is removed in an acetone bath.

### 3.2.2 Nanofabrication steps

Throughout this thesis, two strategies have been adopted for the fabrication process. They differ in the way the carbon nanotube is integrated into the circuit. The first one is a stamping technique [121] in which the carbon nanotube is transferred to the circuit chip after the Nb resonator fabrication, and then contacts and gates are deposited on top of it. This technique has been developed before the beginning of this thesis work, and has revealed to be very efficient for combining high quality factor cavity ( $Q \simeq 10^4$ ) and carbon nanotube based quantum dot circuit. But in such devices, the carbon nanotube undergoes chemical processes which can result in resist residue in the environment of the CNT or some adsorbate on the CNT. Consequently, the electronic confinement potential in the quantum dots will suffer from this disordered environment, and the resulting devices will be weakly tunable by gate voltages. The second strategy consists in integrating the carbon nanotube at the very end of the nanofabrication and this allows to produce a pristine carbon nanotube based quantum dot circuit. The main steps of those two processes are briefly described in the following:

#### Stamping process

1. **Alignment crosses and pre-contact** The alignment crosses are references for all the following steps. In particular, they allow for a 50 nm-accurate alignment between the electronic lithography of contacts and gates of the quantum dot circuit. The pre-contacts are made of gold and are the bridge between the fine electrodes of the quantum dot circuit and the larger niobium lines. Because niobium oxidizes and not gold this pre-contact is essential for ensuring an electrical contact between niobium lines and circuit electrodes. This step is done by electronic lithography (see figure 3.4).
2. **Niobium resonator** It contains the coplanar waveguide (CPW) resonator [129] and the large part of the circuit line and bonding pad. Because niobium is not compatible with lift-off techniques on large scales, it is first deposited on all the chip and then one selectively etches it using electronic lithography and a dry etching process based on  $SF_6$ .

3. **Carbon nanotube growth and stamping** carbon nanotube are grown with a Chemical Vapor Deposition technique (CVD) on a quartz substrate with a predefined mesa structures. Then they are stamped on the circuit chip in a MJB4 mask aligner. The mesa structure allows for a very local transfer of carbon nanotube, hence maintaining a good quality factor of the microwave cavity.
4. **Carbon nanotube localization** Prior to the fabrication of contacts and gates that realize the quantum dot circuit, one need to localize the transferred carbon nanotubes on the circuit chip and choose the most suitable one.
5. **Contact and gates of the nano-circuit** This step include the smallest structure of the device, namely the QD-circuit. It typically consists in two or three electronic lithography steps for which the design and the evaporated metals vary greatly with the realized circuit.

### Stapling process

1. **Alignment crosses and pre-contact**
2. **Niobium cavity**
3. **Contact and gates of the nano-circuit**
4. **Etching side trenches** Two trenches on both sides of the quantum dot circuit are needed for the stapling steps. This step combines optical lithography and dry etching of the silicon oxide and silicon preformed in a Reactive Ion Etching (RIE) equipment.
5. **Growth of carbon nanotubes on a comb of cantilever and localization**  
This step is similar to the one in the stamping process except to the growth chip which is now a cantilever comb. This new design enables the growth of suspended carbon nanotubes. Then we identify good candidates carbon nanotubes for stapling by observing the cantilever comb using a scanning electron microscope (SEM).
6. **Stapling** Last step before mounting in the cryostat. It is performed in a dedicated vacuum chamber where a nano-motor stage allows us to accurately position of the

cantilever comb with respect to the circuit chip. The alignment is made possible thanks to an optical access in the chamber.

Because the development of this stapling technique represent an important part of this thesis, in the following, we focus on the different steps of the stapling process.

### 3.2.3 Niobium cavity fabrication

The fabrication of the niobium coplanar waveguide resonator is done by an etching process. 100 nm of Niobium is evaporated on the whole surface of the substrate in a ultra high vacuum (UHV) electron gun evaporator reaching pressures below  $5 \cdot 10^{-10}$ . In such low pressure, evaporated atoms follow ballistic trajectories over few meters ensuring high purity metallic films. Because Niobium is a refractory metal, the heating necessary for its evaporation is usually a limitation for reaching a good vacuum quality during the evaporation, and it may prevents from getting a good quality thin film. Nevertheless, this issue can be circumvent by a powerful cooling system of the deposition chamber. Indeed, the chamber is fitted with cryogenic panels which can be cooled down with liquid nitrogen allowing to stay below  $1 \cdot 10^{-9}$  mbar during the niobium evaporation. It is worth noting that Niobium is more commonly deposited by a sputtering technique, which have the merit to produce more sticking thin film, nevertheless in the ENS clean room facility, such sputtering equipment was not available. After the niobium deposition, all the steps of the electronic lithography technique are followed (cf. figure 3.4), with an extra cleaning of the substrate in a 5 minutes ultrasonic bath in acetone followed by a 3 minutes soft oxygen plasma in the RIE chamber to completely remove resist residues. Because all the dimensions in the CPW design are larger than  $1 \mu\text{m}$ , this step can in principle be done by optical lithography which is much faster than the electronic one. However, optical lithography requires to fabricate a mask for a specific design, which is not convenient when one is often introducing small changes in the cavity design. For this reason we favored electronic lithography even for the fabrication of the microwave cavity.

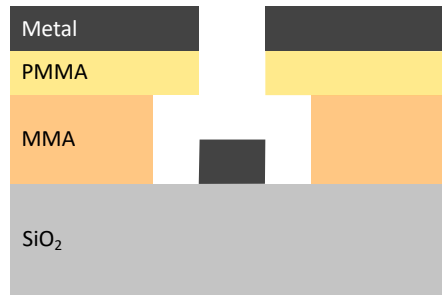


FIGURE 3.5: **PMMA/MMA stack**

Thanks to this resist structure, the deposited metal is not in contact with resist, which facilitate the following lift-off.

### 3.2.4 Quantum dot circuit contacts and gates

To define the contact and the gate electrodes, the standard lithography technique is used (cf. figure 3.4). These steps of the process only act in the  $100\ \mu\text{m} \times 100\ \mu\text{m}$  area where the quantum dot circuit is located. This allows us to precisely align a lithography with respect to the previous ones. Indeed, the SEM can sweep a  $100\ \mu\text{m} \times 100\ \mu\text{m}$  area only by deflecting the e-beam and without any mechanical displacement, which allows to easily reach an alignment accuracy as low as 50 nm.

For the lithography of the gate electrodes which is the thinner structure of the device, a stack of 100 nm of MMA resist (Methyl methacrylate) and 50 nm of PMMA resist has been used. This stack is useful for two reasons. First, for the same dose factor, the MMA resist is developed faster than PMMA, this way the opening in the MMA will end-up larger than the PMMA one, which truly defines the width of metallic electrode (see figure 3.5). This way the deposited metal is not in contact with resist on its edges, which can be a problem at the lift-off step for a single layer of PMMA. Second, The total thickness of the resist layer is lower than the standard layer of 500 nm of PMMA, allowing for a better writing resolution. Details about each metal depositions are given in appendix A.

### 3.2.5 Etching side trenches

To ensure the contact between the nanotube and the circuit electrodes, two trenches on both side of the quantum dot circuit have to be etched to host the comb of cantilevers (in blue in figure 3.3). Since these trenches are 2 mm long for  $200\ \mu\text{m}$  wide, they can be defined by optical lithography. Moreover, the used optical resist (AZ5214) is 1.5

$\mu\text{m}$  thick and is more resistant to  $SF_6$  plasma etching than PMMA resist. Thereby it provides a resistant enough mask to withstand reactive ion etching of  $15\ \mu\text{m}$  of silicon. Once the two adjacent trenches have been etched, we can cleave the sample in two chip of  $5\ \text{mm} \times 10\ \text{mm}$ , and then *staple* a carbon nanotube to complete the circuit.

### 3.2.6 Growth of carbon nanotube

The carbon nanotubes are grown by Chemical Vapor Deposition (CVD) in a home made furnace (see figure 3.6-a). In the CVD process, catalytic metallic nanoparticles are used as a precursor for the growth. The used recipe has been developed in Basel by J. Furer [130] and is optimized to obtain single walled carbon nanotubes. The catalyst solution is composed of 39 mg of  $Fe(NO_3)_3 - 9H_2O$ , 7.9 mg of  $MoO_2$  and 39 mg of  $Al_2O_3$  nanoparticles diluted in 30 mL of IPA. The  $Al_2O_3$  nanoparticles serve as a support for iron and molybdenum and tend to form clusters. Hence, before the deposition of the catalyst solution on the growth chip, one need to sonicate it for one hour in order to break apart alumina clusters which are believed to favor the formation of bundles of CNT. Then the catalyst solution is left for decantation during 45 minutes and a small volume is taken off at the surface of the solution. A few drops are deposited on the growth chip, then it is partially rinsed in IPA before drying it with nitrogen. Rinsing in IPA allows to obtain a more uniform catalyst deposition.

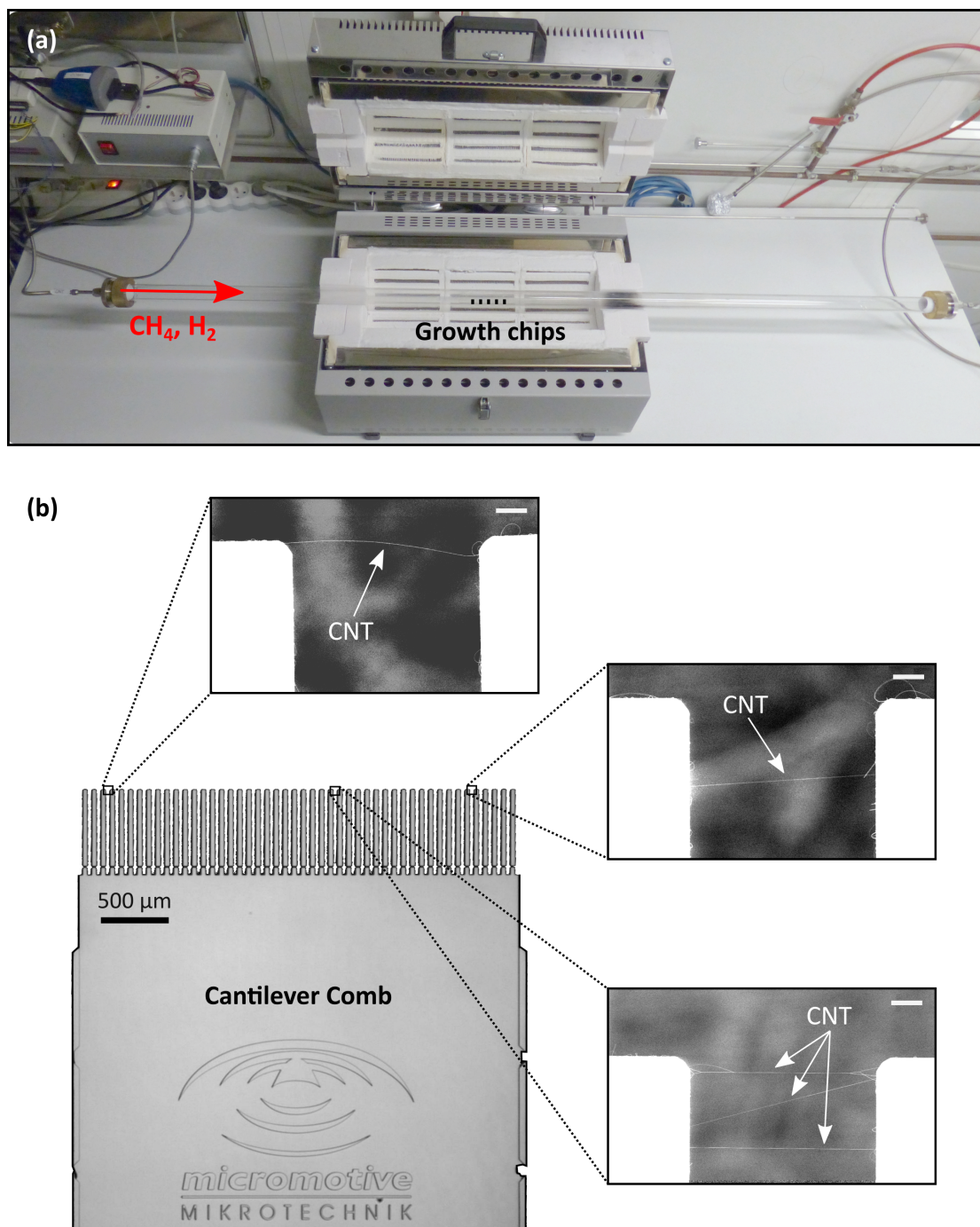


FIGURE 3.6: **CVD growth on a comb of cantilevers:**

**a.** The CVD setup consists in a 1.5m long quartz tube whose central portion is caught in a furnace reaching 900° C. Growth gases are injected at one extremity of the quartz tube. **b.** The growth of carbon nanotubes is performed on commercial combs with about 50 cantilevers. We obtain typically between 5 and 10 suspended carbon nanotube suitable for the stapling. Prior to use commercial cantilevers we have been using home-made one whose process development have been carried out by J.Palomo. The process is based on a wet etching process of the silicon (see appendix A). Scale bar: 5  $\mu\text{m}$ .

The distribution density is a key parameter: a high density favors the formation of CNT bundles (as the chance of two CNTs meeting increases), while a too low density results

in a small number of CNTs. The catalyst density can be estimated by using optical microscope in *dark field* mode (using a low-angle light). Additional catalyst can be deposited as long as the satisfying distribution density is not reached. The growth chip can then be inserted in the quartz tube of the CVD furnace and the growth can start (further details on the growth recipe are given in appendix A).

During the development of the stapling process other options have been explored such as using suspended CNTs over pillars (in the spirit of [41], [123]). In this perspective, the strategy is to initiate the growth at one location of the chip and then obtain long enough CNTs to reach the pillars few hundred of micrometers away. This strategy is highly beneficial for limiting the number of CNT bundles, but it requires a directional growth. Guided by this idea, we followed the growth recipe of [131], reported to produce long CNTs and aligned along the gas flow. The growth results are presented in figure 3.7. Nevertheless, because of a low success on the transfer of CNT, (most likely due to the uncontrolled angle between the growth chip and the circuit chip) we decided to use cantilevers which have a much better tolerance on the approach angle.

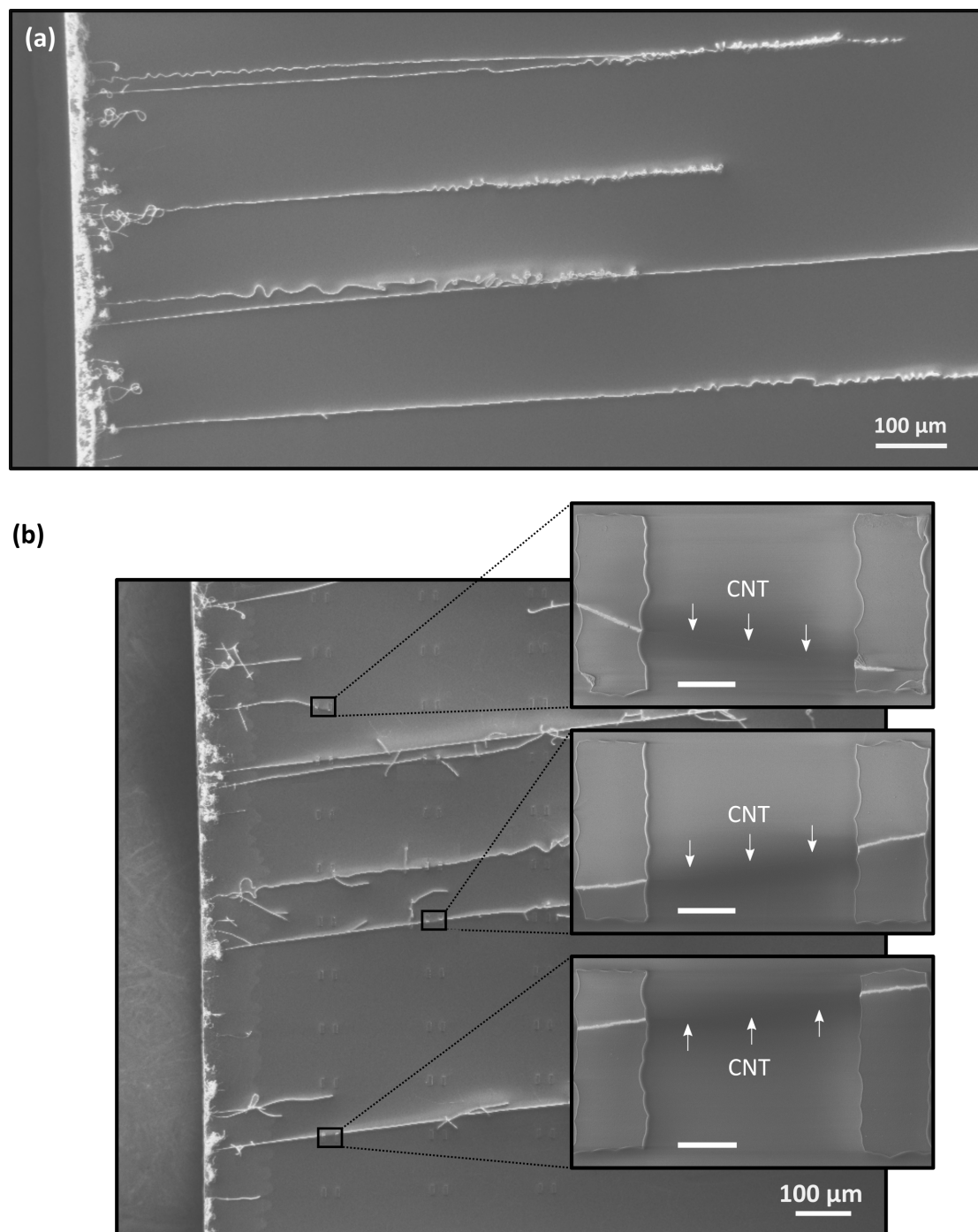


FIGURE 3.7: **Directional growth based low-flow recipe:**

**a.** The catalyst deposition is critical for getting long CNTs. It has been found that depositing the catalyst on the edge is an efficient way to obtain a decent number of long CNTs (longer than 500  $\mu\text{m}$ ). In this low flow growth recipe, the *kite-mechanism* [132] is taking place, where the catalyst nanoparticles are floating above the substrate and dragging the growing CNTs. The edge is believed to lift the nanoparticles because of local turbulent flow, then they are maintained thanks to the buoyant force. In such a situation, CNTs can easily reach few millimeters. **b.** Similar growth with pillars pre-patterned on the substrate resulting in suspended CNTs. The fact that the trajectories of the long CNTs are not modified by the pillars is consistent with the *kite-mechanism*.

Scale bar: 5  $\mu\text{m}$ .

### 3.2.7 Embedding of the carbon nanotube

**The Stapler** The integration of the carbon nanotube is accomplished inside a vacuum chamber dedicated for this task (see figure 3.8). This chamber contains a micro-manipulator stage responsible for coarse motion and a piezo-motor stage allowing a fine positioning of the cantilever chip with respect to the circuit chip. The system is also DC wired for transport measurements during the stapling. An argon gun is integrated to clean the circuit chip surface prior to stapling a carbon nanotube, or to remove the stapled CNT if this one does not meet the desired criteria. In this scenario the cantilever chip can be isolated in a buffer chamber while the circuit chip is being cleaned. A window is also encrusted in the cover of the main chamber to optically align the two chips with respect to each other. This equipment has been design to fit with 4K-measurements by adding a cold finger through the bottom flange.

**Stapling principle** After the carbon nanotube growth on the cantilever comb, the CNTs are localized by SEM. The goal of this SEM observation is to sort the pairs of cantilever depending on whether they contain a CNT suitable for stapling. A suitable nanotube for stapling has to be as close as possible to the tip of the cantilever (in the first 10  $\mu\text{m}$ ), it has to be isolated enough from other possible suspended CNTs (at least 5  $\mu\text{m}$ ), and in the ideal scenario, it should be a unique single walled carbon nanotube. Although the SEM is not suited to characterize carbon nanotubes, it allows at least to distinguish between a bundle composed of plenty of CNTs and one which contains only 2 or 3 CNTs, by looking at the contrast and at the Y shape characteristic of the braiding of two CNTs (see figure 3.6). More details are given in appendix C. Once this localization step is finished, the cantilever chip is ready to be glued with PMMA to the piezo-motor stage inside the *Stapler*.

A very close attention is given to the time spent by the cantilever chip in ambient atmosphere. CNT are well known to have a high adsorption capacity, which is exploited to design gas sensor based on carbon nanotubes [133]. For our use, this property is rather a drawback and we want to limit as much as possible the exposition time to the atmosphere, in order to avoid such contamination. For that reason the cantilever chips are stored in a primary vacuum between the carbon nanotube growth and the stapling step.

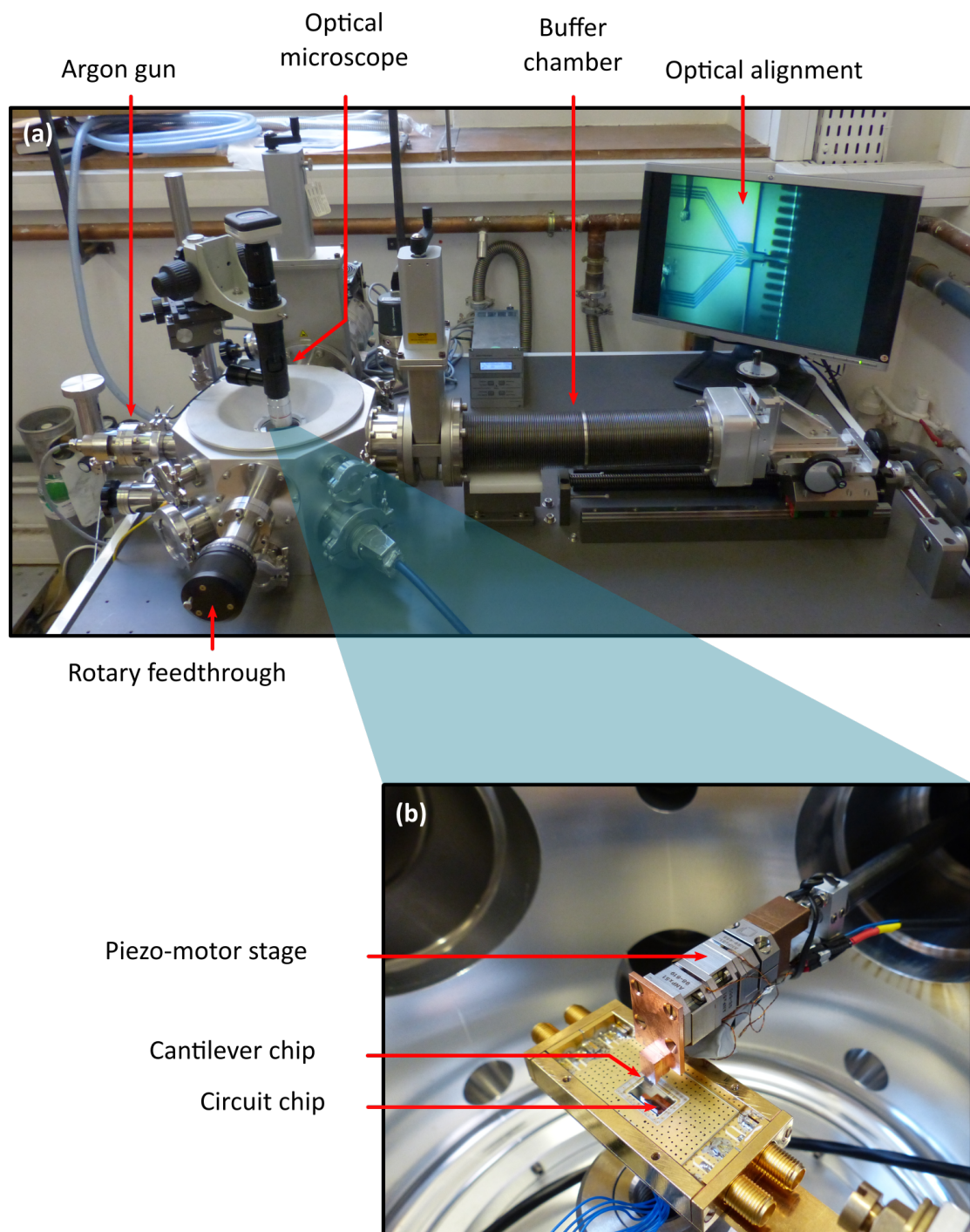


FIGURE 3.8: **The stapler:**

**a.** The system is placed on top of a air-cushion table to mechanically decoupled it from its environment. **b.** Zoom-in on the inside of the main chamber. Here the cantilever chip and the circuit chip are in the stapling configuration.

Once the circuit chip and the cantilever comb are inserted in the stapler, we can start the stapling procedure. The global strategy for stapling is the following:

- Slowly lowering the cantilevers using the nano-positionner stage until a current is detected in the circuit, ensuring that a nanotube has been contacted.

Driving a high current in the external sections of the CNT to cut it by Joule heating.

- Rising the cantilevers enough to avoid any dramatic collision during the extraction of the circuit chip from the stapler.
- Measuring the gate dependence of the current through the central section of the CNT.
- Depending on the resistance of the central section, it might be needed to improve the contact resistance by driving a high current through the central section.
- Transferring the sample holder from the stapler to the cryostat, while keeping all electrodes grounded and the circuit chip under Nitrogen atmosphere to limit the reactivity of the CNT to the oxygen.

**Contact detection** During the approach, a bias voltage (typically around 500 mV) is applied to the outermost contact electrodes while keeping the other electrodes grounded (see figure 3.9). Keeping the gate electrodes grounded during the approach is an important point to prevent the CNT to snap to the gates. The current is monitored by measuring the voltage drop across a 100 k $\Omega$  resistor, hence any current between the biased contacts and the ground will be detected, in particular current in the two cutting sections. This setup provides large chance to detect a CNT regardless of the approach angle.

**Cutting and room temperature characterization** After mating the CNT to the circuit, the next step is to separate it from the cantilevers, to avoid detaching the CNT from the circuit when raising the cantilevers. This is done by driving a large current between two adjacent contact electrodes up to a threshold value after what the CNT burns [124]. Examples of  $I_{cut}(V_{bias})$  line traces are shown in figure 3.10. The current increases until it reaches a threshold value  $I_{threshold}$ , then it abruptly falls to zero indicating the cutting of the CNT. The value of  $I_{threshold}$  is instructive about the

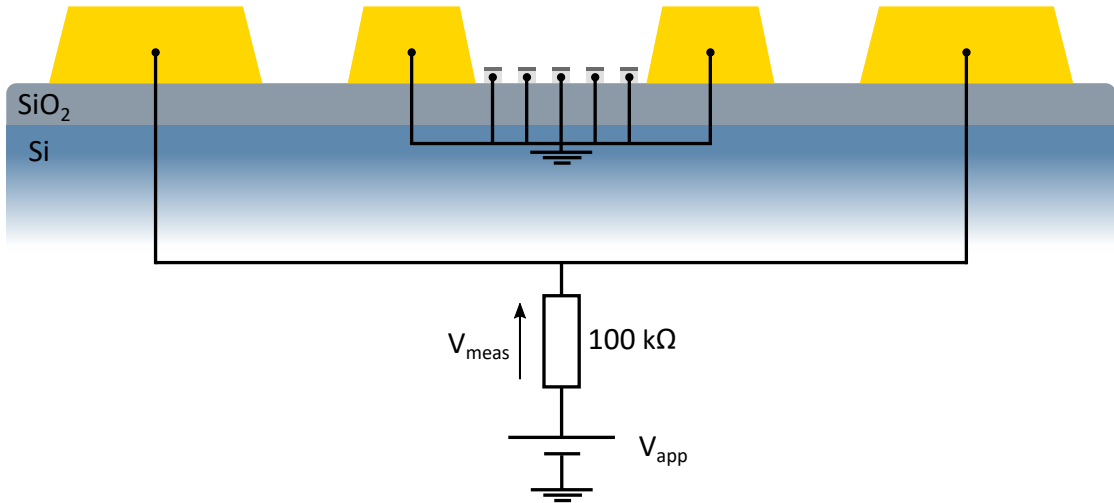


FIGURE 3.9: **DC detection circuit:** This is the circuit used to detect the contact between the CNT and the circuit chip while the cantilever chip is lowered. A typical value for  $V_{app}$  is 500 mV, which allows for easy detection of the contact.  $V_{meas}$  range from 10  $\mu$ V to 2 mV, which correspond to contact resistance of few hundreds of M $\Omega$ .

current carrying capacity of the CNT which vary a lot from single walled CNT to multi-walled CNT or bundles [134]. Another signature of multi-walled CNTs or bundles is the presence of multiple current drops in the cutting I-V curve (see figure 3.10 (b)), which is consistent with sequential cuts of the different shells of multi-walled CNT or the different CNTs in case of a bundle.

The cutting mechanism is believed to be due to Joule heating rather than electromigration [135]. Indeed the highest temperature in the CNT is reached at the center of the suspended segment since it is the farthest point from the contact electrodes that act as thermal sinks. In that respect, the fact that the cut of the CNT always occurs at the center of the suspended segment is consistent with a Joule heating mechanism.

These cutting curves also provide information about the cleanliness of the CNT. In absence of local disorder, one expect similar cutting curves at different position of the CNT, which are only defined by intrinsic properties of the CNT. This symmetric behavior has been observed on several devices (see figure 3.11).

This operation is also highly beneficial for the total resistance of the resulting device. Indeed, the cut of the CNT acts as a local annealing. This drastically improves the contact resistance between the CNT and the two contacts of the resulting circuit. The contact resistance after mating is typically between a few tens of M $\Omega$  and hundreds of M $\Omega$ , which is too high for any transport measurements at millikelvins temperature.

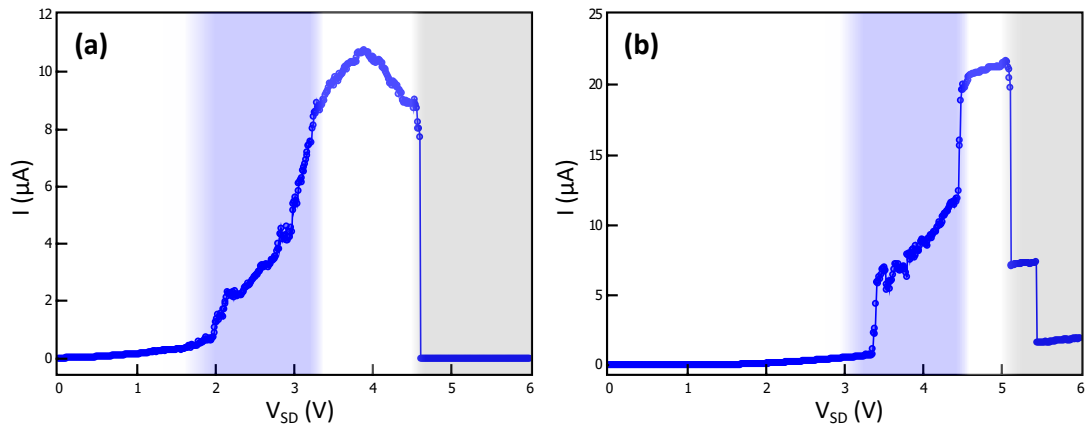


FIGURE 3.10: **I-V curve during the cutting of a CNT**

(a) Three distinct regimes can be identified in the cutting I-V curve. First, between 2 V and 3.5 V the current increases step-wisely due to a sequential improvement of the contact. Then the current reaches its threshold value (between 3.5 V and 4.5 V for this CNT). For some of the contacted CNTs, a decrease of the current is observed before the CNT is cut. This reflects the suspended behavior of the CNT [136], and is due to electron-optical phonon scattering. (b) I-V curve for a multi-walled CNT or a bundle displaying characteristic multiple current drops. On this I-V curve, the current is not reaching zero after the cut of the CNT. This residual current, which can be large, is attributed to a contact between the CNT and the silicon at the bottom of the trenches which is grounded. No current is measured when the source and drain are exchanged which confirms this scenario.

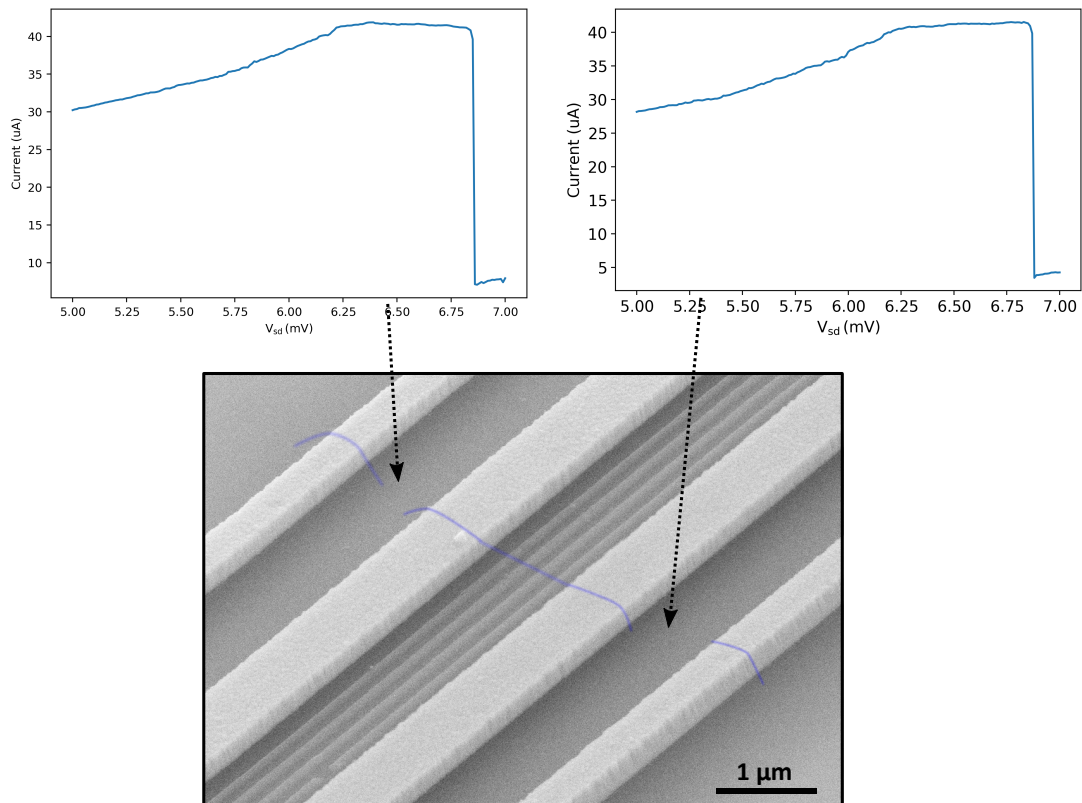


FIGURE 3.11: **Cutting I-V curves on two distant sections of a CNT**

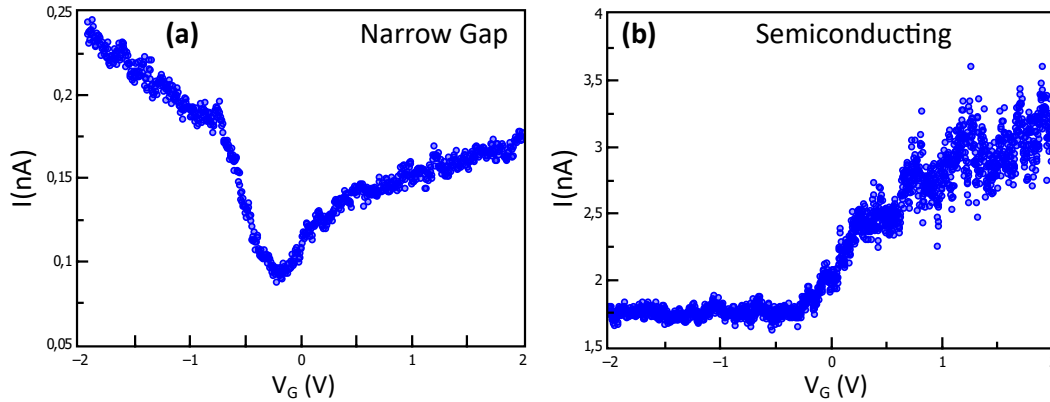


FIGURE 3.12: **Gate Dependencies in transport measurement**

- a.** Gate dependence of a narrow-gap CNT, and **b.** of a semiconducting CNT. For metallic CNT the current does not depend on the gate voltage  $V_G$ .

After the cutting of the CNT, the total resistance of the device lay in between 100 k $\Omega$  and few M $\Omega$ . If the circuit is still too resistive after this step, a post annealing is worth considering (more details in the next paragraph).

To discriminate between a semiconducting or a metallic CNT, one can measure the current in the central section as a function of gate voltage  $V_G$ , at a fixed bias voltage. The gate voltage shifts the chemical potential in the CNT with respect to the Fermi energy  $E_F$  of the leads. Thus one can tune  $E_F$  into the band gap of the CNT, leading to a current suppression. For carbon nanotubes, three different behaviors can be identified: semiconducting, narrow-gap, or metallic (see figure 3.12). According to the zone folding approximation, only semiconducting and metallic CNTs are expected [3]. Nevertheless a narrow gap behavior can be explained by transverse curvature or strain in CNTs predicted to be metallic by the zone folding approximation [3].

**Post annealing** After cutting the external section of the CNT, the resistance of the central portion can remain too high for low temperature transport measurement (above 3 M $\Omega$  no current was detected below  $V_{SD} = 50$  mV, due to a too high contact barrier). A solution is to drive a high current (typically a few  $\mu$ A) through the central section to enhance the wetting between the metal and the CNT, therefore improving the contact resistance. Similarly to the cutting step this can be understood as a local annealing of the contact, with the only difference, here  $V_{app}$  do not exceed  $V_{threshold}$ .

**Transfer of the chip carrier** Once the stapled carbon nanotube has a good enough resistance, one has to transfer the chip carrier inside the cryostat. This is one of the tricky steps in the process since carbon nanotubes are very sensitive to any electrical discharges originating from triboelectric effect or transient current during connections. Such sensitivity is believed to be due to a self-heating of the CNT, and its reaction with oxygen, causing the breakdown of the CNT [135]. The main precautions consist in always keeping the DC lines of the circuit grounded and maintaining the chip carrier in a nitrogen atmosphere to avoid the CNT to be in contact with  $O_2$ . The vacuum chamber is vented with nitrogen, and right after the opening of the chamber, we close the chip carrier, then the circuit lines are connected to the ground of the cryostat via a  $10\text{ M}\Omega$  resistor to avoid high transient currents. All DC lines of the circuit are connected to two output lines, allowing for a smooth ground transfer and preventing the circuit lines to be at a floating potential during the transfer into the cryostat. During the transfer the inside of the chip carrier is kept under nitrogen atmosphere by flushing it via holes in the chip carrier. Electrical discharges are more likely to happen during the connection of the DC lines to the cryostat lines. To limit such transient current during the connection of the DC lines, additional  $10\text{ M}\Omega$  resistors are added on the lines of the cryostat. Ongoing work focuses on improving the yield of transferred CNTs by designing a vacuum-tight sample holder (see figure 3.13). Although maintaining the sample holder under nitrogen atmosphere has revealed to be very efficient, and brought the success yield close to 100%, strong variations of the circuit resistance still remain. Keeping the circuit chip under vacuum during all electrical connections should limit those uncontrolled variations of resistance.

**Circuit chip design** Dimensions of the circuit play a critical role for the smooth running of the stapling. The ratio between the QD-circuit length and the height of the contacts with respect to the gates is decisive to obtain a suspended carbon nanotube (see figure 3.14). Another important parameter which affects the suspended nature of the CNT once it is stapled, is the slack of grown CNTs in between cantilevers. Although, our growth recipe does not provide any control over the slack of CNTs, most of them are taut. The rule of thumb is to keep this aspect ratio below 15.

The length of the cutting section (see figure 3.14) determines the current  $I_{threshold}$  needed to cut the CNT. Indeed, by increasing the distance between the two adjacent contacts

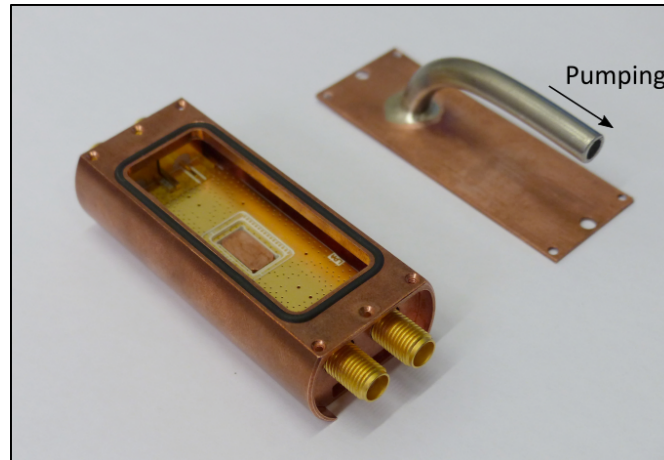


FIGURE 3.13: **Vacuum tight sample holder**

Such a sample holder is expected to diminish the variations of resistance during the connection to the cryostat. It also reduces the overall atmosphere exposition time of the CNT.

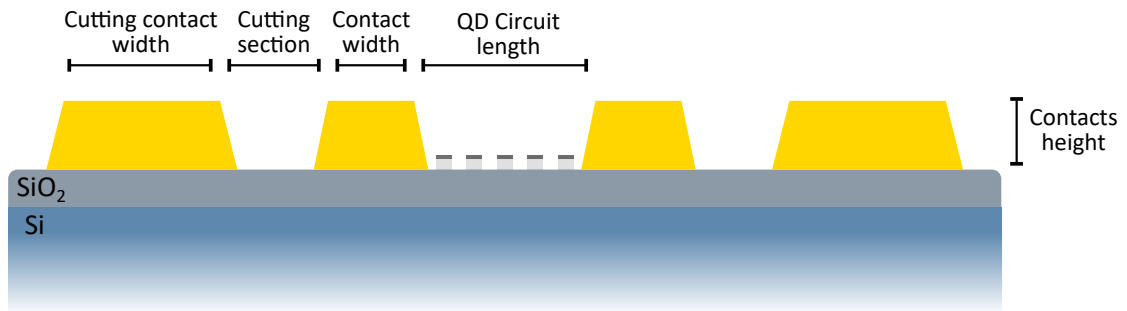


FIGURE 3.14: **Quantum dot circuit profile including cutting contacts**

the center of the suspended segment will be more thermally decoupled from them. On one hand, it is preferable to keep  $V_{threshold}$  high enough to avoid accidental cutting of the CNT. On the other hand, going to high bias voltage (typically above 10 V) might break the gates oxide if the CNT is not suspended. This can causes the burning of the CNT due to a high transient current and also the melting of the contacted gates. Typical spacing between the contact electrode and the cutting contact is 1  $\mu\text{m}$ , which correspond to a  $V_{threshold}$  lying in between 4 V and 6 V.

The width of the cutting contact defines the contact resistance with the CNT, which affects the detectability of the CNT during the lowering of the cantilevers. It will also influence  $V_{threshold}$ : a wider cutting contacts result in a lower  $V_{threshold}$ .

Development in progress focus on the characterization of the CNT when it is still suspended on the cantilever comb, in order to post select the single walled carbon nanotubes. Raman spectroscopy and Rayleigh spectroscopy are the two techniques considered.

### 3.3 Measurement techniques

In this section we describe the setup for transport measurement as well as for RF measurement of the cavity.

#### 3.3.1 Isolating the device from environment

**Chip carrier and PCB** Once the chip has been cut in pieces of  $5 \times 10$  mm, it is glued with PMMA resist to the sample holder and can be micro-bonded to the Printed Circuit Board (PCB). A multi-layer PCB is used where DC and RF lines are on two different layers with a ground plane in between to suppress cross-talk between RF and DC signals. Two additional ground planes serve to encapsulate the whole stack. These three ground planes are connected to each other with via holes. One of the objective of the PCB design is to eliminate RF modes in the vicinity of the cavity resonance (around 6.5 GHz). Because of the dimensions of the inside sample holder ( $15 \text{ mm} \times 45 \text{ mm} \times 5 \text{ mm}$ ) 3D box modes can act as parasitic resonance. In order to push at higher frequency those modes, a copper cover has been design to reduce the box volume over the chip to  $10 \text{ mm} \times 5 \text{ mm} \times 5 \text{ mm}$  and push 3D modes above 9 GHz. To ensure a good electrical contact an Indium seal is used between the top layer ground plane and the cover. Another possible parasitic mode is the slot line mode where the two ground planes oscillate in phase opposition. Micro-bonds are used to link the two ground planes, hence supressing the slot line mode.

**Cryostat and wiring** All the experiments presented in this thesis work have been carried out in a dry dilution refrigerator (HEXADRY 200 Cryoconcept) at a base temperature of 20 mK. The RF and DC wiring of this cryostat has been done by a previous PhD student, Laure Bruhat. The temperature needed for an experiment is determined by the smaller energy scale one want to resolve. In the case of the Cooper pair splitter experiment (Chapter 4) this energy is the proximitized superconducting gap of Pd/Al which is of the order of  $100 \mu\text{eV}$ . This set the condition on the temperature:  $3.5 k_B T \ll 100 \mu\text{eV}$  which correspond to  $T \ll 335 \text{ mK}$ . For the spin-qubit experiment (Chapter 5) the smaller energy scale is the Zeeman splitting ( $3.5 k_B T \ll g \mu_B B$  giving rise to  $T \ll 385 \text{ mK}$  at 1 Tesla). One thing worth notice is that with such base temperature,

the microwave cavity is not thermally populated (photon number =  $\frac{1}{e^{\hbar\omega_c/k_B T} - 1} \simeq 10^{-2}$ ), hence when no microwave tone is applied, the cavity is in its ground state. In order to preserve this very low thermal population, one need also to cool down the incoming drive field. This is done by thermalizing the input lines at each stage and by attenuating the 50  $\Omega$  thermal noise of each stage as illustrated in the figure 3.15. For the output line, one require as less attenuation as possible since it carries the signal of interest. Therefore a NbTi microwave cable with low attenuation is used up to the 4 K stage where a HEMT cryogenic amplifier is inserted. On the 20 mK stage, two cryogenic circulators are placed on the output line to protect the microwave cavity from 4 K thermal noise originating from reflections on the HEMT amplifier (see figure 3.15).

### 3.3.2 Transport measurements

All the transport measurements performed in this thesis work are either differential conductance, or current measurements. To measure the current, a bias voltage is applied on one of the contact electrode of the carbon nanotube circuit with a *Yokogawa GS200*. A voltage divider and a RC filter ( $f_{cut-off} = 1.6$  kHz) at room temperature are used to minimized noise in addition to the second order RC filter at 20 mK. At the output of the CNT the current is of the order of 100 pA, thus we use a home-made current amplifier with a gain of  $10^7$  (Electrical schematic available in the PhD thesis of Jeremie Viennot [138]), then the voltage is read by a *Keithley 2000*. For the gate voltages, an *Itest* rack ( $\mu$ *BILT BN103*) with five modules (*BE2141*) providing 20 output voltages is necessary. Indeed the number of gate electrodes can go up to 18 for two circuits on the same chip. The whole measurement setup is presented in figure 3.16 and a typical measurement with this setup is shown in figure 3.17. The room-temperature CNT resistance typically ranges from 50 k $\Omega$  to 2 M $\Omega$ .

Differential conductance provides direct measurement of the density of states in the quantum dots which is highly desirable in such experiments. The measurement of the differential conductance is based on a lock-in detection scheme where an AC bias voltage (at 77.77 Hz) is applied to the CNT circuit. The output current is then demodulated by this input frequency, thus moving the relevant signal to DC, which justify the use of a subsequent low pass filter inside the lock-in amplifier (*SIGNAL RECOVERY 7265*). This technique is very efficient to extract a specific signal from a noisy environment.

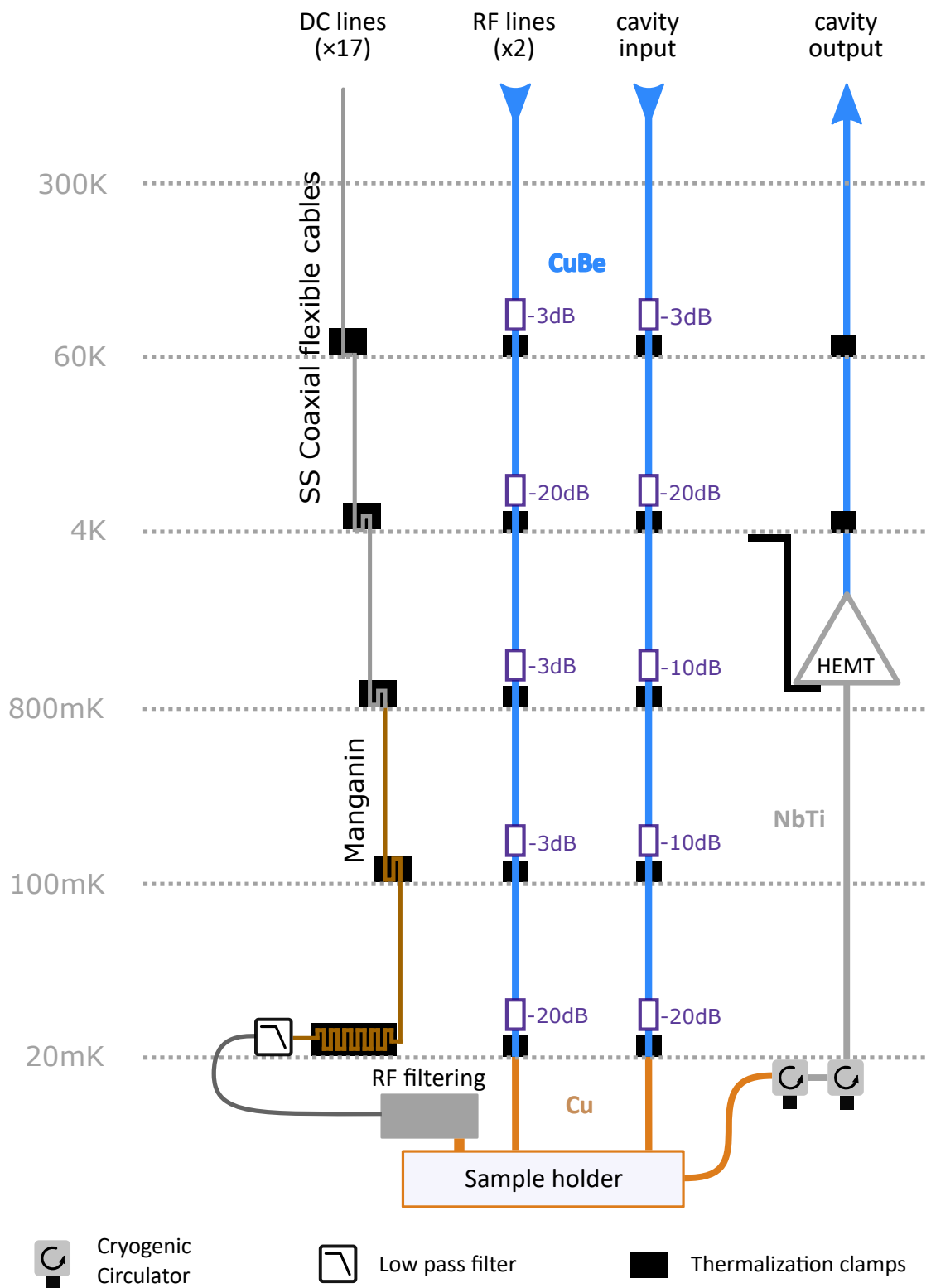


FIGURE 3.15: **Schematic of the cryostat wiring:**

In addition to the cavity input and output lines, there are two other RF lines designed to address the quantum dot circuit in the microwave range (they are less attenuated).

Further details about the wiring are given in the PhD thesis of Laure Bruhat [137].

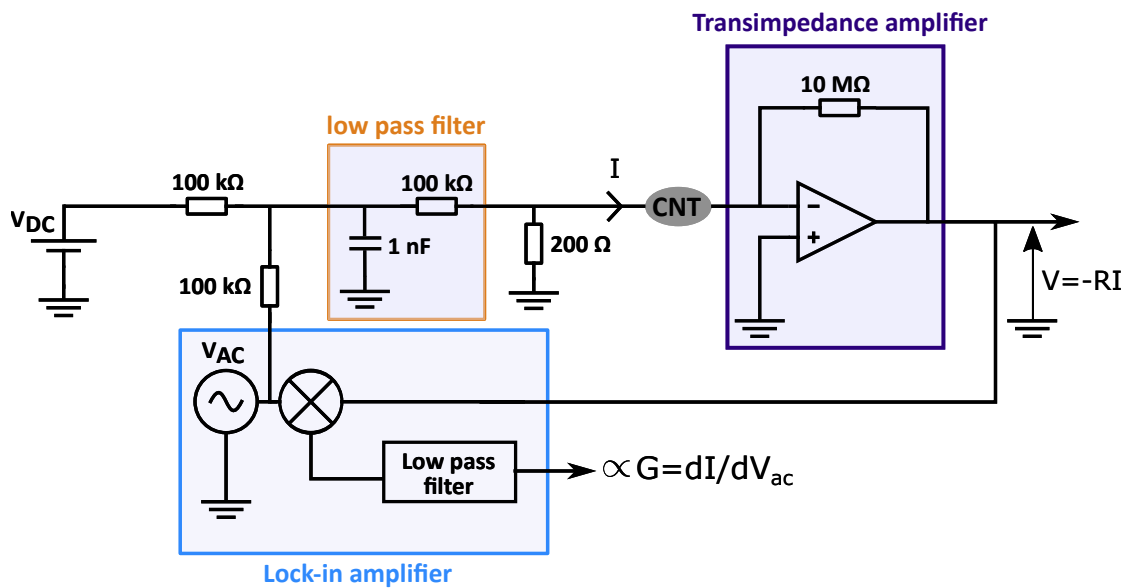


FIGURE 3.16: Transport measurement setup

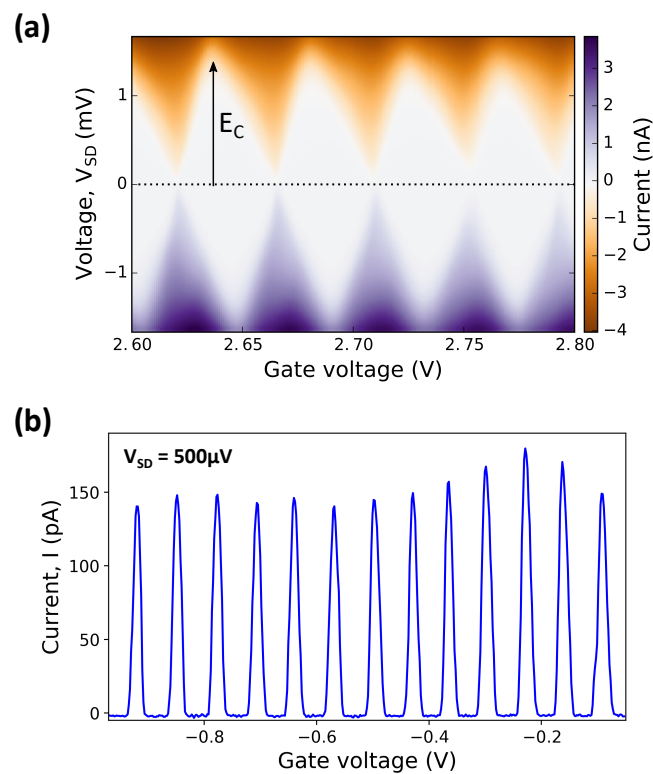


FIGURE 3.17: Coulomb diamonds and peaks measurements:

**a.** Current measurement through a single quantum dot circuit in the Coulomb blockade regime as a function of the bias voltage ( $V_{SD}$ ), and the gate voltage ( $V_G$ ). In the white diamonds region, the transport is blocked due to the large charging energy of the dot (measurement taken on device STADQD22LR). **b.** Current through a double quantum dot circuit in the Coulomb blockade regime as a function of a gate voltage tuning energy levels in one of the two dots (measurement taken on device SPN15R).

### 3.3.3 Cavity transmission measurement

Measuring the cavity transmission provides information about the internal dynamic of the quantum dot circuit. In that sense, it is complementary to transport measurements which probes the circuit only via its coupling to the leads.

#### 3.3.3.1 RF setup

During this thesis multiple RF measurement setup have been used. The initial one is based on a Lock-In detection scheme and is presented in [137]. This setup benefit from the ability of Lock-In amplifier to extract signal at a given frequency in a noisy environment. Nevertheless such a setup is not fitted for time resolved measurement since it is unable to do pulse sequences. A simpler setup consists in directly connecting a VNA (Vector Network Analyser) to the two ports of the cavity, and all the demodulation is carried out inside the VNA. This setup has been widely used for quick characterization of the cavity resonance during development phases.

The setup illustrated in figure 3.18 is the last one used and allows to perform time domain measurements. The cavity drive tone (typically around 6.5 GHz), called Local Oscillator (LO), is generated at room temperature and is mixed in a single side band mixer with a 20 MHz signal generated by a Arbitrary Waveform Generator (AWG), called Intermediate Frequency (IF). Such a mixer is able to output only one of the two side-bands (in this case the lower side-band) and ensure a 30 dB isolation from the upper side-band and the direct transmission. This signal is then sent to the cavity input after going through approximately 60 dB of attenuation inside the cryostat (see figure 3.15). After passing through the cavity, the signal is amplified and filtered before being down converted in a I/Q mixer. This component allows to obtain the two quadratures of the demodulated signal by mixing the RF output signal to the LO signal (providing the I-quadrature) and also a 90° phase shifted LO signal (providing the Q-quadrature). In principle a basic mixer would be sufficient since the Analogic Digital Converter (ADC) collects the full traces of the down converted signal from which the two quadratures can then be calculated. Nevertheless, collecting the traces for the in-phase and out-of-phase signals allows to gain a factor 2 on the Signal to Noise Ratio (see appendix D



### 3.3.3.2 Continuous measurements

Most of the RF measurements presented in chapters 4 and 5 are continuous measurements, since time resolved measurements require a better control of the system which was not the case at the beginning of this thesis work. A typical cavity transmission measurement is shown in figure 3.19. The ADC collects traces (typically 10000 traces) then average them and extract the I and Q quadratures by multiplying the averaged trace with  $\cos(\omega_{IF}t)$  and  $\sin(\omega_{IF}t)$ . Knowing I and Q one can calculate the phase and the amplitude of the output signal using:

$$A = \sqrt{I^2 + Q^2} \quad \varphi = -\arctan\left(\frac{Q}{I}\right)$$

Depending on where the coherent state of the cavity field is displaced in the I/Q space by the circuit state, it can be relevant to look at other quadratures than the amplitude and the phase of the coherent state of the cavity field. Nevertheless the phase and the amplitude have the advantage of being directly link to physical quantities: Dissipation or photon emission for amplitude and dispersive shift of the cavity resonance for the phase (see section 2.3).

**Qubit spectroscopy** In a qubit spectroscopy measurement, the qubit state is brought out of  $\langle\sigma_z\rangle = -1$  (north pole of the Bloch sphere) by applying an additional tone resonant with the qubit frequency. According to the formula 2.27, this change of state is visible in the cavity transmission signal. Therefore, such measurement allows to access the qubit energy dispersion with respect to any parameter of the system (typically a gate voltage or the magnetic field). In this procedure the qubit is manipulated while the cavity is filled with photons, which could be detrimental for the qubit coherence. Indeed, photon shot noise in the cavity gives rise to random fluctuations of the qubit frequency because of the AC-Stark shift (see formula 2.17), resulting in a broadening of the qubit linewidth, hence a lower visibility in the measurement. This phenomenon is often referred to as measurement-induced-dephasing [139].

A cleaner way to perform the spectroscopy of the qubit is to separate in time the manipulation and the read-out. This can be done by performing a  $\pi$ -pulse (a  $\frac{\pi}{2}$ -pulse also works but results in lower contrast) on the qubit and subsequently filling the cavity with photons (see figure 3.20). If the calibration of  $\pi$ -pulse is not possible, the poor

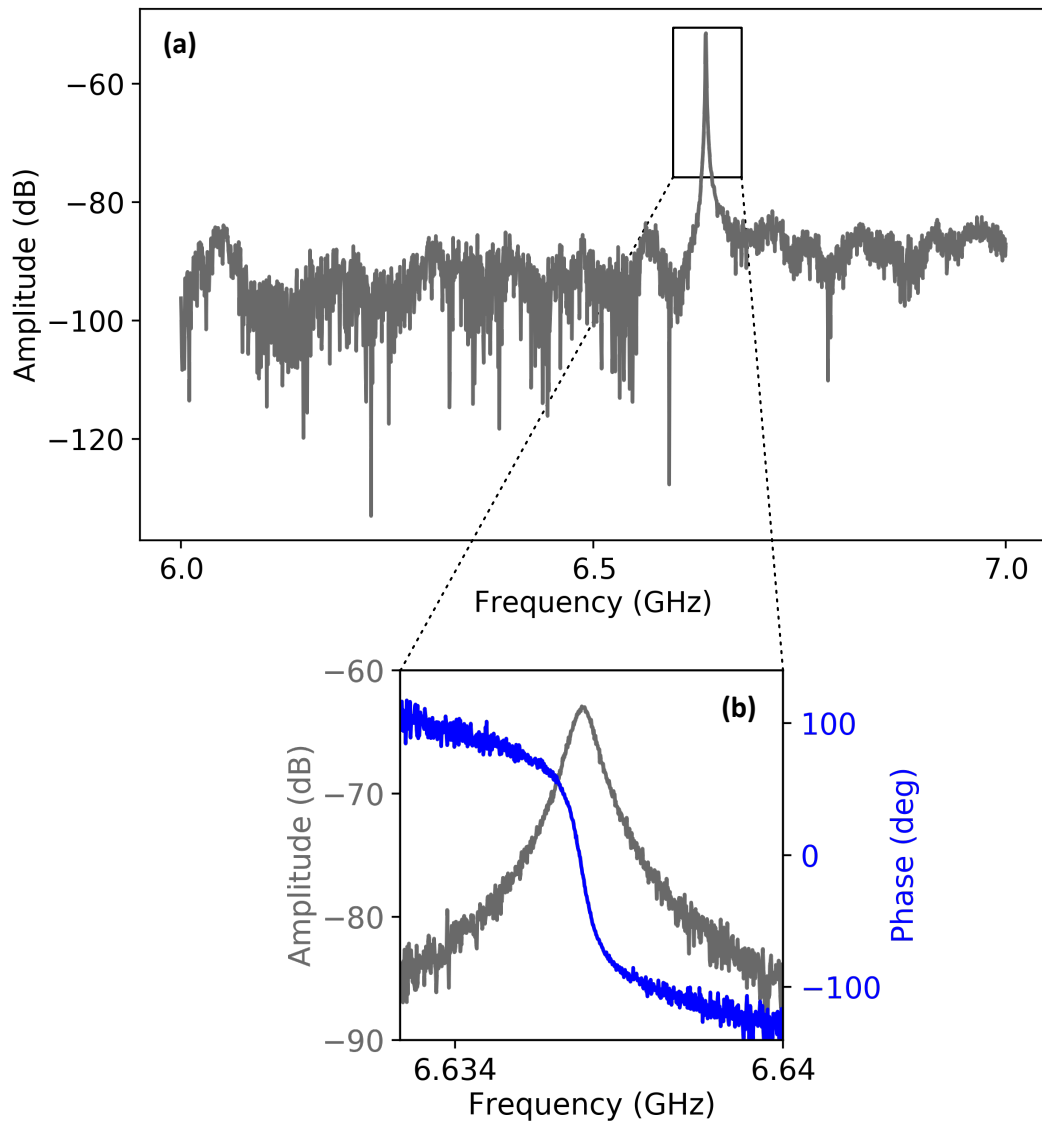


FIGURE 3.19: **Cavity transmission measurement:**

**a.** RF transmission measurement between 6 GHz and 7 GHz of a coplanar waveguide cavity as shown in section 3.2.1. **b.** Zoom-in on the cavity fundamental mode resonance. The FWHM (Full Width Half Maximum) of the resonance is  $\Delta f_{-3dB} = 530$  kHz corresponding to a quality factor  $Q = 12500$ . The measurement is performed at an input power such that the average photon number at the resonance is about  $n_{ph} \simeq 10$ . The estimation of the photon number requires to know the input and output powers at the cavity ports, which are known with a 3 dB precision.

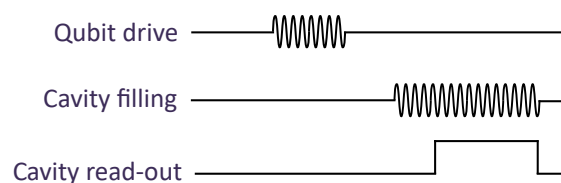


FIGURE 3.20: **Pulse sequence for qubit spectroscopy**

man's method consists in driving the qubit transition strongly enough to saturate the transition, hence the qubit ends up in a statistical mixture (center of the Bloch sphere) satisfying  $\langle \sigma_z \rangle = 0$ . This sequential procedure impose to have a qubit relaxation time  $T_1$  longer than the time needed for filling the cavity with photons (namely its relaxation time  $1/\kappa$ ). If this condition is not fulfilled, one can also start to fill the cavity before the end of the qubit manipulation.

### 3.3.3.3 Time domain measurement

This type of measurement are more demanding in terms of calibrations than continuous ones, since the duration and the power of the applied tone can be very critical. During those measurements, the AWG is repeatedly providing pulse sequence and the ADC is waiting for a trigger signal as soon as it is not acquiring-processing data anymore. Only a small selection of the possible pulse sequences is presented here, namely  $T_1$ -measurement and Rabi oscillations.

**$T_1$ -measurement** The longitudinal relaxation of the qubit is described by the characteristic time  $T_1$ . To measure it, the standard way is to do a  $\pi$ -pulse on the qubit (placing it in its excited state:  $\langle \sigma_z \rangle = 1$ ), then read the cavity after a variable time  $\tau$  allowing to reconstruct the full exponential relaxation (see figure 3.21-a).  $\frac{\pi}{2}$ -pulse and saturation pulse also work. Indeed, all pulses which drive the qubit out of  $\langle \sigma_z \rangle = -1$  are valid, even though driving the qubit in  $\langle \sigma_z \rangle = 1$  leads to the highest contrast. An other possible strategy is to drive the qubit, then directly look at the time traces after the qubit drive tone has been turned off [140], [51].

**Rabi oscillations** In Rabi oscillations, the qubit is rotating in a perpendicular plane to the equator of the Bloch sphere, hence oscillating between its ground and excited states with frequency  $\frac{\Omega_R}{2\pi}$ , and finally ends up at the center of the Bloch sphere. Such oscillations are performed by applying a drive pulse of variable duration (see figure 3.21-b). The period of the oscillations indicates how fast we are able to manipulate the qubit, which is of paramount importance in the perspective of quantum computing. They are also very instructive since they allows to calibrate the duration of  $\pi$  and  $\frac{\pi}{2}$ -pulses at a given power of the drive tone. If the qubit is driven via cavity photons, the Rabi

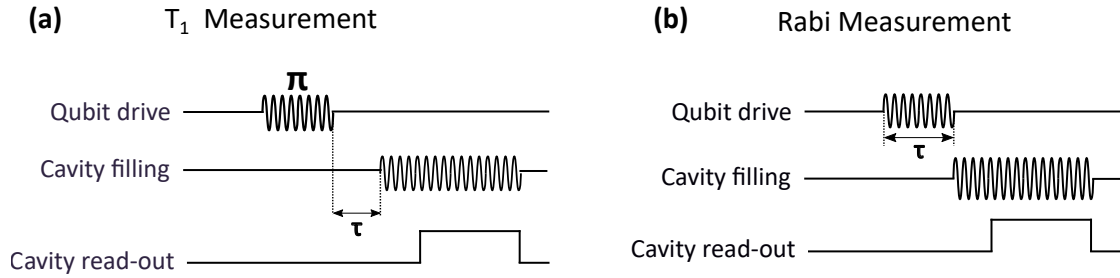


FIGURE 3.21: **Pulse sequences for  $T_1$ -measurement and Rabi oscillations**

The delay between the filling and the read-out of the cavity is set to  $1/\kappa$ . In all the presented pulse sequences the re-initialization of the system is done by waiting long enough for the cavity and the qubit to relax in their ground states.

frequency reads (see supplements of ref. [141]):

$$\frac{\Omega_R}{2\pi} = \frac{g\epsilon_d}{\Delta_{qubit-cavity}} \quad (3.1)$$

Where  $\epsilon_d$  is the amplitude of the drive tone,  $g$  is the qubit-photon coupling, and  $\Delta_{qubit-drive} = f_{qubit} - f_{cavity}$  is the frequency detuning between the qubit and the cavity. Measurements of the dependence of  $\frac{\Omega_R}{2\pi}$  according to  $\epsilon_d$  (Power dependence), and  $\Delta_{qubit-drive}$  (Chevron pattern) are the two standard sanity checks.



## Chapter 4

# The superconducting double quantum dot

Coupling double quantum dot circuits to microwave cavities provides a new powerful means to control, couple and manipulate qubits based on the charge or spin of individual electrons. In this chapter, we revisit this standard configuration by adding superconductivity to the circuit. We combine theory and experiment to study a superconductor-double quantum dot circuit coupled to microwave cavity photons. First, we use the cavity as a spectroscopic probe. This allows us to determine the low energy spectrum of the device and to reveal directly Cooper pair assisted tunneling between the two dots. Second, we observe a vacuum Rabi splitting which is a signature of strong charge-photon coupling and a premiere with carbon nanotube based quantum dot circuits. We show that our circuit design intrinsically combines a novel set of key features to achieve the strong coupling regime to the cavity. A low charging energy reduces the device sensitivity to charge noise, while sufficient coupling is provided by the shaping of the spectrum of the double quantum dot by the superconducting reservoir. Our findings could be adapted to many other circuit designs and shed new light on the coupling of superconducting nanoscale devices to microwave fields.

This chapter reproduces an article: *Circuit-QED with a quantum dot charge qubit dressed by Cooper pairs*, published in Phys. Rev. B **98**, 155313. Besides a preliminary version of this work was communicated at the conference ICPS (August 2016) in Beijing and on condmat as arXiv:1612.05214.

## 4.1 Introduction

Circuit quantum electrodynamics (cQED) allows one to probe, manipulate and couple superconducting quantum bits at an exquisite level using cavity photons. Transferring the methods of cavity quantum electrodynamics to quantum dots circuits is appealing for multiple reasons [113]. Electrons confined in quantum dots can be used as quantum bits based on their spin or charge degree of freedom. In the context of quantum information processing, cavity photons were first envisioned as a powerful way to manipulate such quantum bits. Therefore, most experimental efforts [12, 26, 44, 50, 89, 142, 143] have been directed towards achieving the strong coupling regime, which allows one to

hybridize coherently light and matter [97]. To that purpose, tunneling between the double quantum dot and metallic contacts is usually considered as an undesired dissipation channel and minimized.

However, metallic reservoirs can also be seen as a resource, as quantum dot circuits can include a variety of normal metal, ferromagnetic or superconducting electrodes. The engineering of electronic states in devices combining materials with different electronic properties is at the heart of many recent methods put forward for quantum information processing. One particularly promising venue is the coupling of superconductors to nanoconductors. For example, semiconducting nanowires proximized by superconductors are under active investigation because of the possibility to induce non-local superconducting correlations in the topological regime [18, 144]. Double quantum dots with a central superconducting contact are sought for creating distant entangled spins by the splitting of Cooper pairs [23, 24, 65, 74].

Combining cQED architectures with hybrid superconducting mesoscopic circuits is only at its premises. This has been successful in the case of superconducting quantum point contacts, as epitomized by the recent manipulation of an Andreev qubit by a microwave resonator [145]. Looking at hybrid superconductor quantum dot circuits, a single experiment has been reported so far, with a single dot [146].

Here, we present the first implementation of a hybrid superconductor-double quantum dot circuit coupled to a microwave cavity. Such an experiment was theoretically proposed to test the coherence of Cooper pair splitting between the two dots [72, 73]. As we will show below, our circuit operates in a parameter regime where the coherent injection of Cooper pair appears in a different way as was theoretically considered in those references. Nevertheless, our results confirm the idea that cQED tools are a powerful method to probe the spectrum of hybrid superconductor-quantum dot circuits. Surprisingly, our work also demonstrates the reciprocal, namely that adding a superconducting electrode to a double quantum dot circuit can be instrumental in building a strongly coupled mesoscopic cQED system.

As observed in previous experiments, the cavity transmission shows a resonance between the cavity mode and a circuit transition. We find that the behavior of our hybrid double dot is dominated by tunnel coupling between the left and the right dot, which results in a "charge qubit"-like transition. However the cavity transmission reveals the shaping of the

spectrum of the double quantum dot by the superconducting reservoir. This represents the first spectroscopic observation of Cooper pair assisted cotunnelling between the left and the right dot [147–149], in equilibrium conditions. So far this effect had been observed only indirectly through out-of equilibrium transport measurements [25, 150]. We present a theoretical description of the new eigenenergies and eigenmodes of the dressed superconductor-charge qubit. The interplay between bare interdot tunneling and the superconducting proximity effect was not considered in previous derivations of the spectrum of superconductor-double quantum dots. Our theoretical results are validated by their ability to reproduce the very peculiar features of our measurements.

Importantly, the superconductor does not only modify the spectrum but also the electron-photon coupling. In addition to the usual coupling mechanism where cavity photons modulate the energy difference between the two dots, our theoretical model clearly highlights the possibility of coupling via a symmetric modulation of the dot energies. In presence of a superconducting central electrode, such a common mode excitation effectively results in a strong sensitivity of the double dot tunnel barrier to the cavity electric field. This corresponds to the original driving mechanism proposed by DiVincenzo [42, 86–88], which is implemented here for the first time in a cavity.

Our new coupling mechanism is more than a simple curiosity as it actually provides a way to reach the strong coupling regime between the cavity and our modified charge qubit. Such a regime was obtained recently using two different approaches [12, 13]. Mi et al. built their double quantum dot in a low charge noise material, namely SiGe. Stockklauser et al. used a squid array resonator to boost the value of the electron-photon coupling. Here we demonstrate a third approach: the common mode coupling scheme allows us to decrease the charging energy of our device and correspondingly decrease the device sensitivity to charge noise, while keeping a sufficient coupling strength. It is worth noting that the strong electron-photon coupling was also obtained with the spin degree of freedom very recently [53, 55, 151].

This chapter is organized as follows. Section 4.2 presents our experimental setup. Section 4.3 presents our theoretical derivation of the spectrum of the hybrid superconductor-charge qubit in absence of the cavity. Section 4.4 gives and discusses the expression of the coupling of the dressed charge qubit to the cavity. The theoretical description is confronted to experimental data in section 4.5. Section 4.6 shows our experimental

observation of the strong coupling regime. Section 4.7 summarizes our results and gives various perspectives.

Appendices B.1, B.2 and B.3 provide experimental, theoretical and simulation details, respectively.

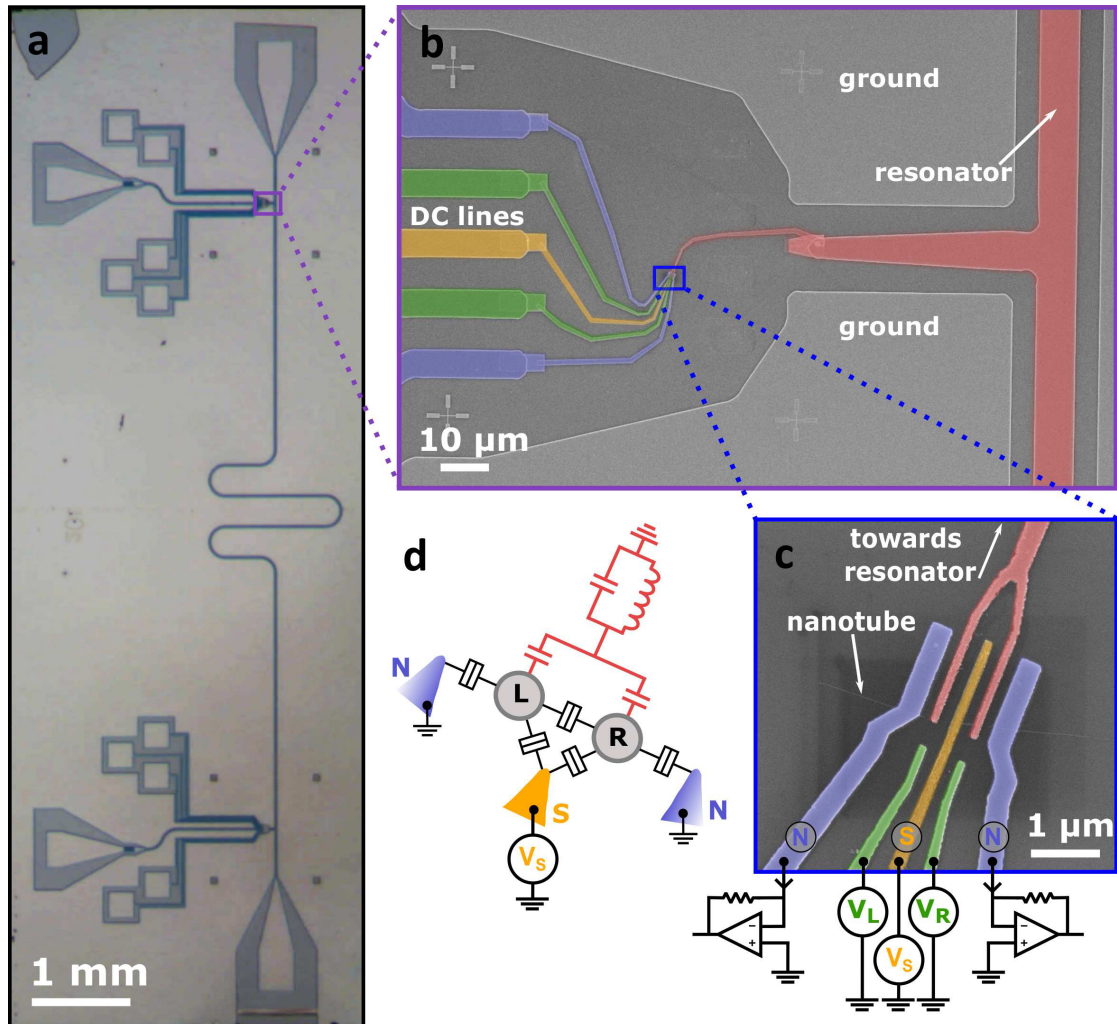


FIGURE 4.1: **a.** Optical photograph of the layout of our cavity QED architecture on a large scale. **b.** and **c.** SEM micrographs of our devices on two different scales in false colours. The ‘fork’ coupling gate is coloured in red. The superconducting electrode is coloured in orange. The normal (non-superconducting) electrodes are coloured blue. The gates are coloured in green. **d.** Circuit diagram of our hybrid double quantum dot highlighting the symmetric coupling scheme between the two dots and the resonator in red.

## 4.2 Sample and Measurement setup

We use carbon nanotube based double quantum dot circuits embedded in a high finesse superconducting microwave cavity [26, 45, 138]. The microwave cavity is a Nb coplanar

waveguide cavity with resonance frequency of about 6.636 GHz and a quality factor of about 16000. Throughout the paper, we describe results obtained with two different devices (sample A and sample B) which had exactly the same layout. Figure 4.1-a, b and c show optical as well as scanning electron microscope pictures of one of our devices. A single wall carbon nanotube is tunnel-coupled to a central superconducting finger (in orange) and two outer non-superconducting electrodes (in blue). Two side gates (in green) are used to tune the double dot energy levels. A finger galvanically coupled to the central conductor of our cavity (in red) is attached to two top gates in a fork geometry. This coupling scheme is markedly different from the double-dot/cavity coupling schemes used so far in that context [12, 13, 26, 44, 50, 89]. Instead of favoring a microwave modulation of the difference of the energy between the left and the right dot, the fork geometry shown in figure 4.1c favors the modulation of the sum of the left and right dot energies by microwave photons.

All the measurements have been carried out at about 18 mK. We simultaneously measure DC transport through the quantum dot device and microwave transmission through the coplanar waveguide resonator. Our control parameters of the quantum dot circuit are the bias voltage  $V_S$  applied to the superconducting electrode and the gate voltages  $V_L$  and  $V_R$ . For convenience, measurements are often taken in the rotated frame  $V_\Sigma$ - $V_\delta$ , as defined in Appendix B.2. Concerning the cavity, the tunable parameters are the frequency and power of the probe tone. Details about sample fabrication and measurement setup are given in Appendix B.2.

From the transport measurement shown in figure 4.2-a we are able to assess the electrical contact between the double dot and a superconducting reservoir. We measure a superconducting gap  $\Delta$  of about  $150\mu\text{eV}$ . The fact that we do not observe any measurable subgap currents indicate that our tunnel barriers are rather opaque. In the following, transport data will be omitted, as it would be blank at most working points (see appendix B.2). However, we will show that cavity signals can be very strong and contain signatures of tunneling processes between the dots and the superconducting lead. This is mainly because the charge qubit transition of a double dot is modified by the superconducting reservoir, as we explain now.

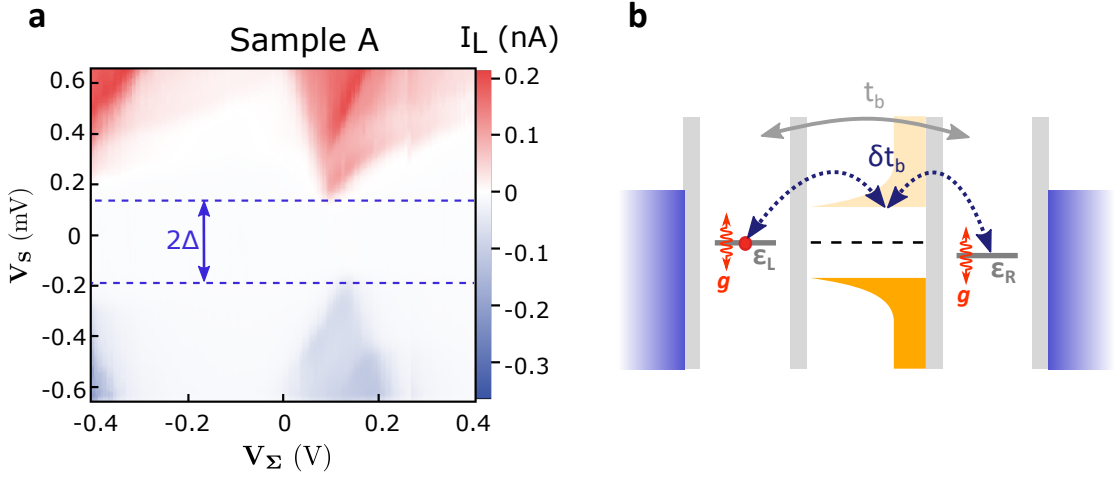


FIGURE 4.2: **a.** Colorscale map of the current  $I_L$  flowing through the left (L) normal metal contact as a function of bias voltage  $V_S$  and the gate voltage  $V_\Sigma$  for sample A. From this map, we read-off a superconducting gap  $\Delta \sim 150\mu\text{eV}$ . **b.** Cotunneling scheme accounting for the renormalization of the hopping constant between the left and the right quantum dot.

### 4.3 Low energy spectrum of the hybrid superconductor DQD in the absence of the cavity

Contrarily to normal contacts, a superconducting contact is expected to modify coherently the spectrum of a double quantum dot. Let us first recall the double dot spectrum in absence of superconductor. The double dot hamiltonian reads:

$$H_{DQD} = \epsilon_L \hat{n}_L + \epsilon_R \hat{n}_R + t_b (c_{L\uparrow}^\dagger c_{R\uparrow} + c_{L\downarrow}^\dagger c_{R\downarrow}) + h.c. \quad (4.1)$$

$$+ U_m \hat{n}_L \hat{n}_R + \frac{1}{2} U_L \hat{n}_L (\hat{n}_L - 1) + \frac{1}{2} U_R \hat{n}_R (\hat{n}_R - 1)$$

where, for each dot  $i \in \{L, R\}$ ,  $\epsilon_i$  denotes the orbital energy,  $U_i$  the charging energy,  $c_{i\sigma}^\dagger$  the electron creation operator with spin  $\sigma \in \{\downarrow, \uparrow\}$ , and  $\hat{n}_i$  the electron number operator. The mutual charging energy between the two dots is  $U_m$  and  $t_b$  is the direct hopping strength between the L and the R dot. Close to the (0,1)/(1,0) degeneracy line, the relevant eigenstates are the antibonding and bonding states:

$$|+\rangle = u |L\rangle + v |R\rangle, |-\rangle = -v |L\rangle + u |R\rangle \quad (4.2)$$

with the eigenenergies:

$$E_\pm = \frac{-U_m + \epsilon_\Sigma \pm \sqrt{\epsilon_\delta^2 + 4t_b^2}}{2} \quad (4.3)$$

Where  $\epsilon_\delta = \epsilon_L - \epsilon_R$ ,  $\epsilon_\Sigma = \epsilon_L + \epsilon_R + U_m$ ,  $u = \sqrt{\frac{1}{2} - \frac{1}{2} \frac{\epsilon_\delta}{\sqrt{\epsilon_\delta^2 + 4t_b^2}}}$  and  $v = \sqrt{\frac{1}{2} + \frac{1}{2} \frac{\epsilon_\delta}{\sqrt{\epsilon_\delta^2 + 4t_b^2}}}$ . This gives a transition energy of the double quantum dot:

$$\hbar\omega_{DQD} = E_+ - E_- = \sqrt{\epsilon_\delta^2 + 4t_b^2} \quad (4.4)$$

We will see below that this quantity is deeply modified by the presence of the superconducting lead.

Figure 4.2-b gives a qualitative picture of the main process responsible for dressing the bonding and antibonding states of a double dot charge qubit. In addition to the bare tunneling between the two dots (grey solid arrow), the superconductor induces cotunneling processes: an electron from one dot can virtually excite a quasiparticle in the superconductor and tunnel to the other dot (blue dotted arrows).

We now outline the formal derivation of the spectrum of the double quantum dot in presence of a superconductor (see Appendix B.1 for details). We start by considering the hamiltonian of our double quantum dot-superconductor device:

$$H = H_{DQD} + H_S + H_{S-DQD}, \quad (4.5)$$

which naturally contains the double quantum dot hamiltonian  $H_{DQD}$  discussed above. Additionally, there is a term describing the quasiparticles in the superconductor:

$$H_S = \sum_{k\sigma} E_k \gamma_{k\sigma}^\dagger \gamma_{k\sigma} \quad (4.6)$$

where  $\gamma_{k\sigma}^\dagger$  ( $\gamma_{k\sigma}$ ) are the creation (annihilation) Bogoliubov quasiparticle operators. Finally,  $H_{S-DQD}$  accounts for electron tunneling between the superconductor and the two dots and can be written:

$$H_{S-DQD} = \sum_{k\sigma, i \in \{L, R\}} t_i^* \mathcal{A}_{k\sigma}^i c_{j\sigma}^\dagger + h.c. \quad (4.7)$$

where  $t_i \equiv \sqrt{\Gamma_{S_i}}$  is the hopping strength between the superconductor and dot  $i$  and  $\mathcal{A}_{k\sigma}^i$  is a linear combination of Bogoliubov operators (formula given in Appendix B.1). At second order in  $t_i$ , the states  $|+\rangle$  and  $|-\rangle$  become coupled to the singlet and triplet states:  $|S\rangle$ ,  $|T_0\rangle$ ,  $|T_+\rangle$ ,  $|T_-\rangle$ , whose energies are, close to the degeneracy line:

$$E_S = E_{T_0} = E_{T_+} = E_{T_-} \simeq \epsilon_L + \epsilon_R + U_m \equiv \epsilon_\Sigma \quad (4.8)$$

The low energy spectrum of the system can be obtained by a Schrieffer-Wolf transformation  $\hat{H} = e^{-S} \hat{H} e^S$  corresponding to tracing out the superconducting quasiparticles. Taking the same path as previous theoretical work on Cooper pair splitters [152, 153] we look for the appropriate S operator which eliminates  $H_{S-DQD}$  to first order, resulting in an effective hamiltonian to second order in the tunnel couplings  $t_i$  of the superconductor to the two dots. While this method is well known, it had so far always been applied to the case of two completely decoupled dots, namely  $t_b = 0$ . By including a finite hopping  $t_b$  between the left and the right dot, our derivation yields novel results, which are crucial to interpret our experimental findings. Projecting the effective hamiltonian on the subspace  $\{|+\rangle, |-\rangle\}$ , we get:

$$\hat{H}_{eff} = (E_+ + \delta E_+) |+\rangle \langle +| + (E_- + \delta E_-) |-\rangle \langle -| + \delta t_b |+\rangle \langle -| + \delta t_b |-\rangle \langle +| \quad (4.9)$$

Below we focus close to the degeneracy line between (0,1)/(1,0) charge states but the (1,1)/(0,2) lines give rise to similar expressions. After tedious but straightforward calculations, the perturbative elements have the following expressions:

$$\begin{aligned} \delta t_b = & (\Gamma_{SR} - \Gamma_{SL}) \frac{t_b}{\sqrt{\epsilon_\delta^2 + 4t_b^2}} \left\{ 4Ln \frac{2\hbar\omega_D}{\Delta} + \pi \frac{U_m}{\Delta} + \frac{U_m^2 + \epsilon_\Sigma^2 + \epsilon_\delta^2 + 4t_b^2}{\Delta^2} \right\} \\ & - \pi t_{eh}^0 \frac{\epsilon_\Sigma}{\Delta} \frac{\epsilon_\delta}{\sqrt{\epsilon_\delta^2 + 4t_b^2}} \left( 1 - \frac{2}{\pi} \frac{U_m}{\Delta} \right) \end{aligned} \quad (4.10)$$

$$\begin{aligned} \delta E_- = & - (\Gamma_{SR} - \Gamma_{SL}) \frac{\epsilon_\delta}{\sqrt{\epsilon_\delta^2 + 4t_b^2}} \left\{ Ln \frac{2\hbar\omega_D}{\Delta} - \frac{\pi}{2} \frac{U_+}{\Delta} + \frac{U_+^2 + \epsilon_\Sigma^2}{\Delta^2} \right\} \\ & - \frac{\pi}{2} \frac{\epsilon_\Sigma}{\Delta} (\Gamma_{SR} + \Gamma_{SL}) \left( 1 + \frac{1}{\pi} \frac{U_+}{\Delta} \right) \\ & - \pi t_{eh}^0 \frac{\epsilon_\Sigma}{\Delta} \frac{t_b}{\sqrt{\epsilon_\delta^2 + 4t_b^2}} \left( 1 + \sqrt{\frac{2|\delta r|}{\pi \xi_0}} \frac{U_+}{\Delta} \right) \end{aligned} \quad (4.11)$$

$$\begin{aligned}
\delta E_+ = & (\Gamma_{SR} - \Gamma_{SL}) \frac{\epsilon_\delta}{\sqrt{\epsilon_\delta^2 + 4t_b^2}} \left\{ Ln \frac{2\hbar\omega_D}{\Delta} - \frac{\pi U_-}{2\Delta} + \frac{U_-^2 + \epsilon_\Sigma^2}{\Delta^2} \right\} \\
& - \frac{\pi \epsilon_\Sigma}{2\Delta} (\Gamma_{SR} + \Gamma_{SL}) \left( 1 - \frac{1}{\pi} \frac{U_-}{\Delta} \right) \\
& + \pi t_{eh}^0 \frac{\epsilon_\Sigma}{\Delta} \frac{t_b}{\sqrt{\epsilon_\delta^2 + 4t_b^2}} \left( 1 - \sqrt{\frac{2|\delta r|}{\pi\xi_0}} \frac{U_-}{\Delta} \right)
\end{aligned} \tag{4.12}$$

where  $t_{eh}^0$  is the Cooper pair splitting amplitude (see Eq. B.9 in Appendix B.1),  $\delta r$  is the distance between tunnel contacts from the superconductor to each dot,  $\xi_0$  is the superconducting coherence length and  $\omega_D$  is the Debye frequency, used as a cut-off. The following notation was introduced:

$$U_\pm = \pm U_m + \sqrt{\epsilon_\delta^2 + 4t_b^2} \tag{4.13}$$

The new eigenenergies are:

$$\tilde{E}_\pm = \frac{E_+ + \delta E_+ + E_- + \delta E_- \pm \sqrt{(E_+ + \delta E_+ - E_- - \delta E_-)^2 + \delta t_b^2}}{2} \tag{4.14}$$

which leads to a new transition energy of the form:

$$\hbar\omega_{S-DQD} = \sqrt{(\epsilon_\delta^2 + 4t_b^2)Z(\epsilon_\delta, \epsilon_\Sigma)^2 + t(\epsilon_\delta, \epsilon_\Sigma)^2}, \tag{4.15}$$

with

$$Z(\epsilon_\delta, \epsilon_\Sigma) = 1 + \frac{\delta E_+ - \delta E_-}{E_+ - E_-} \tag{4.16}$$

and:

$$t(\epsilon_\delta, \epsilon_\Sigma) = \delta t_b \tag{4.17}$$

It is important to notice here the major modification induced by the superconductor: the transition energy of the circuit does now also depend on the sum of the two dot energies  $\epsilon_\Sigma$ , rather than only on their difference  $\epsilon_\delta$ .

Before concluding this section, we would like to point out that the calculation is essentially the same if there is an additional quantum number (e.g. a valley quantum

number) ruling the states of the double quantum dot. This naturally leads to a second transition similar to the one considered above but with different parameters. This can account for the two transition structure which is used to understand quantitatively our experimental findings.

#### 4.4 Electron-photon coupling of the hybrid DQD

We now evaluate the effect of the superconductor on the coupling to the cavity. The conventional coupling mechanism of a double quantum dot to the cavity in the absence of the superconductor takes the form (cf: formula 2.6):

$$\langle + | (g_L \hat{n}_L + g_R \hat{n}_R) (\hat{a} + \hat{a}^\dagger) | - \rangle = uv (g_L - g_R) (\hat{a} + \hat{a}^\dagger) \quad (4.18)$$

where  $\hat{a}$  is the annihilation operator of the photonic cavity mode.

This leads to the usual coupling mechanism of a double quantum dot to a cavity mode which vanishes in case of a symmetric coupling ( $g_L = g_R$ ), ie L and R orbitals couple equally to the cavity electric field. However, the superconductor gives rise to a new coupling mechanism which works also in case of symmetric coupling. In order to evaluate it, one can still rely on the Schrieffer-Wolf transformation by including formally the operator  $(\hat{a} + \hat{a}^\dagger)$  into the derivation and expanding in powers of  $g_L + g_R$  (since one assumes that  $g_L - g_R \ll g_L + g_R$ ). To first order, this adds a term of the form:

$$2 \frac{\partial \delta t_b}{\partial \epsilon_\Sigma} (g_L + g_R) (\hat{a} + \hat{a}^\dagger) \quad (4.19)$$

It is important to note that although the above expression is in principle perturbative, it can in fact be much larger than the usual coupling term since in case of symmetric or nearly symmetric coupling ( $g_L - g_R \ll g_L + g_R$ ). One can note that this “common mode” coupling mechanism is in fact not restricted to our situation but would hold for any double quantum dot with a tunable barrier [42]. In our case, since the energy scale ruling the barrier tunability is the superconducting gap which is smaller than the semiconducting gaps of usual semiconducting materials, our tunability is very efficient. Finally, the effective Hamiltonian of our device in cavity, projected on the  $|+\rangle, |-\rangle$  states

reads:

$$\hat{H}_{eff,c} = \hat{H}_{eff} + \hbar\omega_{cav}\hat{a}^\dagger\hat{a} + \hat{H}_{Baths} + \hbar\tilde{g}(|+\rangle\langle-| + |- \rangle\langle+|)(\hat{a} + \hat{a}^\dagger) \quad (4.20)$$

With the following coupling strength:

$$\begin{aligned} \tilde{g} \approx & (g_L - g_R) \frac{2t_b}{\sqrt{\epsilon_\delta^2 + 4t_b^2}} \\ & + (g_L + g_R) \frac{4t_b}{\sqrt{\epsilon_\delta^2 + 4t_b^2}} \frac{\Gamma_{SR} - \Gamma_{SL}}{\Delta} \frac{\epsilon_\Sigma}{\Delta} \\ & - (g_L + g_R) \pi \frac{t_{eh}^0}{\Delta} \frac{2\epsilon}{\sqrt{\epsilon_\delta^2 + 4t_b^2}} \end{aligned} \quad (4.21)$$

The above equation contains three different terms: the first is the usual coupling term between a double quantum dot bonding/anti-bonding transition and a microwave cavity which needs to have asymmetric  $g_L$  and  $g_R$ . The second term corresponds to the fact that the superconductor renormalizes the energy levels of each dot with a strength proportional to each tunnel coupling  $\Gamma_{SL(R)}$ . It corresponds to an indirect Cooper pair assisted tunneling modulation between the two dots. The last term arises from the direct modulation of the Cooper pair assisted tunneling between the two dots by the cavity photons. The two last terms only exist in the presence of a superconductor. In the next section, we will illustrate with experimental values that the “common mode ” coupling mechanism can yield a sizable electron-photon coupling strength.

## 4.5 Resonant interaction between the hybrid DQD and the cavity

The interaction between our hybrid double quantum dot and the cavity photons is conveniently probed by measuring the microwave signal transmitted through the cavity. Figure 4.3-a and 4.3-b (resp. 4.3-c and 4.3-d) display the phase (resp. amplitude) contrasts for sample A for two different gate voltage tunings called Aa and Ab. The avoided crossing lines are characteristic of a double dot stability diagram and correspond to tunneling between the dots and the leads. We focus now on the most striking features, which lie within the area delimited by the avoided crossing. In figure 4.3-a, one observes

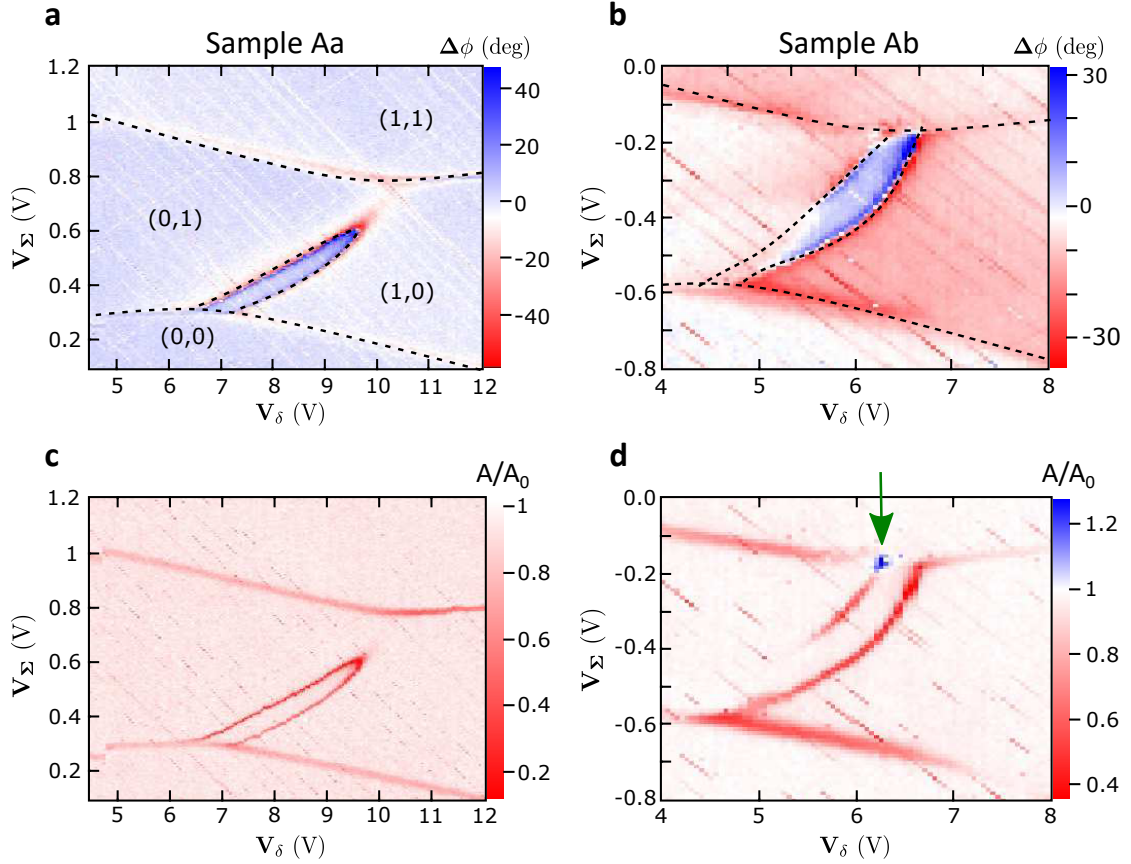


FIGURE 4.3: **a.** and **b.** (resp. **c.** and **d.**) Microwave phase contrasts (resp. amplitude) maps at the bare resonator frequency  $f_c$  for sample A for two different gate voltage tunings (labeled Aa and Ab) as a function of the gate voltages. The charge occupation  $(i,j)$  of the double dot is indicated in panel a. The sign changes demonstrate resonant interaction between the hybrid double quantum dot and the cavity photons. The elongated 0 phase line demonstrates the dependence of hopping with  $\epsilon_\Sigma$ . The black dashed lines were obtained from theoretical expressions for the conditions  $\omega_{cav} = \omega_{S-DQD}$  and  $E_N = E_{N+1}$  with parameters given in the main text. In panel d, the blue dot indicated by a green arrow is the sign of photon gain.

a “crescent” shaped 0 phase contour line with a phase shift spanning from  $-40^\circ$  to  $+40^\circ$ . These features are similar for sample Ab presented in figure 4.3-b although the “crescent” shape is cut by the electron lead transition lines. Similar to what has already been observed in double quantum dot setups[26, 44, 50, 89], the sign change of the phase contrast signals a resonant interaction between a transition involving one or two electrons on the double dot and the cavity photons. Specifically, the cavity provides a “cut ” of the dispersion relation of the circuit spectrum [26]. The contour line for  $0^\circ$  corresponds to the resonant condition:  $\omega_{cav} \approx \omega_{S-DQD}$ , where  $\omega_{cav}$  is the cavity resonance frequency and  $\omega_{S-DQD}$  is the hybrid double quantum dot resonance frequency. However, in contrast with the standard double quantum dot response, the resonance contour line is not along the zero-detuning line  $\epsilon_\delta = 0$  between the left(L)

and the right(R) dot, but is distorted in the perpendicular direction. This means that the transition frequency of our circuit does not only depend on  $\epsilon_\delta$ , but also on the average energy of the two dots  $\epsilon_\Sigma = \epsilon_L + \epsilon_R + U_m$ . Qualitatively, this agrees with the theoretical expression for the transition frequency which we derived in section 4.3 from a microscopic theory of our hybrid superconductor-double quantum dot:

$$\hbar\omega_{S-DQD} = \sqrt{(\epsilon_\delta^2 + 4t_b^2)Z(\epsilon_\delta, \epsilon_\Sigma)^2 + t(\epsilon_\delta, \epsilon_\Sigma)^2} \quad (4.22)$$

The crescent shape of the transition line can be recast from the dependence of the functions  $Z$  and  $t$  on  $\epsilon_\delta$  and  $\epsilon_\Sigma$  (see formulas 4.16 and 4.17). As shown in figure 4.4-a, the transition frequency map expected from the theory as a function of  $\epsilon_\delta$  and  $\epsilon_\Sigma$ , displayed in light brown is cut by the blue plane at the cavity frequency. This results naturally in a crescent shaped transition frequency contour line.

All these experimental signatures can be captured more quantitatively by an input-output formalism of the coupled equations of the cavity field in the semiclassical limit and the electronic degrees of freedom [113, 146]. Specifically, the transmission  $t$  through the cavity reads:

$$t = \frac{\sqrt{\kappa_L \kappa_R}}{\omega - \omega_{cav} - i\kappa/2 + g^2 \chi_{dot-dot}(\omega) + g_c^2 \chi_{dot-lead}(\omega)} \quad (4.23)$$

where  $\kappa_L$  (resp.  $\kappa_R$ ) is the photon loss rates through the left (resp. right) coupling ports of the resonator and  $\kappa$  is the total cavity photon loss rate. The bare cavity transition is modified by  $\chi_{dot-dot}(\omega)$  (the charge susceptibility associated to internal transitions of the circuit), and  $\chi_{dot-lead}(\omega)$  (the charge susceptibility associated to electronic transitions between the dot and the leads). In our case, these susceptibilities read:

$$\begin{aligned} \chi_{dot-dot}(\omega) &= \frac{1}{\omega - \omega_{S-DQD} - i\Gamma/2} \\ \chi_{dot-lead}(\omega) &= \frac{1}{1 - i\omega/\gamma} \frac{\hbar}{4k_B T \cosh\left(\frac{E_N - E_{N+1}}{2k_B T}\right)} \end{aligned} \quad (4.24)$$

where  $\Gamma$  is the decoherence rate of the internal transition of the DQD and  $E_N$  is energy of the DQD for  $N$  charges in total. The  $\chi_{dot-dot}(\omega)$  susceptibility can give the strong electron-photon coupling if  $g > \Gamma, \kappa$ . This susceptibility yields a resonance in the transmission  $t$  when  $\omega_{cav} = \omega_{S-DQD}$  and allows to map the dispersion relation of our hybrid DQD. The  $\chi_{dot-lead}(\omega)$  susceptibility is resonant when  $E_N = E_{N+1}$  and allows to map the stability diagram of the DQD. We display in figure 4.3-a and 4.3-b the theory for the lines  $\omega_{cav} = \omega_{S-DQD}$  and  $E_N = E_{N+1}$  in black dashed lines, using the following parameters: besides the measured value  $\Delta/h = 37.5$  GHz (see figure 4.2-a), we have for sample Aa:

$$t_b/h = 6.3 \text{ GHz}$$

$$\Gamma_{SR}/h = 400 \text{ MHz}$$

$$\Gamma_{SL}/h = 900 \text{ MHz}$$

$$t_{eh}^0/h = 400 \text{ MHz}$$

$$U_L/h = 29 \text{ GHz}$$

$$U_R/h = 71 \text{ GHz}$$

$$U_m/h = 16 \text{ GHz}$$

and for sample Ab, we have:

$$t_b/h = 5.5 \text{ GHz}$$

$$\Gamma_{SR}/h = 330 \text{ MHz}$$

$$\Gamma_{SL}/h = 900 \text{ MHz}$$

$$t_{eh}^0/h = 350 \text{ MHz}$$

$$U_L/h = 32 \text{ GHz}$$

$$U_R/h = 42 \text{ GHz}$$

$$U_m/h = 24 \text{ GHz}$$

The quantitative agreement with the  $\omega_{cav} = \omega_{S-DQD}$  (internal) transition lines validates the low energy spectrum of our device and is the first direct observation of Cooper pair assisted tunneling between two quantum dots.

Noticeably, the renormalization of the hopping between the two dots is related to the

Cooper pair splitting amplitude  $t_{eh}^0$  (see section 4.4). Therefore, we can extract a value for  $t_{eh}^0/h = 400$  MHz even without direct observation of Cooper pair splitting. Our measurement demonstrates that cavity photons can be used to probe very small energy scales, inaccessible to transport, related to superconducting proximity effect in quantum dots. Such a scheme could be generalized to superconducting hybrid structures with topological properties.

Additionally, it is important to notice that the dependence of  $t(\epsilon_\delta, \epsilon_\Sigma)$  upon  $\epsilon_\Sigma$  yields a new light-matter coupling term for our device as shown in the previous section. This follows the original Loss and DiVincenzo proposal [42, 86–88] and recent cavity-double quantum dot coupling proposals [154–156]. Our work provides the first example of this common mode coupling to a microwave cavity. Indeed, in the Bloch sphere representation of figure 4.4-b, the north and south poles are more along the detuning axis  $\epsilon_\delta$  and the light-matter coupling indicated by a red arrow is mainly along the tunnel coupling axis, in stark contrast with the usual case for double quantum dots [12, 13, 26, 44, 50, 89], where it is along  $\epsilon_\delta$ . The electron-photon coupling strength is controlled by the sum  $g_L + g_R$  which can easily be of the order of  $2\pi \times 100$  MHz, as shown for example in reference [146], which is a large magnitude. Using expression 4.21 of section 4.4 with the circuit parameters of sample Aa given above, we get along the crescent contour a  $\tilde{g}$  between  $2\pi \times 1$  MHz ( $\epsilon_\delta \approx 0$ ,  $\epsilon_\Sigma \approx \Delta/2$ ) and  $2\pi \times 4.7$  MHz ( $\epsilon_\delta \approx 2t_b$ ,  $\epsilon_\Sigma \approx 0$ ). This shows that the “common mode” coupling mechanisms can yield a sizable electron-photon coupling strength, even if it originates from second order tunneling through the superconductor.

Finally, we briefly comment on an interesting feature of our light-matter interface which appears on figure 4.3-d. The amplitude map displays a “bright” spot, in blue, corresponding to photon gain (of about 1.3). Microwave photon emission from quantum dot circuits was recently investigated in double quantum dots [105, 157–159] and hybrid superconductor single quantum dot [146]. It is interesting to see that it also appears in our hybrid double quantum dot circuit, although we did not study this effect quantitatively. Qualitatively, it is consistent with having a coherent interface. In the next session, we show an even more striking consequence of the high cooperativity of our device, namely the vacuum Rabi splitting of the cavity when it is brought into resonance with the DQD transition properly tuned.

## 4.6 Strong coupling

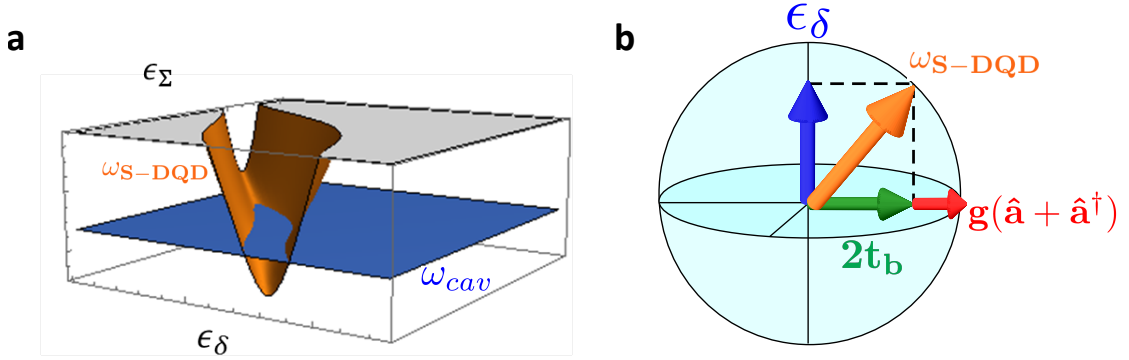


FIGURE 4.4: **a.** Diagram of the transition map of the hybrid double quantum dot intersecting with the cavity resonance frequency. This results in the phase contrast maps of figure 4.3-a and 4.3-b. The axis are the orbital detuning  $\epsilon_\delta$  and the average orbital energy  $\epsilon_\Sigma$  of the double dot. **b.** Bloch sphere diagram depicting the active states of our hybrid double quantum dot and the tunable hopping strength. This symmetric coupling scheme is crucial for the strong electron-photon coupling.

In the previous section, we have focused on characterizing our hybrid double dot circuit, using the microwave resonator as a spectroscopic probe. However, looking at the large phase and amplitude contrasts measured in figure 4.3, one can wonder what happens to the cavity spectrum when the cavity is resonant with the DQD circuit transition. We tune the double dot gate voltages to the point of maximum phase contrast and there, we measure the resonator transmission as a function of frequency (supplementary data in appendix B.2). The top panel of figure 4.5-a shows the result of the measurement for sample B, for which we measured the strongest effect. We observe a splitting of the order of 10 MHz in the cavity resonance for an average number of photons  $\bar{n}$  of about 1. This observation persists down to the lowest input power which corresponds to  $\bar{n} \ll 1$ . This is the hallmark of a vacuum Rabi splitting which indicates the strong coupling between our hybrid double quantum dot and the microwave cavity photons. The fact that we observe this splitting implies that the coupling strength  $g$  between the circuit transition and the cavity is larger than half the linewidth of the cavity  $\kappa/2$  and half the linewidth of the double quantum dot transition involved  $\Gamma/2$ . The intrinsic linewidth of the cavity can be directly measured from the transmission spectrum when the double dot is detuned and is  $\kappa/2\pi = 0.5$  MHz. Therefore, the linewidth of the double dot transition can be inferred from the linewidth of each peak observed in figure 4.5-a, of about 3 MHz. For the simplest case of a single transition [97], the linewidth is equal to  $(\Gamma/2\pi + \kappa/2\pi)/2$ . This would lead to  $\Gamma/2\pi \sim 5.5$  MHz. In order to account

quantitatively for the observed transmission spectrum (and in particular for the very low transmission maximum), we can rely on a two transition scheme (one very coherent, one less coherent). Using a modeling based on two independent transitions depicted in figure 4.5-b, we are able to fit the data using a fully quantum numerical code (QuTip, see Appendix B.3 for details). The use of two transitions anticipates on the existence of a K/K' valley degree of freedom commonly observed in nanotubes. We use the following parameters  $g_K=2\pi\times 4.6$  MHz,  $\Gamma_K=2\pi\times 2$  MHz,  $g_{K'}=2\pi\times 16.8$  MHz,  $\Gamma_{K'}=2\pi\times 100$  MHz (see Table B.1 in Appendix B.3 for all the parameters). It is important to note here that the K/K' valleys are in general coupled by weak disorder in carbon nanotubes [3]. Therefore, the K/K' eigenstates correspond to linear combinations of the original (degenerate) valley states. Their coupling to the field and decoherence rates are therefore different in general. As one can see in Table B.1, a low coupling strength is accompanied by a low decoherence rate (K mode) whereas a large coupling strength is accompanied by a large decoherence rate (K' mode).

As expected for a few level system, we are able to saturate the transitions and to recover the bare transmission of the cavity by injecting a large number of photons inside the cavity. In the present case, this saturation occurs for  $\bar{n} \approx 100$ . As shown in figure 4.5-c, there is a continuous evolution from the vacuum Rabi splitting to a single off-centered lorentzian peak from  $\bar{n} \approx 0.1$  to  $\bar{n} \approx 300$ . Such a peculiar saturation is well reproduced by the QuTip numerical simulation and arises from the two transition structure mentioned above. Note that the splitting at low power is slightly smaller (about 6 MHz) in figure 4.5-c than in figure 4.5-a because this measurement was done for a different working point of our device.

Reaching the strong coupling regime with an excitation, which is primarily charge-like is non-trivial and has been the main challenge of the mesoscopic cQED community for years until recently. The main limitation of all the charge qubit like setups in cavity is the linewidth of the double dot transition which is typically reported to be at least in the few 100 MHz range [44, 50, 89]. One important decoherence source explaining such a large linewidth is the background charge noise. One can think of several strategies to overcome this difficulty. One possible path is to reduce the charge noise in the material. Recently, this idea was successfully implemented by Mi et al in a SiGe based two-dimensional electron gas double quantum dot [12], with a linewidth  $\Gamma/2\pi = 2.6$  MHz lower than the coupling  $g/2\pi = 13.4$  MHz. An alternative strategy to reach the strong coupling

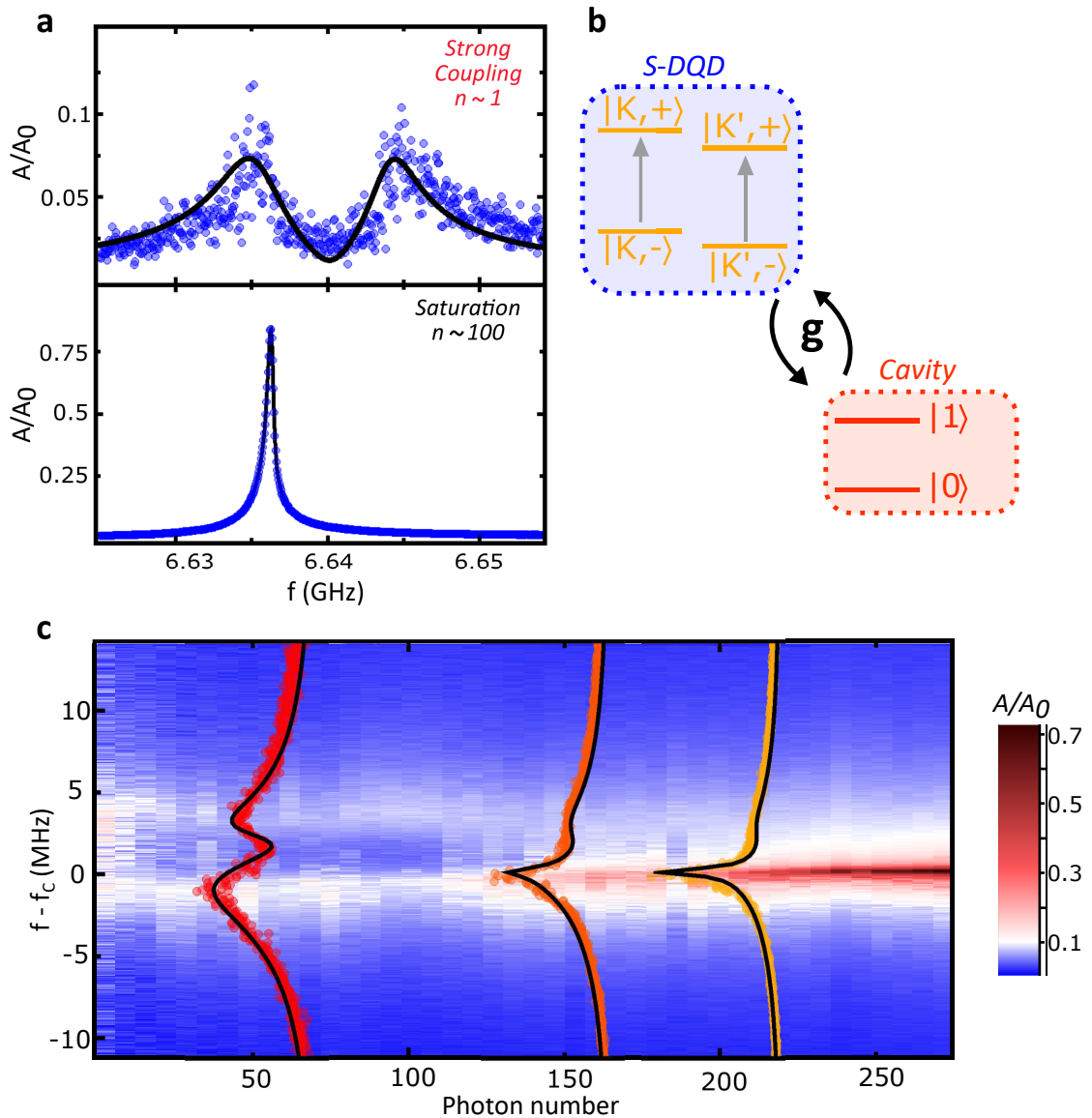


FIGURE 4.5: **a.** Top panel: Vacuum Rabi splitting for sample B with  $n \sim 1$  photon. Bottom panel: Saturation of the mode splitting for a large number of photons. The open blue circles are the data points and the black solid line is the theory. **b.** Level structures explaining the strong coupling and its power dependence. The K, K' labels indicate the valley degree of freedom arising from the band structure of carbon nanotubes. **c.** Power dependence of the mode splitting showing the gradual saturation of the coherent transition. Each cut can be fitted using the fully quantum light-matter interaction theory (QuTip).

regime despite the presence of large charge noise was demonstrated by Stockklauser et al. [13]: by using a squid array resonator, the electron-photon coupling was increased to  $g/2\pi = 238$  MHz, which exceeds the DQD charge qubit linewidth  $\Gamma/2\pi = 93$  MHz. Our ability to reach the strong coupling regime relies on a third approach, namely reducing our qubit linewidth by reducing the device sensitivity to charge noise. In this scheme, our specific common mode coupling mechanism plays a crucial role to keep a sufficient coupling strength. Now we successively detail each of these two key ingredients.

In presence of the noise spectral density  $S(f) = \langle \delta n^2 \rangle / f$ , where  $f$  is the frequency, the dephasing rate  $\Gamma_\varphi$  of the double dot can be expressed as:

$$\Gamma_\varphi \approx \frac{\partial \omega}{\partial \epsilon} E_C \sqrt{\langle \delta n^2 \rangle} + \frac{1}{2} \frac{\partial^2 \omega}{\partial \epsilon^2} E_C^2 \langle \delta n^2 \rangle + \dots \quad (4.25)$$

which is strongly influenced by the charging energy  $E_C \sim e^2/C_\Sigma$ , where  $C_\Sigma$  is the total capacitance of the device [50, 83, 119, 160]. The expression of  $\Gamma_\varphi$  takes the above simple form only if the transition frequency  $\omega$  depends on a single parameter  $\epsilon$ . This is the case for the standard double quantum dot charge qubit transition  $\omega_{DQD}$ , which dispersion relation is governed by  $\epsilon_\delta$ . In our case, the expression of  $\Gamma_\varphi$  is more complex since it involves all the derivatives of the transition  $\omega_{S-DQD}$ , with respect to its control parameters  $\epsilon_\delta$  and  $\epsilon_\Sigma$ . Nevertheless, its dependence as a function of the total charging energy and the transition frequency derivatives remains qualitatively the same. The points where all the first order derivatives vanish are called sweet spots [154–156] because the double dot is insensitive at first order to charge noise. The usual method to reduce  $\Gamma_\varphi$  is therefore to operate the system close to a sweet spot which implies that only the second order terms are present in the expression of  $\Gamma_\varphi$ . To reduce the second order term at constant noise density and without engineering the dispersion relation [161], it is a priori very efficient to go towards small charging energy, in analogy with the transmon qubit [119]. The charging energy of sample A and B can simply be read-off from the transport stability diagram which is shown in figure 4.2-a for sample A. Due to the fork-shaped top gates that increase the capacitance to the ground, our charging energy is 2 meV, about 10 times smaller than what we find typically for similar devices with a conventional top gate setting [26, 50]. Since  $\Gamma_\varphi/2\pi \approx 400$  MHz in those conventional settings, a reduction of 10 of  $E_C$  is expected to reduce  $\Gamma_\varphi$  by a factor of 100, i.e.  $\Gamma_\varphi/2\pi \approx 4$  MHz, which is consistent with the order of magnitude of  $\Gamma/2\pi \sim$  few MHz inferred from the cavity spectroscopy of figure 4.5-a.

Importantly, this reduction of  $E_C$  also implies a decrease of the lever arm between the orbital energies  $\epsilon_L$ ,  $\epsilon_R$  of the dots and the cavity potentials. The coupling of photons through the variable  $\epsilon_\delta$  used in former experiments [26, 44, 50, 89] thus becomes too small to be exploited. However, our hopping  $t(\epsilon_\delta, \epsilon_\Sigma)$  is tunable with the parameter  $\epsilon_\Sigma$ , which is naturally more strongly coupled to the cavity potential than  $\epsilon_\delta$ . This compensates the decrease of  $E_C$  and gives us a large charge-photon coupling strength of about  $2\pi \times 10$  MHz which allows us to reach the strong coupling regime.

## 4.7 Conclusion

We have presented the first experimental study of a hybrid superconductor-double quantum dot in a microwave cavity. The resonant interaction between cavity photons and a charge qubit-like transition of our circuit reveals a peculiar dispersion map as a function of the dot gate voltages. We are able to interpret our data by theoretically deriving the device energy level structure, which is dressed by cotunnelling processes between the left and the right dot induced by the superconductor. This is the first direct observation of Cooper pair assisted cotunneling in a double quantum dot. Due to its relation to the Cooper pair splitting, we are able to extract a value for  $t_{eh}^0/h \sim 400$  MHz, which is inaccessible to transport measurements. A natural perspective of our work is to use the theoretical and experimental tools developed here to study the same type of device with a more transparent superconducting contact, i.e. with larger  $t_{eh}^0$ . In principle, such a regime would allow to study the physics of Cooper pair splitting more directly [72, 73]. The same methods could also be instrumental to the study of Majorana bound states through microwave cavities [162, 163].

Importantly, our novel qubit design demonstrates a new way of reaching the strong electron-photon coupling based on a tunable hopping barrier and a low charging energy. These ingredients are very generic and could be used in many other setups [154–156]. In our case, the tunable hopping is due to the use of a hybrid superconductor double quantum dot setup, thanks to superconductor induced cotunneling processes. However, using local gates, one could also engineer a direct electrostatic control over the hopping strength. Our findings open the path for entanglement of individual electron states [164] and teleportation of electronic entanglement over macroscopic distances.



## Chapter 5

# Carbon nanotube platform for spin qubit

We use a circuit QED spin-photon interface to drive a single electronic spin in a carbon nanotube based double quantum dot using cavity photons. The microwave spectroscopy allows us to identify an electrically controlled spin transition with a decay rate which can be tuned to be as low as 250kHz. By performing time domain manipulations via pulses in the cavity field, we demonstrate a Rabi decay time of about  $2\mu s$ . We also extract both the spectral linewidth and spin-photon coupling attributed to this transition, allowing us to establish a decoherence model and identify an optimal operating point. These coherence properties, which are attributed to the use of pristine carbon nanotubes stapled inside the cavity, should enable coherent spin-spin interaction via cavity photons and compare favorably to the ones recently demonstrated in Si-based circuit QED experiments.

## 5.1 Highly coherent spin transition

### 5.1.1 Introduction

Spins confined in quantum dots are considered as a promising platform for quantum information processing [42]. While many advanced quantum operations have been demonstrated, experimental as well as theoretical efforts are now focusing on the development of scalable spin quantum bit architectures. One particularly promising method relies on the coupling of single spins to microwave cavity photons [26]. This would enable the coupling of distant spins via the exchange of virtual photons [83, 165–167] for two qubit gate applications, which still remains to be demonstrated with spin qubits.

Very recently, the observation of strong coupling between the charge or the spin confined in a quantum dot circuit and cavity photons has been reported [12–14, 53, 55, 151], bringing closer the demonstration of distant spin-spin interaction. One critical parameter of a spin-photon platform is the linewidth of the spin transition which sets the maximum number of coherent swap operations between a spin and a photon. Whereas they are well documented in Si or GaAs, the coherence properties of single electronic spins in carbon nanotubes are still debated [3, 168].

Here, we use a spin qubit scheme based on a carbon nanotube embedded in a microwave cavity. Our device is made using a stapling technique developed for cQED architectures,

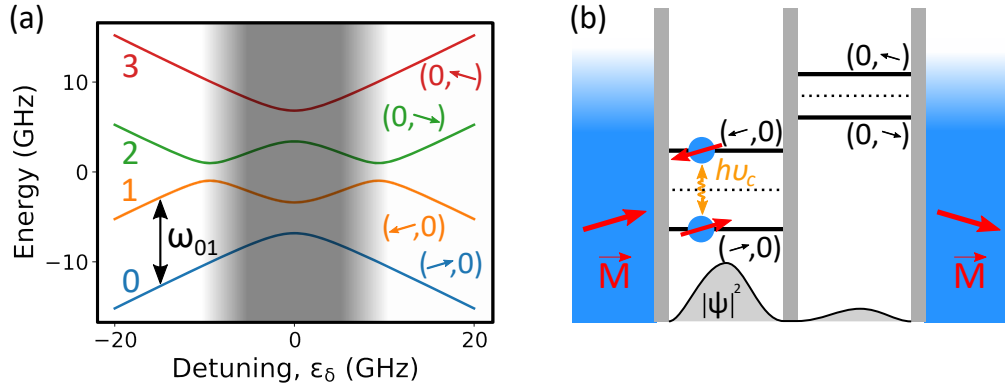


FIGURE 5.1: **Spin-qubit spectrum:** **a.** One electron spectrum of the ferromagnetic spin qubit as a function of the detuning between the two dots energies:  $\epsilon_\delta$ . In this work, we address the 01 transition in the large detuning region (black arrow). **b.** Schematic of the double quantum dot electronic states, showing the concept of the spin-photon coupling. When the energy difference between the two dots is such that one electron is mostly localized on one dot but slightly spread over the other one, the DQD-dipole modulation due to cavity photons allows to manipulate this electron spin.

which produces ultraclean double quantum dot devices with near-ideal spectra. We use the circuit QED platform to perform a microwave spectroscopy of the spin transition as well as time domain experiments. We observe the characteristic dispersion of the spin transition of our spin qubit. When the qubit states are tuned to be almost pure spin states (at large detuning, see figure 5.1-a), the measured decoherence rate is found to be as low as 250kHz. Strikingly, such a figure of merit is more than 100 times better than in previous work on carbon nanotubes [3, 168] and compares favorably to the very recent values reported for Si based devices in a circuit QED environment [53, 55]. From the gate dependence of the decoherence rate, we show that the charge noise is the main source of decoherence for the spin at low detuning, but that it can be made negligible compared to nuclear spin induced noise at large detuning.

### 5.1.2 Working principle

The principle of our spin photon coupling relies on two non-collinear Zeeman fields on each quantum dot (see figure 5.1-b and 5.2-c) in a double quantum dot, originating from zig-zag shaped ferromagnetic contacts. These non-collinear Zeeman fields can be achieved by interface exchange fields [83] or by stray magnetic fields [166, 169] which both give the same hamiltonian. In our case, the interface exchange fields a priori dominate [26]. In the adiabatic regime, if an electronic spin is located on the left dot, it aligns along the left spin quantization axis whereas if it is located on the right dot,

it aligns along the right spin quantization axis. Since the two dots are separated by few hundreds of  $nm$ , there is a large (mesoscopic) electric dipole between the left and the right dots which is given to the spin thanks to the non-collinear magnetizations. The photons of the cavity convey an electrical field which couples to this electric dipole and therefore to the spin. An alternative wording is to state that the ferromagnetic electrodes give rise to a two-site artificial spin orbit coupling, which makes the spin sensitive to the cavity electric field [26]. It is interesting to note that such an "orbitally" mediated spin-photon coupling allows one to increase the natural spin-photon coupling by about 5 orders of magnitude [26, 53, 55] without degrading substantially the inherent good coherence properties of a single spin if the device is used in the limit where the electron is trapped almost completely in one of the two dots (left or right). This can be achieved by detuning the left gate with voltage  $V_L$  from the right gate with voltage  $V_R$ , as sketched in figure 5.1-b. At this working point, the charge noise sensitivity of the spin-qubit is low because of the energy dispersion but keeps a large coupling to the cavity field [83, 169].

### 5.1.3 Nano-fabrication

Our devices are made with a complete dry transfer nanotube technique adapted from previous works [41, 121, 170–172] which allows us to integrate as-grown carbon nanotubes in a microwave cavity. The full chip, comprising the cavity, the bottom gates and the non-collinear ferromagnetic contacts shown in figures 5.2-a, 5.2-b, and 5.2-c respectively, is placed in a vacuum chamber with a base pressure of  $5 \times 10^{-7} mbar$ . The zig-zag contacts visible in figure 5.2-b and partially in figure 5.2-c are NiPd ferromagnetic contacts with transverse magnetization [26]. Carbon nanotubes are grown on a Si comb with a standard Chemical Vapor Deposition (CVD) recipe with  $CH_4$  as feedstock gas.

The comb is mounted inside the chamber on a stage with micro- and nano-manipulators which allow us to place the nanotube on the chip with controlled approach steps of about 100nm. The assembly of the carbon nanotube and the ferromagnetic contacts is done under vacuum in order to ensure a clean interface. This results in the device shown in figure 5.2-c where a nanotube bridges the two ferromagnetic contacts and is a priori suspended over bottom gates. The wider gate visible in the SEM picture of figure

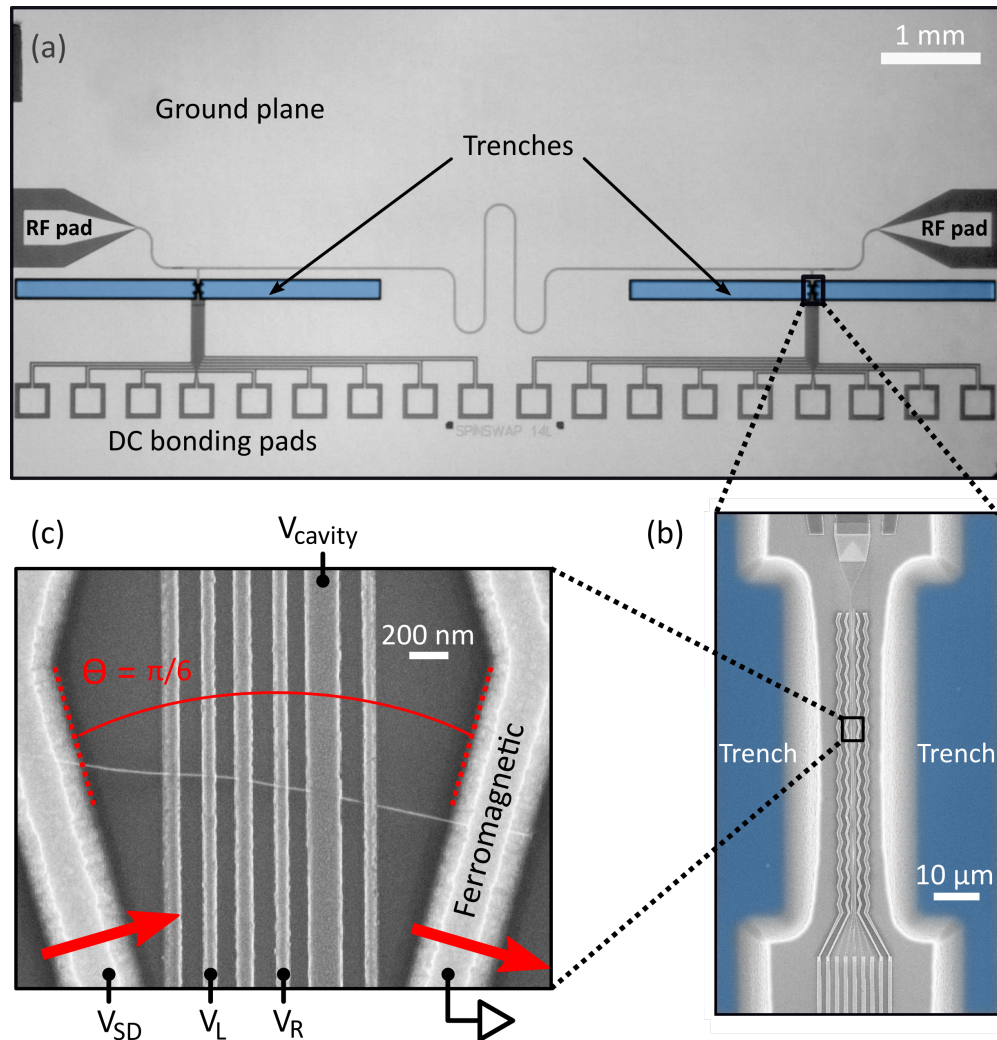


FIGURE 5.2: **circuit-QED device with a carbon nanotube spin-qubit:** **a.** Large scale view of our circuit QED setup. Two carbon nanotubes spin qubits can be integrate in such a geometry, in between the two pairs of trenches (shaded blue). **b.** Scanning electron micrograph of one of the two spin-qubit region. The circuit is realized in between two trenches  $15\mu m$  deep, enabling the insertion of the carbon nanotube. **c.** Zoom on the embedded carbon nanotube showing the two non-collinear ferromagnetic contacts, and the array of gates below the suspended carbon nanotube.

5.2-c is galvanically coupled to the central conductor of the Nb cavity visible in figure 5.2-a. The cavity fundamental resonance frequency is  $6.424GHz$  and its quality factor is about 4200. In the double quantum dot regime, each ferromagnetic contact in our device polarizes one quantum dot. This generates the spectrum depicted in figure 5.1-a [83, 169].

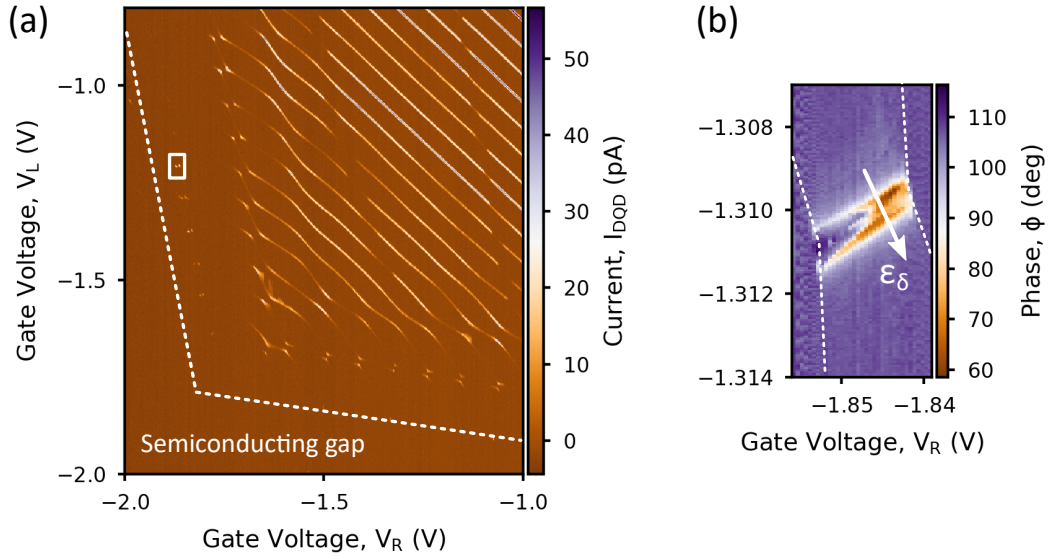


FIGURE 5.3: **Charge stability diagram of the double quantum dot:** **a.** Current measured through the spin-qubit circuit as a function of the left gate  $V_L$  and the right gate  $V_R$ . The Semiconducting gap of the carbon nanotube is visible in the bottom left corner. This indicates that the two dots are negatively charged. **b.** Phase of the transmitted cavity signal measured in the gate-gate region indicated by the white square in **a.** In this region left/right tunneling transition occurs and manifests in the strong phase shift.

#### 5.1.4 Stability diagram

The devices obtained with our fabrication technique are more tunable than previous nanotube based spin quantum bits and much less disordered [26]. The measurement setup is similar to the setup of ref. [26]. We measure simultaneously the DC current  $I$  flowing through the device and the microwave signal transmitted through the cavity in amplitude  $A$  and phase  $\phi$ . The control which we have on the spectrum of the device is visible from the stability diagram shown in figure 5.3-a which displays the current under a bias of  $V_{SD} = 100\mu V$ . Several features indicate very weak disorder and electrostatic control of the potential landscape of confined electrons via the bottom gates: a clear "electron-electron quadrant" delimited by the semiconducting gap controlled by two of the bottom gates ( $V_L$  and  $V_R$ ), continuous transition from double-dot spectrum (triple points and avoided crossings) to single dot spectrum (parallel transverse lines) and rather regularly spaced Coulomb blockade peaks. At the edges of the electron-electron quadrant of the stability diagram, we can form a double quantum dot in a controlled way in the few electron regime. We focus here on a degeneracy line between two charge states highlighted by a white square in figure 5.3-a. The phase contrast of the microwave

signal in this region is displayed on figure 5.3-b. This allows to define the detuning  $\epsilon_\delta = \alpha_L V_L - \alpha_R V_R + \epsilon_0$  along the white arrow,  $\alpha_{L(R)}$  being given by the slope of the degeneracy line.

The phase of the microwave signal displays the characteristic sign change of a resonant interaction between the cavity and the double quantum dot. A transition to the dispersive (off-resonant) regime is also visible by a gradual change of phase contrast along this degeneracy line. In the resonant regime, the dependence of the phase contrast  $\Delta\phi$  as a function of  $\epsilon_\delta$  which has maxima/minima of about  $\pm 15\%$  provides an estimate of the charge coupling strength  $g_C \approx 2\pi \times (21 \pm 1) MHz$  and of the charge decay rate  $\gamma_C \approx 2\pi \times (1.35 \pm 0.16) GHz$ .

### 5.1.5 Two-tone spectroscopy

In the double quantum dot regime, the tunnel coupling between the two dots and the non-collinear ferromagnetic contacts generate a spin dependent hybridization between the left and the right dot which allows to implement a spin photon coupling [26, 83]. This implies that the phase can a priori read-out the spin state of a trapped electron.

The measured phase is determined by an average of the dispersive shifts induced by each transition, weighted by the steady-state occupation of each state (see figure 5.3-b). Applying a second tone allows to individually address the different transitions, and to recover their respective coupling strength to cavity photons, as explained in the next paragraph.

The microwave spectroscopy of our ferromagnetic spin qubit is conveniently done by reading out in the dispersive regime the phase  $\phi$  of the cavity signal when a second tone is applied through the cavity and its frequency is swept, which is mainly sensitive to the expectation value of the spin projection on the Z axis of the left (right) dot,  $\langle \hat{\sigma}_z \rangle$ , at large detuning  $\epsilon_\delta$ . In the dispersive regime, at large detuning  $\epsilon_\delta$ , the expression of the phase reads:

$$\phi = \frac{2g_S^2}{\kappa\Delta} \langle \hat{\sigma}_z \rangle + \phi_0 \quad (5.1)$$

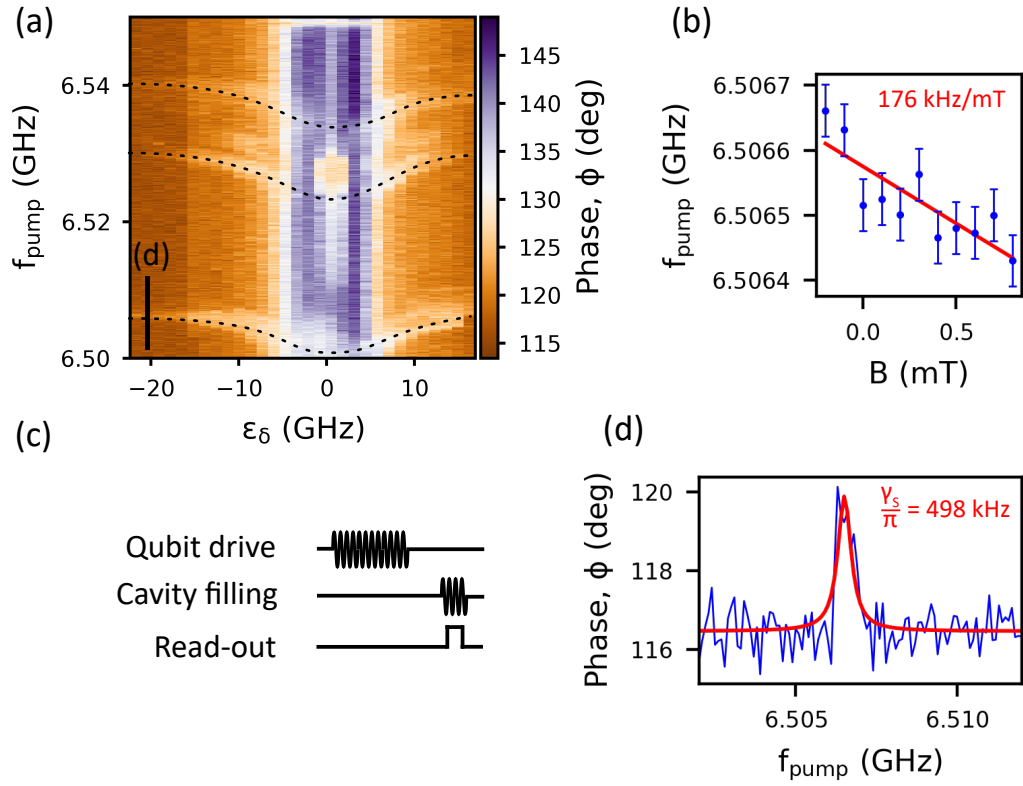


FIGURE 5.4: **Two-tone spectroscopy of the spin transition:** **a.** Phase contrast measured during a two-tone spectroscopy of the ferromagnetic spin-qubit as a function of the detuning  $\epsilon_\delta$ . The overall behavior of the transition: saturation at large detuning  $\epsilon_\delta$  and a minimum at  $\epsilon_\delta = 0$  is reminiscent of a spin transition such as the 01-transition shown in fig 5.1-a. The presence of three different spectroscopic lines can be explained by the lifting of the K/K' degeneracy in the carbon nanotube. **b.** Magnetic field dependence of the lower transition in **a.**. **c.** Pulse sequence used for the two tone spectroscopy. The qubit drive pulse last  $t = 3\mu s$ , then the cavity is filled for  $2\mu s$ , during when the cavity output signal is read-out using a fast data acquisition card for  $t = 700ns$ . **d.** Phase contrast as a function of the qubit drive frequency  $f_{\text{pump}}$  taken for the lower transition shown in **a.**. The spectroscopic linewidth of this transition correspond to a decoherence rate of  $\gamma_S = 2\pi \times 249kHz$ .

where  $\phi_0$  is a constant which only depends on the microwave setup,  $\kappa$  is the linewidth of the cavity,  $g_S$  is the spin-photon coupling strength and  $\Delta = f_{\text{cav}} - f_{\text{spin}}$  is the detuning between the cavity frequency  $f_{\text{cav}}$  and the spin qubit frequency  $f_{\text{spin}}$ . Such a measurement is shown in figure 5.4-a which displays the phase contrast  $\Delta\phi$  as a function of the tone frequency  $f_{\text{pump}}$  and  $\epsilon_\delta$ . In order to avoid cavity photon back-action on the spin qubit, we use a pulsed microwave spectroscopy with the pulse sequence shown in figure 5.4-c. The qubit is first driven for  $t = 3\mu s$ , then the cavity is filled after  $90ns$  during  $2\mu s$  and finally read-out using a fast data acquisition card for  $t = 700ns$ . Apart from the frequency independent vertical blue stripe which simply signals the left/right degeneracy

line at zero detuning, we observe 3 resonances which disperse close to zero detuning and saturate at  $6.506GHz$ ,  $6.530GHz$  and  $6.540GHz$  respectively. The dispersion of each of these transitions with a minimum at zero detuning and a saturation at large detuning is characteristic of a transition which becomes a pure spin transition in the large detuning limit due to the perfect localization of the electron in one quantum dot (see figure 5.1-a). The saturation value is given by the effective Zeeman field felt by the (pure) spin state at large detuning. The fact that we observe several spin transitions is attributed to the K/K' valley degeneracy of the nanotube as well as from the fact that we are not in the single electron regime. As expected for a spin transition, we can tune the value of this saturation with the external magnetic field. The resulting linear dependence is shown in figure 5.4-b. The low slope is consistent previous measurements in a similar architecture with non-stapled nanotube material [26].

A cut along the lowest resonance at large detuning is shown in figure 5.4-d. This measurement fitted by a lorentzian has a full width at half maximum of  $2\gamma_S = 2\pi \times (498 \pm 80)kHz$  which corresponds to a decay rate about  $2\pi \times 249kHz$ . Such a narrow linewidth is two orders of magnitude lower than that found in the valley-spin qubit in previous work with carbon nanotubes [92] and compares favorably to the very recent figures of merit reported for Si based platforms [53, 55]. From the phase contrast of about  $4^\circ$ , and assuming that the transition is fully saturated ( $\Delta\langle\hat{\sigma}_z\rangle = 1$ ) we can estimate a lower bound of the spin photon coupling strength  $g_S \approx 2\pi \times 2.0MHz$ , which exceeds the decoherence rate of the spin states and of the cavity. This implies that the spin is strongly coupled to the cavity photons although they are not resonant. As a comparison, we have  $g_S/\gamma_S \geq 8$  for the spin transition whereas  $g_C/\gamma_C \approx 0.015$  for the charge like transition. There is therefore a very large gain in the coherence properties of our device when we switch from the charge like transitions to the spin transitions.

### 5.1.6 Time-domain measurement

We further substantiate our microwave spectroscopy measurements by time domain measurements. For that purpose, we use a similar pulse sequence than the one shown in figure 5.4-c, except that we have a varying qubit drive pulse length. Such a pulse sequence is the one traditionally used to observe Rabi oscillations. The resulting variations of the in-phase quadrature I and the out-of-phase quadrature Q of the cavity field as a function

of qubit pulse duration  $\tau$  are displayed in figure 5.5-a and 5.5-b. A slowly modulated decaying signal is observed. It is well accounted for by the full cavity-Bloch coupled set of equation of motions of the cavity field and the spin [140] shown in red line. This allows us to extract a relaxation rate  $\gamma_1 \approx 2\pi \times 45kHz$  and a pure dephasing rate  $\gamma_\phi \approx 2\pi \times 55kHz$ . The other main parameter entering the theory is the cavity pull  $\chi \approx 2\pi \times 150kHz$ , which is consistent with the obtained spin-photon coupling value and the frequency detuning  $\Delta = f_{cav} - f_{spin}$  (since  $\chi = \frac{g_s^2}{\Delta}$ ). The Rabi frequency  $\Omega_R = 2\pi \times 140kHz$  found is low due to the limited coupling strength of the spin to the photons and to the fact that we drive the spin through cavity photons <sup>1</sup>.

### 5.1.7 Cavity-Bloch equations

To account for the measured cavity field quadratures I and Q shown in figure 5.5, we used the cavity-Bloch equations (given in ref. [140]). The dynamics of the coupled qubit-cavity system is described by the master equation:

$$\frac{d}{dt}P = MP + E_{source} \quad (5.2)$$

where M is the matrix containing the prefactors of the coupled equations (those prefactor can be found in ref. [140]),  $E_{source}$  is the vector containing source terms such as the externally applied microwave field, and  $P$  is the population vector and reads:

$$P^\top = \left( \langle \hat{a} \rangle \quad \langle \hat{\sigma}_z \rangle \quad \langle \hat{\sigma}_x \rangle \quad \langle \hat{\sigma}_y \rangle \quad \langle \hat{a}\hat{\sigma}_z \rangle \quad \langle \hat{a}\hat{\sigma}_x \rangle \quad \langle \hat{a}\hat{\sigma}_y \rangle \quad \langle \hat{a}^\dagger \hat{a} \rangle \right) \quad (5.3)$$

To account for the nonlinear terms in the numerical solving, the matrix  $M$  contains populations such as  $\langle \hat{a}^\dagger \hat{a} \rangle$  obtained at the previous iteration. We then simulate the full pulse sequence used in the Rabi measurement including the drive of the qubit (with the envelop  $\Omega(t)$ ) during a time  $\tau$ , the drive of the cavity (with the envelop  $\epsilon_m(t)$ ) during  $1.5\mu s$ , and the time window over which the cavity output signal is acquired, which last  $1\mu s$ . The fit procedure is done on the two quantities  $I = Re\langle \hat{a} \rangle$  and  $Q = Im\langle \hat{a} \rangle$ , and the result is superimposed in red in figure 5.5.

<sup>1</sup>In such a situation, the Rabi frequency reads:  $\Omega_R = \frac{g_s}{\Delta} \epsilon_d$ , where  $\epsilon_d$  is the qubit pulse amplitude (see supplemental material of ref. [141]). Therefore, the prefactor  $\frac{g_s}{\Delta}$  limits the Rabi frequency  $\Omega_R$ . In the measurement presented in figure 5.5, we have  $\frac{g_s}{\Delta} \approx 0.025$ .

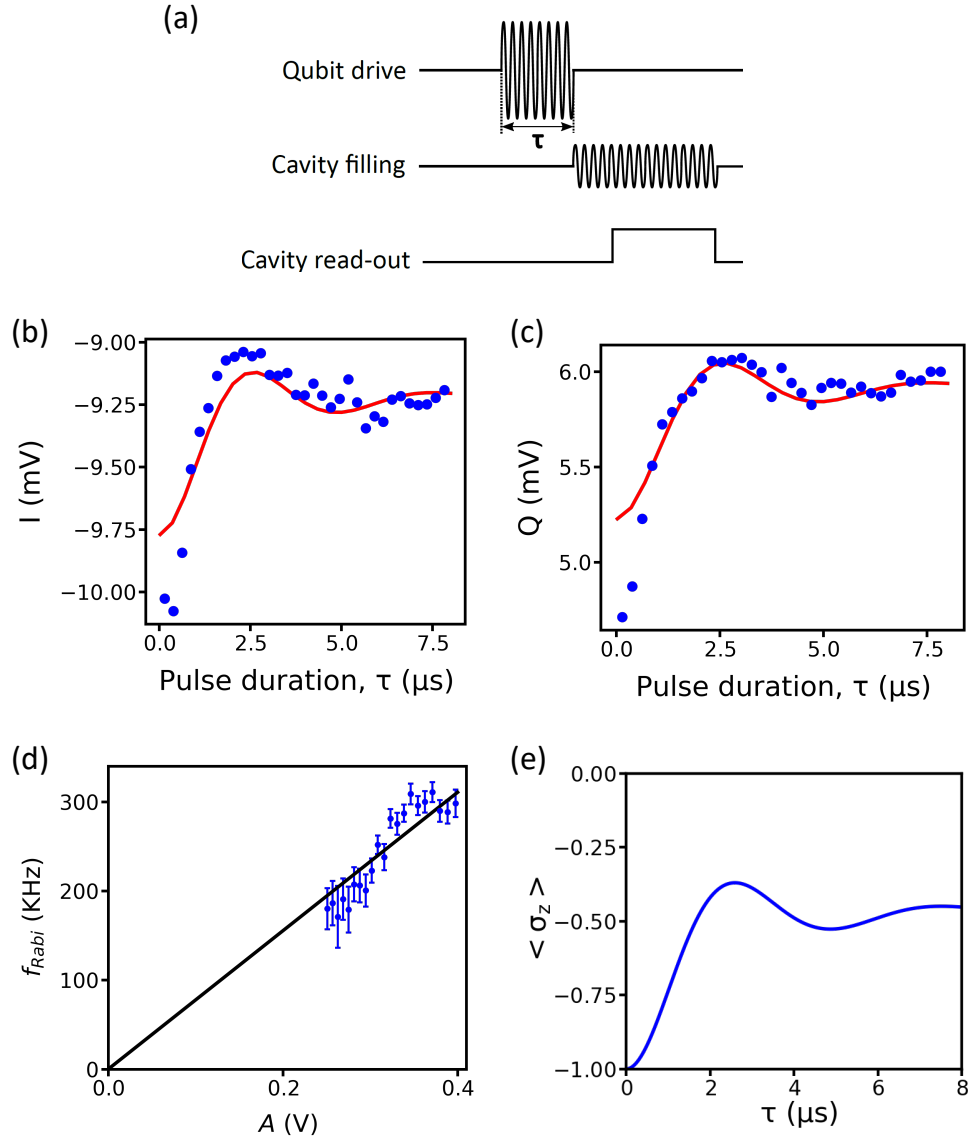


FIGURE 5.5: **Rabi measurement:** **a.** Pulse sequence used for the Rabi measurement with qubit drive pulse duration varying  $\tau \in [0\mu s, 8\mu s]$ . **b.** and **c.** In-phase quadrature  $I$  and out-of-phase quadrature  $Q$  of the cavity field respectively, as a function of the qubit pulse duration  $\tau$ . **d.** Extracted Rabi frequency for a varying qubit drive amplitude. A roughly linear dependence is obtained. **e.** Reconstructed  $\langle \hat{\sigma}_z \rangle$  evolution while the qubit is driven, using cavity-Bloch equations [140] (see section 5.1.7).

In figure 5.6 we show the  $\langle \sigma_z \rangle$  evolution, for the pulse sequence with the longest qubit-pulse:  $\tau_{pulse} = 8\mu s$  (corresponding to the last point of the Rabi measurement). Importantly one can see that  $\langle \sigma_z \rangle$  saturates at  $-0.5$ , instead of 0 as one would expect for a strong qubit-drive with respect to the relaxation rate of the qubit. Such a saturation can also be explained by a finite detuning between the qubit frequency and the qubit drive frequency.

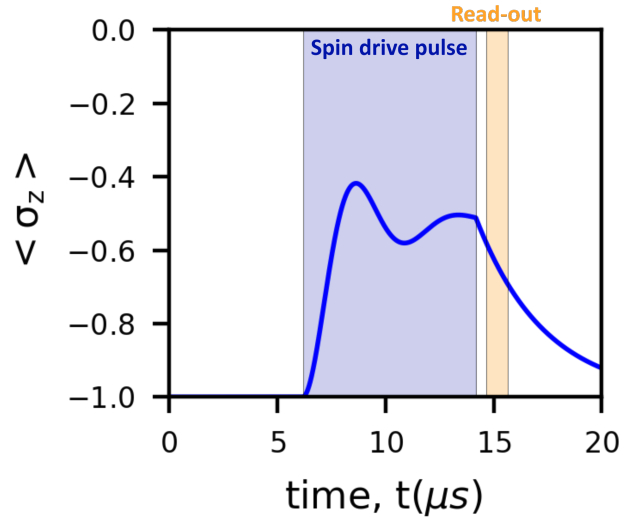


FIGURE 5.6:  $\langle \sigma_z \rangle$  evolution for the pulse sequence with  $\tau_{\text{pulse}} = 8\mu\text{s}$ .

From the saturation value of  $\Delta\langle \sigma_z \rangle = 0.5$ , one can deduce the spin-photon coupling strength :

$$g_S = \sqrt{\frac{\Delta_{qc}\kappa\Delta\phi}{2\Delta\langle \sigma_z \rangle}} \simeq 3\text{MHz} \quad (5.4)$$

### 5.1.8 Decoherence model

In order to specify the decoherence mechanism explaining the linewidth found for our spin transition, we have measured the dependence of the decoherence rate as a function of the detuning between the left and right dots. Such a measurement is displayed in figure 5.7-a. Two main decoherence sources are expected for the electronic spin in double quantum dots: charge noise and nuclear spin. Our  $^{12}\text{C}$  platform is grown from a natural  $\text{CH}_4$  feedstock gas and therefore is expected to have a low concentration of nuclear spins (1.1% of  $^{13}\text{C}$  with a nuclear spin  $I = 1/2$ ). The charge noise is related to the fact that the transition frequency may fluctuate if offset charges nearby the device change the detuning. Therefore, it should induce a decoherence rate  $\gamma_S$  proportional to the derivative of the transition with respect to the detuning [83]. For a large detuning  $\epsilon_\delta$ , the nuclear spin bath is on the contrary expected to give a nearly independent contribution as a function of the detuning. The decoherence rate  $\gamma_S$  and the derivative  $\partial\omega/\partial\epsilon_\delta$  as a function of detuning  $\epsilon_\delta$  are shown to overlap well provided we add a constant of about 500kHz to the derivative in figure 5.7-a. The linear behavior of the decoherence rate  $\gamma_S$

as a function of the derivative  $\partial\omega/\partial\epsilon_\delta$ , displayed in inset, shows that our spin-photon interface is dominated by charge noise at small detuning. Interestingly, it allows us from the slope of the linear behavior to extract a charge noise detuning variance of about  $34\mu\text{eV}$ . While this noise is larger than in previous work in carbon nanotubes [50] and could be in principle easily lowered, it is interesting to see that we can make its influence negligible compares to nuclear spin noise by going at large detuning while keeping a large spin-photon coupling strength with respect to  $\gamma_S$ . The shaded grey corresponds to the residual decoherence mechanisms with a decay rate in the range  $2\pi \times (250\text{kHz} - 500\text{kHz})$ .

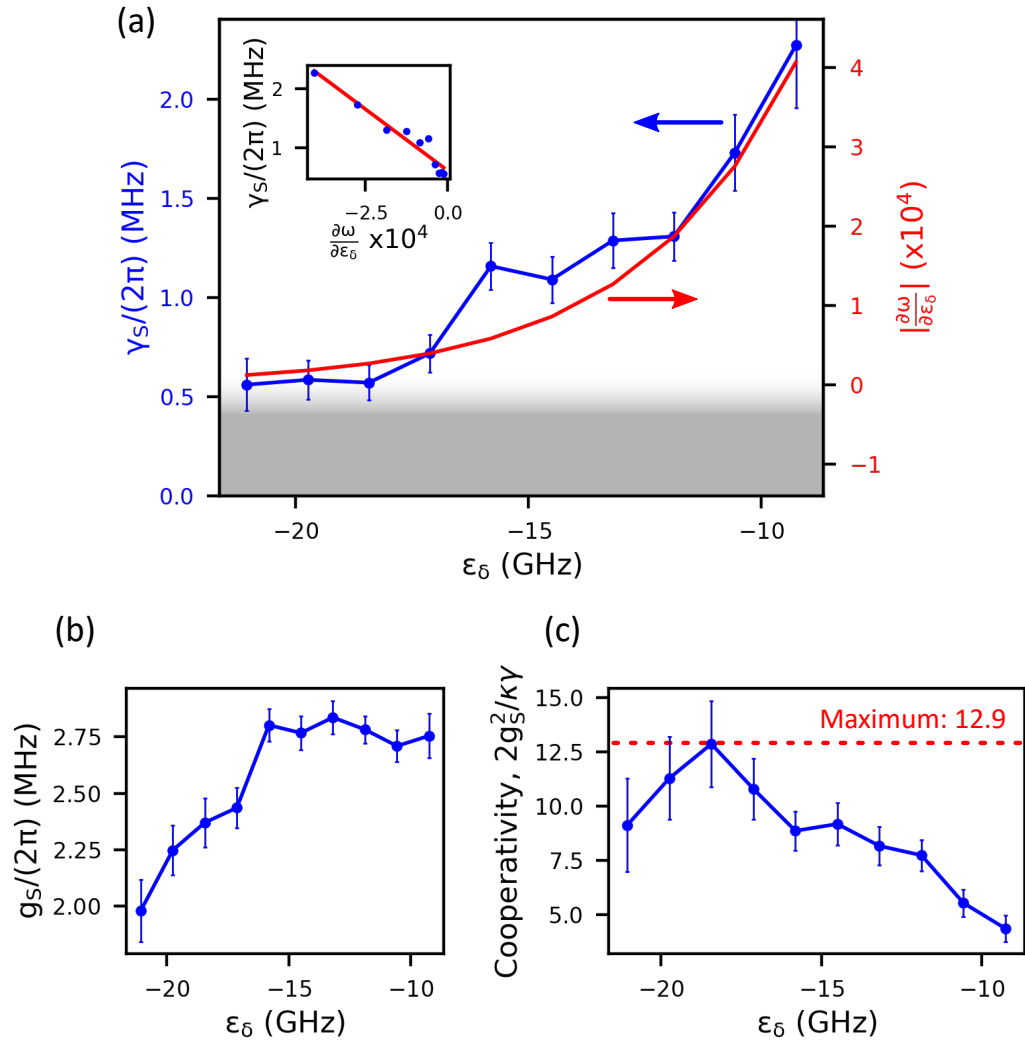


FIGURE 5.7: Charge stability diagram of the double quantum dot:

Interestingly, the residual decoherence rate allows us to give an upper bound of the contribution of the nuclear spins of the 1.1% of  $^{13}\text{C}$  and therefore of the hyperfine coupling  $\mathcal{A}$ . From the estimated diameter of our CVD nanotubes  $D \approx 2\text{nm}$  and the

length of each dot  $d \approx 500nm$ , we get a number of nuclear spins of  $N \approx 0.011 \times 3 \times 10^5$  which yields  $\gamma_S \approx 2\pi \times 200kHz$  if  $A = 0.1\mu eV$ . Our measurements are therefore fully in agreement with the tabulated values for the hyperfine coupling expected in CNTs of  $A \approx 0.1 - 0.5\mu eV$  contrarily to previous work [168, 173]. In addition to the decoherence rate, we also present the spin-photon coupling strength and the cooperativity of the spin-photon interface  $C = \frac{2g_S^2}{\kappa\gamma_S}$  as a function of the detuning (figure 5.7-b and 5.7-c respectively). Interestingly this last quantity allows to identify an optimal detuning working point around  $\epsilon_\delta = -18GHz$ . For this detuning point, the hybridization with the charge creates a sizeable spin-photon coupling while maintaining a low decoherence rate. Our results suggests that carbon, like silicon, can be a promising host for electronic spins encoding quantum information. This is enabled by our clean and controlled nano-assembly technique of carbon nanotubes in cavity.

In summary, we have demonstrated that carbon nanotube based double quantum dots can provide a tunable and coherent spin-photon interface. The figures of merit of coupling strength of  $g_S = 2\pi \times 2.0MHz$  and low decoherence rate  $\gamma_S = 2\pi \times 250kHz$  are suitable for future swap experiments.

## 5.2 Design and characterization of the spin-qubit device

### 5.2.1 Design of Ferromagnetic contacts

The design of the ferromagnetic contacts is determinant to the spin-charge hybridization. It has been shown that the geometry of the magnetic domains of PdNi nanostrip is fixed by the anisotropy of the nanostructure and results from the so-called inverse magnetostriction effect [174]. In the case of PdNi electrode with thickness about  $30nm$ , and width below  $500nm$  the magnetization is perpendicular to the electrode direction (see figure 5.8). Therefore, one can control the magnetization axis by changing the electrode orientation. In our architecture, suspended carbon nanotubes requires high enough contacts electrodes (with a typical height of  $200nm$ , see section 3.2.7 of the chapter 3), which is incompatible with the appearance of perpendicular magnetic domain in the ferromagnetic contact. Thus, a first thick metallic layer is used to elevate the PdNi magnetic texture without affecting to much the inverse magnetostriction effect. The emergence of constraints in the PdNi is due to a mismatch between thermal expansion

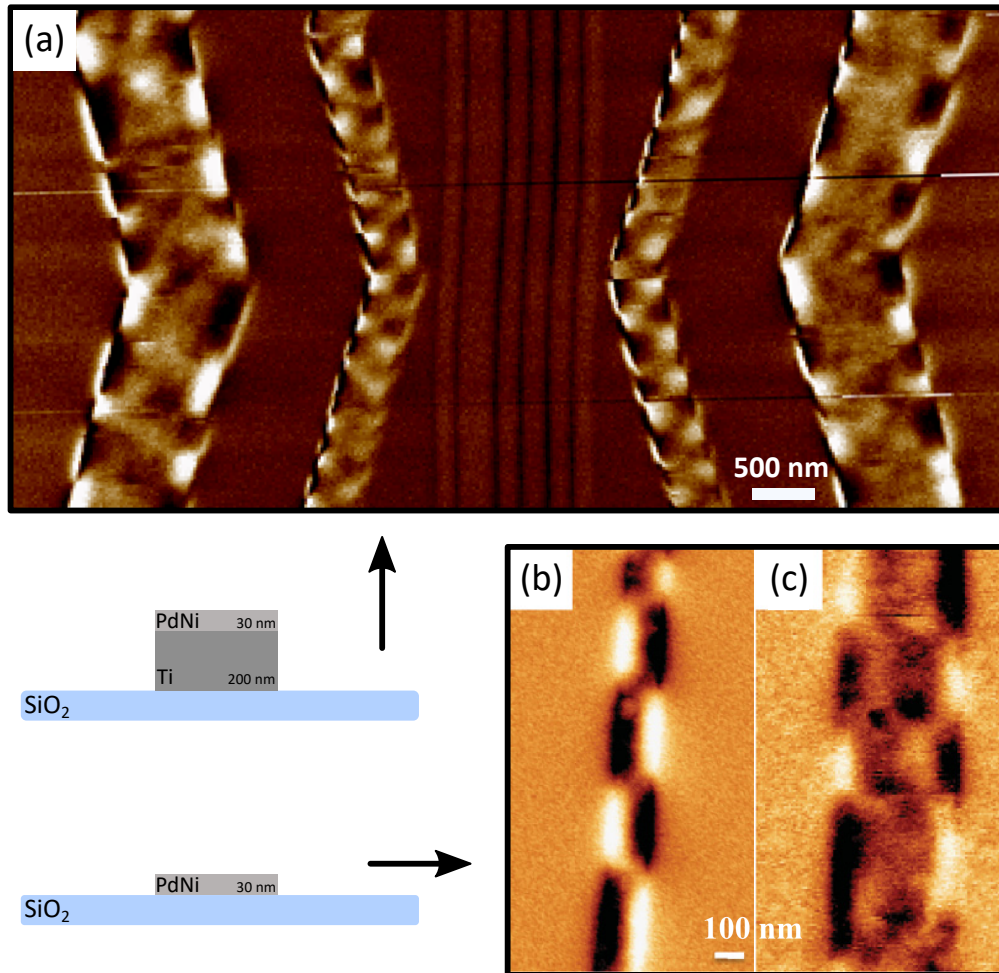


FIGURE 5.8: **MFM image of the ferromagnetic contacts:** **a.** Magnetic force micrograph (MFM) of the ferromagnetic contact geometry used for the spin-qubit experiment. The two larger contacts are used only for the integration of the carbon nanotube, hence they do not belong to the spin-qubit circuit. **b., c.** Magnetic force micrograph (MFM) for single ferromagnetic electrode lying directly on a  $SiO_2$  substrate.

coefficient of PdNi and the thick layer metal. Indeed, two main cool-down occurs during the fabrication: first, when the sample is cooled down at room temperature after the metal evaporation, and then at the cryogenic cool-down (expected to reinforce the effect [174]). In the device presented in this chapter, we use Titanium as the thick layer metal, which is the metal maximizing the thermal expansion coefficient mismatch among the metals directly accessible in the clean room facility (thermal expansion coefficient for Ti and PdNi:  $\alpha_{Ti} = 8.6 \times 10^{-6}$  and  $\alpha_{PdNi} \simeq 12.5 \times 10^{-6}$ ). The magnetic domains obtained with such a metallic stack are shown in figure 5.8-a.

The angle between the two ferromagnetic contacts is a key parameter in the spin-photon interface. Indeed, the hamiltonian of a double quantum dot with only one orbital in each

dots, and two Zeeman fields of amplitude  $E_z$ , with an axis misalignment defined by an angle  $\theta$  reads [83]:

$$\hat{H} = -\frac{\epsilon_\delta}{2}\hat{\tau}_3\hat{\sigma}_0 + t\hat{\tau}_1\hat{\sigma}_0 - E_z\left(\hat{\sigma}_3\frac{\hat{\tau}_0 + \hat{\tau}_3}{2} + (\cos(\theta)\hat{\sigma}_3 + \sin(\theta)\hat{\sigma}_1)\frac{\hat{\tau}_0 - \hat{\tau}_3}{2}\right) \quad (5.5)$$

Where  $\hat{\sigma}_i$  with  $i \in [0, 3]$  are the Pauli matrices acting on the spin degree of freedom ( $\hat{\sigma}_0$  is the identity), and  $\hat{\tau}_i$  with  $i \in [0, 3]$  are the Pauli matrices acting on the orbital degree of freedom. The spin-charge hybridization arises from the term  $\sin(\theta)\hat{\sigma}_1\frac{\hat{\tau}_0 - \hat{\tau}_3}{2}$ , which is the strongest for  $\theta = \pi/2$ . Although a large spin-charge hybridization provides a large coupling to the cavity photons, it also strongly affects the sensitivity of the 0-1 transition (see figure 5.1-a) to charge noise. The sensitivity to charge noise is captured (at first order) by the derivative  $\frac{\partial\omega_{01}}{\partial\epsilon_\delta}$  and is shown in figure 5.9 along with the coupling strength between cavity photons and excitations in the 01 transition.

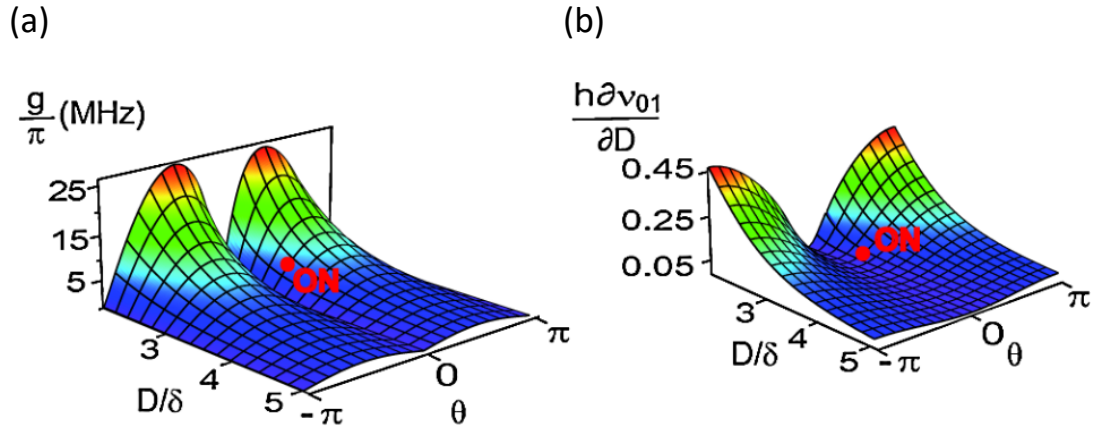


FIGURE 5.9: **Influence of the Zeeman angle:** **a.** Coupling strength between cavity photons and excitation in the 01 transition, as a function of the detuning (here labeled  $D = \epsilon_L - \epsilon_R$ ) and the Zeeman angle  $\theta$ . **b.** the derivative  $\frac{\partial\omega_{01}}{\partial\epsilon_\delta}$  as a function of same two parameters. The red point labeled ON, corresponds to the working point for which  $D = 2.8\delta$  and  $\theta = \pi/6$ .

## 5.2.2 Further characterization of the circuit

**Charge transition properties** On the left part of the degeneracy region shown in the figure 5.3-b (and reproduce in figure 5.10-a), the phase signal display the characteristic profil of a resonant situation between a transition in the quantum dot circuit and the cavity. A cut along the  $V_L$ -axis in this region is shown in figure 5.10.b. The strong

phase contrast ( $\Delta\phi \simeq 30$  degrees) suggests that in addition to the spin transition, the left/right charge transition is also resonant with the cavity and dominates the signal.

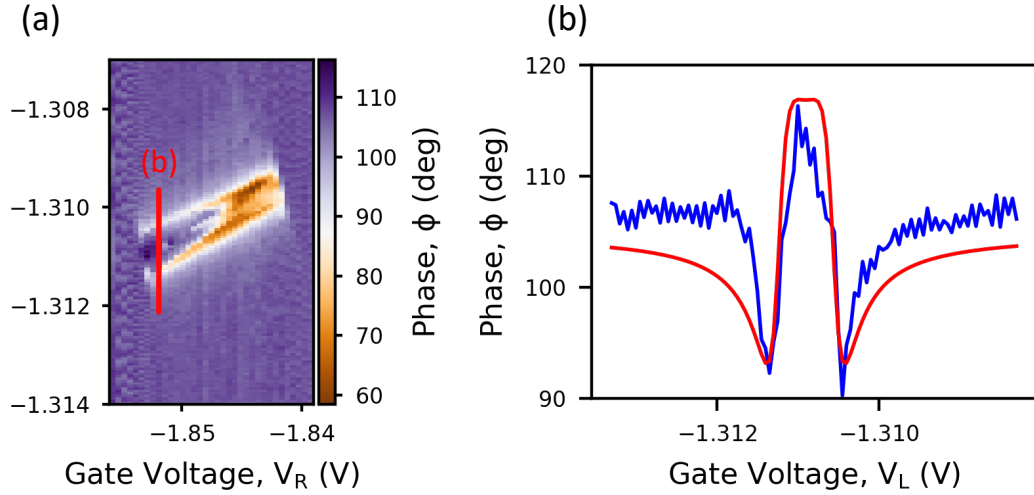


FIGURE 5.10: **Phase signal in the resonant region:** **a.** reproduction of figure 5.3.b. **b.**(Blue line) Extracted sweep from the 2D plot shown in **a.** at  $V_R = -1.852V$ . (Red line) Fit of the measured blue line.

Using the expression of the interdot transition frequency  $\omega_{charge} = \sqrt{\epsilon_\delta^2 + 4t^2}$  and writing the phase contrast:

$$\Delta\phi = \arg\left(\frac{1}{i\kappa/2 - \frac{g_c^2}{(\omega_{cav} - \omega_{charge} + i\Gamma_C)}}\right) \quad (5.6)$$

Allows to estimate the charge-photon coupling strength and the charge transition decoherence rate:

$$g_C = 2\pi \times (21 \pm 1) MHz$$

$$\Gamma_C = 2\pi \times (1.35 \pm 0.16) GHz$$

$$t = 2\pi \times (2.40 \pm 0.06) GHz$$

**Amplitude signal in the spectroscopy** For a small dispersive shift of the cavity resonance, a change in the cavity linewidth  $\kappa$  reflects in the amplitude at resonance  $A_0$ , as  $A_0 \propto 1/\kappa$ . The figure 5.11 shows the amplitude at the bare resonance frequency measured simultaneously to the phase signal presented in figure 5.4-a. Notice that the amplitude is not affected by the transition is the region where a  $4^\circ$  phase shift has been measured. This observation shows that one can consider the cavity linewidth  $\kappa$  to be very close to its bare value  $2\pi \times 1.44 MHz$ , when estimating the spin-photon coupling.

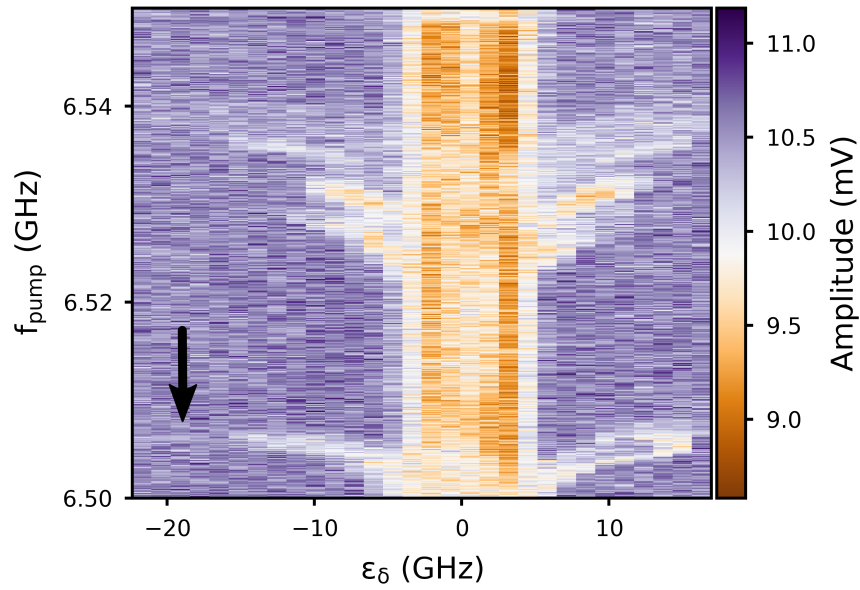


FIGURE 5.11: **Amplitude signal for the two-tone spectroscopy:** The black arrow is pointing toward the region where the spin transition caused a  $4^\circ$  phase shift in the cavity transmission signal.

**Tunnel barrier tunability** An advantage of using a five gates geometry for a double quantum dot, is the possibility to tune the tunnel barrier between the two dots in a controlled manner. In case of charge like transition in a double quantum dot ( $E_{DQD} = \sqrt{\epsilon_\delta^2 + 4t^2}$ ), changing the tunnel coupling  $t$  allows to go from the resonant regime to the dispersive regime at will. A transition between a resonant situation to a dispersive situation is shown in figure 5.12.

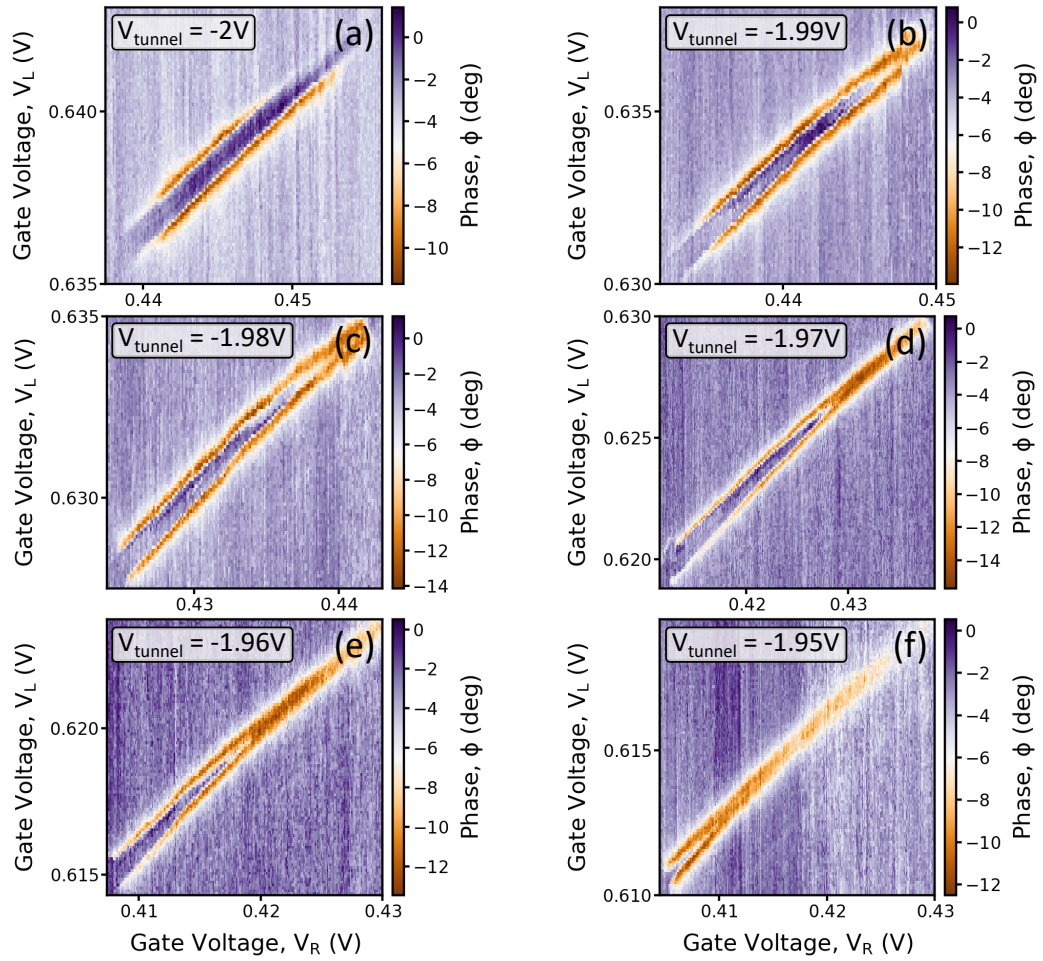


FIGURE 5.12: **Tunnel barrier tunability:** The height of the tunnel barrier is proportional to  $-eV_{\text{tunnel}}$ , which corresponds to the middle gate in a five gate geometry. In **a.** the charge transition is fully resonant with the cavity frequency. In **b.**, **c.**, **d.**, **e.** the dispersive region progress from the top right corner, and in **f.** the charge transition frequency is almost completely dispersive with respect to the cavity frequency.



# Conclusion and perspectives

**Summary** The experiments presented in this thesis are performed in carbon nanotube based quantum dot circuits coupled to a microwave cavity. Such circuit-QED platform has proven to be very powerful to probe the internal dynamics of quantum dot circuits. While the contact electrodes in quantum dot circuits are necessary to perform quantum transport, the choice of a specific contact metal is also instrumental to engineer specific electronic states in the circuit. In chapter 4, we presented results on a Cooper pair splitter experiment, in which a superconducting contact is used as a resource to generate non-local entangled electronic states in a double quantum dot. We show that the bonding and anti-bonding states in the double quantum dot are dressed by Cooper pair injection, giving rise to a renormalized tunneling rate between the two dots. This effect has been exploited to engineer a new coupling scheme between cavity photons and electronic transitions, and enabled us to reach the strong charge-photon coupling in this quantum-dot circuit [14]. A nanofabrication technique has also been developed during this thesis, allowing to integrate pristine carbon nanotubes in a circuit-QED device architecture. This technique produces quantum dot circuit with a much higher electrical tunability. In the second experiment we make use of this integration technique to create a ferromagnetic spin-qubit displaying unprecedented long coherence time of a spin transition in carbon nanotubes.

**Perspectives** In the Cooper pair splitter experiment (chapter 4), the results presented on the dispersion of the superconductivity dressed states provide a first insight in the Cooper pair splitting physics, but a lot remains to be done. The first investigation would be to use a stapled carbon nanotube and exploit the greater tunability that they

provide. Hence one could perform two-tone spectroscopy of these dressed states and study their magnetic field dependence [72, 175]. In the long term, several directions are envisioned. One could provide a more complete characterization of the dressed states by performing tomography of the photon states when coupled to electronic states dressed by the Cooper pair injection. In a circuit-QED perspective one could also work on the manipulation of such states using the coupling with cavity photons. A second direction, is to combine the two ingredients of chapters 4, and 5, and realize a Cooper pair splitter including two non-collinear spin-valves [176]. Such a circuit would allow a better control over the spin states in the double quantum dot, and favor states  $|\uparrow\downarrow\rangle$  with respect to  $|\downarrow\uparrow\rangle$  for instance.

Concerning the spin-qubit experiment (chapter 5), it would be very instructive to probe the full tunability of the ferromagnetic spin-qubit by changing in-situ the two local effective Zeeman fields using gate voltages on the side of the double quantum dot. This feature is specific to this spin-qubit design, hence, it would be very instructive to demonstrate them. In particular, one could identify the mechanism responsible for the polarization of the spectrum: transmission or reflection in the spin valves. Another direction of research would be to couple two ferromagnetic spin-qubits through exchange of virtual photons [98] or direct energy exchange [99].

Finally, both of these experiments could benefit from a better cavity-carbon nanotube interface by increasing the charge-photon coupling strength. One could use an higher impedance resonator, either by changing the cavity material (for instance: NbTi) or the cavity design (lumped-element resonator, Josephson junction array, ...), or combine the two approaches. Simulating the cavity field inside the quantum dot circuit geometry using softwares such as HFSS (High Frequency Simulation Software) could also be very instructive to estimate the charge-photon coupling strength in a double quantum dot, and therefore to tune the cavity field gradient over the circuit in order to increase the charge-photon coupling strength.

# Appendix A

## Detailed fabrication recipes

### A.1 Spin-qubit circuit recipe

#### A.1.1 First cleaning

The wafer used is a undoped high resistivity silicon ( $10 \text{ k}\Omega\cdot\text{cm}$ ) covered with 500 nm of silicon oxide, and it is dined into  $10\text{mm}\times 10\text{mm}$  chips. The first step is to remove the PMMA resist layer used to protect the wafer during the dicing.

- **20 minutes:** Acetone at  $50^\circ\text{C}$  (all the chips inside the same becher).
- **30 secondes:** Shaking in acetone.
- **1 minutes:** (Chip one by one) Acetone at  $50^\circ\text{C}$  + sonic-bath (force 9). Use a second acetone becher for this step.
- **30 secondes:** (Chip one by one) Move the acetone becher from the sonic-bath and vigorously shake the chip in order to remove the fragment of silicon that sonic-bath may have created.
- **30 secondes:** Vigorous shaking in IPA.

## A.1.2 Gold crosses and device name

### A.1.2.1 PMMA 500 spin coating

- Launch the pumping of the chip and remove the possible dirt from your chip using the nitrogen blower.
- Depose 3 drops of PMMA 550 resist, then launch the 4000-4000-30 program (4000 turns/s<sup>2</sup>, 4000 turn/s, 30 s).
- Bake the chip at **185°C** for 3 minutes.
- check at the microscope if there are bubbles, or dirt on the chip. If so, you should start over again the first cleaning step and the PMMA spin coating.

### A.1.2.2 Two-current e-beam lithography

SEM paramters:

- Aperture: 7.5  $\mu\text{m}$  and 120  $\mu\text{m}$
- Acceleration voltage: 20 kV

Procedure:

- Measure the currents for the 7.5  $\mu\text{m}$ -aperture and the 120  $\mu\text{m}$ -aperture.
- Localize the origin and the angle of the chip.
- Make a contamination dot at the center of the chip (with the 7.5  $\mu\text{m}$ -aperture with a zoom = x200k): Focus on the dot + WF alignment at 5  $\mu\text{m}$  then at 1  $\mu\text{m}$ .
- Save the column parameter for the 7.5  $\mu\text{m}$ -aperture.
- Call the 120  $\mu\text{m}$ -aperture column parameter, and the WF parameter for the 120  $\mu\text{m}$ -aperture.
- Zoom-out up to x10k-20k, Focus on the dot + center the contamination by adjusting the beam shift (DO NOT TOUCH THE JOYSTICK).
- Launch the WF alignment procedure at 5  $\mu\text{m}$ .

- Save the column parameter for the 120  $\mu\text{m}$ -aperture.
- Scan the following position list.

Position list:

- Loading of the 7.5  $\mu\text{m}$ -aperture parameters.
- Loading of the writefield parameters for the 7.5  $\mu\text{m}$ -aperture (zoom, shift, rotation).
- Exposition of the layer 10 (pre-contact + small crosses for the layer 63).
- Loading of the 120  $\mu\text{m}$ -aperture parameters.
- Loading of the writefield parameters for the 120  $\mu\text{m}$ -aperture (zoom, shift, rotation)
- Exposition of the layer 11 (name of the chip + large crosses for the 3-point alignment)

Exposure properties:

- Structure: Wafer
- Exposed layer: 10 or 11
- Working Area: “*Boundaries*”
- Position:  $U = 0.05 \text{ mm}$ ,  $V = 0.05 \text{ mm}$

Exposure parameters:

- Area step sizes:  $U = V = 20 \text{ nm}$
- Dose:  $350 \mu\text{C}/\text{cm}^2$

### A.1.2.3 Reveal and evaporation

- **1 min 10 sec:** Reveal in MIBK/IPA solution (1:MIBK, 3:IPA).
- **30 secondes:** Rinse in IPA then dry. Check if the lithography went well at the optical microscope.
- **10 secondes** Stripping.
- Evaporate 5 nm of Ti, and 45 nm of Au.

### A.1.2.4 Lift-off

- **20 minutes:** Acetone at **50°C**.
- **1 minutes:** Acetone at **50°C** + pipette, until there is no visible remaining of metal on the chip.
- **1 minutes:** (Chips one by one) Acetone at **50°C** + sonic-bath (force 9).
- **30 secondes:** Vigorous shaking in acetone.
- **30 secondes:** Vigorous shaking in IPA.

## A.1.3 Cavity

### A.1.3.1 Niobium evaporation

- **3 minutes:** Stripping.
- Load the chip in the load-lock of the Plassys evaporator immediately after the stripping.
- Launch the cool-down of the evaporator cryo-panels by filling them with liquid nitrogen ( $\approx 30$  minutes).
- Evaporate 100 nm of Nb at 10 Å/sec.

### A.1.3.2 Laser lithography

- Launch the pumping of the chip and remove the possible dirt from your chip using the nitrogen blower.
- Depose 3 drops of S1805 resist, then launch the program 10.
- Bake the chip at **115°C** for 1 minutes.
- check at the microscope if there are bubbles, or dirt on the chip. If so, you should start over again the first cleaning step and the PMMA spin coating.
- Laser lithography parameters: alignment procedure A+B, lens: 5, filter: 3 %, gain: 11 (203 mJ.cm<sup>-2</sup>), D-step: 1, pos: 1 mm.s<sup>-1</sup>.
- Reveal: 1 min in MF319 + 1 min in DI H<sub>2</sub>O + blow dry.

### A.1.3.3 Niobium etching

- Load the chips, then when the penning pressure is below 15 nbars, start the “*test*” program and purge the SF<sub>6</sub> line.
- Launch the “*Nb*” program, and monitor the progress using the reflectometry measurement. First the reflectivity slowly increases, then it decreases abruptly and reach a minimum signaling that the Nb has been etched away.
- Do 20 secondes of overetch after that reflectivity minimum.

### A.1.3.4 Cleaning

- **20 minutes**: Acetone at **50°C**.
- **30 secondes**: Vigorous shaking in acetone.
- **1 minutes**: (Chips one by one) Acetone at **50°C** + sonic-bath (force 9).
- **30 secondes**: Vigorous shaking in acetone.
- **30 secondes**: Vigorous shaking in IPA.
- **2 minutes**: Stripping.

### A.1.4 Gate electrodes

#### A.1.4.1 MMA/PMMA spin-coating

- Launch the pumping of the chip, and remove the possible dirt from your chip using the nitrogen blower.
- Depose 3 drops of diluted MMA resist (from the HQC bottle with “110 nm” written on it), then launch the program number 10 (called “jpc”).
- Bake the chip at **185°C** for 3 minutes.
- Cool-down the chip for 20 secondes on the metal of the table.
- Depose 3 drops of diluted PMMA resist (from the HQC bottle with “40 nm” written on it), then launch the 4000-4000-30 program.
- Bake the chip at **185°C** for 3 minutes.
- check at the microscope if there are bubbles, or dirt on the chip. If so, you should clean again the chip and spin-coat the bi-layer MMA/PMMA.

#### A.1.4.2 Lithography

The dose used for the gate lithography can be quite critical, so it is better to perform a dose test prior to the real lithography (if there has not been one in the past few weeks). With the current design (gate width = 60 nm, gate spacing = 140 nm, cavity gate width = 150 nm), the good dose has been found to fluctuate between 320 and 360.

- Measure current with the 7.5  $\mu\text{m}$  aperture.
- Origin/Angle alignment.
- Pre-focus on a defect close to the edge of the chip.
- 3-point alignment on the large crosses (position with respect to the center of the chip:  $U = \pm 450 \mu\text{m}$ ,  $V = \pm 550 \mu\text{m}$ ).
- As the focus can vary from positions that are few millimeters away, it is preferable to adjust the focus on a contamination dot each time you go to an other region

(basically this means to do 4 contamination dots for one chip). The dot can be done 100-200  $\mu\text{m}$  away from the quantum dot circuit region, in a niobium region.

- After the focus on the dot, you can launch the lithography (Structure: Wafer, Exposed layer: 63 and 4, Working Area: one of the six predefined  $100\mu\text{m}\times 100\mu\text{m}$ , Area step sizes:  $U = V = 20 \text{ nm}$ ).

#### A.1.4.3 Reveal, evaporation, and lift-off

- **18 sec:** Reveal in MIBK/IPA solution (1:MIBK, 3:IPA).
- **30 secondes:** Rinse in IPA then dry. Check if the lithography went well at the optical microscope.
- **10 secondes** Stripping, then load in the load-lock right after, and let it pump overnight.
- Evaporate 5 nm of Ti, and 50 nm of Al, then 10 minutes of oxidation at 1 mbar of  $\text{O}_2$  in the SAS.
- ( $\times 2$ ) Evaporate 1.5 nm of Al, then 10 minutes of oxidation at 1 mbar of  $\text{O}_2$  in the load-lock.
- Use the same lift-off procedure than the one for the gold crosses.

#### A.1.5 Contact electrodes

This step is very similar to the one of the gate electrodes, so I will not go into the details.

- Spin-coating of PMMA 500 resist.
- E-beam lithography: 7.5  $\mu\text{m}$ -aperture, dose: 360, layer: 6.
- Reveal: 1 min MIBK/IPA (1/3) + 30 sec IPA + 10 sec stripping.
- Evaporation: 211 nm of Ti + WAIT 14 min + 20 nm of PdNi (use the film parameters of Pd and not the one of PdNi) + 4 nm of Pd.
- Use the same lift-off procedure than the one for the gold crosses.

### A.1.6 Trenches

- Launch the pumping of the chip, and remove dirt using the nitrogen blower.
- Depose 3 drops of AZ5214, then launch the 4000-4000-30 program.
- Bake the chip at **115°C** for 1 min 30 sec.
- Check at the microscope if there are bubbles, or dirt on the chip.
- Laser lithography parameters: alignment procedure A+B, lens: 5, filter: 3 %, gain: 13.6 (250 mJ.cm<sup>-2</sup>), D-step: 1, pos: 1 mm.s<sup>-1</sup>.
- Reveal: 40 sec in AZ726MIF + 1 min in DI H<sub>2</sub>O + blow dry.
- SiO<sub>2</sub> etching: program “*DavidSiO<sub>2</sub>*” (CHF<sub>3</sub> only), at the end of the SiO<sub>2</sub> etching the reflectivity starts to be constant at the summit of an oscillation (last approximately 25 min) + 2 minutes of overetch.
- Si etching: program “*Si100W\_O<sub>2</sub>-80mT*” (SF<sub>6</sub> + O<sub>2</sub>) for 7 minutes.
- Cleaving of the chip using the scribe, with the chip still covered with AZ5214 resist.
- Cleaning: Same procedure than the first cleaning + 2 min stripping + 1 min of vigorous shaking in IPA.

## A.2 Carbon nanotube growth

### A.2.1 Low flow recipe

This recipe is largely inspired from ref. [131], and is supposed to provide longer and oriented carbon nanotubes. In the oven of the ENS, millimeter-long CNT has been obtained (see chapter 3) only when the catalyst was deposited on the edge of the chip.

- Be careful to use the “*CNT std*” labeled quartz tube.
- Load the sample into the quartz tube by the right extremity, and connect it to the “*CNT*” output circuit.

- open the bottle of Argon, Methane, and Dihydrogene, and note the pressures before and after the pressure regulator in the notebook. After the regulator, all pressure should be set at 1 bar.
- Launch the monitoring program (*control\_four2*), and note the three measured flows (which correspond to the offset value of the flowmeters).
- **Purge of lines (5 min):** Open all the three valves on the valve panel plus the main valve at the exit of the panel. Note the three pressures. The target values (subtracting the offset values) are:
  - Ar: 700 sccm
  - H<sub>2</sub>: 100 sccm
  - CH<sub>4</sub>: 50 sccm
- **900°C heating (≈ 20 min):** Heating of the oven up to 900°C under **Ar and H<sub>2</sub> flow**.
- **H<sub>2</sub> Flash (20 min):** Inject only H<sub>2</sub> during 20 minutes. This step is supposed to chemically reduce the possibly oxidized catalyst.
- **Heating from 900°C to 950°C (5 min):** Heating of the oven up to 950°C under **H<sub>2</sub> flow only**.
- **Growth (15 min):** Inject only CH<sub>4</sub> and H<sub>2</sub>. After 15 minutes, close the CH<sub>4</sub> valve, open the Ar valve, and turn-off the heating of the oven.
- **Cool-down (2 hours):** When the temperature goes below 400°C, it is possible to open the oven to speed-up the cool-down. When the temperature is below 200°C (10 minutes later), one can close the H<sub>2</sub> valve, to save some H<sub>2</sub>.
- When the temperature displayed by the oven is below 80°C (this is the temperature inside the oven close to the resistors and does not correspond to the real temperature of the chip.), close all the valves, and open the oven.
- Do not forget to close all the bottles.

### A.2.2 high flow (standard) recipe

This growth recipe has been developed in Basel by J. Furer [130]. The growth should be done as close as possible to the stapling step (ideally the day before).

- Be careful to use the “*CNT std*” labeled quartz tube.
- Load the sample into the quartz tube by the right extremity, and connect it to the “*CNT*” output circuit.
- open the bottle of Argon, Methane, and Dihydrogene, and note the pressures before and after the pressure regulator in the notebook. After the regulator, all pressure should be set at 1 bar.
- Launch the monitoring program (*control\_four2*), and note the three measured flows (which correspond to the offset value of the flowmeters).
- **Purge of lines (5 min):** Open all the three valves on the valve panel plus the main valve at the exit of the panel. Note the three pressures. The target values (subtracting the offset values) are:
  - Ar: 1450 sccm
  - H<sub>2</sub>: 200 sccm
  - CH<sub>4</sub>: 1100 sccm
- **900°C heating (≈ 20 min):** Heating of the oven up to 900°C under **Ar flow**.
- **H<sub>2</sub> Flash (8 min):** Inject only H<sub>2</sub> during 8 minutes. This step is supposed to chemically reduce the possibly oxidized catalyst.
- **Growth (10 min):** Inject only CH<sub>4</sub> and H<sub>2</sub>. After 10 minutes, close the CH<sub>4</sub> valve, open the Ar valve, and turn-off the heating of the oven.
- **Cool-down (1 hour 30 minutes):** When the temperature goes below 400°C, it is possible to open the oven to speed-up the cool-down. When the temperature is below 200°C (10 minutes later), one can close the H<sub>2</sub> valve, to save some H<sub>2</sub>.
- When the temperature displayed by the oven is below 80°C (this is the temperature inside the oven close to the resistors and does not correspond to the real temperature of the chip.), close all the valves, and open the oven.

- Do not forget to close all the bottles.

# Appendix B

## Supplementary material on chapter 4

### B.1 Theory of the low energy spectrum of a Cooper pair splitter

This appendix is a more detailed version of the derivation of the low energy spectrum of a hybrid superconductor double quantum dot given in section 4.3 of the main text. The hamiltonian of a double dot with a central superconducting lead can be written as  $H = H_0 + H_{S-DQD}$ , where  $H_0 = H_{DQD} + H_S$  is the sum of the individual hamiltonians and  $H_{S-DQD}$  describes the coupling between them. Let us recall the explicit expressions for each term:

$$H_{DQD} = \epsilon_L \hat{n}_L + \epsilon_R \hat{n}_R + t_b (c_{L\uparrow}^\dagger c_{R\uparrow} + c_{L\downarrow}^\dagger c_{R\downarrow}) + h.c. \quad (\text{B.1})$$
$$+ U_m \hat{n}_L \hat{n}_R + \frac{1}{2} U_L \hat{n}_L (\hat{n}_L - 1) + \frac{1}{2} U_R \hat{n}_R (\hat{n}_R - 1)$$

$$H_S = \sum_{k\sigma} E_k \gamma_{k\sigma}^\dagger \gamma_{k\sigma} \quad (\text{B.2})$$

$$H_{S-DQD} = \sum_{k\sigma, i \in \{L, R\}} t_i^* \mathcal{A}_{k\sigma}^i c_{j\sigma}^\dagger + h.c. \quad (\text{B.3})$$

where  $t_i \equiv \sqrt{\Gamma_{S_i}}$  and:

$$\mathcal{A}_{k\sigma}^j = \sum_{k\sigma, j \in \{L, R\}} e^{ik \cdot r_j} u_k \gamma_{k\sigma} + \sigma e^{-ik \cdot r_j} v_{-k} \gamma_{\bar{\sigma}}^\dagger \quad (\text{B.4})$$

with  $u_k$  and  $v_k$  as conventionally defined in the BCS theory.

The main step of the derivation is to write an effective hamiltonian to second order in the tunnel couplings  $t_i$  of the superconductor to the two dots using a Schrieffer-Wolf transformation, also called adiabatic elimination in atomic physics [74, 153]. The idea is to find a unitary transformation which cancels the tunneling term up to second order in tunneling. The effective hamiltonian reads:

$$\hat{H}_{eff} = e^{-S} \hat{H} e^S \approx \hat{H} - [S, \hat{H}] + \frac{1}{2} [S, [S, \hat{H}]] + \dots$$

If S is constructed such that  $[S, \hat{H}_0] = \hat{H}_{S-DQD}$ , the effective hamiltonian becomes:

$$\hat{H}_{eff} \approx \hat{H}_0 - \frac{1}{2} [S, \hat{H}_{S-DQD}]$$

One seeks for the operator S in the following form:

$$S = \sum_{k, \sigma, j \in \{L, R\}} \gamma_{k\sigma} X_{k\sigma}^j - h.c$$

The constraints for the operator S can be fulfilled if  $X_{k\sigma}^j$  has the following matrix elements:

$$\langle l | X_{k\sigma}^j | m \rangle = \frac{-t_j \sigma e^{ik \cdot r_j} v_{-k}^* \langle l | d_{j\sigma} | m \rangle + t_j^* e^{ik \cdot r_j} u_k \langle l | d_{j\sigma}^\dagger | m \rangle}{E_k + E_m - E_l} \quad (\text{B.5})$$

This allows us to calculate explicit expressions of the double quantum dot effective hamiltonian by using the ground state of the superconductor in the initial and final states and states in which one quasiparticle is excited in the superconductor as intermediate states. In the bonding/antibonding basis, we get, setting  $\delta r = r_L - r_R$  the distance between tunneling to left and right dots:

$$\begin{aligned}
& \langle +|[S, \hat{H}_{S-DQD}]|-\rangle = \tag{B.6} \\
& \sum_k |u_k|^2 \left( \frac{1}{E_k - E_+} + \frac{1}{E_k - E_-} \right) \{ -uv(|t_L|^2 - |t_R|^2) + t_L^* t_R e^{ik \cdot \delta r} u^2 - t_R^* t_L e^{-ik \cdot \delta r} v^2 \} \\
& - |v_{-k}|^2 \left( \frac{1}{E_k - E_+ + \epsilon_\Sigma} + \frac{1}{E_k - E_- + \epsilon_\Sigma} \right) \{ (uv(|t_L|^2 - |t_R|^2) + t_L^* t_R e^{-ik \cdot \delta r} u^2 - t_R^* t_L e^{ik \cdot \delta r} v^2) \}
\end{aligned}$$

We get similar expressions for  $\langle +|[S, \hat{H}_{S-DQD}]|+\rangle$  and  $\langle -|[S, \hat{H}_{S-DQD}]|-\rangle$ . In order to obtain useful analytical expressions, we use the following identities, taking the 1D limit similarly to ref. [177], assuming the tunnel coupling  $t_i$  is real and setting  $t_i = \sqrt{\Gamma_{Si}}$ , to second order in  $\frac{\epsilon}{\Delta}$  where  $\epsilon$  is the energy of the state:

$$\begin{aligned}
& t_i t_j \sum_k u_k v_{-k} \frac{e^{ik \cdot \delta r}}{E_k + \epsilon} = \tag{B.7} \\
& \sqrt{\Gamma_{Si} \Gamma_{Sj}} \left( \pi - \frac{2\epsilon}{\Delta} + \frac{\pi}{2} \frac{\epsilon^2}{\Delta^2} + \dots \right) \text{ for } \delta r = 0 \\
& \pi \sqrt{\Gamma_{Si} \Gamma_{Sj}} \cos(k_F \delta r) e^{-\delta r / \xi_0} \left( 1 - \sqrt{\frac{2|\delta r|}{\pi \xi_0}} \frac{\epsilon}{\Delta} + \frac{|\delta r|}{2\xi_0} \frac{\epsilon^2}{\Delta^2} + \dots \right) \text{ for } \delta r \gg \xi_0
\end{aligned}$$

$$\begin{aligned}
& t_i t_j \sum_k |u_k|^2 \frac{e^{ik \cdot \delta r}}{E_k + \epsilon} = \tag{B.8} \\
& \sqrt{\Gamma_{Si} \Gamma_{Sj}} \left( \text{Ln} \frac{2\omega_D}{\Delta} - \frac{\pi}{2} \frac{\epsilon}{\Delta} + \frac{\epsilon^2}{\Delta^2} + \dots \right) \text{ for } \delta r = 0 \\
& \pi \sqrt{\Gamma_{Si} \Gamma_{Sj}} \cos(k_F \delta r) e^{-\delta r / \xi_0} \left( \sqrt{\frac{\pi \xi_0}{2|\delta r|}} - \frac{\pi}{2} \frac{\epsilon}{\Delta} + \sqrt{\frac{\pi |\delta r|}{2\xi_0}} \frac{\epsilon^2}{\Delta^2} + \dots \right) \text{ for } \delta r \gg \xi_0
\end{aligned}$$

where  $\omega_D$  is the Debye angular frequency, used as a cut-off and  $\Delta$  is the superconducting gap. It is interesting to note that  $\sqrt{\Gamma_{SL} \Gamma_{SRC}} \cos k_F \delta r e^{-\delta r / \xi_0}$  is the Cooper pair splitting amplitude which appears both here in the renormalization of the bonding/anti-bonding states as well as in the hybridization between the  $|S\rangle$  and the  $|0,0\rangle$ . We note:

$$t_{eh}^0 = \sqrt{\Gamma_{SL} \Gamma_{SRC}} \cos k_F \delta r e^{-\delta r / \xi_0}. \tag{B.9}$$

Projecting the effective hamiltonian on the  $\{|+\rangle, |-\rangle\}$ , we get:

$$\hat{H}_{eff} = (E_+ + \delta E_+) |+\rangle \langle +| + (E_- + \delta E_-) |-\rangle \langle -| + \delta t_b |+\rangle \langle -| + \delta t_b |-\rangle \langle +| \quad (\text{B.10})$$

where the expressions for the perturbative elements close to the degeneracy line between (0,1)/(1,0) charge states are given in the main text.

## B.2 Experimental details

### B.2.1 Sample fabrication and measurement setup

The sample fabrication process is the following. A 150nm thick Nb film is first evaporated on a thermal silicon oxide (500nm)/high resistivity ( $10k\Omega\cdot\text{cm}$ ) silicon substrate at rate of 1nm/s and a pressure of  $10^{-9}$  mbar. The cavity is made subsequently using photolithography combined with reactive ion etching (SF6 process). Carbon nanotubes are grown with Chemical Vapor Deposition technique (CVD) at about 900°C using a methane process on a separate quartz substrate and stamped inside the cavity. The nanotubes are then localized. The fork top gate oxide is made using 3 evaporation steps of Al (2nm) followed each by an oxidation of 10 min under an O<sub>2</sub> pressure of 1 mbar. The Alox is covered by a Al(40nm)/Pd(20nm) layer. The nanotube is contacted with a central Pd(4nm)/Al(80nm) finger and two Pd(70nm) outer electrodes.

The DC measurements are carried out using standard lock-in detection techniques with a modulation frequency of 137 Hz and an amplitude of 10  $\mu\text{V}$ . The base temperature of the experiment is 18 mK. The microwave measurements are carried out using room temperature microwave amplifiers and a cryogenic amplifier (noise temperature about 5K) with a total gain of about 90 dB. We measure both quadratures of the transmitted microwave signal using an I-Q mixer and low frequency modulation at 2.7 kHz.

### B.2.2 Supplementary data: double dot stability diagram

Fig. B.1 shows current (a) and phase contrast (b) color maps as a function of the two side gate voltages  $V_L$  and  $V_R$  for sample A. For this measurement, the two normal electrodes were biased with equal voltages with respect to the superconducting electrode, where the

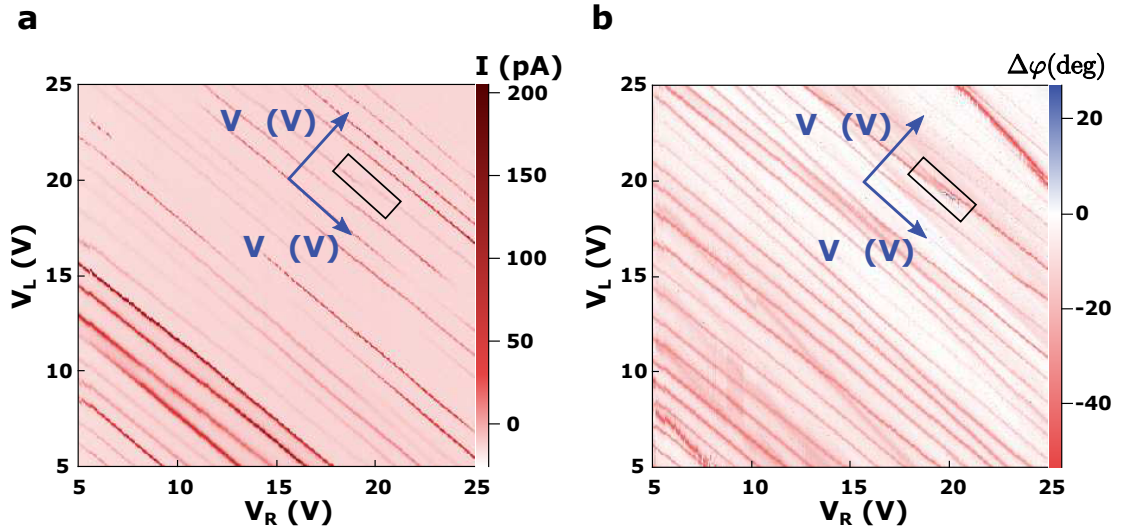


FIGURE B.1: Large scale characterization of sample A in the  $V_L$ - $V_R$  plane. Current (a) and phase contrast (b) color maps as a function of the two side gate voltages  $V_L$  and  $V_R$  for sample A. The black rectangle indicates the area Aa under study in the main text. The blue axis show the relative orientation of the  $V_\Sigma$ - $V_\delta$  frame, which was used to measure all data presented in this paper for sample A. Note that for clarity the frame origin chosen at ( $V_L = 20$  V ;  $V_R = 20$  V) is shifted on the figure.

current was measured. The zone labelled Aa in the paper is enclosed in a black rectangle. The lines avoided crossing in the current and the sign change of the phase contrast are indicative of a local double dot behaviour, where an internal transition is resonant with the cavity. To better resolve the features of this area in a shorter time, further measurements were carried out using the orthonormal frame  $V_\Sigma$ - $V_\delta$ , which results from a 42 degrees clockwise rotation of the original frame  $V_L$ - $V_R$  and a translation of the origin to ( $V_L = 20$  V ;  $V_R = 20$  V).

Such a resolved characterization of Sample Aa resonant area is presented on Fig. 4.3a, 4.3 c and B.2 showing the simultaneously measured transmitted cavity signal phase and amplitude and differential conductances respectively. Fig. B.2 shows a clear avoided crossing in transport measurements, which means that sample A locally behaves as a double quantum dot. The transport characterization of Sample B does not show any measurable currents above our noise level  $\sim 1$  pA.

### B.2.3 Supplementary data: hybridization of cavity-dot system

Figure B.3 illustrates how the photonic and electronic degrees of freedom hybridize when the gates of the devices are tuned into the strong coupling region. Fig. B.3b (resp. B.3d)

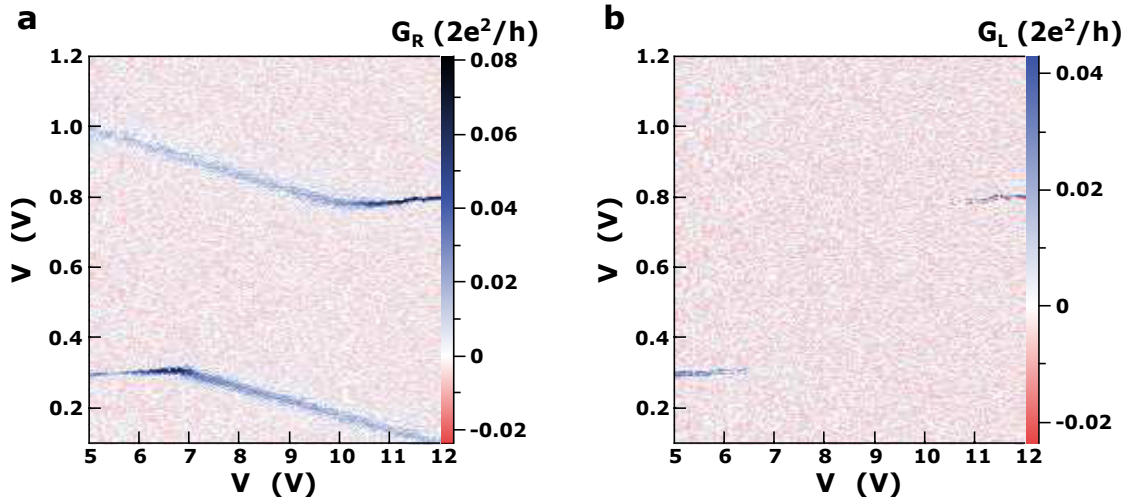


FIGURE B.2: Double dot stability diagram in transport measurement for sample A. Right (a) and left (b) differential conductance maps in the rotated gate-gate frame  $V_{\Sigma} - V_{\delta}$  with a bias voltage  $V_S = -0.16$  mV applied to the superconducting electrode. This measurement is simultaneous with the cavity transmission measurement presented in Fig. 4.3a for the phase and 4.3c for the amplitude.

displays for sample A (resp. Sample B) the amplitude of the microwave transmitted signal as a function of the detuning  $f - f_c$  between probe frequency  $f$  and cavity bare resonance frequency  $f_c$  and the gate voltage  $V_{\delta}$  (resp.  $V_L$ ). The latter parameter range together with the constant value of  $V_{\Sigma}$  (resp.  $V_R$ ) where the measurement is performed, is indicated by a black dashed line on panel a (resp. b). Changing the dot gate voltage tunes the quantum dot circuit transition frequency in and out of resonance with the cavity: the resonance condition is accompanied by large distortions in the cavity transmission demonstrating a strong coupling between photonic and electronic degrees of freedom.

### B.3 Vacuum Rabi splitting power dependence modelling

In this section we present the modelling of the vacuum Rabi splittings shown in figure 4.5a and 4.5c of the main text. In both figures, a misalignment is visible between the center of the Rabi splitting peaks and the recovered coherent state at high power, whereas the spectral weight of the two peaks at low power remains the same. Such a misalignment can be accounted for by a two transition structure depicted in figure 4.5b. This contrasts with the case of a single electronic transition involved, where this shift would automatically be accompanied by asymmetric spectral weights on the two peaks.

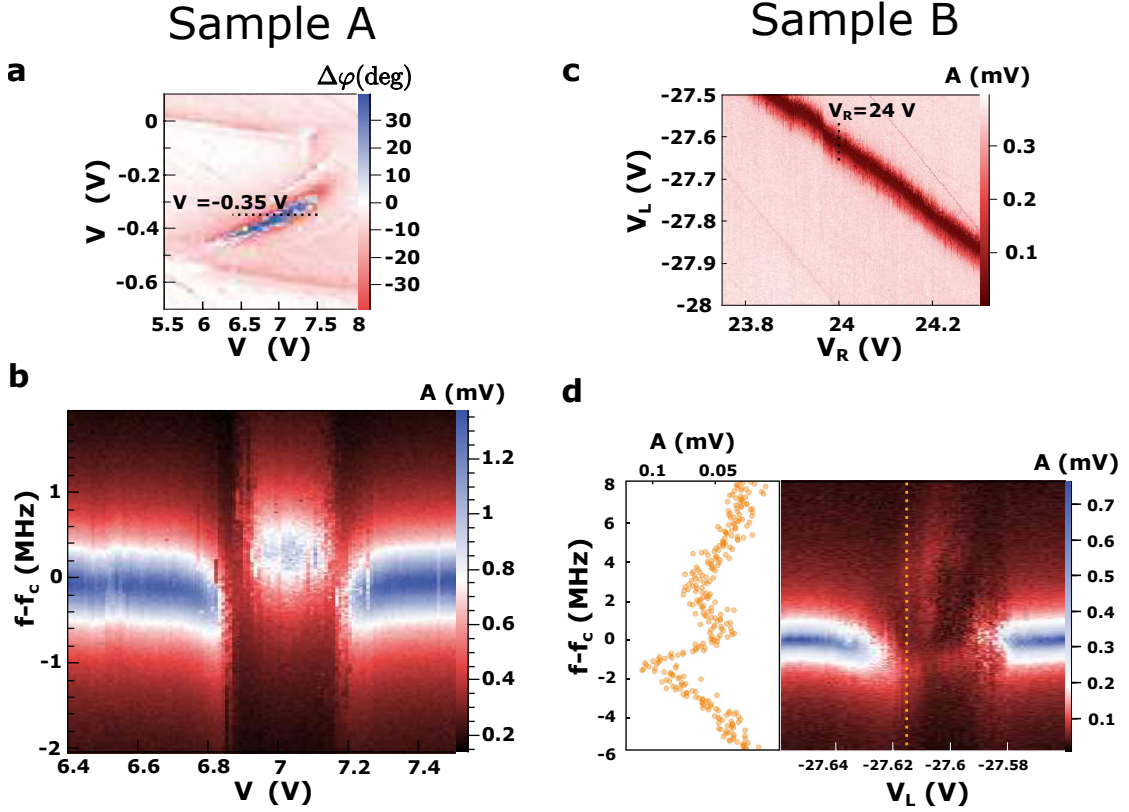


FIGURE B.3: Phase map as a function of  $V_\delta$  and  $V_\Sigma$  for sample A. The black dotted line indicate for which parameters the cavity spectra are shown on b. **b.** Cavity spectrum as a function  $V_\delta$  for sample A. **c.** Phase map as a function of  $V_L$  and  $V_\Sigma$  for sample B. The black dotted line indicate for which parameters the cavity spectra are shown on d. **d.** Cavity spectrum as a function  $V_L$  for sample B. The orange vertical dotted line shows the cut along which the spectrum showing the Rabi splitting on the left has been taken.

	$\frac{\kappa}{2\pi}$	$f_c$	$\frac{g_K}{2\pi}$	$f_K$	$\frac{\Gamma_{\varphi,K}}{2\pi}$	$\frac{\gamma_K}{2\pi}$	$\frac{g_{K'}}{2\pi}$	$f_{K'}$	$\frac{\Gamma_{\varphi,K'}}{2\pi}$	$\frac{\gamma_{K'}}{2\pi}$
Fig 5a	0.57	6636.4	4.6	6640.5	0	2	16.8	6586	0	100
Fig 5c	0.42	6636.2	1.4	6637.8	0.4	0.8	4.2	6636	5	6

TABLE B.1: Summary of parameters used in the two transitions modelling (in MHz).  $\kappa$ ,  $f_c$  are respectively the decay rate and the resonance frequency of the cavity.  $g_i$ ,  $f_i$ ,  $\Gamma_{\varphi,i}$ , and  $\gamma_i$  are respectively the coupling strength, the frequency, the dephasing rate, and the decay rate of transition  $i \in \{K, K'\}$ .

We can account for this asymmetric splitting with respect to the coherent state peak at the cavity frequency recovered at high power, while keeping similar spectral weight on each peak, with the two transition scheme depicted in figure 4.5b. As an example, we give three different transmission spectra with their theoretical fit in figure 4.5c. The sets of parameters used to reproduce all the transmission spectra are given in table B.1. The photon number used in the model is 7dB lower than the estimated experimental photon number used as x-axis in figure 4.5c.

# Appendix C

## Stapling carbon nanotubes

### C.1 Growth and localization of the carbon nanotubes

#### C.1.1 Catalyst recipe

- Rinse the catalyst bottle with IPA in the sonic-bath for 10 minutes.
- With a buret, take 60mL of IPA.
- Weigh 78mg of  $Fe(NO_3)_3 - H_2O$  in a handmade aluminum cup using the weighing scale of Vincent Croquette. Put the  $Fe(NO_3)_3 - H_2O$  in the catalyst bottle, and rinse the aluminum cup with a small portion of the 60mL of IPA into the catalyst bottle.
- Do the same with 15.8mg of  $MoO_2$ , and 64mg of  $Al_2O_3$ .
- Put the remaining of IPA in the catalyst bottle.

#### C.1.2 Catalyst deposition

- Put the catalyst solution in the sonic-bath for **1 hour**.
- Let the catalyst solution decant for **45 minutes**. unscrew the cover before this step in order to shake the solution as less as possible once the decantation is over.

- Fill a becher with IPA. This becher will be used for rinsing the cantilever chip after the catalyst deposition, so it is better to use a dedicated becher that is polluted with catalyst nanoparticles.
- With a pipette, take a bit of the catalyst solution from the surface. Maintain the cantilever chip on the clean room paper using the tweezers (with the cantilever surface on the top), and put 2 or 3 drops on the chip.
- Quickly after the deposition, rinse the cantilever chip with IPA for 10 seconds in the dedicated becher. This step allows to obtain a more homogeneous catalyst deposition, in particular, catalyst particles reach more easily the tips of the cantilever.
- Dry the cantilever chip using the pressurized nitrogen gun, while maintaining it on the clean room paper with tweezers.
- Observe with the optical microscope in the “*Dark field*” mode the catalyst density at the tips of the cantilevers. If the catalyst density is too low, the deposition of few drops of catalyst can be repeated using the same technique.

### C.1.3 CNT growth

The growth recipe used is the so-called “*standard*” recipe:

- Note the offset values of the  $Ar$ ,  $CH_4$ , and  $H_2$  flows.

**8 mins Purge of the lines:** Open the valves of the  $Ar$ ,  $CH_4$ , and  $H_2$  lines. The flows used in the growth recipe are:  $Flow(Ar) = 1350sccm$ ,  $Flow(CH_4) = 1100sccm$ , and  $Flow(H_2) = 300sccm$  with respect to the offset values. If the measured flows are far from those target values (more than  $100sccm$ ), you can tune them on the valves panel.

**25 mins Heating of the oven  $900^\circ C$**  under a  $Ar$  flow.

**5 mins Flash  $H_2$ :** Close the  $Ar$  valve, and open the  $H_2$  one.

**15 mins Carbone nanotubes growth:** Open the  $CH_4$  valve.

- **Oven cooling down:** Close the  $CH_4$  valve, open the  $Ar$  valve, and turn off the oven heating. When the oven temperature is below  $200^\circ C$  you can close the  $H_2$  valve, and open the oven to speed-up the cooling down. Once the oven temperature is below  $70^\circ C$ , you can take the cantilever chips out of the quartz tube.

In order to limit the exposition of the CNT to the air, it is important to schedule a SEM time slot for the localization of the CNT the same day of the growth, and then store the CNT gelpak in the stapler chamber.

#### C.1.4 CNT localization

To localize the CNTs suspended between cantilevers, an easy way is to use SEM (even if the common belief is that it creates amorphous carbon around the CNT). An undamaged chip possesses 48 cantilevers. In case of broken cantilevers, one should take a picture of all the cantilever to avoid mistakes in the numbering of the CNTs.



FIGURE C.1: Convention of position of the cantilever chip inside the SEM, and numbering of the cantilevers.

One can do the focus/stigmatism tuning on the catalyst nanoparticles at the tips of the cantilevers, which is the area of interest. The column parameters are:

- Magnification:  $\times 2000$
- EHT:  $2kV$
- aperture size:  $30\mu m$
- High brightness: the cantilevers have to be completely white to hope seeing suspended CNTs in between.

**Criteria to choose a CNT** The SEM is definitely not the best tool to characterize carbon nanotubes (single or multi-walled, bundle or not, diameter, chirality), but it allows at least to know their position and whether or not they are huge bundles. Here are a few criteria to identify CNTs good for stapling:

- The CNT has to be in the first  $10\mu\text{m}$  starting from the tips of the cantilevers.
- It has to be well separated from other suspended CNTs (more than  $5\mu\text{m}$ , see figure C.2.c).
- It should look like a single-walled carbon nanotube, or at least not a huge bundle of CNTs. This means that it should be thin, and there should be no visible braiding (V-shape) at the attach on the cantilevers (see figure C.2.b and C.2.d).
- It is preferable to have a taut CNT, in order to obtain a suspended CNT in the resulting circuit (see figure C.2.a).

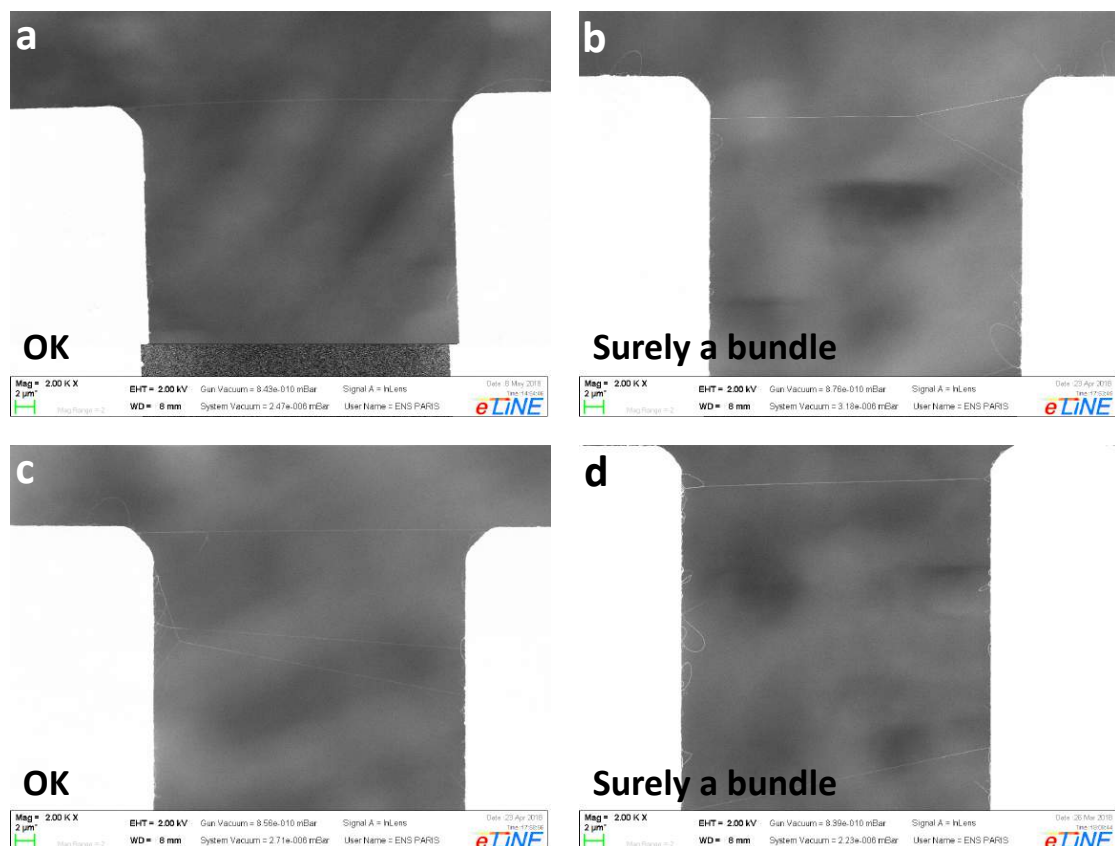


FIGURE C.2: **a.** This CNT fulfills all the criteria, and it is quite well taut. **b.** This CNT seems to be a bundle, based on the V-shape at the right cantilever, its high contrast, and its width. **c.** There are multiple CNTs, but the first one is sufficiently separated from the other ones.

## C.2 Preparation of the stapling

### C.2.1 Fixing of the sample holder to the rotating arm

The positioning of the sample holder can be tricky. First, it has to be low enough such that the cantilever holder (see figure C.3) fit in between the sample holder and the window of the cover. Secondly, it has to be high enough to be able to do the focus with the microscope on the circuit chip surface through the window of the stapler's cover. It is possible that those two conditions are not fulfilled (depending on the geometry of the sample holder), in this case, one can envision to rotate the sample holder when the cantilever chip is brought over the circuit.

One also has to **check the possible shunts** in the circuit chip by testing individually each contacts and gates while leaving the others grounded (this can be done using the *cutting* electrical setup (see figure C.7).

### C.2.2 Fixing of the cantilever chip and tuning its angle

Choose the cantilever chip with most of the CNTs fulfilling the previous criteria.

#### **Fixing the cantilever chip:**

- Unscrew the piezo-motor block (see figure C.3), and rotate it so that the cantilever chip holder (see figure C.3) is pointing up.
- Glue the chosen cantilever on the cantilever chip holder with PMMA (you can use a toothpick to drop the PMMA off), and wait 5 minutes for the PMMA to dry. During this waiting time, one can close the vacuum chamber with the cover (without pumping) to protect the CNTs.

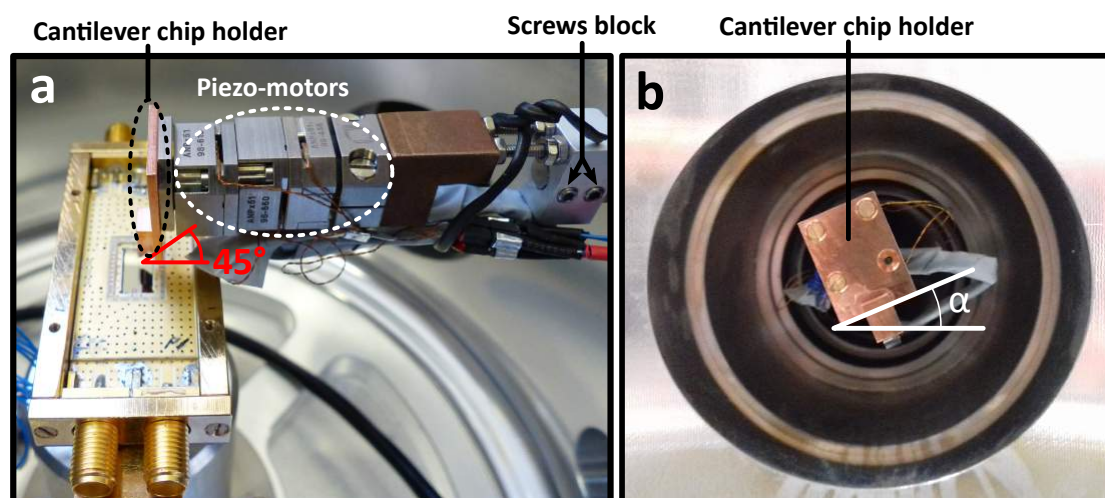


FIGURE C.3: The stapling chamber: **a.** The circuit and the cantilevers in the stapling configuration. The piezo-motor block is quite delicate and should be manipulated only via the screws block. **b.** View of the cantilever holder in the axis of the accordion. The angle  $\alpha$  determines which cantilever will touch first the circuit chip.

**Tuning of the cantilever chip angle:** The idea is to have a small angle between the cantilevers and the circuit chip in order to know which side of the cantilever chip will touch the circuit chip first. Thus, you have to choose if you want the cantilever 48 to touch first or the cantilever 1, depending on where are the good looking CNTs.

- Rotate back the piezo-motor block so that the cantilevers are pointing down (in the stapling position). Normally, the cantilever 1 should be on the side of the turbomolecular pump, and the cantilever 48 should be on the side of the rotary feedthrough (to which the sample holder is attached).
- Screw the piezo-motor block, but not too tight so that it is still possible to rotate it.
- With the micromanipulator place the cantilever chip over a reflecting surface, for instance you can use the cover of the sample holder.
- To estimate the angle  $\alpha$  (see figure C.3.b) of the cantilever chip, first one has to do the focus on the tips of the cantilever 1 for instance, and then check if the cantilever 48 is above or below the focus plan of cantilever 1. Then adjust the angle  $\alpha$  manually, so that the desired cantilever (1 or 48) touch first. A difference of 50 graduations between the focus on the cantilever 1 and the cantilever 48 is sufficient.

## Pumping

- Before to launch the pumping of the stapling chamber, be sure that the cantilever chip is far from any object in the chamber (more than 1 centimetre), since at the beginning of the pumping the accordion is contracting and this make the cantilever chip to translate by few millimetres.
- Open the valve to the primary pump, V1 (see figure C.4).
- Wait for the pressure to be below  $5 \times 10^{-1}$  mbar, close V1, and open V2 then V3.

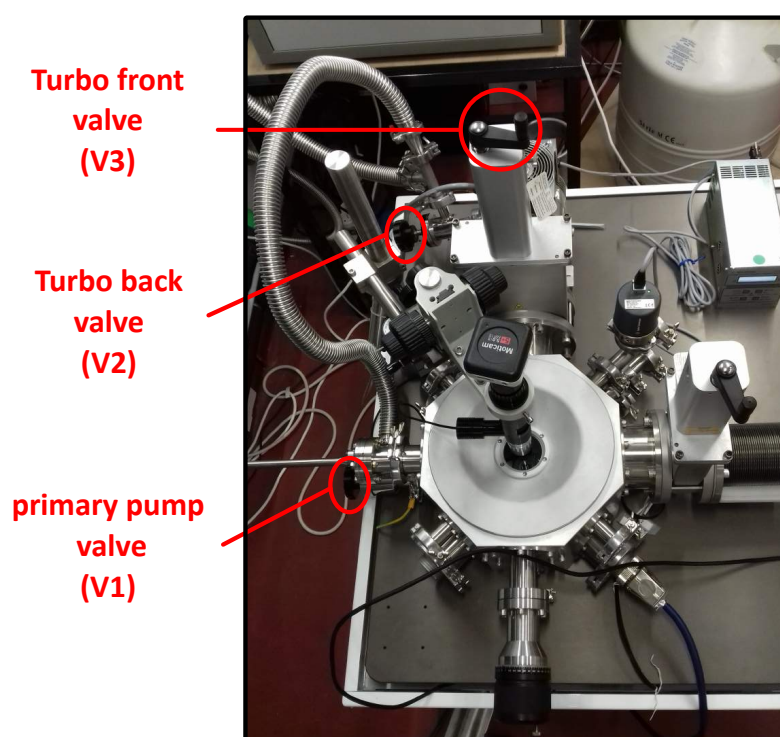


FIGURE C.4: The Stapler

## C.3 Stapling

- Wait for the pressure to be in the range of  $10^{-7}$  mbar.
- Align the pair of cantilevers with the desired CNT with respect to the circuit lines using the micromanipulator for the coarse alignment, and the piezo-motors for the fine one (the range of each piezo-motor is  $\pm 1$  mm). At this stage, one has to be very careful not to touch the stapler table. It is quite easy to break all the cantilevers in a single shot...

- Set the detection setup (see figure C.5), with a bias voltage  $V_{app} = 500mV$ .

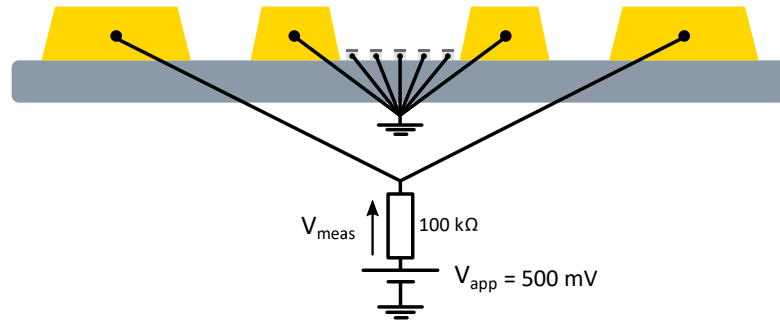


FIGURE C.5: Detection setup

- Lower the cantilever chip first using the "continuous" option (see figure C.6) as long as the cantilever chip is far enough from the circuit (more than 500 graduations on the focus between the circuit and the cantilevers), and then for the fine approach use the "step" option. You know when a cantilever is touching the bottom of the trench, when it start to elongate from our top view (due to its deflection).



FIGURE C.6: Piezo-motor controller

- Depending on the contacts width, the detection signal can be a current spike as low as  $100pA$  simultaneous to a step of the piezo motors. Thus it is important to look constantly at the current measurement during the approach stage.
- Once the contact with a CNT has been detected, the next step is to cut sequentially it on the two external sections sequentially. Apply the bias voltage on one of the external cutting contact, put the neighboring contact to the ground, and all the

other contacts and gates to a floating potential (i.e. in the 'connected' position on the switch box but with no cable on the SMA port) as shown in figure C.7.

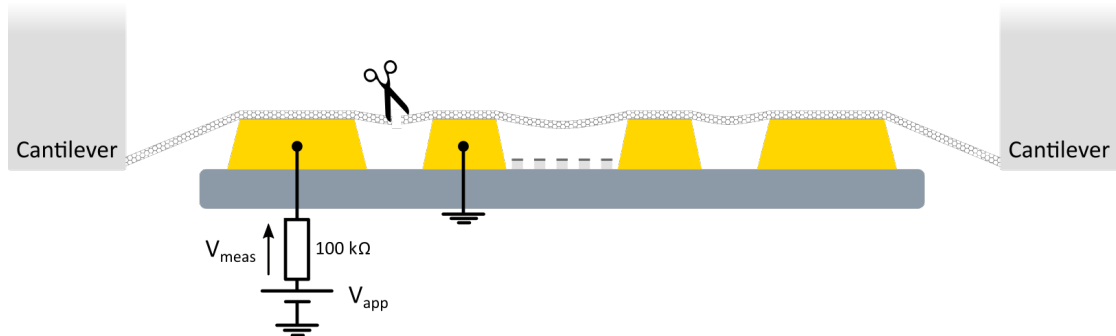


FIGURE C.7: Cutting setup

- Launch a *sweep\_Vsd...* measurement on Exopy to follow the cutting (do not forget to increment the measurement index by 1...), and be ready to stop the measurement when the current collapses. There is no need to go too much above the cutting voltage. Do the same on the other external section. In figure C.8, few examples of cutting curves are shown.
- once the CNT has been cut on the two external sections, one can check if the CNT is still connected to the source and drain contacts (it happened that the cutting procedure also cut the central portion...).
- Now one can safely raise the cantilever using the piezo-motor, while measuring the current in the central portion (but in principle it should not be affected by the raising of the cantilever chip). Retract the cantilever chip using the micromanipulator and put it back in the accordion.
- Measure the resistance of the central portion at  $V_{SD} = 10mV$  (including the voltage divider). To characterize the quality of the contacts, it is important to always measure the resistance at the same bias since the current does not have a linear behavior with respect to the bias voltage.
- If the resistance of the central portion is too high (few  $M\Omega$ ), one can try to decrease it by driving a large current through the central portion by means of the cutting setup. One can launch a *monitoring...* measurement on Exopy to follow the evolution of the current with time, while increasing step by step the bias voltage.

The risk here is to accidentally cut the CNT. The rule of thumb is to not exceed the cutting current of the two external sections. Measure again the resistance of the central portion at  $V_{SD} = 10mV$  to quantify the improvement of the contact resistance using the setup shown in figure C.9.

- One can measure the gate dependence of the Source-Drain current (*sweep  $V_g$ ...* measurement in Exopy), to know whether the CNT is a semiconducting, a metallic or a narrow gap CNT (with the setup in figure C.9).

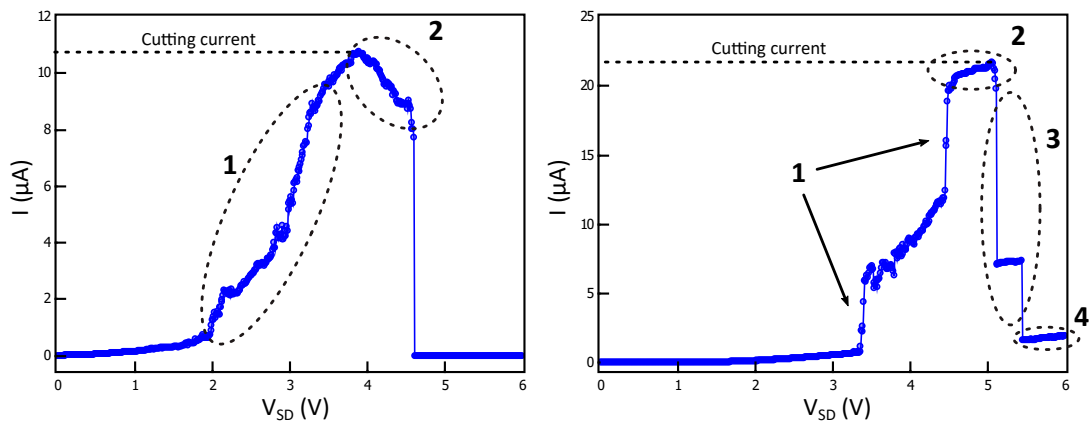


FIGURE C.8: **I-V curves during the cutting of the CNT:** **1.** Improvement of the contact resistance. **2.** Before the cutting of the CNT, the current saturates, and in some case it can even decrease with increasing bias voltage. This last behavior can be explained by electron scattering by optical phonons. The **cutting current** typically lay in between  $10\mu A$  and  $20\mu A$ . The cutting current value is connected to the ability of the CNT to dissipate heat. Thus it will depends on the intrinsic properties of the CNT, but also on the length over which the CNT is suspended. A large cutting current value ( $> 20-30\mu A$ ) can have several reasons: a short distance between the two contacts involved in the cutting (make the heat dissipation easier), the presence of multiple CNT (a bundle), a CNT with a large diameter. **3.** The presence of multiple drop is a strong indicator for bundles. **4.** A remaining current after the current fall can be either due to a second CNT still standing, or due to a contact between the CNT and the silicon at the bottom of the trench. To check this last possibility, one can put all the contacts to a floating potential (except the one which is biased) and see if the current remains. The CNT cutting can be seen as a first electrical characterization of the stapled CNT.

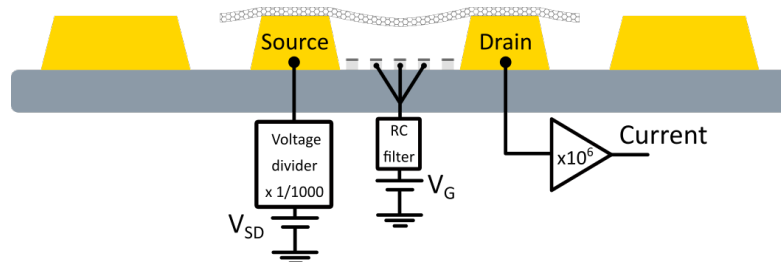


FIGURE C.9: Setup for measurement of the resistance of the circuit and its gate dependence.

## C.4 Tranfering the circuit to the cryostat

- Put  $10M\Omega$  resistors on the DC box of the cryostat on the lines you will use as the source and drain contacts. This is a safety to limit possible transient currents during the connection of the stapled CNT to the cryostat DC lines.
- Put the switches on the DC box in the *connected* position (acting on the switches while the CNT is in ambient air may burn the CNT due to the believed high transient currents at the switching moment).
- Check the DC setup of the cryostat by testing the DC lines you will use with a resistor box.
- Check that the voltage source you will use is set to **0 Volt**, and **OUTPUT ON**.
- Take the ground of the cryostat using the cable with  $10M\Omega$  inside (see figure C.10). You will connect the DC lines of the sample holder to it.

To limit the exposition of the stapled CNT to ambient air, it is important to do the transfer to cryostat as fast as possible. Thus, prior to vent the stapler vacuum chamber, one should rehears the different following steps:

- On the cryostat computer, launch a *monitoring...* measurement on Exopy to be able to follow the resistance of the CNT once it has been connected to the cryostat lines.
- Close the sample holder with the cover using the wobble stick.
- Close V3, and V2.
- Put yourself to the ground of the cryostat using the cable with  $10M\Omega$  inside (see figure C.10) and the dedicated wristband.
- Vent the vacuum chamber of the stapler with argon, while maintaining the cover on the sample holder.
- Connect the DC lines of the sample holder to the grounding cable (which is connected to the ground of the cryostat), then disconnect them from the lines of the stapler.

- Unscrew the sample holder from the rotary arm.
- Screw it to the cold arm of the cryostat.
- Connect the DC lines of the sample holder to the lines of the stapler, then disconnect them from the grounding cable.

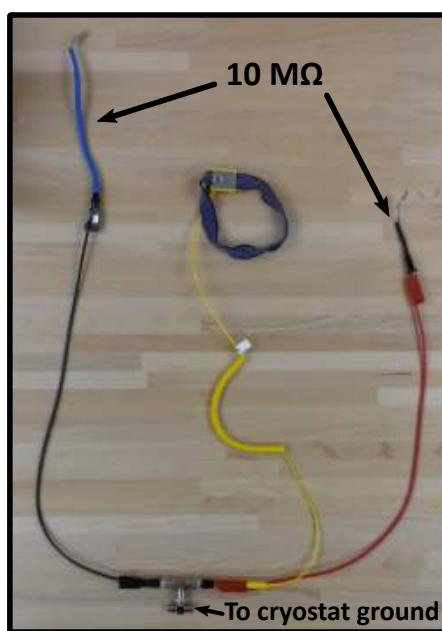


FIGURE C.10: Grounding cable including  $10M\Omega$  resistors.

## Appendix D

# SNR improvement with a I/Q-mixer

Before to be acquired by the ADC card, the signal is first down-converted in a mixer. In order to improve the Signal to Noise Ratio (SNR), one can use a IQ-mixer for this purpose, as depicted in figure D.1.

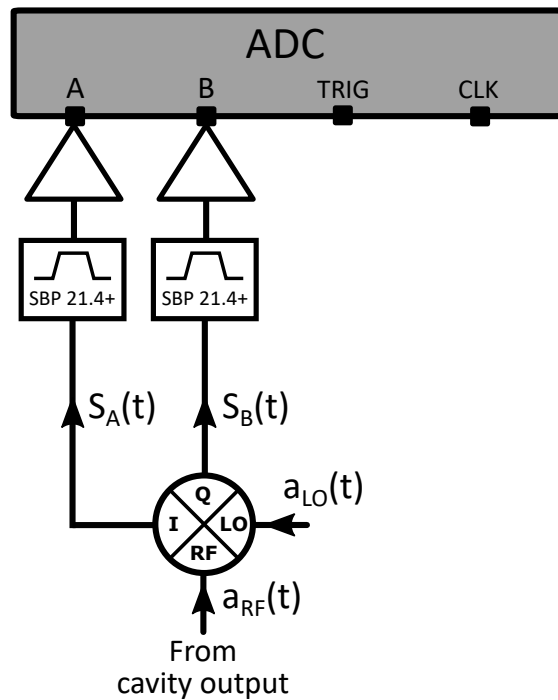


FIGURE D.1: RF circuit at the ADC card input

The signal at the output of the cavity reads:

$$a_{RF}(t) = I(t)\cos(\omega_C t) + Q(t)\sin(\omega_C t) + n(t) \quad (\text{D.1})$$

with  $n(t)$  the noise in the cavity output signal:

$$\begin{aligned} n(t) &= n_1(t)\cos(\omega_C t) + n'_1(t)\sin(\omega_C t) \\ &+ n_2(t)\cos(\omega_C t + 2\Delta t) + n'_2(t)\sin(\omega_C t + 2\Delta t) \end{aligned} \quad (\text{D.2})$$

Here we only focus on the noise at the pulsations  $\omega_C$ , and  $\omega_C + \Delta$ , where  $\Delta = \omega_{LO} - \omega_C \simeq 20\text{MHz}$ , because these are the two frequencies that will not be attenuated by the band-pass filter (minicircuit SBP 21.4+). After the demodulation by the local oscillator signal ( $a_{LO}(t) = a_{LO}\cos(\omega_{LO}t)$ ), the incoming signal on port A (connected to the I-port of the mixer !),  $S_A(t)$  reads:

$$\begin{aligned} S_A(t) &= \frac{a_{LO}(t)}{2} \left[ I(t)\cos((\omega_C - \omega_{LO})t) + Q(t)\sin((\omega_C - \omega_{LO})t) \right. \\ &+ n_1(t)\cos((\omega_C - \omega_{LO})t) + n'_1(t)\sin((\omega_C - \omega_{LO})t) \\ &\left. + n_2(t)\cos((\omega_C - \omega_{LO} + 2\Delta)t) + n'_2(t)\sin((\omega_C - \omega_{LO} + 2\Delta)t) \right] \end{aligned} \quad (\text{D.3})$$

$$S_A(t) = \underbrace{\frac{a_{LO}(t)}{2} [I(t) + n_1(t) + n_2(t)]}_{I_A(t)} \cos(\Delta t) + \underbrace{\frac{a_{LO}(t)}{2} [-Q(t) - n'_1(t) + n'_2(t)]}_{Q_A(t)} \sin(\Delta t) \quad (\text{D.4})$$

where the terms with a frequency out of the filter band have already been eliminated.

Similarly, we have:

$$S_B(t) = \underbrace{\frac{a_{LO}(t)}{2} [Q(t) + n'_1(t) + n'_2(t)]}_{I_B(t)} \cos(\Delta t) + \underbrace{\frac{a_{LO}(t)}{2} [I(t) - n_2(t) + n_1(t)]}_{Q_B(t)} \sin(\Delta t) \quad (\text{D.5})$$

Hence, one can define  $I_{tot}(t)$  and  $Q_{tot}(t)$  such that:

$$\boxed{I_{tot}(t) = I_A(t) + Q_B(t) = a_{LO}(t)(I(t) + n_1(t))} \quad (\text{D.6})$$

$$\boxed{Q_{tot}(t) = I_B(t) - Q_A(t) = a_{LO}(t)(Q(t) + n'_1(t))} \quad (\text{D.7})$$

one can notice that in the terms  $I_A(t)$ ,  $I_B(t)$ ,  $Q_A(t)$ , and  $Q_B(t)$  there are always two terms of noise, while in  $I_{tot}(t)$ , and  $Q_{tot}(t)$  there is only one. A sanity check consists in measuring  $I_A(t) - Q_B(t)$ , and  $I_B(t) + Q_A(t)$  which should give only noise.

# Bibliography

- [1] B. J. van Wees, H. van Houten, C. W J Beenakker, J. G. Williamson, L. P. Kouwenhoven, D. van der Marel, and C. T. Foxon. Quantized conductance of point contacts in a two-dimensional electron gas. *Physical Review Letters*, 60(9): 848–850, feb 1988. ISSN 0031-9007. doi: 10.1103/PhysRevLett.60.848. URL <https://link.aps.org/doi/10.1103/PhysRevLett.60.848>.
- [2] D A Wharam, T J Thornton, R Newbury, M Pepper, H Ahmed, J E F Frost, D G Hasko, D C Peacock, D A Ritchie, and G A C Jones. One-dimensional transport and the quantisation of the ballistic resistance. *Journal of Physics C: Solid State Physics*, 21(8):L209–L214, mar 1988. ISSN 0022-3719. doi: 10.1088/0022-3719/21/8/002. URL <http://stacks.iop.org/0022-3719/21/i=8/a=002?key=crossref.40ba473b30570130e0293beaa10e4cf6>.
- [3] Edward a. Laird, Ferdinand Kuemmeth, Gary A. Steele, Kasper Grove-Rasmussen, Jesper Nygård, Karsten Flensberg, and Leo P. Kouwenhoven. Quantum transport in carbon nanotubes. *Reviews of Modern Physics*, 87(3):703–764, jul 2015. ISSN 0034-6861. doi: 10.1103/RevModPhys.87.703. URL <https://link.aps.org/doi/10.1103/RevModPhys.87.703>.
- [4] J. Waissman, M. Honig, S. Pecker, A. Benyamini, A. Hamo, and S. Ilani. Realization of pristine and locally tunable one-dimensional electron systems in carbon nanotubes. *Nature Nanotechnology*, 8(8):569–574, aug 2013. ISSN 1748-3387. doi: 10.1038/nnano.2013.143. URL <http://www.nature.com/articles/nnano.2013.143>.
- [5] Clément Sayrin, Igor Dotsenko, Xingxing Zhou, Bruno Peaudecerf, Théo Rybarczyk, Sébastien Gleyzes, Pierre Rouchon, Mazyar Mirrahimi, Hadis Amini, Michel Brune, Jean-Michel Raimond, and Serge Haroche. Real-time quantum

- feedback prepares and stabilizes photon number states. *Nature*, 477(7362):73–77, sep 2011. ISSN 0028-0836. doi: 10.1038/nature10376. URL <http://www.nature.com/articles/nature10376>.
- [6] J. M. Raimond, M. Brune, and S. Haroche. Manipulating quantum entanglement with atoms and photons in a cavity. *Reviews of Modern Physics*, 73(3):565–582, aug 2001. ISSN 0034-6861. doi: 10.1103/RevModPhys.73.565. URL <https://link.aps.org/doi/10.1103/RevModPhys.73.565>.
- [7] I. Dotsenko, M. Mirrahimi, M. Brune, S. Haroche, J.-M. Raimond, and P. Rouchon. Quantum feedback by discrete quantum nondemolition measurements: Towards on-demand generation of photon-number states. *Physical Review A*, 80(1):013805, jul 2009. ISSN 1050-2947. doi: 10.1103/PhysRevA.80.013805. URL <https://link.aps.org/doi/10.1103/PhysRevA.80.013805>.
- [8] Luigi Frunzio, Andreas Wallraff, David Schuster, Johannes Majer, and Robert Schoelkopf. Fabrication and Characterization of Superconducting Circuit QED Devices for Quantum Computation. *IEEE Transactions on Applied Superconductivity*, 15(2):860–863, jun 2005. ISSN 1051-8223. doi: 10.1109/TASC.2005.850084. URL <http://ieeexplore.ieee.org/document/1439774/>.
- [9] MH Devoret, A Wallraff, and JM Martinis. *Experimental Aspects of Quantum Computing*. Springer US, Boston, MA, 2005. ISBN 978-0-387-23045-0. doi: 10.1007/0-387-27732-3. URL <http://arxiv.org/abs/cond-mat/0411174>.
- [10] Matthew Reagor, Wolfgang Pfaff, Christopher Axline, Reinier W. Heeres, Nissim Ofek, Katrina Sliwa, Eric Holland, Chen Wang, Jacob Blumoff, Kevin Chou, Michael J. Hatridge, Luigi Frunzio, Michel H. Devoret, Liang Jiang, and Robert J. Schoelkopf. Quantum memory with millisecond coherence in circuit QED. *Physical Review B*, 94(1):014506, jul 2016. ISSN 2469-9950. doi: 10.1103/PhysRevB.94.014506. URL <https://link.aps.org/doi/10.1103/PhysRevB.94.014506>.
- [11] L. Childress, A. S. Sørensen, and M. D. Lukin. Mesoscopic cavity quantum electrodynamics with quantum dots. *Physical Review A*, 69(4):042302, 2004. ISSN 1050-2947. doi: 10.1103/PhysRevA.69.042302. URL <http://link.aps.org/doi/10.1103/PhysRevA.69.042302>.

- [12] X Mi, J V Cady, D M Zajac, P W Deelman, and J R Petta. Strong coupling of a single electron in silicon to a microwave photon. *Science*, 355(6321):156–158, jan 2017. ISSN 0036-8075. doi: 10.1126/science.aal2469. URL <http://www.sciencemag.org/lookup/doi/10.1126/science.aal2469>.
- [13] A. Stockklauser, P. Scarlino, J. V. Koski, S. Gasparinetti, C. K. Andersen, C. Reichl, W. Wegscheider, T. Ihn, K. Ensslin, and A. Wallraff. Strong Coupling Cavity QED with Gate-Defined Double Quantum Dots Enabled by a High Impedance Resonator. *Physical Review X*, 7(1):011030, mar 2017. ISSN 2160-3308. doi: 10.1103/PhysRevX.7.011030. URL <https://link.aps.org/doi/10.1103/PhysRevX.7.011030>.
- [14] L. E Bruhat, T. Cubaynes, J. J. Viennot, M. C. Dartiailh, M. M. Desjardins, A. Cottet, and T. Kontos. Circuit QED with a quantum-dot charge qubit dressed by Cooper pairs. *Physical Review B*, 98(15):155313, oct 2018. ISSN 2469-9950. doi: 10.1103/PhysRevB.98.155313. URL <https://link.aps.org/doi/10.1103/PhysRevB.98.155313>.
- [15] T. H. Oosterkamp, L. P. Kouwenhoven, A. E. A. Koolen, N. C. van der Vaart, and C. J. P. M. Harmans. Photon Sidebands of the Ground State and First Excited State of a Quantum Dot. *Physical Review Letters*, 78(8):1536–1539, feb 1997. ISSN 0031-9007. doi: 10.1103/PhysRevLett.78.1536. URL <https://link.aps.org/doi/10.1103/PhysRevLett.78.1536>.
- [16] Nakul Shaji, C. B. Simmons, Madhu Thalakulam, Levente J. Klein, Hua Qin, H. Luo, D. E. Savage, M. G. Lagally, A. J. Rimberg, R. Joynt, M. Friesen, R. H. Blick, S. N. Coppersmith, and M. A. Eriksson. Spin blockade and lifetime-enhanced transport in a few-electron Si/SiGe double quantum dot. *Nature Physics*, 4(7):540–544, jul 2008. ISSN 1745-2473. doi: 10.1038/nphys988. URL <http://www.nature.com/articles/nphys988>.
- [17] C. Thelander, T. Mårtensson, M. T. Björk, B. J. Ohlsson, M. W. Larsson, L. R. Wallenberg, and L. Samuelson. Single-electron transistors in heterostructure nanowires. *Applied Physics Letters*, 83(10):2052–2054, sep 2003. ISSN 0003-6951. doi: 10.1063/1.1606889. URL <http://aip.scitation.org/doi/10.1063/1.1606889>.

- [18] V. Mourik, K. Zuo, S. M. Frolov, S. R. Plissard, E. P. a. M. Bakkers, and L. P. Kouwenhoven. Signatures of Majorana Fermions in Hybrid Superconductor-Semiconductor Nanowire Devices. *Science*, 336(6084):1003–1007, may 2012. ISSN 0036-8075. doi: 10.1126/science.1222360. URL <http://www.sciencemag.org/cgi/doi/10.1126/science.1222360>.
- [19] J. Güttinger, T. Frey, C. Stampfer, T. Ihn, and K. Ensslin. Spin States in Graphene Quantum Dots. *Physical Review Letters*, 105(11):116801, sep 2010. ISSN 0031-9007. doi: 10.1103/PhysRevLett.105.116801. URL <https://link.aps.org/doi/10.1103/PhysRevLett.105.116801>.
- [20] N Mason. Local Gate Control of a Carbon Nanotube Double Quantum Dot. *Science*, 303(5658):655–658, jan 2004. ISSN 0036-8075. doi: 10.1126/science.1093605. URL <http://www.sciencemag.org/cgi/doi/10.1126/science.1093605>.
- [21] Pablo Jarillo-Herrero, Jorden a. van Dam, and Leo P. Kouwenhoven. Quantum supercurrent transistors in carbon nanotubes. *Nature*, 439(7079):953–956, feb 2006. ISSN 0028-0836. doi: 10.1038/nature04550. URL <http://www.nature.com/articles/nature04550>.
- [22] J.-P. Cleuziou, W. Wernsdorfer, V. Bouchiat, T. Ondarçuhu, and M. Monthieux. Carbon nanotube superconducting quantum interference device. *Nature Nanotechnology*, 1(1):53–59, oct 2006. ISSN 1748-3387. doi: 10.1038/nnano.2006.54. URL <http://www.nature.com/articles/nnano.2006.54>.
- [23] L Hofstetter, S Csonka, J Nygard, and C Schonenberger. Cooper pair splitter realized in a two-quantum-dot Y-junction. *Nature*, 461(7266):960–963, 2009. ISSN 0028-0836. doi: 10.1038/nature08432. URL <http://www.ncbi.nlm.nih.gov/pubmed/19829377>.
- [24] L. G. Herrmann, F. Portier, P. Roche, a. Levy Yeyati, T. Kontos, and C. Strunk. Carbon Nanotubes as Cooper-Pair Beam Splitters. *Physical Review Letters*, 104(2):026801, jan 2010. ISSN 0031-9007. doi: 10.1103/PhysRevLett.104.026801. URL <https://link.aps.org/doi/10.1103/PhysRevLett.104.026801>.
- [25] Z.B. Tan, D. Cox, T. Nieminen, P. Lähteenmäki, D. Golubev, G.B. Lesovik, and P.J. Hakonen. Cooper Pair Splitting by Means of Graphene Quantum Dots. *Physical Review Letters*, 114(9):096602, 2015. ISSN 0031-9007. doi:

- 10.1103/PhysRevLett.114.096602. URL <http://link.aps.org/doi/10.1103/PhysRevLett.114.096602>.
- [26] J. J. Viennot, M. C. Dartiailh, Audrey Cottet, and Takis Kontos. Coherent coupling of a single spin to microwave cavity photons. *Science*, 349(6246):408–411, jul 2015. ISSN 0036-8075. doi: 10.1126/science.aaa3786. URL <http://www.sciencemag.org/cgi/doi/10.1126/science.aaa3786>.
- [27] F. Kuemmeth, S. Ilani, D. C. Ralph, and P. L. McEuen. Coupling of spin and orbital motion of electrons in carbon nanotubes. *Nature*, 452(7186):448–452, mar 2008. ISSN 0028-0836. doi: 10.1038/nature06822. URL <http://www.nature.com/articles/nature06822>.
- [28] C. R. Dean, A. F. Young, I. Meric, C. Lee, L. Wang, S. Sorgenfrei, K. Watanabe, T. Taniguchi, P. Kim, K. L. Shepard, and J. Hone. Boron nitride substrates for high-quality graphene electronics. *Nature Nanotechnology*, 5(10):722–726, oct 2010. ISSN 1748-3387. doi: 10.1038/nnano.2010.172. URL <http://www.nature.com/articles/nnano.2010.172>.
- [29] E. D. Minot, Yuval Yaish, Vera Sazonova, Ji-Yong Park, Markus Brink, and Paul L. McEuen. Tuning Carbon Nanotube Band Gaps with Strain. *Physical Review Letters*, 90(15):156401, apr 2003. ISSN 0031-9007. doi: 10.1103/PhysRevLett.90.156401. URL <https://link.aps.org/doi/10.1103/PhysRevLett.90.156401>.
- [30] Thomas Sand Jespersen, Kasper Grove-Rasmussen, Jens Paaske, Koji Muraki, Toshimasa Fujisawa, Jesper Nygård, and Karsten Flensberg. Gate-dependent spinorbit coupling in multielectron carbon nanotubes. *Nature Physics*, 7(4):348–353, apr 2011. ISSN 1745-2473. doi: 10.1038/nphys1880. URL <http://www.nature.com/articles/nphys1880>.
- [31] G.A. Steele, F. Pei, E.A. Laird, J.M. Jol, H.B. Meerwaldt, and L.P. Kouwenhoven. Large spin-orbit coupling in carbon nanotubes. *Nature Communications*, 4(1):1573, dec 2013. ISSN 2041-1723. doi: 10.1038/ncomms2584. URL <http://www.nature.com/articles/ncomms2584>.
- [32] Ali Javey, Jing Guo, Qian Wang, Mark Lundstrom, and Hongjie Dai. Ballistic carbon nanotube field-effect transistors. *Nature*, 424(6949):654–657, aug 2003. ISSN

- 0028-0836. doi: 10.1038/nature01797. URL <http://www.nature.com/articles/nature01797>.
- [33] J. Gorman, D. G. Hasko, and D. A. Williams. Charge-Qubit Operation of an Isolated Double Quantum Dot. *Physical Review Letters*, 95(9):090502, aug 2005. ISSN 0031-9007. doi: 10.1103/PhysRevLett.95.090502. URL <https://link.aps.org/doi/10.1103/PhysRevLett.95.090502>.
- [34] J R Petta. Coherent Manipulation of Coupled Electron Spins in Semiconductor Quantum Dots. *Science*, 309(5744):2180–2184, sep 2005. ISSN 0036-8075. doi: 10.1126/science.1116955. URL <http://www.sciencemag.org/cgi/doi/10.1126/science.1116955>.
- [35] M. Pioro-Ladrière, T. Obata, Y. Tokura, Y.-S. Shin, T. Kubo, K. Yoshida, T. Taniyama, and S. Tarucha. Electrically driven single-electron spin resonance in a slanting Zeeman field. *Nature Physics*, 4(10):776–779, oct 2008. ISSN 1745-2473. doi: 10.1038/nphys1053. URL <http://www.nature.com/articles/nphys1053>.
- [36] W. G. van der Wiel, S. De Franceschi, J. M. Elzerman, T. Fujisawa, S. Tarucha, and L. P. Kouwenhoven. Electron transport through double quantum dots. *Reviews of Modern Physics*, 75(1):1–22, dec 2002. ISSN 0034-6861. doi: 10.1103/RevModPhys.75.1. URL <https://link.aps.org/doi/10.1103/RevModPhys.75.1>.
- [37] R. Hanson, L. P. Kouwenhoven, J. R. Petta, S. Tarucha, and L. M K Vandersypen. Spins in few-electron quantum dots. *Reviews of Modern Physics*, 79(4):1217–1265, oct 2007. ISSN 0034-6861. doi: 10.1103/RevModPhys.79.1217. URL <https://link.aps.org/doi/10.1103/RevModPhys.79.1217>.
- [38] Sami Sapmaz, Carola Meyer, Piotr Beliczynski, Pablo Jarillo-Herrero, and Leo P. Kouwenhoven. Excited State Spectroscopy in Carbon Nanotube Double Quantum Dots. *Nano Letters*, 6(7):1350–1355, jul 2006. ISSN 1530-6984. doi: 10.1021/nl052498e. URL <http://pubs.acs.org/doi/abs/10.1021/nl052498e>.
- [39] F. Molitor, H. Knowles, S. Dröscher, U. Gasser, T. Choi, P. Rouleau, J. Güttinger, A. Jacobsen, C. Stampfer, K. Ensslin, and T. Ihn. Observation of excited states in a graphene double quantum dot. *EPL (Europhysics Letters)*, 89(6):67005, mar 2010. ISSN 0295-5075. doi: 10.1209/0295-5075/

- 89/67005. URL <http://stacks.iop.org/0295-5075/89/i=6/a=67005?key=crossref.06698f460e1c67f7a09873c40f13c8de>.
- [40] Xing Lan Liu, Dorothee Hug, and Lieven M. K. Vandersypen. Gate-defined graphene double quantum dot and excited state spectroscopy. *Nano Letters*, 10(5):1623–1627, may 2010. ISSN 1530-6984. doi: 10.1021/nl9040912. URL <http://pubs.acs.org/doi/abs/10.1021/nl9040912>.
- [41] Fei Pei, Edward a. Laird, Gary a. Steele, and Leo P. Kouwenhoven. Valley spin blockade and spin resonance in carbon nanotubes. *Nature Nanotechnology*, 7(10):630–634, oct 2012. ISSN 1748-3387. doi: 10.1038/nnano.2012.160. URL <http://www.nature.com/articles/nnano.2012.160>.
- [42] Daniel Loss and David P. DiVincenzo. Quantum computation with quantum dots. *Physical Review A*, 57(1):120–126, jan 1998. ISSN 1050-2947. doi: 10.1103/PhysRevA.57.120. URL <https://link.aps.org/doi/10.1103/PhysRevA.57.120>.
- [43] L. M K Vandersypen and I. L. Chuang. NMR techniques for quantum control and computation. *Reviews of Modern Physics*, 76(4):1037–1069, jan 2005. ISSN 0034-6861. doi: 10.1103/RevModPhys.76.1037. URL <https://link.aps.org/doi/10.1103/RevModPhys.76.1037>.
- [44] T. Frey, P. J. Leek, M. Beck, A. Blais, T. Ihn, K. Ensslin, and A. Wallraff. Dipole Coupling of a Double Quantum Dot to a Microwave Resonator. *Physical Review Letters*, 108(4):046807, jan 2012. ISSN 0031-9007. doi: 10.1103/PhysRevLett.108.046807. URL <https://link.aps.org/doi/10.1103/PhysRevLett.108.046807>.
- [45] M. R. Delbecq, V. Schmitt, F. D. Parmentier, N. Roch, J. J. Viennot, G. Fève, B. Huard, C. Mora, A. Cottet, and T. Kontos. Coupling a Quantum Dot, Fermionic Leads, and a Microwave Cavity on a Chip. *Physical Review Letters*, 107(25):256804, dec 2011. ISSN 0031-9007. doi: 10.1103/PhysRevLett.107.256804. URL <https://link.aps.org/doi/10.1103/PhysRevLett.107.256804>.
- [46] Zhan Shi, C. B. Simmons, Daniel R. Ward, J. R. Prance, R. T. Mohr, Teck Seng Koh, John King Gamble, Xian Wu, D. E. Savage, M. G. Lagally, Mark Friesen, S. N. Coppersmith, and M. A. Eriksson. Coherent quantum oscillations and echo measurements of a Si charge qubit. *Physical Review B*, 88(7):075416, aug 2013.

- ISSN 1098-0121. doi: 10.1103/PhysRevB.88.075416. URL <https://link.aps.org/doi/10.1103/PhysRevB.88.075416>.
- [47] T. Hayashi, T. Fujisawa, H. D. Cheong, Y. H. Jeong, and Y. Hirayama. Coherent Manipulation of Electronic States in a Double Quantum Dot. *Physical Review Letters*, 91(22):226804, nov 2003. ISSN 0031-9007. doi: 10.1103/PhysRevLett.91.226804. URL <https://link.aps.org/doi/10.1103/PhysRevLett.91.226804>.
- [48] Gang Cao, Hai-Ou Li, Tao Tu, Li Wang, Cheng Zhou, Ming Xiao, Guang-Can Guo, Hong-Wen Jiang, and Guo-Ping Guo. Ultrafast universal quantum control of a quantum-dot charge qubit using LandauZenerStückelberg interference. *Nature Communications*, 4(1):1401, dec 2013. ISSN 2041-1723. doi: 10.1038/ncomms2412. URL <http://www.nature.com/articles/ncomms2412>.
- [49] K. D. Petersson, J. R. Petta, H. Lu, and A. C. Gossard. Quantum Coherence in a One-Electron Semiconductor Charge Qubit. *Physical Review Letters*, 105(24):246804, dec 2010. ISSN 0031-9007. doi: 10.1103/PhysRevLett.105.246804. URL <https://link.aps.org/doi/10.1103/PhysRevLett.105.246804>.
- [50] J. J. Viennot, M. R. Delbecq, M. C. Dartiailh, A. Cottet, and T. Kontos. Out-of-equilibrium charge dynamics in a hybrid circuit quantum electrodynamics architecture. *Physical Review B*, 89(16):165404, 2014. ISSN 1098-0121. doi: 10.1103/PhysRevB.89.165404. URL <http://link.aps.org/doi/10.1103/PhysRevB.89.165404>.
- [51] P Scarlino, D. J. van Woerkom, A Stockklauser, J V Koski, M C Collodo, S Gasparinetti, C Reichl, W Wegscheider, T Ihn, K Ensslin, and A Wallraff. All-Microwave Control and Dispersive Readout of Gate-Defined Quantum Dot Qubits in Circuit Quantum Electrodynamics. *arXiv*, 1(1), 2017. URL <http://arxiv.org/abs/1711.01906>.
- [52] N. Bar-Gill, L. M. Pham, A. Jarmola, D. Budker, and R. L. Walsworth. Solid-state electronic spin coherence time approaching one second. *Nature Communications*, 4:1743–1746, 2013. ISSN 20411723. doi: 10.1038/ncomms2771. URL <http://dx.doi.org/10.1038/ncomms2771>.
- [53] N Samkharadze, G Zheng, N Kalhor, D Brousse, A Sammak, U C Mendes, A Blais, G Scappucci, and L M K Vandersypen. Strong spin-photon coupling in silicon.

- Science*, 359(6380):1123–1127, mar 2018. ISSN 0036-8075. doi: 10.1126/science.aar4054. URL <http://www.ncbi.nlm.nih.gov/pubmed/29371427><http://www.sciencemag.org/lookup/doi/10.1126/science.aar4054>.
- [54] A J Landig, J. V. Koski, P. Scarlino, U. C. Mendes, A. Blais, C. Reichl, W. Wegscheider, A. Wallraff, K. Ensslin, and T. Ihn. Coherent spinphoton coupling using a resonant exchange qubit. *Nature*, 560(7717):179–184, aug 2018. ISSN 0028-0836. doi: 10.1038/s41586-018-0365-y. URL <http://www.nature.com/articles/s41586-018-0365-y>.
- [55] X. Mi, M. Benito, S. Putz, D. M. Zajac, J. M. Taylor, Guido Burkard, and J. R. Petta. A coherent spinphoton interface in silicon. *Nature*, 555(7698):599–603, feb 2018. ISSN 0028-0836. doi: 10.1038/nature25769. URL <http://www.nature.com/doi/10.1038/nature25769>.
- [56] S. R. Foltyn, L. Civale, J. L. MacManus-Driscoll, Q. X. Jia, B. Maiorov, H. Wang, and M. Maley. Materials science challenges for high-temperature superconducting wire. *Nature Materials*, 6(9):631–642, sep 2007. ISSN 1476-1122. doi: 10.1038/nmat1989. URL <http://www.nature.com/articles/nmat1989>.
- [57] H. Fröhlich. Theory of the Superconducting State. I. The Ground State at the Absolute Zero of Temperature. *Physical Review*, 79(5):845–856, sep 1950. ISSN 0031-899X. doi: 10.1103/PhysRev.79.845. URL <https://link.aps.org/doi/10.1103/PhysRev.79.845>.
- [58] John Bardeen and David Pines. Electron-Phonon Interaction in Metals. *Physical Review*, 99(4):1140–1150, aug 1955. ISSN 0031-899X. doi: 10.1103/PhysRev.99.1140. URL <https://link.aps.org/doi/10.1103/PhysRev.99.1140>.
- [59] Leon N. Cooper. Bound Electron Pairs in a Degenerate Fermi Gas. *Physical Review*, 104(4):1189–1190, nov 1956. ISSN 0031-899X. doi: 10.1103/PhysRev.104.1189. URL <https://link.aps.org/doi/10.1103/PhysRev.104.1189>.
- [60] J. Bardeen, L. N. Cooper, and J. R. Schrieffer. Theory of Superconductivity. *Physical Review*, 108(5):1175–1204, dec 1957. ISSN 0031-899X. doi: 10.1103/PhysRev.108.1175. URL <https://link.aps.org/doi/10.1103/PhysRev.108.1175>.
- [61] Michael Tinkham. *Introduction to Superconductivity*, volume 38. Dover, dover edition, 2004.

- [62] James F. Annett. *Superconductivity, Superfluids and Condensates*. Number May. Oxford, oxford edition, 2004.
- [63] A Yu Kitaev. Unpaired Majorana fermions in quantum wires. *Physics-Uspekhi*, 44(10S):131–136, oct 2001. ISSN 1468-4780. doi: 10.1070/1063-7869/44/10S/S29. URL <http://arxiv.org/abs/cond-mat/0010440>.
- [64] J-D. Pillet, C. H. L. Quay, P. Morfin, C. Bena, a. Levy Yeyati, and P. Joyez. Andreev bound states in supercurrent-carrying carbon nanotubes revealed. *Nature Physics*, 6(12):965–969, dec 2010. ISSN 1745-2473. doi: 10.1038/nphys1811. URL <http://www.nature.com/articles/nphys1811>.
- [65] Patrik Recher, Eugene V. Sukhorukov, and Daniel Loss. Andreev tunneling, Coulomb blockade, and resonant transport of nonlocal spin-entangled electrons. *Physical Review B*, 63(16):11, 2001. ISSN 0163-1829. doi: 10.1103/PhysRevB.63.165314. URL <http://link.aps.org/doi/10.1103/PhysRevB.63.165314>.
- [66] D. F. Walls and Gerard J. Milburn. *Quantum Optics*. Springer-Verlag Berlin Heidelberg, 2nd editio edition, 2008.
- [67] L. Hofstetter, S. Csonka, A. Baumgartner, G. Fülöp, S. D’Hollosy, J. Nygård, and C. Schönenberger. Finite-Bias Cooper Pair Splitting. *Physical Review Letters*, 107(13):136801, sep 2011. ISSN 0031-9007. doi: 10.1103/PhysRevLett.107.136801. URL <https://link.aps.org/doi/10.1103/PhysRevLett.107.136801>.
- [68] Anindya Das, Yuval Ronen, Moty Heiblum, Diana Mahalu, Andrey V Kretinin, and Hadas Shtrikman. High-efficiency Cooper pair splitting demonstrated by two-particle conductance resonance and positive noise cross-correlation. *Nature Communications*, 3(May):1165, 2012. ISSN 2041-1723. doi: 10.1038/ncomms2169. URL <http://dx.doi.org/10.1038/ncomms2169>.
- [69] J. Schindele, A. Baumgartner, and C. Schönenberger. Near-Unity Cooper Pair Splitting Efficiency. *Physical Review Letters*, 109(15):157002, oct 2012. ISSN 0031-9007. doi: 10.1103/PhysRevLett.109.157002. URL <https://link.aps.org/doi/10.1103/PhysRevLett.109.157002>.
- [70] I. V. Borzenets, Y. Shimazaki, G. F. Jones, M. F. Craciun, S. Russo, M. Yamamoto, and S. Tarucha. High Efficiency CVD Graphene-lead (Pb) Cooper Pair

- Splitter. *Scientific Reports*, 6:1–8, 2016. ISSN 20452322. doi: 10.1038/srep23051. URL <http://dx.doi.org/10.1038/srep23051>.
- [71] R S Deacon, a Oiwa, J Sailer, S Baba, Y Kanai, K Shibata, K Hirakawa, and S Tarucha. Cooper pair splitting in parallel quantum dot Josephson junctions. *Nature communications*, 6(May 2015):7446, 2015. ISSN 2041-1723. doi: 10.1038/ncomms8446. URL <http://www.ncbi.nlm.nih.gov/pubmed/26130172>.
- [72] Audrey Cottet. Probing coherent Cooper pair splitting with cavity photons. *Physical Review B*, 90(12):125139, sep 2014. ISSN 1098-0121. doi: 10.1103/PhysRevB.90.125139. URL <https://link.aps.org/doi/10.1103/PhysRevB.90.125139>.
- [73] Audrey Cottet, Takis Kontos, and Alfredo Levy Yeyati. Subradiant Split Cooper Pairs. *Physical Review Letters*, 108(16):166803, apr 2012. ISSN 0031-9007. doi: 10.1103/PhysRevLett.108.166803. URL <https://link.aps.org/doi/10.1103/PhysRevLett.108.166803>.
- [74] Patrik Recher, Eugene V. Sukhorukov, and Daniel Loss. Andreev tunneling, Coulomb blockade, and resonant transport of nonlocal spin-entangled electrons. *Physical Review B*, 63(16):165314, apr 2001. ISSN 0163-1829. doi: 10.1103/PhysRevB.63.165314. URL <https://link.aps.org/doi/10.1103/PhysRevB.63.165314>.
- [75] Abram L. Falk, Bob B. Buckley, Greg Calusine, William F. Koehl, Viatcheslav V. Dobrovitski, Alberto Politi, Christian A. Zorman, Philip X L Feng, and David D. Awschalom. Polytype control of spin qubits in silicon carbide. *Nature Communications*, 4(May):1–7, 2013. ISSN 20411723. doi: 10.1038/ncomms2854. URL <http://dx.doi.org/10.1038/ncomms2854>.
- [76] Jarryd J. Pla, Kuan Y. Tan, Juan P. Dehollain, Wee H. Lim, John J.L. Morton, David N. Jamieson, Andrew S. Dzurak, and Andrea Morello. A single-atom electron spin qubit in silicon. *Nature*, 489(7417):541–544, 2012. ISSN 00280836. doi: 10.1038/nature11449. URL <http://dx.doi.org/10.1038/nature11449>.
- [77] L Childress, M V Gurudev Dutt, J M Taylor, a S Zibrov, F Jelezko, J Wrachtrup, P R Hemmer, M D Lukin, and M V Gurudev Dutt. Coherent Dynamics of Coupled Electron and Nuclear Spin Qubits in Diamond. *Science*, 314(5797):281, 2006. ISSN

- 1095-9203. doi: 10.1126/science.1131871. URL <http://www.ncbi.nlm.nih.gov/pubmed/16973839>.
- [78] R. Maurand, X. Jehl, D. Kotekar-Patil, A. Corna, H. Bohuslavskyi, R. Laviéville, L. Hutin, S. Barraud, M. Vinet, M. Sanquer, and S. De Franceschi. A CMOS silicon spin qubit. *Nature Communications*, 7:13575, nov 2016. ISSN 2041-1723. doi: 10.1038/ncomms13575. URL <http://www.nature.com/doifinder/10.1038/ncomms13575>.
- [79] S. Amasha, K. MacLean, Iuliana P. Radu, D. M. Zumbühl, M. A. Kastner, M. P. Hanson, and A. C. Gossard. Electrical Control of Spin Relaxation in a Quantum Dot. *Physical Review Letters*, 100(4):046803, jan 2008. ISSN 0031-9007. doi: 10.1103/PhysRevLett.100.046803. URL <https://link.aps.org/doi/10.1103/PhysRevLett.100.046803>.
- [80] Filip K. Malinowski, Frederico Martins, Peter D. Nissen, Edwin Barnes, Łukasz Cywiński, Mark S. Rudner, Saeed Fallahi, Geoffrey C. Gardner, Michael J. Manfra, Charles M. Marcus, and Ferdinand Kuemmeth. Notch filtering the nuclear environment of a spin qubit. *Nature Nanotechnology*, 12(1):16–20, oct 2016. ISSN 1748-3387. doi: 10.1038/nnano.2016.170. URL <http://www.nature.com/doifinder/10.1038/nnano.2016.170>.
- [81] Y. Kubo, F. R. Ong, P. Bertet, D. Vion, V. Jacques, D. Zheng, A. Dréau, J.-F. Roch, A. Auffeves, F. Jelezko, J. Wrachtrup, M. F. Barthe, P. Bergonzo, and D. Esteve. Strong Coupling of a Spin Ensemble to a Superconducting Resonator. *Physical Review Letters*, 105(14):140502, sep 2010. ISSN 0031-9007. doi: 10.1103/PhysRevLett.105.140502. URL <https://link.aps.org/doi/10.1103/PhysRevLett.105.140502>.
- [82] S. Nadj-Perge, S M Frolov, E P A M Bakkers, and L P Kouwenhoven. Spin-orbit qubit in a semiconductor nanowire. *Nature*, 468(7327):1084–1087, 2010. ISSN 00280836. doi: 10.1038/nature09682. URL <http://dx.doi.org/10.1038/nature09682>.

- [83] Audrey Cottet and Takis Kontos. Spin Quantum Bit with Ferromagnetic Contacts for Circuit QED. *Physical Review Letters*, 105(16):160502, oct 2010. ISSN 0031-9007. doi: 10.1103/PhysRevLett.105.160502. URL <https://link.aps.org/doi/10.1103/PhysRevLett.105.160502>.
- [84] Maximilian Russ and Guido Burkard. Three-electron spin qubits. *Journal of Physics Condensed Matter*, 29(39):aa761f, 2017. ISSN 1361648X. doi: 10.1088/1361-648X/aa761f. URL <https://doi.org/10.1088/1361-648X/aa761f>.
- [85] Xian Wu, D. R. Ward, J. R. Prance, Dohun Kim, John King Gamble, R. T. Mohr, Zhan Shi, D. E. Savage, M. G. Lagally, Mark Friesen, S. N. Coppersmith, and M. A. Eriksson. Two-axis control of a singlet-triplet qubit with an integrated micromagnet. *Proceedings of the National Academy of Sciences*, 111(33):11938–11942, aug 2014. ISSN 0027-8424. doi: 10.1073/pnas.1412230111. URL <http://www.pnas.org/cgi/doi/10.1073/pnas.1412230111>.
- [86] Benoit Bertrand, Hanno Flentje, Shintaro Takada, Michihisa Yamamoto, Seigo Tarucha, Arne Ludwig, Andreas D. Wieck, Christopher Bäuerle, and Tristan Meunier. Quantum Manipulation of Two-Electron Spin States in Isolated Double Quantum Dots. *Physical Review Letters*, 115(9):096801, aug 2015. ISSN 0031-9007. doi: 10.1103/PhysRevLett.115.096801. URL <https://link.aps.org/doi/10.1103/PhysRevLett.115.096801>.
- [87] M. D. Reed, B. M. Maune, R. W. Andrews, M. G. Borselli, K. Eng, M. P. Jura, A. A. Kiselev, T. D. Ladd, S. T. Merkel, I. Milosavljevic, E. J. Pritchett, M. T. Rakher, R. S. Ross, A. E. Schmitz, A. Smith, J. A. Wright, M. F. Gyure, and A. T. Hunter. Reduced Sensitivity to Charge Noise in Semiconductor Spin Qubits via Symmetric Operation. *Physical Review Letters*, 116(11):110402, mar 2016. ISSN 0031-9007. doi: 10.1103/PhysRevLett.116.110402. URL <https://link.aps.org/doi/10.1103/PhysRevLett.116.110402>.
- [88] Frederico Martins, Filip K. Malinowski, Peter D. Nissen, Edwin Barnes, Saeed Fallahi, Geoffrey C. Gardner, Michael J. Manfra, Charles M. Marcus, and Ferdinand Kuemmeth. Noise Suppression Using Symmetric Exchange Gates in Spin Qubits. *Physical Review Letters*, 116(11):116801, mar 2016. ISSN 0031-9007. doi: 10.1103/PhysRevLett.116.116801. URL <https://link.aps.org/doi/10.1103/PhysRevLett.116.116801>.

- [89] K D Petersson, L W McFaul, M D Schroer, M Jung, J M Taylor, A A Houck, and J R Petta. Circuit quantum electrodynamics with a spin qubit. *Nature*, 490(7420):380–383, oct 2012. ISSN 0028-0836. doi: 10.1038/nature11559. URL <http://www.nature.com/articles/nature11559>.
- [90] J. Medford, J. Beil, J. M. Taylor, E. I. Rashba, H. Lu, A. C. Gossard, and C. M. Marcus. Quantum-Dot-Based Resonant Exchange Qubit. *Physical Review Letters*, 111(5):050501, jul 2013. ISSN 0031-9007. doi: 10.1103/PhysRevLett.111.050501. URL <https://link.aps.org/doi/10.1103/PhysRevLett.111.050501>.
- [91] E. Kawakami, P. Scarlino, D. R. Ward, F. R. Braakman, D. E. Savage, M. G. Lagally, Mark Friesen, S. N. Coppersmith, M. A. Eriksson, and L. M.K. Vandersypen. Electrical control of a long-lived spin qubit in a Si/SiGe quantum dot. *Nature Nanotechnology*, 9(9):666–670, 2014. ISSN 17483395. doi: 10.1038/nnano.2014.153. URL <http://dx.doi.org/10.1038/nnano.2014.153>.
- [92] E a Laird, F Pei, and L P Kouwenhoven. A valleypin qubit in a carbon nanotube. *Nature Nanotechnology*, 8(8):565–568, aug 2013. ISSN 1748-3387. doi: 10.1038/nnano.2013.140. URL <http://www.nature.com/articles/nnano.2013.140>.
- [93] Jonathan H. Prechtel, Andreas V. Kuhlmann, Julien Houel, Arne Ludwig, Sascha R. Valentin, Andreas D. Wieck, and Richard J. Warburton. Decoupling a hole spin qubit from the nuclear spins. *Nature Materials*, 15(9):981–986, sep 2016. ISSN 1476-1122. doi: 10.1038/nmat4704. URL <http://www.nature.com/articles/nmat4704>.
- [94] A. Cottet, T. Kontos, W. Belzig, C. Schönenberger, and C. Bruder. Controlling spin in an electronic interferometer with spin-active interfaces. *Europhysics Letters (EPL)*, 74(2):320–326, apr 2006. ISSN 0295-5075. doi: 10.1209/epl/i2006-10006-0. URL <http://stacks.iop.org/0295-5075/74/i=2/a=320?key=crossref.fee7f5fbddf5347a12685cbe5a27b956>.
- [95] D Leibfried, R Blatt, C Monroe, and D Wineland. Quantum dynamics of single trapped ions. *Reviews of Modern Physics*, 75(1):281–324, mar 2003. ISSN 0034-6861. doi: 10.1103/RevModPhys.75.281. URL <https://link.aps.org/doi/10.1103/RevModPhys.75.281>.

- [96] Alexandre Blais, Ren-Shou Huang, Andreas Wallraff, S. M. Girvin, and R. J. Schoelkopf. Cavity quantum electrodynamics for superconducting electrical circuits: An architecture for quantum computation. *Physical Review A*, 69(6):062320, jun 2004. ISSN 1050-2947. doi: 10.1103/PhysRevA.69.062320. URL <https://link.aps.org/doi/10.1103/PhysRevA.69.062320>.
- [97] I. Chiorescu, P. Bertet, K. Semba, Y. Nakamura, C. J. P. M. Harmans, and J. E. Mooij. Coherent dynamics of a flux qubit coupled to a harmonic oscillator. *Nature*, 431(7005):159–162, sep 2004. ISSN 0028-0836. doi: 10.1038/nature02831. URL <http://www.nature.com/articles/nature02831>.
- [98] J. Majer, J. M. Chow, J. M. Gambetta, Jens Koch, B. R. Johnson, J. A. Schreier, L. Frunzio, D. I. Schuster, A. A. Houck, A. Wallraff, A. Blais, M. H. Devoret, S. M. Girvin, and R. J. Schoelkopf. Coupling superconducting qubits via a cavity bus. *Nature*, 449(7161):443–447, sep 2007. ISSN 0028-0836. doi: 10.1038/nature06184. URL <http://www.nature.com/articles/nature06184>.
- [99] Mika A. Sillanpää, Jae I. Park, and Raymond W. Simmonds. Coherent quantum state storage and transfer between two phase qubits via a resonant cavity. *Nature*, 449(7161):438–442, sep 2007. ISSN 0028-0836. doi: 10.1038/nature06124. URL <http://www.nature.com/articles/nature06124>.
- [100] A Fedorov, L Steffen, M Baur, M. P. da Silva, and A Wallraff. Implementation of a Toffoli gate with superconducting circuits. *Nature*, 481(7380):170–172, jan 2012. ISSN 0028-0836. doi: 10.1038/nature10713. URL <http://www.nature.com/articles/nature10713>.
- [101] M. M. Desjardins, J. J. Viennot, M. C. Dartailh, L. E. Bruhat, M. R. Delbecq, M. Lee, M.-S. Choi, A. Cottet, and T. Kontos. Observation of the frozen charge of a Kondo resonance. *Nature*, 545(7652):71–74, apr 2017. ISSN 0028-0836. doi: 10.1038/nature21704. URL <http://dx.doi.org/10.1038/nature21704><http://www.nature.com/doifinder/10.1038/nature21704>.
- [102] a. Cottet, T. Kontos, and B. Douçot. Electron-photon coupling in mesoscopic quantum electrodynamics. *Physical Review B*, 91(20):1–16, 2015. ISSN 1098-0121. doi: 10.1103/PhysRevB.91.205417. URL <http://link.aps.org/doi/10.1103/PhysRevB.91.205417>.

- [103] A. A. Clerk, M. H. Devoret, S. M. Girvin, Florian Marquardt, and R. J. Schoelkopf. Introduction to quantum noise, measurement, and amplification. *Reviews of Modern Physics*, 82(2):1155–1208, apr 2010. ISSN 0034-6861. doi: 10.1103/RevModPhys.82.1155. URL <https://link.aps.org/doi/10.1103/RevModPhys.82.1155>.
- [104] Guang-Wei Deng, Da Wei, J. R. Johansson, Miao-Lei Zhang, Shu-Xiao Li, Hai-Ou Li, Gang Cao, Ming Xiao, Tao Tu, Guang-Can Guo, Hong-Wen Jiang, Franco Nori, and Guo-Ping Guo. Charge Number Dependence of the Dephasing Rates of a Graphene Double Quantum Dot in a Circuit QED Architecture. *Physical Review Letters*, 115(12):126804, sep 2015. ISSN 0031-9007. doi: 10.1103/PhysRevLett.115.126804. URL <https://link.aps.org/doi/10.1103/PhysRevLett.115.126804>.
- [105] A Stockklauser, V. F. Maisi, J Basset, K Cujia, C Reichl, W Wegscheider, T Ihn, A Wallraff, and K Ensslin. Microwave Emission from Hybridized States in a Semiconductor Charge Qubit. *Physical Review Letters*, 115(4):046802, jul 2015. ISSN 0031-9007. doi: 10.1103/PhysRevLett.115.046802. URL <https://link.aps.org/doi/10.1103/PhysRevLett.115.046802>.
- [106] A. Wallraff, D. I. Schuster, A. Blais, L. Frunzio, J. Majer, M. H. Devoret, S. M. Girvin, and R. J. Schoelkopf. Approaching Unit Visibility for Control of a Superconducting Qubit with Dispersive Readout. *Physical Review Letters*, 95(6):060501, aug 2005. ISSN 0031-9007. doi: 10.1103/PhysRevLett.95.060501. URL <https://link.aps.org/doi/10.1103/PhysRevLett.95.060501>.
- [107] Nicolas Didier, Jérôme Bourassa, and Alexandre Blais. Fast Quantum Nondemolition Readout by Parametric Modulation of Longitudinal Qubit-Oscillator Interaction. *Physical Review Letters*, 115(20):203601, nov 2015. ISSN 0031-9007. doi: 10.1103/PhysRevLett.115.203601. URL <https://link.aps.org/doi/10.1103/PhysRevLett.115.203601>.
- [108] M. Brune, F. Schmidt-Kaler, A. Maali, J. Dreyer, E. Hagley, J. M. Raimond, and S. Haroche. Quantum Rabi Oscillation: A Direct Test of Field Quantization in a Cavity. *Physical Review Letters*, 76(11):1800–1803, mar 1996. ISSN 0031-9007. doi: 10.1103/PhysRevLett.76.1800. URL <https://link.aps.org/doi/10.1103/PhysRevLett.76.1800>.

- [109] Lev S. Bishop, J. M. Chow, Jens Koch, A. A. Houck, M. H. Devoret, E. Thuneberg, S. M. Girvin, and R. J. Schoelkopf. Nonlinear response of the vacuum Rabi resonance. *Nature Physics*, 5(2):105–109, 2009. ISSN 17452473. doi: 10.1038/nphys1154. URL <http://dx.doi.org/10.1038/nphys1154>.
- [110] D. I. Schuster, A. A. Houck, J. A. Schreier, A. Wallraff, J. M. Gambetta, A. Blais, L. Frunzio, J. Majer, B. Johnson, M. H. Devoret, S. M. Girvin, and R. J. Schoelkopf. Resolving photon number states in a superconducting circuit. *Nature*, 445(7127):515–518, feb 2007. ISSN 0028-0836. doi: 10.1038/nature05461. URL <http://www.nature.com/doi/10.1038/nature05461>.
- [111] M. Brune, P. Nussenzveig, F. Schmidt-Kaler, F. Bernardot, A. Maali, J. M. Raimond, and S. Haroche. From Lamb shift to light shifts: Vacuum and subphoton cavity fields measured by atomic phase sensitive detection. *Physical Review Letters*, 72(21):3339–3342, may 1994. ISSN 0031-9007. doi: 10.1103/PhysRevLett.72.3339. URL <https://link.aps.org/doi/10.1103/PhysRevLett.72.3339>.
- [112] Karl Blum. *Density Matrix Theory and Applications*. Springer-Verlag Berlin Heidelberg, 3 edition, 2012.
- [113] Audrey Cottet, Matthieu C Dartiailh, Matthieu M Desjardins, Tino Cubaynes, Lauriane C. Contamin, Matthieu Delbecq, Jérémie J. Viennot, Laure E. Bruhat, Benoit Douçot, and Takis Kontos. Cavity QED with hybrid nanocircuits: from atomic-like physics to condensed matter phenomena. *Journal of Physics: Condensed Matter*, 29(43):433002, nov 2017. ISSN 0953-8984. doi: 10.1088/1361-648X/aa7b4d. URL <http://stacks.iop.org/0953-8984/29/i=43/a=433002?key=crossref.f8ce2c6ac32ae5d10535da5e30e94929>.
- [114] K. Geerlings, S. Shankar, E. Edwards, L. Frunzio, R. J. Schoelkopf, and M. H. Devoret. Improving the quality factor of microwave compact resonators by optimizing their geometrical parameters. *Applied Physics Letters*, 100(19):192601, may 2012. ISSN 0003-6951. doi: 10.1063/1.4710520. URL <http://aip.scitation.org/doi/10.1063/1.4710520>.
- [115] N. Samkharadze, A. Bruno, P. Scarlino, G. Zheng, D. P. DiVincenzo, L. DiCarlo, and L. M. K. Vandersypen. High Kinetic Inductance Superconducting Nanowire

- Resonators for Circuit QED in a Magnetic Field. *arXiv*, 1(d):1–10, 2015. URL <http://arxiv.org/abs/1511.01760>.
- [116] Jiansong Gao, Miguel Daal, Anastasios Vayonakis, Shwetank Kumar, Jonas Zmuidzinas, Bernard Sadoulet, Benjamin A. Mazin, Peter K. Day, and Henry G. Leduc. Experimental evidence for a surface distribution of two-level systems in superconducting lithographed microwave resonators. *Applied Physics Letters*, 92(15):152505, apr 2008. ISSN 0003-6951. doi: 10.1063/1.2906373. URL <http://aip.scitation.org/doi/10.1063/1.2906373>.
- [117] Alexander V. Khaetskii, Daniel Loss, and Leonid Glazman. Electron Spin Decoherence in Quantum Dots due to Interaction with Nuclei. *Physical Review Letters*, 88(18):186802, apr 2002. ISSN 0031-9007. doi: 10.1103/PhysRevLett.88.186802. URL <https://link.aps.org/doi/10.1103/PhysRevLett.88.186802>.
- [118] R. Barends, N. Verduyn, A. Endo, P. J. de Visser, T. Zijlstra, T. M. Klapwijk, P. Diener, S. J. C. Yates, and J. J. A. Baselmans. Minimal resonator loss for circuit quantum electrodynamics. *Applied Physics Letters*, 97(2):023508, jul 2010. ISSN 0003-6951. doi: 10.1063/1.3458705. URL <http://aip.scitation.org/doi/10.1063/1.3458705>.
- [119] Jens Koch, Terri M. Yu, Jay Gambetta, A. A. Houck, D. I. Schuster, J. Majer, Alexandre Blais, M. H. Devoret, S. M. Girvin, and R. J. Schoelkopf. Charge-insensitive qubit design derived from the Cooper pair box. *Physical Review A*, 76(4):042319, oct 2007. ISSN 1050-2947. doi: 10.1103/PhysRevA.76.042319. URL <https://link.aps.org/doi/10.1103/PhysRevA.76.042319>.
- [120] M. Bockrath. Single-Electron Transport in Ropes of Carbon Nanotubes. *Science*, 275(5308):1922–1925, mar 1997. ISSN 00368075. doi: 10.1126/science.275.5308.1922. URL <http://www.sciencemag.org/cgi/doi/10.1126/science.275.5308.1922>.
- [121] J. J. Viennot, J. Palomo, and T. Kontos. Stamping single wall nanotubes for circuit quantum electrodynamics. *Applied Physics Letters*, 104(11):113108, mar 2014. ISSN 0003-6951. doi: 10.1063/1.4868868. URL <http://aip.scitation.org/doi/10.1063/1.4868868>.

- [122] S. Blien, K. J. G. Götz, P. L. Stiller, T. Mayer, T. Huber, O. Vavra, and A. K. Hüttel. Towards carbon nanotube growth into superconducting microwave resonator geometries. *physica status solidi (b)*, 253(12):2385–2390, dec 2016. ISSN 03701972. doi: 10.1002/pssb.201600217. URL <http://doi.wiley.com/10.1002/pssb.201600217>.
- [123] Chung Chiang Wu, Chang Hua Liu, and Zhaohui Zhong. One-Step Direct Transfer of Pristine Single-Walled Carbon Nanotubes for Functional Nanoelectronics. *Nano Letters*, 10(3):1032–1036, mar 2010. ISSN 1530-6984. doi: 10.1021/nl904260k. URL <http://pubs.acs.org/doi/abs/10.1021/nl904260k>.
- [124] J. Waissman, M. Honig, S. Pecker, A. Benyamini, A. Hamo, and S. Ilani. Realization of pristine and locally tunable one-dimensional electron systems in carbon nanotubes. *Nature Nanotechnology*, 8(8):569–574, aug 2013. ISSN 1748-3387. doi: 10.1038/nnano.2013.143. URL <http://www.nature.com/articles/nnano.2013.143>.
- [125] Jörg Gramich, Andreas Baumgartner, Matthias Muoth, Christofer Hierold, and Christian Schönenberger. Fork stamping of pristine carbon nanotubes onto ferromagnetic contacts for spin-valve devices. *physica status solidi (b)*, 252(11):2496–2502, nov 2015. ISSN 03701972. doi: 10.1002/pssb.201552213. URL <http://doi.wiley.com/10.1002/pssb.201552213>.
- [126] S. Blien, P. Steger, A. Albang, N. Paradiso, and A. K. Hüttel. Quartz tuning-fork based carbon nanotube transfer into quantum device geometries. *arXiv*, 1:1–5, 2018. URL <http://arxiv.org/abs/1803.07584>.
- [127] G. A. Steele, A. K. Huttel, B. Witkamp, M. Poot, H. B. Meerwaldt, L. P. Kouwenhoven, and H. S. J. van der Zant. Strong Coupling Between Single-Electron Tunneling and Nanomechanical Motion. *Science*, 325(5944):1103–1107, aug 2009. ISSN 0036-8075. doi: 10.1126/science.1176076. URL <http://www.sciencemag.org/cgi/doi/10.1126/science.1176076>.
- [128] Tal Sharf, Joshua W. Kevek, Tristan DeBorde, Jenna L. Wardini, and Ethan D. Minot. Origins of Charge Noise in Carbon Nanotube Field-Effect Transistor Biosensors. *Nano Letters*, 12(12):6380–6384, dec 2012. ISSN 1530-6984. doi: 10.1021/nl303651t. URL <http://pubs.acs.org/doi/10.1021/nl303651t>.

- [129] M. Goppl, A. Fragner, M. Baur, R. Bianchetti, S. Filipp, J. M. Fink, P. J. Leek, G. Puebla, L. Steffen, and A. Wallraff. Coplanar waveguide resonators for circuit quantum electrodynamics. *Journal of Applied Physics*, 104(11):113904, 2008. ISSN 00218979. doi: 10.1063/1.3010859. URL <http://scitation.aip.org/content/aip/journal/jap/104/11/10.1063/1.3010859>.
- [130] J. Furer. Growth of Single-Wall Carbon Nanotubes by Chemical Vapor Deposition for Electrical Devices. *Thesis*, 2006.
- [131] Zhong Jin, Haibin Chu, Jinyong Wang, Jinxing Hong, Wenchang Tan, and Yan Li. Ultralow Feeding Gas Flow Guiding Growth of Large-Scale Horizontally Aligned Single-Walled Carbon Nanotube Arrays. *Nano Letters*, 7(7):2073–2079, jul 2007. ISSN 1530-6984. doi: 10.1021/nl070980m. URL <http://pubs.acs.org/doi/abs/10.1021/nl070980m>.
- [132] Shaoming Huang, Mike Woodson, Richard Smalley, and Jie Liu. Growth Mechanism of Oriented Long Single Walled Carbon Nanotubes Using Fast-Heating Chemical Vapor Deposition Process. *Nano Letters*, 4(6):1025–1028, jun 2004. ISSN 1530-6984. doi: 10.1021/nl049691d. URL <http://pubs.acs.org/doi/abs/10.1021/nl049691d>.
- [133] Yun Wang and John T W Yeow. A Review of Carbon Nanotubes-Based Gas Sensors. *Journal of Sensors*, 2009:1–24, 2009. ISSN 1687-725X. doi: 10.1155/2009/493904. URL <http://www.hindawi.com/journals/js/2009/493904/>.
- [134] P. G. Collins. Engineering Carbon Nanotubes and Nanotube Circuits Using Electrical Breakdown. *Science*, 292(5517):706–709, apr 2001. ISSN 00368075. doi: 10.1126/science.1058782. URL <http://www.sciencemag.org/cgi/doi/10.1126/science.1058782>.
- [135] Philip G. Collins, M. Hersam, M. Arnold, R. Martel, and Ph. Avouris. Current Saturation and Electrical Breakdown in Multiwalled Carbon Nanotubes. *Physical Review Letters*, 86(14):3128–3131, apr 2001. ISSN 0031-9007. doi: 10.1103/PhysRevLett.86.3128. URL <https://link.aps.org/doi/10.1103/PhysRevLett.86.3128>.

- [136] Ioan M Pop, Kurtis Geerlings, Gianluigi Catelani, Robert J Schoelkopf, Leonid I Glazman, and Michel H Devoret. Coherent suppression of electromagnetic dissipation due to superconducting quasiparticles. *Nature*, 508(7496):369–372, apr 2014. ISSN 0028-0836. doi: 10.1038/nature13017. URL <http://www.nature.com/articles/nature13017>.
- [137] Laure BRUHAT. Microwave as a probe of quantum dot circuits: From Kondo dynamics to mesoscopic quantum electrodynamics. *Thesis*, 2016.
- [138] Jeremie Viennot. Charge and spin dynamics in a hybrid circuit quantum electrodynamics architecture. *Thesis*, 2014.
- [139] D. I. Schuster, A. Wallraff, A. Blais, L. Frunzio, R. S. Huang, J. Majer, S. M. Girvin, and R. J. Schoelkopf. Ac Stark shift and dephasing of a superconducting qubit strongly coupled to a cavity field. *Physical Review Letters*, 94(12):123602, mar 2005. ISSN 00319007. doi: 10.1103/PhysRevLett.94.123602. URL <http://link.aps.org/doi/10.1103/PhysRevLett.94.123602>.
- [140] R. Bianchetti, S. Filipp, M. Baur, J. M. Fink, M. Göppl, P. J. Leek, L. Steffen, A. Blais, and A. Wallraff. Dynamics of dispersive single-qubit readout in circuit quantum electrodynamics. *Physical Review A*, 80(4):043840, oct 2009. ISSN 1050-2947. doi: 10.1103/PhysRevA.80.043840. URL <https://link.aps.org/doi/10.1103/PhysRevA.80.043840>.
- [141] K. W. Murch, U. Vool, D. Zhou, S. J. Weber, S. M. Girvin, and I. Siddiqi. Cavity-Assisted Quantum Bath Engineering. *Physical Review Letters*, 109(18):183602, oct 2012. ISSN 0031-9007. doi: 10.1103/PhysRevLett.109.183602. URL <https://link.aps.org/doi/10.1103/PhysRevLett.109.183602>.
- [142] J. Basset, D.-D. Jarausch, A. Stockklauser, T. Frey, C. Reichl, W. Wegscheider, T. M. Ihn, K. Ensslin, and A. Wallraff. Single-electron double quantum dot dipole-coupled to a single photonic mode. *Physical Review B*, 88(12):125312, sep 2013. ISSN 1098-0121. doi: 10.1103/PhysRevB.88.125312. URL <https://link.aps.org/doi/10.1103/PhysRevB.88.125312>.
- [143] A. Stockklauser, P. Scarlino, J. V. Koski, S. Gasparinetti, C. K. Andersen, C. Reichl, W. Wegscheider, T. Ihn, K. Ensslin, and A. Wallraff. Strong Coupling Cavity QED with Gate-Defined Double Quantum Dots Enabled by a High

- Impedance Resonator. *Physical Review X*, 7(1):011030, mar 2017. ISSN 2160-3308. doi: 10.1103/PhysRevX.7.011030. URL <https://link.aps.org/doi/10.1103/PhysRevX.7.011030>.
- [144] S. M. Albrecht, A. P. Higginbotham, M. Madsen, F. Kuemmeth, T. S. Jespersen, J. Nygård, P. Krogstrup, and C. M. Marcus. Exponential protection of zero modes in Majorana islands. *Nature*, 531(7593):206–209, 2016. ISSN 14764687. doi: 10.1038/nature17162. URL <http://dx.doi.org/10.1038/nature17162>.
- [145] C Janvier, L Tosi, L Bretheau, Ç Ö Girit, M Stern, P Bertet, P Joyez, D Vion, D Esteve, M F Goffman, H Pothier, and C Urbina. Coherent manipulation of Andreev states in superconducting atomic contacts. *Science*, 349(6253):1199–202, 2015. ISSN 1095-9203. doi: 10.1126/science.aab2179. URL <http://www.sciencemag.org/content/349/6253/1199.abstract>.
- [146] L. E. Bruhat, J. J. Viennot, M. C. Dartailh, M. M. Desjardins, T. Kontos, and A. Cottet. Cavity Photons as a Probe for Charge Relaxation Resistance and Photon Emission in a Quantum Dot Coupled to Normal and Superconducting Continua. *Physical Review X*, 6(2):021014, may 2016. ISSN 2160-3308. doi: 10.1103/PhysRevX.6.021014. URL <http://link.aps.org/doi/10.1103/PhysRevX.6.021014>.
- [147] Olivier Sauret, Denis Feinberg, and Thierry Martin. Quantum master equations for the superconductor-quantum dot entangler. *Physical Review B*, 70(24):245313, dec 2004. ISSN 1098-0121. doi: 10.1103/PhysRevB.70.245313. URL <https://link.aps.org/doi/10.1103/PhysRevB.70.245313>.
- [148] Olivier Sauret, Thierry Martin, and Denis Feinberg. Spin-current noise and Bell inequalities in a realistic superconductor-quantum dot entangler. *Physical Review B*, 72(2):024544, jul 2005. ISSN 1098-0121. doi: 10.1103/PhysRevB.72.024544. URL <https://link.aps.org/doi/10.1103/PhysRevB.72.024544>.
- [149] D. Chevallier, J. Rech, T. Jonckheere, and T. Martin. Current and noise correlations in a double-dot Cooper-pair beam splitter. *Physical Review B*, 83(12):125421, mar 2011. ISSN 1098-0121. doi: 10.1103/PhysRevB.83.125421. URL <https://link.aps.org/doi/10.1103/PhysRevB.83.125421>.

- [150] L. Hofstetter, S. Csonka, A. Baumgartner, G. Fülöp, S. D'Hollosy, J. Nygård, and C. Schönenberger. Finite-Bias Cooper Pair Splitting. *Physical Review Letters*, 107(13):136801, sep 2011. ISSN 0031-9007. doi: 10.1103/PhysRevLett.107.136801. URL <https://link.aps.org/doi/10.1103/PhysRevLett.107.136801>.
- [151] A. J. Landig, J. V. Koski, P. Scarlino, U. C. Mendes, A. Blais, C. Reichl, W. Wegscheider, A. Wallraff, K. Ensslin, and T. Ihn. Coherent spinphoton coupling using a resonant exchange qubit. *Nature*, 560(7717):179–184, aug 2018. ISSN 0028-0836. doi: 10.1038/s41586-018-0365-y. URL <http://www.nature.com/articles/s41586-018-0365-y>.
- [152] James Eldridge, Marco G Pala, Michele Governale, and Jürgen König. Superconducting proximity effect in interacting double-dot systems. *Physical Review B*, 82(18):184507, nov 2010. ISSN 1098-0121. doi: 10.1103/PhysRevB.82.184507. URL <https://link.aps.org/doi/10.1103/PhysRevB.82.184507>.
- [153] Simon E Nigg, Rakesh P Tiwari, Stefan Walter, and Thomas L Schmidt. Detecting nonlocal Cooper pair entanglement by optical Bell inequality violation. *Physical Review B*, 91(9):094516, mar 2015. ISSN 1098-0121. doi: 10.1103/PhysRevB.91.094516. URL <https://link.aps.org/doi/10.1103/PhysRevB.91.094516>.
- [154] Mark Friesen, Joydip Ghosh, M. A. Eriksson, and S. N. Coppersmith. A decoherence-free subspace in a charge quadrupole qubit. *Nature Communications*, 8(May):1–7, 2017. ISSN 20411723. doi: 10.1038/ncomms15923. URL <http://dx.doi.org/10.1038/ncomms15923>.
- [155] V. Srinivasa, Jacob M Taylor, and Charles Tahan. Entangling distant resonant exchange qubits via circuit quantum electrodynamics. *arXiv:1603.04829*, pages 55–61, 2016. ISSN 2469-9950. doi: 10.1051/0004-6361/201527236. URL <http://arxiv.org/abs/1603.04829>.
- [156] Maximilian Russ and Guido Burkard. Long distance coupling of resonant exchange qubits. *Physical Review B*, 92(20):205412, nov 2015. ISSN 1098-0121. doi: 10.1103/PhysRevB.92.205412. URL <https://link.aps.org/doi/10.1103/PhysRevB.92.205412>.
- [157] J. Stehlik, Y.-Y. Liu, C. Eichler, T. R. Hartke, X. Mi, M. J. Gullans, J. M. Taylor, and J. R. Petta. Double Quantum Dot Floquet Gain Medium. *Physical Review X*,

- 6(4):041027, nov 2016. ISSN 2160-3308. doi: 10.1103/PhysRevX.6.041027. URL <https://link.aps.org/doi/10.1103/PhysRevX.6.041027>.
- [158] Y.-Y. Liu, J Stehlik, C Eichler, M J Gullans, J M Taylor, and J R Petta. Semiconductor double quantum dot micromaser. *Science*, 347(6219):285–287, jan 2015. ISSN 0036-8075. doi: 10.1126/science.aaa2501. URL <http://www.sciencemag.org/cgi/doi/10.1126/science.aaa2501>.
- [159] Y.-Y. Liu, J. Stehlik, M. J. Gullans, J. M. Taylor, and J. R. Petta. Injection locking of a semiconductor double-quantum-dot micromaser. *Physical Review A*, 92(5):053802, nov 2015. ISSN 1050-2947. doi: 10.1103/PhysRevA.92.053802. URL <https://link.aps.org/doi/10.1103/PhysRevA.92.053802>.
- [160] A. Cottet, D. Vion, A. Aassime, P. Joyez, D. Esteve, and M.H. Devoret. Implementation of a combined charge-phase quantum bit in a superconducting circuit. *Physica C: Superconductivity*, 367(1-4):197–203, feb 2002. ISSN 09214534. doi: 10.1016/S0921-4534(01)01014-0. URL <http://linkinghub.elsevier.com/retrieve/pii/S0921453401010140>.
- [161] Maximilian Russ, Florian Ginzl, and Guido Burkard. Coupling of three-spin qubits to their electric environment. *Physical Review B*, 94(16):165411, oct 2016. ISSN 2469-9950. doi: 10.1103/PhysRevB.94.165411. URL <https://link.aps.org/doi/10.1103/PhysRevB.94.165411>.
- [162] Audrey Cottet, Takis Kontos, and Benoit Douçot. Squeezing light with Majorana fermions. *Physical Review B*, 88(19):195415, nov 2013. ISSN 1098-0121. doi: 10.1103/PhysRevB.88.195415. URL <https://link.aps.org/doi/10.1103/PhysRevB.88.195415>.
- [163] Matthieu C. Dartiailh, Takis Kontos, Benoit Douçot, and Audrey Cottet. Direct Cavity Detection of Majorana Pairs. *Physical Review Letters*, 118(12):126803, mar 2017. ISSN 0031-9007. doi: 10.1103/PhysRevLett.118.126803. URL <https://link.aps.org/doi/10.1103/PhysRevLett.118.126803>.
- [164] Guido Burkard and Atac Imamoglu. Ultra-long-distance interaction between spin qubits. *Physical Review B*, 74(4):041307, jul 2006. ISSN 1098-0121. doi: 10.1103/PhysRevB.74.041307. URL <https://link.aps.org/doi/10.1103/PhysRevB.74.041307>.

- [165] Mircea Trif, Vitaly N. Golovach, and Daniel Loss. Spin dynamics in InAs nanowire quantum dots coupled to a transmission line. *Physical Review B*, 77(4):045434, jan 2008. ISSN 1098-0121. doi: 10.1103/PhysRevB.77.045434. URL <https://link.aps.org/doi/10.1103/PhysRevB.77.045434>.
- [166] Xuedong Hu, Yu-xi Liu, and Franco Nori. Strong coupling of a spin qubit to a superconducting stripline cavity. *Physical Review B*, 86(3):035314, jul 2012. ISSN 1098-0121. doi: 10.1103/PhysRevB.86.035314. URL <https://link.aps.org/doi/10.1103/PhysRevB.86.035314>.
- [167] S. P. Harvey, C. G. L. Böttcher, L. A. Orona, S. D. Bartlett, A. C. Doherty, and A. Yacoby. Coupling two spin qubits with a high-impedance resonator. *Physical Review B*, 97(23):235409, jun 2018. ISSN 2469-9950. doi: 10.1103/PhysRevB.97.235409. URL <https://link.aps.org/doi/10.1103/PhysRevB.97.235409>.
- [168] T. Pei, A. Pályi, M. Mergenthaler, N. Ares, A. Mavalankar, J. H. Warner, G. A. D. Briggs, and E. A. Laird. Hyperfine and Spin-Orbit Coupling Effects on Decay of Spin-Valley States in a Carbon Nanotube. *Physical Review Letters*, 118(17):177701, apr 2017. ISSN 0031-9007. doi: 10.1103/PhysRevLett.118.177701. URL <http://link.aps.org/doi/10.1103/PhysRevLett.118.177701>.
- [169] M. Benito, X. Mi, J. M. Taylor, J. R. Petta, and Guido Burkard. Input-output theory for spin-photon coupling in Si double quantum dots. *Physical Review B*, 96(23):235434, dec 2017. ISSN 2469-9950. doi: 10.1103/PhysRevB.96.235434. URL <https://link.aps.org/doi/10.1103/PhysRevB.96.235434>.
- [170] Chung Chiang Wu, Chang Hua Liu, and Zhaohui Zhong. One-Step Direct Transfer of Pristine Single-Walled Carbon Nanotubes for Functional Nanoelectronics. *Nano Letters*, 10(3):1032–1036, mar 2010. ISSN 1530-6984. doi: 10.1021/nl904260k. URL <http://pubs.acs.org/doi/abs/10.1021/nl904260k>.
- [171] J. Waissman, M. Honig, S. Pecker, A. Benyamini, A. Hamo, and S. Ilani. Realization of pristine and locally tunable one-dimensional electron systems in carbon nanotubes. *Nature Nanotechnology*, 8(8):569–574, aug 2013. ISSN 1748-3387. doi: 10.1038/nnano.2013.143. URL <http://www.nature.com/articles/nnano.2013.143>.

- [172] V Ranjan, G Puebla-Hellmann, M Jung, T Hasler, A Nunnenkamp, M Muoth, C Hierold, A Wallraff, and C Schönenberger. Clean carbon nanotubes coupled to superconducting impedance-matching circuits. *Nature Communications*, 6(1):7165, dec 2015. ISSN 2041-1723. doi: 10.1038/ncomms8165. URL <http://www.nature.com/articles/ncomms8165>.
- [173] Edward A. Laird, Ferdinand Kuemmeth, Gary A. Steele, Kasper Grove-Rasmussen, Jesper Nygård, Karsten Flensberg, and Leo P. Kouwenhoven. Quantum transport in carbon nanotubes. *Reviews of Modern Physics*, 87(3):703–764, jul 2015. ISSN 0034-6861. doi: 10.1103/RevModPhys.87.703. URL <https://link.aps.org/doi/10.1103/RevModPhys.87.703>.
- [174] J.-Y. Chauleau, B. J. McMorran, R. Belkhou, N. Bergéard, T. O. Mente, M.Á. Niño, A. Locatelli, J. Unguris, S. Rohart, J. Miltat, and A. Thiaville. Magnetization textures in NiPd nanostructures. *Physical Review B*, 84(9):094416, sep 2011. ISSN 1098-0121. doi: 10.1103/PhysRevB.84.094416. URL <https://link.aps.org/doi/10.1103/PhysRevB.84.094416>.
- [175] Audrey Cottet. Microwave spectroscopy of a Cooper pair beam splitter. *Physical Review B*, 86(7):075107, aug 2012. ISSN 1098-0121. doi: 10.1103/PhysRevB.86.075107. URL <https://link.aps.org/doi/10.1103/PhysRevB.86.075107>.
- [176] Kacper Wrześniewski, Piotr Trocha, and Ireneusz Weymann. Current cross-correlations in double quantum dot based Cooper pair splitters with ferromagnetic leads. *Journal of Physics: Condensed Matter*, 29(19):195302, may 2017. ISSN 0953-8984. doi: 10.1088/1361-648X/aa682d. URL <http://stacks.iop.org/0953-8984/29/i=19/a=195302?key=crossref.03ea30f428e95c9f8141f15f12d6e4d5>.
- [177] Martin Leijnse and Karsten Flensberg. Coupling Spin Qubits via Superconductors. *Physical Review Letters*, 111(6):060501, aug 2013. ISSN 0031-9007. doi: 10.1103/PhysRevLett.111.060501. URL <https://link.aps.org/doi/10.1103/PhysRevLett.111.060501>.